



UNIVERSITÄT ROSTOCK

# Computational Challenges in Many-Particle Simulations of Extreme Matter

Kumulative Dissertation  
zur Erlangung des akademischen Grades  
doctor rerum naturalium (Dr. rer. nat.)  
der Mathematisch-Naturwissenschaftlichen Fakultät  
der Universität Rostock

vorgelegt von  
**Maximilian Tobias Schörner**,  
geboren am 5. Juli 1995 in Witten

Rostock, August 21, 2023

[https://doi.org/10.18453/rosdok\\_id00004533](https://doi.org/10.18453/rosdok_id00004533)

Datum der Disputation: 19. Dezember 2023

1. Gutachter und Betreuer: Prof. Dr. R. Redmer
2. Gutachter und Betreuer: Prof. Dr. S.H. Glenzer
3. Gutachter: Prof. Dr. S. Scandolo
4. Gutachter: Dr. T. Tschentscher

Adresse: Universität Rostock  
Institut für Physik  
18051 Rostock

Tel: +49 381 498-6914

Internet: <http://www.physik.uni-rostock.de>

E-Mail: [maximilian.schoerner@uni-rostock.de](mailto:maximilian.schoerner@uni-rostock.de)

# Abstract

A profound understanding of warm dense matter (WDM) properties is essential to unraveling the mysteries of planetary and stellar formation, evolution, and interior structure, as well as establishing inertial confinement fusion as a potential energy source. In the center of attention is the dynamic behavior of such matter, which can be characterized in terms of material, transport, and optical properties, e.g., conductivity, opacity, and sound speed. Powerful laser facilities such as the National Ignition Facility (NIF) are capable of recreating these high-pressure states in the laboratory. In addition, recent innovations to the spectral resolution at X-ray free electron laser (XFEL) facilities now enable studying ion dynamics in shock compression experiments. The computational side of WDM research is faced with the challenge of leveraging these experimental capabilities. This thesis combines modern machine-learning approaches with *ab initio* simulation to overcome some of the challenges and enhance the interface of simulations and experiments. In the context of scattering experiments, the dynamic structure factor (DSF) of the ions and electrons is employed to connect the simulations with scattering experiments on different energy scales.

Neural-network-based potentials are employed to connect the microscopic ion dynamics observed in simulations with material and transport properties in the hydrodynamic limit. Combined with the improved spectral resolution at XFEL facilities, which permits the measurement of the ionic DSF, this enables the study of material and transport properties at extreme conditions.

Furthermore, the DSF of the electrons is computed from density functional theory molecular dynamics (DFT-MD) simulations and compared to analytic descriptions that are traditionally used in WDM scattering experiments. This enables insights into the ionization state and the electron-ion collision frequency in extreme matter.

Both electron and ion dynamics are simulated in a consistent *ab initio* framework to analyze an X-ray Thomson scattering experiment at the NIF. On the basis of these simulations, a Bayesian analysis of the scattering spectra, accounting for the influence of the intricate experimental setup on the results, reveals that the experiment reached conditions present in the interior of red dwarfs.

Finally, electrical conductivity, which is one of the properties of interest in collective scattering experiments, is studied. The long-standing question of whether electron-electron collisions are included in the electrical conductivity computed via the Kubo-Greenwood formula is resolved. It is shown that, in the ideal plasma limit, the direct current electrical conductivity only accounts for electron-ion collisions.

The methodological advances presented in this thesis will aid in establishing robust platforms for studying matter in extreme conditions at modern XFEL and high-powered laser facilities.

# Kurzzusammenfassung

Ein tiefgreifendes Verständnis der Eigenschaften von warmer dichter Materie (WDM) ist unerlässlich, um die Geheimnisse der Planeten- und Sternentstehung, der Evolution und der inneren Struktur zu lüften und die Trägheitsfusion als potenzielle Energiequelle zu etablieren. Im Mittelpunkt des Interesses steht das dynamische Verhalten dieser Materie, das anhand von Material-, Transport- und optischen Eigenschaften wie Leitfähigkeit, Opazität und Schallgeschwindigkeit charakterisiert werden kann. Leistungsstarke Laseranlagen wie die National Ignition Facility (NIF) sind in der Lage, diese Hochdruckzustände im Labor nachzubilden. Darüber hinaus ermöglichen die jüngsten Innovationen bei der spektralen Auflösung von Röntgen-Freielektronen-Lasern (XFEL) nun die Untersuchung der Ionendynamik in Stoßkompressionsexperimenten. Die computergestützte Seite der WDM-Forschung steht vor der Herausforderung, diese experimentellen Möglichkeiten zu nutzen. In dieser Arbeit werden moderne Ansätze des maschinellen Lernens mit Ab-Initio-Simulationen kombiniert, um einige der Herausforderungen zu bewältigen und die Schnittstelle zwischen Simulationen und Experimenten zu verbessern. Im Zusammenhang mit Streuexperimenten wird der dynamische Strukturfaktor (DSF) der Ionen und Elektronen verwendet, um die Simulationen mit Streuexperimenten auf verschiedenen Energieskalen zu verbinden.

Auf neuronalen Netzen basierende Potenziale werden eingesetzt, um die in Simulationen beobachtete mikroskopische Ionendynamik mit Material- und Transporteigenschaften im hydrodynamischen Grenzbereich zu verbinden. In Kombination mit der verbesserten spektralen Auflösung an XFEL-Anlagen, die die Messung des ionischen DSF erlaubt, ermöglicht dies die Untersuchung von Material- und Transporteigenschaften unter extremen Bedingungen.

Darüber hinaus wird der DSF der Elektronen aus Simulationen der Dichtefunktionaltheorie mit Molekulardynamik (DFT-MD) berechnet und mit analytischen Beschreibungen verglichen, die traditionell in WDM-Streuexperimenten verwendet werden. Dies ermöglicht Einblicke in den Ionisationszustand und die Elektron-Ionen-Kollisionsfrequenz in extremer Materie.

Sowohl die Elektronen- als auch die Ionendynamik werden in einem konsistenten ab-initio-Rahmen simuliert, um ein Röntgen-Thomson-Streuungsexperiment am NIF zu analysieren. Auf der Grundlage dieser Simulationen zeigt eine Bayes'sche Analyse der Streuspektren, die den Einfluss des komplizierten Versuchsaufbaus auf die Ergebnisse berücksichtigt, dass das Experiment Bedingungen im Inneren von Roten Zwergen erreicht hat.

Schließlich wird die elektrische Leitfähigkeit, eine der Eigenschaften, die bei Experimenten zur kollektiven Streuung von Interesse ist, untersucht. Die seit langem bestehende Frage, ob Elektron-Elektron-Kollisionen in die mit der Kubo-Greenwood-Formel berechnete elektrische Leitfähigkeit einbezogen werden, wird geklärt. Es wird gezeigt, dass im idealen Plasmalimit die elektrische Gleichstromleitfähigkeit nur Elektron-Ionen-Kollisionen berücksichtigt.

Die in dieser Arbeit vorgestellten methodischen Fortschritte werden dazu beitragen, robuste Plattformen für die Untersuchung von Materie unter extremen Bedingungen an modernen XFEL- und Hochleistungslaseranlagen zu schaffen.



# Contents

<b>1</b>	<b>Introduction</b>	<b>1</b>
1.1	Characterization of warm dense matter . . . . .	2
1.2	Warm dense matter experiments . . . . .	4
1.2.1	Achieving extreme conditions . . . . .	4
1.2.2	Diagnosing extreme conditions . . . . .	6
1.3	Outline of this thesis . . . . .	10
<b>2</b>	<b>Computational methods</b>	<b>11</b>
2.1	Density functional theory molecular dynamics . . . . .	11
2.2	Ion dynamics . . . . .	15
2.2.1	High-dimensional neural network potential . . . . .	17
2.2.2	Generalized collective modes . . . . .	19
2.3	Electron dynamics . . . . .	20
2.3.1	Linear-response time-dependent density functional theory . . . . .	22
2.3.2	Electrical conductivity . . . . .	23
2.4	Bayesian inference . . . . .	24
<b>3</b>	<b>Results</b>	<b>27</b>
3.1	New insights into ion dynamics at extreme conditions through high-dimensional neural network potentials [Papers I & II] . . . . .	28
3.2	Inelastic electronic dynamic structure factor at extreme conditions [Papers III & IV] . . . . .	31
3.3	Collective X-ray Thomson scattering at the National Ignition Facility [Paper V] . . . . .	34
3.4	Benchmarking density functional theory conductivity in the ideal-plasma limit [Papers VI & VII] . . . . .	37
3.5	Additional publications . . . . .	40
3.6	Ongoing work at high-energy-density facilities . . . . .	41
3.6.1	GSI facility & European X-ray free electron laser . . . . .	41
3.6.2	Linac Coherent Light Source . . . . .	44
3.7	Summary and outlook . . . . .	45
<b>4</b>	<b>Publications</b>	<b>47</b>
4.1	Extending <i>ab initio</i> simulations for the ion-ion structure factor of warm dense aluminum to the hydrodynamic limit using neural network potentials . . . . .	47
4.2	<i>Ab initio</i> study of shock-compressed copper . . . . .	60
4.3	X-ray Thomson scattering spectra from density functional theory molecular dynamics simulations based on a modified Chihara formula . . . . .	73
4.4	Carbon ionization at gigabar pressures: An <i>ab initio</i> perspective on astrophysical high-density plasmas . . . . .	88
4.5	Reaching for the stars with an <i>ab initio</i> perspective on collective x-ray Thomson scattering at the National Ignition Facility . . . . .	96

---

4.6	Virial expansion of the electrical conductivity of hydrogen plasmas . . . . .	106
4.7	Electronic transport coefficients from density functional theory across the plasma plane . . . . .	114
	<b>Bibliography</b>	<b>124</b>
	<b>Curriculum vitae</b>	<b>151</b>

## List of abbreviations

<b>ACSF</b>	atom-centered symmetry function . . . . .	18
<b>ALDA</b>	adiabatic local density approximation . . . . .	22
<b>BD</b>	brown dwarf . . . . .	3
<b>C-LFE</b>	crystal LFE . . . . .	21
<b>DAC</b>	diamond anvil cell . . . . .	5
<b>DFT</b>	density functional theory . . . . .	2
<b>DFT-MD</b>	DFT coupled with molecular dynamics . . . . .	2
<b>DOS</b>	density of states . . . . .	32
<b>DSF</b>	dynamic structure factor . . . . .	2
<b>eDSF</b>	electron-electron DSF . . . . .	7
<b>eSSF</b>	electron-electron SSF . . . . .	9
<b>EOS</b>	equation of state . . . . .	1
<b>EuXFEL</b>	European XFEL . . . . .	4
<b>FAIR</b>	Facility for Antiproton and Ion Research . . . . .	4
<b>FLASH</b>	Free Electron LASer Hamburg . . . . .	40
<b>GAP</b>	Gaussian approximation potentials . . . . .	17
<b>GCM</b>	generalized collective modes . . . . .	19
<b>GGA</b>	generalized gradient approximation . . . . .	14
<b>HDNNP</b>	high-dimensional neural network potential . . . . .	17
<b>HIBEF</b>	Helmholtz International Beamline for Extreme Fields . . . . .	4
<b>HSE</b>	hybrid functional by Heyd, Scuseria, and Ernzerhof . . . . .	14
<b>ICF</b>	inertial confinement fusion . . . . .	3
<b>iDSF</b>	ion-ion DSF . . . . .	7
<b>iSSF</b>	ion-ion SSF . . . . .	9
<b>KS</b>	Kohn-Sham . . . . .	13
<b>LCLS</b>	Linac Coherent Light Source . . . . .	4
<b>LDA</b>	local density approximation . . . . .	14
<b>LFE</b>	local field effect . . . . .	21
<b>LMJ</b>	Laser Mégajoule . . . . .	3
<b>LR-TDDFT</b>	linear-response TDDFT . . . . .	4
<b>MCF</b>	magnetic confinement fusion . . . . .	3
<b>MCMC</b>	Markov-Chain Monte-Carlo . . . . .	25
<b>NIF</b>	National Ignition Facility . . . . .	3
<b>PBE</b>	GGA by Perdew, Burke, and Ernzerhof . . . . .	14
<b>PIMC</b>	path integral Monte Carlo . . . . .	4
<b>RPA</b>	random phase approximation . . . . .	7
<b>RTA</b>	relaxation time approximation . . . . .	36
<b>RT-TDDFT</b>	real-time TDDFT . . . . .	4

<b>SNAP</b>	spectral neighbor analysis potentials . . . . .	17
<b>SOP</b>	streaked optical pyrometry . . . . .	6
<b>SSF</b>	static structure factor . . . . .	2
<b>TDDFT</b>	time-dependent DFT . . . . .	4
<b>VISAR</b>	velocity interferometer system for any reflector . . . . .	6
<b>WD</b>	white dwarf . . . . .	3
<b>WDM</b>	warm dense matter . . . . .	1
<b>XC</b>	exchange-correlation . . . . .	13
<b>XC-LFE</b>	exchange-correlation LFE . . . . .	22
<b>XFEL</b>	X-ray free electron laser . . . . .	4
<b>XRTS</b>	X-ray Thomson scattering . . . . .	6

# 1 Introduction

It is often believed that more than 99% of visible matter in the universe is in the plasma state [1–4], where plasma is a state of matter characterized by the presence of separate charged particles, e.g., ions and electrons. In our solar system, it is even estimated to be over 99.98% [2] due to the large fraction of mass made up by the Sun. While matter at the core of our Sun reaches temperatures of up to  $1.5 \times 10^7$  K [5, 6], many of the most exciting phenomena in the solar system are determined by more moderate plasmas. Due to the lower temperatures, the correlations between the charged particles and the quantum mechanical degeneracy play a significant role. This state of matter is termed warm dense matter (WDM) and is loosely defined by matter between the condensed matter and ideal plasma regime. Some of the phenomena driven by the behavior of WDM are the geo dynamo that produces the magnetic field of Earth [7–10], as well as dynamos in other planets [11], e.g., Mars [12], Mercury [13], Jupiter [14], and Saturn [15]. Additionally, high-pressure chemistry in WDM leads to interesting occurrences in planetary interiors, such as the demixing of hydrogen and helium, which produces helium rain in the gas giant planets [16–18]. Moreover, due to the phase separation of hydrogen and carbon, diamonds are proposed to form in the interior of Uranus and Neptune [19–21]. The gravitational energy released by the sinking diamonds might help explain the long-standing issue of differing luminosities in these planets [22, 23].

Furthermore, observations beyond our solar system can provide insight into planetary formation and evolution. In 1995, an exoplanet (51 Pegasi b) orbiting a Sun-like star was detected for the first time [24]. Despite being relatively massive (approximately half of Jupiter’s mass), it was observed to have a close orbit with a duration of less than five days, which called into question our understanding of planetary formation and evolution [25]. This led to the introduction of a new classification of planets, called hot Jupiters, which were commonly observed in subsequent observations of exoplanets by space telescopes, such as Hubble [26] and the Spitzer space telescope [27]. Additionally, other classes of planets which are very atypical for our solar system, e.g., super-Earths and mini-Neptunes, have since been discovered, highlighting the variety of exoplanets and the need to look beyond our solar system to understand planetary formation further. With the James Webb Space Telescope [28] and the European Space Agency-lead PLATO [29] mission coming online, another drastic increase in the number of observed exoplanets is expected. This will further facilitate the search for habitable planets and possible life forms inhabiting them, which has become one of the most critical drivers of exoplanetary research and related fields such as astrobiology. To this end, it is vital to understand how the makeup and behavior of host stars, e.g., their magnetic field and solar flare activity, impact the habitable zone. For instance, the dynamo of red dwarfs [30] was suggested to affect the habitability of orbiting planets [31]. Planetary as well as stellar evolution and structure models rely on equation of state (EOS) data and predictions for transport and material properties, e.g., thermal and electrical conductivity, diffusion, and viscosity, of WDM. Due to its strongly correlated nature with non-negligible degeneracy, it is demanding to model theoretically, requiring computationally expensive many-body simulations. Experimentally, the study of WDM is also challenging on account of the extreme pressure and temperature required. Therefore, the research field of WDM greatly depends on the interplay between simulations and experiments to accurately describe stellar and planetary matter, which can subsequently be used in astrophysical modeling. Observations from space missions and telescopes, e.g., the composition of the outer atmosphere of exoplanets or the gravitational moments, can then constrain these models.

The emergence of machine learning and artificial intelligence promises to alleviate some of the computational restrictions in WDM simulations and help interpret experimental data.

Artificial intelligence has brought about many innovations impacting the general public. Over the last decade, neural-network-based algorithms have beaten humans in popular board games such as chess and Go [32, 33] and predicted protein folding [34], among other achievements. The invention of transformers [35] has enabled the creation of large language models [36], which drive state-of-the-art chatbots and are becoming part of ubiquitous search engines. Furthermore, machine learning approaches, especially neural networks, are applied widely in various areas of the natural sciences [34, 37–40] and have allowed us to overcome previously insurmountable numerical limitations. Also, other machine learning methods, such as Bayesian inference, are applied in astrophysical modeling and observation [39, 41], as well as the analysis of scattering and diffraction experiments [42–45]. Recently, more of these approaches have started to be used in WDM [46–48], enabling the simulation of macroscopic systems at a significantly lower computational cost. Additionally, sophisticated many-body techniques from solid-state theory, such as the real-space Green’s function method [49], the Bethe-Salpeter equation [50], or density functional theory (DFT), have started to be applied more in WDM [51, 52] over the last decades. In this thesis, DFT coupled with molecular dynamics (DFT-MD) is the method of choice to describe the strong many-body correlations in WDM.

This thesis concerns the interface of WDM simulations and experiments. It explores how sophisticated machine learning techniques can enhance both the simulations and the way they are used to analyze experimental data. Additionally, it explores how sophisticated many-body approaches can be related to analytic approaches traditionally used in WDM experiments. Due to the relevance of experimental studies for computational WDM research, a general characterization of the density-temperature plane and a broad overview of experimental capabilities to reach different regimes in that plane are presented in the following sections. Some of the premier diagnostic tools in WDM experiments are discussed with a focus on diffraction and scattering experiments. In this context, the dynamic structure factor (DSF) and the static structure factor (SSF) of ions and electrons are introduced. They can be computed from the microscopic information in the simulations, as detailed in Chapter 2, but also have immense predictive power for diffraction and scattering experiments. Lastly, at the end of this chapter, a detailed outline of the computational methods and research in this thesis is presented.

## 1.1 Characterization of warm dense matter

WDM is a state of matter between condensed matter and plasma physics. It is characterized by temperatures between 0.1 – 100 eV (1 eV  $\approx$  11605 K) and densities from solid density up to very high compression [53]. In the low-temperature regime, quantum mechanical degeneracy, enforced by the antisymmetry of fermionic wave functions under exchange of quantum numbers, and strong correlations, mediated via Coulomb interaction, dominate the behavior of matter. In the condensed matter limit, idealizations, e.g., the description of electrons in a perfect lattice as Bloch states, can be made due to the long-range order at low temperatures. Contrarily, in the high-temperature limit of an ideal plasma, the high thermal energy makes matter homogeneous, and approximations such as the Jellium model are applicable. However, in the intermediate regime, both quantum mechanical degeneracy and correlations between charged particles are relevant. To characterize different regimes in the density-temperature plane, the degeneracy parameter  $\Theta$  and correlation parameter  $\Gamma$  can be used; see Fig. 1.1. The degeneracy parameter

$$\Theta = \frac{E_{\text{Th}}}{E_{\text{F}}} = \frac{2m_e k_{\text{B}} T}{\hbar^2} \left( \frac{1}{3\pi^2 \bar{n}_e} \right)^{2/3} \quad (1.1)$$

is defined by the ratio of thermal energy  $E_{\text{Th}}$  and the Fermi energy  $E_{\text{F}}$  and measures the relevance of quantum mechanical degeneracy to the behavior of matter. Here,  $m_e$  is the

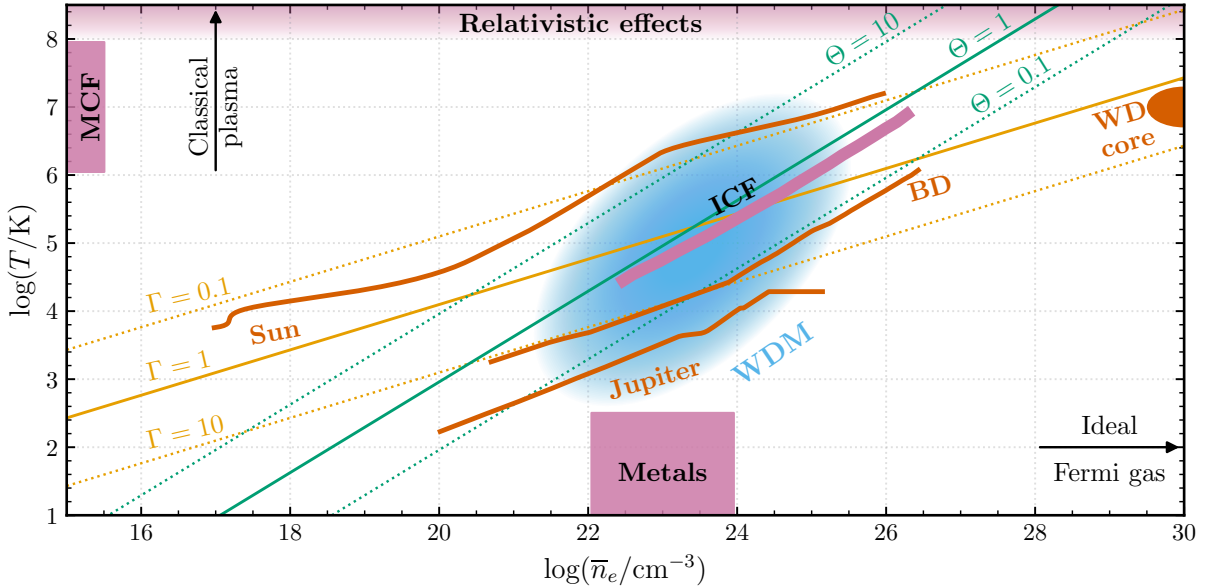


**Figure 1.1:** Electron density  $\bar{n}_e$  and temperature  $T$  plane modeled after Refs. [54, 55]. The degeneracy and correlation parameters characterize the range of conditions; see Eqs. (1.1) and (1.2). The blue-shaded area indicates the approximate location of WDM. Relevant regions for magnetic confinement fusion (MCF) [56], inertial confinement fusion (ICF) [57], relativistic effects [58], and some astrophysical objects, i.e., Jupiter, the Sun, a brown dwarf (BD), and a white dwarf (WD) core [59–61], are indicated. Density profiles of the astrophysical objects are converted to  $\bar{n}_e$  by assuming a fully ionized hydrogen plasma.

electron mass,  $k_B$  is the Boltzmann constant,  $T$  is the temperature and  $\bar{n}_e$  denotes the average electron density.

The correlation parameter

$$\Gamma = \frac{E_C}{E_{Th}} = \frac{e^2}{4\pi\epsilon_0 k_B T} \left( \frac{4\pi\bar{n}_e}{3} \right)^{1/3} \quad (1.2)$$

gives a measure of the importance of correlation effects. Here, the Coulomb energy is denoted by  $E_C$ ,  $e$  is the elementary charge, and  $\epsilon_0$  is the vacuum permittivity. In WDM, both ideal plasma theory and solid state approaches that rely on lattice structures are not applicable. Additionally, the parameters introduced in Eqs. (1.1) and (1.2) are of order 1 in WDM, as can be seen in Fig. 1.1, which prevents analytic perturbation expansions in a suitable small parameter. Consequently, sophisticated many-body approaches that account for quantum mechanical effects must be employed. Despite the theoretical challenges, a profound understanding of matter at WDM conditions is essential for astrophysical modeling, as discussed at the beginning of this chapter. Figure 1.1 demonstrates how several astrophysical objects from our solar system and beyond intersect the WDM region. Only a few selected objects in this regime are shown for illustration; a more exhaustive list can be found in Refs. [53, 62, 63]. Additional practical applications involve the synthesis of novel materials [20, 64, 65] and inertial confinement fusion (ICF) as performed at facilities like the National Ignition Facility (NIF) [66, 67], the OMEGA laser [68] or the Laser Mégajoule (LMJ) [69] among others. In a recent breakthrough, successful ignition was achieved at the NIF [70], promising a revolution in commercial energy generation over the following decades. Figure 1.1 shows the implosion pathway of a deuterium-tritium capsule towards ignition, which passes through the WDM regime [57]. For a more thorough characterization of WDM, see Refs. [54, 55, 71–73].

One of the most popular choices for simulating WDM is DFT-MD using the Kohn-Sham description of DFT; see Sec. 2.1. Some popular extensions and variations of this approach are

orbital-free DFT-MD [74, 75] and time-dependent DFT (TDDFT). The latter can be expressed in its linear response formulation, termed linear-response TDDFT (LR-TDDFT), which is described in Sec. 2.3.1, or its real-time formulation, termed real-time TDDFT (RT-TDDFT) [76–79]. A valuable approach that circumvents some approximations needed in DFT-based methods is path integral Monte Carlo (PIMC) simulations [80–83]. While it is currently restricted to simulations of low- $Z$  materials, e.g., hydrogen and helium, it provides essential reference data for the uniform electron gas.

## 1.2 Warm dense matter experiments

WDM not only poses a substantial theoretical challenge, as discussed in Sec. 1.1 but also requires careful experimental deliberation. If the conditions present in the interior of massive astrophysical objects are to be reproduced in the laboratory, many practical limitations must be considered. Some of the challenges include e.g., sustaining such conditions by an appropriate containment and the inference of properties of interest in the presence of experimental noise. The capability to statically or dynamically induce the warm dense matter state, often via powerful lasers, is required. Furthermore, the ability to extract properties of interest from the target via, e.g., scattering, diffraction, interferometry, or emission spectra measurements must be given.

Due to the considerable challenges of studying WDM at pressures above a few 100 GPa, experiments are primarily performed at a few large-scale facilities worldwide. The high densities reached in these experiments lead to high plasma frequencies, necessitating hard X-rays to penetrate the sample. Furthermore, the most extreme achievable states can only be produced transiently, leading to the need for high brilliance in the probe beam. This is the reason for the prevalence of X-ray free electron lasers (XFELs) in the study of WDM over the traditional synchrotron X-ray sources [84]. Specifically, the Linac Coherent Light Source (LCLS) in Stanford [85, 86] and its current upgrade to the LCLS-II [87], as well as the the European XFEL (EuXFEL) [88], especially the Helmholtz International Beamline for Extreme Fields (HIBEF) [89] represent the state of the art for XFELs in the world.

The most powerful laser system in the world is available at the NIF within the Discovery Science program [90, 91], allowing experimental studies up to the Gbar regime. The OMEGA laser system in Rochester [92] was used heavily in the early development of the WDM field [93–99]. Recently, the capabilities of heavy ion beams, such as at the GSI Helmholtz Centre for Heavy Ion Research [100] and the planned Facility for Antiproton and Ion Research (FAIR) [21, 101–103], have been used more frequently to create and study WDM.

The facilities listed above represent the facilities relevant to the studies presented in this thesis, but the list is far from exhaustive. Various additional XFELs [104], high-powered laser and pulsed power facilities [105–107] are available.

### 1.2.1 Achieving extreme conditions

High temperatures and high densities characterize extreme conditions. The latter can be achieved via compression, where dynamic compression also induces higher temperatures in the target. High temperatures without applying mechanical stress can be accomplished by highly energetic radiation interacting with the target. For a general overview of dynamic and static compression experiments and more detail on the theory of shock compression, see Refs. [108, 109]. Here, a short overview of the most prevalent approaches in WDM experiments is given.



### Dynamic compression

In the simplest case of a rapid (faster than the sound speed) planar shock, it traverses as a discontinuity in density  $\rho$ , pressure  $P$ , and energy  $E$  through the target, where on one side of the discontinuity lies the unshocked material (denoted by subscript 0) and on the other side lies the shocked material (denoted by subscript 1). Using conservation laws of mass, momentum, and energy, an equation for shock compression, the Hugoniot-Rankine relation [110–113]

$$E_1 - E_0 = \frac{1}{2} (P_1 + P_0) \left( \frac{1}{\rho_0} - \frac{1}{\rho_1} \right) \quad (1.3)$$

can be derived. This equation can be solved with a given EOS, resulting in a locus of states achievable via shock compression. EOS data based on DFT-MD simulations have been successfully used in various applications to shock compression experiments [18, 114, 115].

The shock can be induced into the target via a flyer plate accelerated by a gas gun [116–118] or an electromagnetic pulse, e.g., via the Z machine at Sandia [106]. Historically, high explosives in contact with the target [119–121] were also used to produce shocks. Over recent decades, laser-induced shocks have become popular due to the control over the type of induced shock via pulse shaping. In these experiments, the laser irradiates an ablator attached to the target’s surface. The ablator expands outwards and, due to the conservation of momentum, drives a shock into the target. This type of shock is achieved via a flat-top pulse shape with a steep rise, leading to a compression mediated through the target faster than the sound speed. A ramp compression, however, is achieved via a slowly rising pulse shape that induces a series of weak shocks with increasing magnitude. As a result, the target is compressed rapidly enough to avoid heat flow but slowly enough that no shock is induced, leading to a quasi-isentropic compression [122, 123]. This avoids the steep temperature increase at high pressures characteristic of the Hugoniot curve, opening up a new region of  $P$ - $T$  space for experimental investigation. Further techniques to investigate various  $P$ - $T$  conditions are double shocks [124] and isentropic releases [125, 126]. The procedure is called direct-drive ablation if the laser directly irradiates the ablator. Indirect-drive ablation is utilized at the NIF where the lasers hit a gold hohlraum, creating an X-ray bath which subsequently irradiates the ablator to create spherical [90] or planar shocks [127].

### Static compression

Static compression is mostly achieved through diamond anvil cells (DACs) [128, 129], where two diamond anvils push on a target from both sides to produce a static high-pressure state. Although the DAC is capable of reaching pressures comparable to Earth’s core [130], higher pressures are not attainable with the standard configuration. However, new developments over the past decades, e.g., the dynamic DAC [131], micro-ball nanodiamonds [132], the double-stage [133, 134] and toroidal anvils [135], have enabled static pressures up to 10 Mbar. Additionally, higher temperature states in DACs can be achieved via laser heating [136, 137]; conditions beyond 3 Mbar and 6000 K [138] are not attainable, however. Direct resistive heating of the sample [139] or the diamond anvils [140] is also employed. Although these approaches are more controlled, they restrict the accessible  $P$ - $T$  even more than laser heating; see Ref. [137] for a comparison of achievable conditions. In addition, the statically pre-compressed samples can be shock compressed [141]. DACs enable high-quality measurements due to their static nature. However, they also have limitations. Pressures above 10 Mbar, attainable in dynamic compression experiments, cannot currently be reached using static compression. Furthermore, the interaction of the target material with the diamonds can lead to complications. Some materials, e.g., hydrogen and helium, diffuse into the diamond [142] and make it brittle.

### Isochoric & isobaric heating

If no compression of the target is required, isochoric [93, 143, 144] and isobaric heating [145] can be employed. In isochoric heating, energy is transferred to the target via X-ray radiation or ultrafast protons in a short time relative to the time scale of hydrodynamic expansion. If the system is then probed before the onset of expansion, the density remains at the initial density while the temperature is significantly elevated. In isobaric heating, on the other hand, the target is heated and allowed to expand to its equilibrium density, given the ambient pressure. As a result, measurements can be performed over a long time to achieve excellent signal-to-noise ratios. For an example of this approach, see the experimental setup described in Sec. 3.6.1. As a drawback, with increasing temperature, only low-density conditions can be probed, and extreme temperatures cannot be reached because the containment of the target becomes problematic.

### 1.2.2 Diagnosing extreme conditions

As discussed in Sec. 1.2.1, creating WDM is challenging, and the most extreme attainable conditions can only be created transiently. Therefore, suitable diagnostic techniques ought to be used to resolve the quantities of interest on short time scales. Some general properties of the EOS can be measured by methods like the velocity interferometer system for any reflector (VISAR), which measures the velocity of the shock front [146–148] in dynamic shocks, and through pressure gauges can give access to the pressure of the shocked material. Temperature is often determined through streaked optical pyrometry (SOP) [149, 150], which uses the emission of the studied sample to infer its temperature. However, the diagnostic must be calibrated and is often only reliable from 0.5 eV to 25 eV [151]. Here, the focus is on X-ray Thomson scattering (XRTS) and diffraction, which enable insight beyond EOS data, e.g., structural information, electronic configuration, and thermodynamic properties; see also Secs. 2.2 and 2.3.

### X-ray Thomson scattering & the Chihara decomposition

The scattering of X-ray photons off electrons in a many-particle system is referred to as XRTS [152, 153]. The photons are characterized by their wave vector  $\mathbf{k}$ , and their angular frequency  $\omega$ , which are connected via  $\omega = c|\mathbf{k}|$ , the speed of light being  $c$ . Here, the wave number is given by the absolute value of the wave vector  $|\mathbf{k}| = k = \frac{2\pi}{\lambda}$ , where  $\lambda$  is the wavelength. The quantities corresponding to the incoming photons are denoted by the subscript 1, while the outgoing photons after the scattering process are denoted by the subscript 2. For scattering under an arbitrary angle  $\theta$ , a simple geometric consideration of the change in wave vectors and the use of the law of cosines and the dispersion relation for light results in

$$\Delta k = \pm \frac{1}{\hbar c} \sqrt{(\hbar\omega_1)^2 + (\hbar\omega_2)^2 - 2(\hbar\omega_1)(\hbar\omega_2) \cos(\theta)}, \quad (1.4)$$

$$\Delta k \approx 2 \frac{\hbar\omega_1}{\hbar c} \sin\left(\frac{\theta}{2}\right), \quad \text{given that } \hbar|\Delta\omega| = \hbar|\omega_2 - \omega_1| \ll \hbar\omega_1 \quad (1.5)$$

for the change in wave vectors  $\Delta k = |\Delta\mathbf{k}| = |\mathbf{k}_2 - \mathbf{k}_1|$ . Equation (1.5) denotes a common approximation [71, 94, 97, 98] that is made if the change in frequency (or equivalently energy) is small compared to the frequency (energy) of the incoming light.

This is a valid approximation for most XRTS studies for WDM. As an example, with a typical photon energy  $E = 8$  keV at a scattering angle  $\theta = 20^\circ$  and a spectrometer that resolves energy shifts of up to  $\pm 200$  eV, the approximate relation in Eq. (1.5) predicts the scattering length as

$$k = 1.408_{-0.014}^{+0.021} \text{ \AA}^{-1}, \quad (1.6)$$

where the maximum errors are computed from the exact relation in Eq. (1.4) for the maximum energy shifts. In practice, the uncertainty in the wave number is larger due to the finite opening angle of the spectrometer. Nevertheless, the transferred momentum at a given scattering angle is usually assumed to be constant, although a range of different  $k$  could be considered via a convolution. For the scattering process to occur with a given momentum and energy transfer, the photon must couple to charge density fluctuations in the many-particle system, which are described by the electron-electron DSF (eDSF)  $S_{ee}(k, \omega)$ . The eDSF encompasses all electronic fluctuations and the fluctuations of the ions, described by the ion-ion DSF (iDSF)  $S_{ii}(k, \omega)$ , which the electrons follow due to their accumulation around the positively charged ions. Traditionally, the eDSF can be decomposed based on the identification of bound and free electrons in a chemical picture as [153–155]

$$S_{ee}^{\text{tot}}(k, \omega) = \underbrace{|f_i(k) + q(k)|^2 S_{ii}(k, \omega)}_{\text{ion feature}} + \underbrace{Z_f S_{ee}^0(k, \omega)}_{\text{plasmon feature}} + \underbrace{Z_b \int_{-\infty}^{\infty} d\omega' S_{ce}(k, \omega - \omega') S_s(k, \omega')}_{\text{bound-free feature}}. \quad (1.7)$$

The first contribution, termed ion feature, describes the ion dynamics modulated by the ionic form factor  $f_i(k)$  and the form factor of loosely bound electrons  $q(k)$ , which describe how, on average, the electrons are distributed around the ions. The second contribution is the plasmon feature describing collective excitations of free or quasi-free electrons, represented by the eDSF of free electrons  $S_{ee}^0(k, \omega)$ . The last contribution is described as the bound-free feature and is computed from a convolution of the self-part of the ion dynamics  $S_s(k, \omega)$  [156] and the eDSF of the core electrons which describes Raman and Compton-type scattering. The plasmon and bound-free features are weighted by the number of free electrons  $Z_f$  and bound electrons  $Z_b$  per atom, respectively. These contributions are schematically represented in Fig. 1.2. Traditionally, each quantity in Eq. (1.7) is described by a combination of analytical approaches, e.g., the Debye-Hückel theory [157, 158] for  $q(k)$  and  $S_{ii}(k)$ , the random phase approximation (RPA) [159–162] for  $S_{ee}^0(k, \omega)$ , and the impulse approximation [163–165] for the bound-free feature among others.

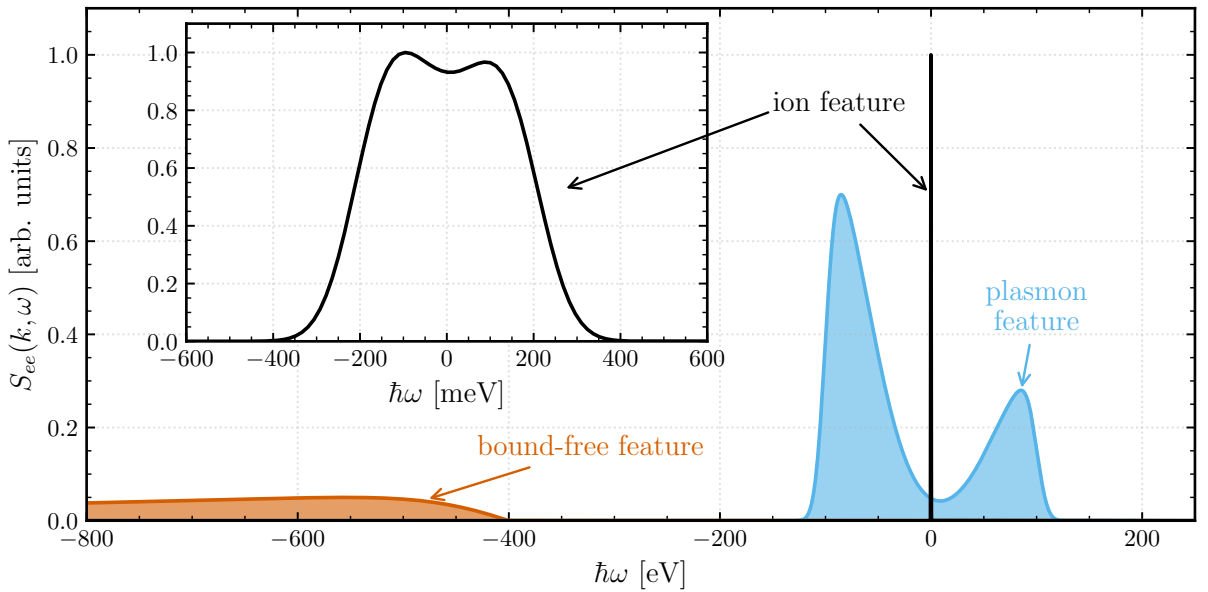


**Figure 1.2:** A schematic of a decomposed XRTS spectrum according to the chemical picture in the Chihara decomposition Eq. (1.7). The inset zooms in on the ion feature, where ion acoustic or phonon modes can be observed. Note the energy unit of the inset. The plasmon feature is due to the collective behavior of free or quasi-free electrons, and the bound-free feature is caused by electronic transitions from bound to free states.

In WDM, the separation into bound and free electrons breaks down, and some of the analytical approaches for the individual constituents of Eq. (1.7) become ill-defined. To circumvent this limitation and enable a unified description solely based on *ab initio* simulations, a modified Chihara decomposition

$$S_{ee}^{\text{tot}}(k, \omega) = \underbrace{|N(k)|^2 S_{\text{ii}}(k, \omega)}_{\text{ion feature}} + \underbrace{Z S_{\text{et}}(k, \omega)}_{\text{electronic transitions feature}} \quad (1.8)$$

has been suggested [166, 167]. Here, the artificial separation into bound and free contributions to the form factor is replaced by a total form factor  $N(k)$ , which can be directly computed from the total electron density in *ab initio* frameworks, e.g., DFT or PIMC. The plasmon and bound-free features are condensed into an eDSF due to electronic transitions  $S_{\text{et}}(k, \omega)$  because both features arise from electronic transitions in a quantum mechanical many-body description. This is discussed in more detail in Sec. 3.2.

Given the knowledge about the eDSF of the target, the differential power spectrum per frequency shift  $\omega$  and solid angle  $\Omega$  can be written as [168–170]

$$\frac{d^2 P}{d\omega d\Omega} = \frac{\sigma_{\text{T}} k_2}{A_{\text{rad}} k_1} \int_{-\infty}^{\infty} \frac{d\omega'}{2\pi} G(\omega - \omega') \int_V d^3 r l(\mathbf{r}) S_{ee}(k, \omega') n_i(\mathbf{r}), \quad (1.9)$$

where  $\sigma_{\text{T}} = 6.65 \cdot 10^{-25} \text{ cm}^2$  [71] is the Thomson scattering cross section,  $A_{\text{rad}}$  is the irradiated area,  $l(\mathbf{r})$  is the power density of incoming photons, and  $n_i(\mathbf{r})$  is the ion density throughout the target of volume  $V$ . The influence of the X-ray source spectrum and the instrumental setup is encoded in  $G(\omega)$ . For a detailed account of the effect  $n_i(\mathbf{r})$  and  $G(\omega)$  have on the scattering spectrum, see Sec. 3.3 and Ref. [171].

With this description, observed spectra can be analyzed to infer information on the eDSF. For a target in thermal equilibrium, the electronic temperature can be determined through the asymmetry of the eDSF according to the detailed balance relation [71]. Furthermore, the eDSF can provide insight into collective and single-particle phenomena depending on the length scale probed relative to typical screening lengths, often described by the electronic screening length  $\lambda_e$ . The regimes are characterized by the scattering parameter  $\alpha = \frac{1}{\lambda_e k}$  [71]. In the collective regime  $\alpha < 1$ , the eDSF exposes the macroscopic dielectric function, which is closely connected to quantities like the electrical conductivity and the absorption coefficient. In the single-particle regime  $\alpha \gg 1$ , the eDSF can be directly connected to the electron density and the distribution of electron velocities [172].

## Diffraction

While XRTS can probe the dynamics and collective effects in the target, diffraction probes its average structural composition. The diagnostic relies on the fact that light or neutrons that scatter from various scattering centers interfere constructively or destructively under certain scattering angles.

Laue developed a general description for diffraction in lattices [173, 174]. For constructive interference to occur, the scattered outgoing light rays must form a coherent wave front which propagates as  $\exp[i(\omega t - \mathbf{k}_2 \cdot \mathbf{r} + \phi_{\text{out}})]$ . This outgoing wavefront is produced by scattering of the incoming light that propagates as  $\exp[i(\omega t - \mathbf{k}_1 \cdot \mathbf{r} + \phi_{\text{in}})]$ . The respective phase constants are given  $\phi_{\text{in}}$  and  $\phi_{\text{out}}$ . These two waves can only coexist if they are in phase at all scattering centers, usually denoted by the lattice positions  $\mathbf{r}_{\text{lat}}$ . This condition is only satisfied if  $\Delta \mathbf{k} \cdot \mathbf{r}_{\text{lat}} = 2\pi n$ , which can be used to identify the transferred wave vector  $\Delta \mathbf{k}$  with the reciprocal lattice

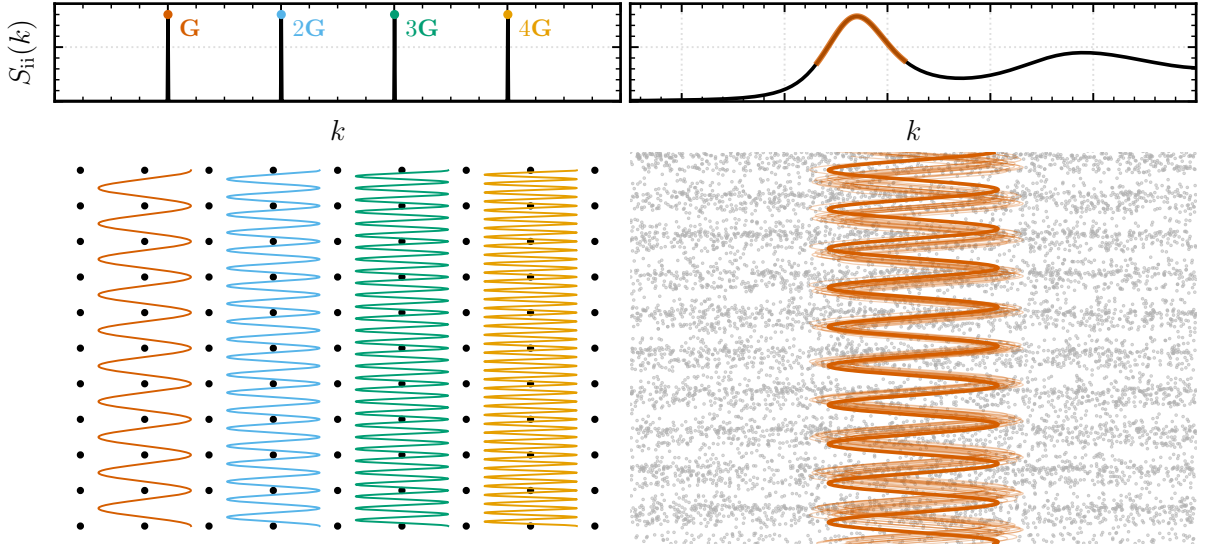


**Figure 1.3:** Schematic representation of the structural analysis in a solid (left) and a strongly correlated liquid (right). Typical iSSFs for solids and liquids are given as a reference in the upper panels. The long-range order in the correlated liquid is exaggerated here for visualization.

vector  $\mathbf{G}$  to arrive at the Laue equation

$$\Delta\mathbf{k} = \mathbf{G}, \quad \mathbf{G} = h\mathbf{b}_1 + k\mathbf{b}_2 + l\mathbf{b}_3, \quad h, k, l \in \mathbb{N}_0 \quad (1.10)$$

with the reciprocal primitive vectors  $\{\mathbf{b}_1, \mathbf{b}_2, \mathbf{b}_3\}$ . In conclusion, constructive interference only arises for scattering processes that transfer some linear combination of reciprocal lattice vectors to the lattice.

This consideration is only valid for a perfect lattice at  $T = 0$  K. Vibrational effects due to relatively low temperatures can be included via the Debye-Waller factor [175–178]. However, the lattice-based description above fails if the temperature is high enough to melt the lattice structure and break long-range order. In this context, a generalization of Eq. (1.10), the ion-ion SSF (iSSF)  $S_{ii}(k)$  can be used. It provides a measure of the time-averaged accumulation of scattering sources on a particular length scale given by the wave number  $k$ . If they tend to bunch up on this length scale, a scattering process transferring momentum corresponding to  $k$  to the target tends to interfere constructively, resulting in a peak of the diffraction pattern. Figure 1.3 shows the contrast between the structural analysis of a solid with a clear lattice structure and a strongly correlated liquid where a much wider range of wave numbers  $k$  results in constructive interference. A clear definition of this quantity is given in Sec. 2.2.

In the above discussion, light scattering was assumed to occur at the ions. However, this assumption is only valid in neutron diffraction experiments. In X-ray and electron scattering experiments, the scattering occurs off the electrons, generally located around the ions. Therefore, the diffraction is governed by the electron-electron SSF (eSSF), which can be expressed as the iSSF modulated by an electron form factor. This form factor describes how the electrons, on average, are distributed around the ions. Due to the strong localization of the electrons, X-ray and electron diffraction also enable a direct inference of the underlying ionic structure. An example where this assumption breaks down due to the localization of binding electrons between the ions is discussed in Sec. 3.6.1.



### 1.3 Outline of this thesis

The field of WDM research is fast-moving and exciting. As mentioned in the previous sections, a host of new and upgraded research facilities have come online over the past decades, enabling access to previously unexplored pressure and temperature regimes. With improved spectral resolution in scattering experiments, it is now possible to resolve dynamics on formerly unattainable energy scales. Along with these experimental advances, computational capacities are ever-increasing, and the advent of machine learning algorithms in WDM enables more advanced and more expansive simulations than ever. Additionally, the capabilities of modern telescopes, such as the James Webb Space Telescope, reduce the uncertainty in astrophysical observations, tightening the constraints on planetary and stellar models. This thesis presents advances in the simulation of WDM and the interpretation of scattering experiments using these simulations by applying modern machine-learning approaches. The results of this thesis will aid in measuring important material and transport properties in matter under extreme conditions at XFEL facilities. Furthermore, the framework for analyzing scattering experiments at the NIF based solely on DFT data presented in this thesis contributes to establishing a reliable platform for studying the interior of low-mass stars in the laboratory.

This introductory Chapter 1 gives a general characterization of WDM and indicates applications where accurate knowledge of matter in these extreme states is paramount, e.g., astrophysical modeling and ICF. Furthermore, an overview of experimental capabilities to achieve extreme states of matter in the laboratory and how different diagnostic techniques can be used to gain insight into the structural makeup and dynamics of WDM is presented.

Chapter 2 tackles the theoretical foundations and computational methods relevant to this thesis. In Sec. 2.1, DFT-MD is introduced, the main simulation method used to produce the results obtained in this thesis. The theoretical foundation is presented, and some implementation details are mentioned. Subsequently, the ion dynamics are discussed in Sec. 2.2. Specifically, in Sec. 2.2.1, the use of high-dimensional neural network potentials (HDNNP) to scale up MD simulations to macroscopic scales is discussed and, in Sec. 2.2.2, the framework used to analyze the ion dynamics, called generalized collective modes (GCM), is introduced. Section 2.3 is concerned with the electronic dynamics, which are treated in linear response here. The framework of time-dependent DFT (TDDFT) is employed to derive response functions in Sec. 2.3.1, while the Kubo-Greenwood formula for electrical conductivity within Kubo theory is presented in Sec. 2.3.2. Finally, a statistical framework for analyzing experimental observations based on models with many input parameters is explored in Sec. 2.4.

The results of this thesis are summarized in Chapter 3. Dynamics on different energy scales accessible through DFT-MD simulations are discussed and compared to scattering experiments. First, a systematic approach to the hydrodynamic limit of ion dynamics using *ab initio* simulations, as well as an application of this technique to a typical WDM experiment, are presented in Sec. 3.1. A new definition of ionization degree in WDM and a comparison between numerical many-body methods and state-of-the-art analytical methods for the description of electron dynamics in XRTS are given in Sec. 3.2. Section 3.3 combines the study of ion and electron dynamics to analyze an experiment at the NIF. The electrical conductivity is one of the central quantities related to electron dynamics. The long-standing question of whether electron-electron collisions are included in the Kubo-Greenwood formalism of conductivity is addressed in Sec. 3.4. Finally, results for ongoing analyses of experiments at the LCLS and GSI are presented in Sec. 3.6. These results are detailed in four first-author articles, three of which are published, one of which is submitted, and three co-author publications. Not explicitly included in this thesis are nine further co-author publications, which are briefly mentioned in Sec. 3.5. Chapter 4 includes the publications described in Chapter 3 and a summary of the individual author contributions.

## 2 Computational methods

An accurate theoretical description of WDM must consider the strong correlations and non-negligible degeneracy effects that characterize this state of matter, as discussed in Chapter 1. To this end, the finite-temperature formulation of density functional theory coupled with molecular dynamics (DFT-MD) simulations is utilized in this thesis. This approach will be detailed in the following section.

The goal is to most efficiently, with the fewest possible approximations, solve the quantum mechanical problem described by the time-dependent Schrödinger equation [179]

$$\hat{H} \Psi_n(\mathbf{R}, \mathbf{r}, t) = i\hbar \frac{\partial}{\partial t} \Psi_n(\mathbf{R}, \mathbf{r}, t), \quad (2.1)$$

with the full wave function  $\Psi_n$  of the nuclei and electrons. Their respective sets of coordinates are given by  $\mathbf{R} = \{\mathbf{R}_I, I = 1, \dots, N_n\}$  and  $\mathbf{r} = \{\mathbf{r}_i, i = 1, \dots, N_e\}$  at time  $t$  where  $N_n$  and  $N_e$  denote the number of nuclei and electrons, respectively. The full Hamiltonian can be decomposed as

$$\begin{aligned} \hat{H} = & - \sum_{i=1}^{N_e} \frac{\hbar^2}{2m_e} \nabla_i^2 + \frac{e^2}{8\pi\epsilon_0} \sum_{i=1}^{N_e} \sum_{j \neq i}^{N_e} \frac{1}{|\mathbf{r}_i - \mathbf{r}_j|} - \frac{e^2}{4\pi\epsilon_0} \sum_{I=1}^{N_n} \sum_{i=1}^{N_e} \frac{Z_I}{|\mathbf{R}_I - \mathbf{r}_i|} \\ & - \sum_{I=1}^{N_n} \frac{\hbar^2}{2M_I} \nabla_I^2 + \frac{e^2}{8\pi\epsilon_0} \sum_{I=1}^{N_n} \sum_{J \neq I}^{N_n} \frac{Z_I Z_J}{|\mathbf{R}_I - \mathbf{R}_J|}, \end{aligned} \quad (2.2)$$

with the mass  $M_I$  and charge  $Z_I$  of the nuclei, the elementary charge  $e$ , the vacuum permittivity  $\epsilon_0$  and the nabla operator  $\nabla$ . The first three terms of Eq. (2.2) are the kinetic energy operator of the electrons  $\hat{T}_e$ , and the Coulomb operators describing the interaction among the electrons  $\hat{U}_{ee}$  and between the electrons and nuclei  $\hat{V}_{ne}$ . These three terms can be summarized into the electronic Hamiltonian  $\hat{H}_e$ . This only leaves the kinetic energy and the Coulomb interaction operators of the nuclei,  $\hat{T}_n$  and  $\hat{V}_{nn}$ , respectively:

$$\hat{H} = \hat{H}_e + \hat{T}_n + \hat{V}_{nn}, \quad \hat{H}_e = \hat{T}_e + \hat{U}_{ee} + \hat{V}_{ne}. \quad (2.3)$$

In the context of DFT,  $\hat{V}_{ne}$  is often replaced by an external potential  $\hat{V}_{\text{ext}}$ , which includes the Coulomb potential between electrons and nuclei and an arbitrary external field. Here, the case with no external field is considered, and  $\hat{V}_{ne}$  is used to highlight this. In the following, it is discussed how Eq. (2.1) is approximated in the context of DFT-MD simulations. A more comprehensive account of DFT can be found in Refs. [180–190] and a further exploration of the MD formalism is available in Refs. [186, 189, 191, 192].

### 2.1 Density functional theory molecular dynamics

Given fixed positions of the nuclei  $\mathbf{R}$ , the solutions  $\Phi_n(\mathbf{r}; \mathbf{R})$  to the time-independent electronic Schrödinger equation

$$\hat{H}_e \Phi_n(\mathbf{r}; \mathbf{R}) = E_n(\mathbf{R}) \Phi_n(\mathbf{r}; \mathbf{R}) \quad (2.4)$$

form a complete basis of the electronic Hilbert space at each point in time with the electronic eigenenergies  $E_n$  that parametrically depend on  $\mathbf{R}$ . Therefore, a solution to Eq. (2.1) can be

constructed in this basis as

$$\Psi(\mathbf{R}, \mathbf{r}, t) = \sum_n \Theta_n(\mathbf{R}, t) \Phi_n(\mathbf{r}; \mathbf{R}), \quad (2.5)$$

where the coefficients  $\Theta_n(\mathbf{R}, t)$  are to be determined. Inserting this expression in the time-dependent Schrödinger equation, Eq. (2.1), reveals that the coupling between the electronic and nuclear system is caused by the kinetic energy operator of the nuclei  $\hat{T}_n$  acting on the solutions to the electronic Schrödinger equation  $\Phi_n(\mathbf{r}; \mathbf{R})$ . If energy shifts of the electronic states induced by nuclear motion are small compared to typical energy gaps between electronic states, this coupling can be neglected, resulting in the adiabatic approximation [193]. In this context, a decoupled time-dependent Schrödinger equation for the nuclei is given by

$$i\hbar \frac{\partial}{\partial t} \Theta_n(\mathbf{R}, t) = (\hat{T}_n + \hat{V}_{nn} + E_n(\mathbf{R})) \Theta_n(\mathbf{R}, t), \quad (2.6)$$

where a non-coupling term on the right side due to the  $\mathbf{R}$ -dependence of  $\Phi_n$  has been neglected according to the Born-Oppenheimer approximation [193, 194]. The inclusion of non-adiabatic effects within DFT-MD simulations has been a topic of research [195–198] and even in WDM, it has been suggested to be relevant near phase transitions [199].

Finally, Eq. (2.6) describes the time evolution of the nuclei, which for all of the conditions in this thesis, can be regarded as classical particles. Therefore, the classical nuclei approximation [188] is employed to identify the equation of motion for the mean values of the nuclear positions  $\mathbf{R}$  determined through the Ehrenfest theorem [200] with its classical counterpart

$$M_I \frac{d^2 \mathbf{R}(t)}{dt^2} = -\nabla_I (V_{nn} + E_n(\mathbf{R})). \quad (2.7)$$

Here,  $V_{nn}$  is the Coulomb potential between the nuclei defined in Eqs. (2.2) and (2.3) but the operator character is dropped. The dependence of the nuclear dynamics on the electrons enters through the eigenenergies  $E_n(\mathbf{R})$  of the electronic Schrödinger equation (2.4). According to the Hellmann-Feynman theorem [201, 202], this contribution can be computed from the expectation value of  $\nabla_I V_{ne}$  in the electronic ground state. To find this ground state, the electronic Schrödinger equation (2.4) must be solved.

### Finite temperature density functional theory

Directly solving the electronic Schrödinger equation for multiple electrons is numerically intractable due to the exponential scaling of memory demands with the number of electrons for the wave function  $\Psi$  [203]. However, the Hohenberg-Kohn theorems [204] establish that the electron density  $n_e(\mathbf{r})$ , for which memory demands do not scale with the number of electrons, can be used to characterize the ground state instead.

The first Hohenberg-Kohn theorem states that the ground state electron density  $n_e^0(\mathbf{r})$  uniquely defines the external potential, which is given by  $\hat{V}_{ne}$  in Eq. (2.3). This can be established by following a proof by contradiction which assumes two different ground state densities can be connected to the same external potential, and, as a result of this, one arrives at an erroneous conclusion [188, 190]. This unique connection further implies that the ground state electron density  $n_e^0(\mathbf{r})$  uniquely defines the electronic Hamiltonian  $\hat{H}_e$ , whose only external contribution is  $\hat{V}_{ne}$ , and as a consequence of the Schrödinger equation (2.4), also the electronic ground state wave function  $\Phi_0$  and energy  $E_0$ . Therefore, these quantities can now be written as functionally dependent on the electron density, i.e., the ground state energy is given by

$$\langle \Phi_0[n_e] | \hat{H}_e | \Phi_0[n_e] \rangle = E_0[n_e] = T_e[n_e] + U_{ee}[n_e] + V_{ne}[n_e], \quad (2.8)$$



where the wave function  $\Phi_0[n_e]$  represents the ground state wave function of an electronic system whose ground state electron density is  $n_e(\mathbf{r})$ . The second Hohenberg-Kohn theorem states that the ground state energy  $E_0$  is only achieved for the true ground state electron density  $n_e^0(\mathbf{r})$  which can be proven via the variational principle by Ritz [205]:

$$\langle \Phi_0[n_e^0] | \hat{H}_e | \Phi_0[n_e^0] \rangle < \langle \Phi_0[\tilde{n}_e] | \hat{H}_e | \Phi_0[\tilde{n}_e] \rangle \quad \forall \tilde{n}_e \neq n_e^0. \quad (2.9)$$

Importantly, the Hamiltonian  $\hat{H}_e$  in this inequality is determined by the external potential  $V_{ne}[n_e^0]$ . Therefore, the left side gives the real ground state energy, whereas, on the right side,  $\hat{H}_e$  is evaluated in a state which is not its ground state. In conclusion, if a global minimum in the energy is found by varying  $n_e(\mathbf{r})$ , the electron density at this minimum necessarily is the ground state electron density and defines all other ground state observables. The theorems were extended to finite temperatures by Mermin [206], and in the following, the minimum free energy

$$F_0[n_e] = E_0[n_e] - TS_e[n_e] \quad (2.10)$$

at the equilibrium electron density  $n_e$  will be discussed. Here,  $T$  is the electron temperature, and  $S_e[n_e]$  is the density functional of the electronic entropy.

### Kohn-Sham theory

Although the equilibrium free energy is completely defined by  $n_e(\mathbf{r})$ , no expressions for  $T_e[n_e]$ ,  $S_e[n_e]$ , and  $U_{ee}[n_e]$  exist. To circumvent this problem, the Kohn-Sham (KS) theory [207, 208] introduces a non-interacting reference system with the density

$$n_e^{\text{ref}}(\mathbf{r}) = \sum_{i=1}^{\infty} f_i |\phi_i(\mathbf{r})|^2, \quad (2.11)$$

where  $f_i$  are the occupation numbers according to the Fermi-Dirac distribution [209, 210] and  $\phi_i$  are the single-particle wave functions, called KS orbitals, describing the non-interacting electrons. In order to compute the free energy in Eq. (2.10), the density functionals are evaluated in the reference system, and an exchange-correlation (XC) functional  $F_{\text{XC}}[n_e]$  is introduced that captures all exchange and correlation effects that are lost in the projection onto the non-interacting system:

$$F_0[n_e] = T_e^{\text{ref}}[n_e] + U_{ee}^{\text{ref}}[n_e] + V_{ne}^{\text{ref}}[n_e] - TS_e^{\text{ref}}[n_e] + F_{\text{XC}}[n_e], \quad (2.12)$$

with the known contributions in the reference system

$$\begin{aligned} T_e^{\text{ref}} &= \langle \Phi^{\text{ref}} | \hat{T}_e | \Phi^{\text{ref}} \rangle = -\frac{\hbar^2}{2m} \sum_{i=1}^{\infty} \int d^3r f_i \phi_i^*(\mathbf{r}) \nabla^2 \phi_i(\mathbf{r}), \\ U_{ee}^{\text{ref}} &= \langle \Phi^{\text{ref}} | \hat{U}_{ee} | \Phi^{\text{ref}} \rangle = \frac{e^2}{8\pi\epsilon_0} \sum_{i,j=1}^{\infty} \int \int d^3r d^3r' f_i |\phi_i(\mathbf{r})|^2 \frac{1}{|\mathbf{r} - \mathbf{r}'|} f_j |\phi_j(\mathbf{r}')|^2, \\ V_{ne}^{\text{ref}} &= \langle \Phi^{\text{ref}} | \hat{V}_{ne} | \Phi^{\text{ref}} \rangle = -\frac{e^2}{4\pi\epsilon_0} \sum_{i=1}^{\infty} \int d^3r f_i |\phi_i(\mathbf{r})|^2 \sum_{I=1}^{N_n} \frac{Z_I}{|\mathbf{r} - \mathbf{R}_I|}, \\ S_e^{\text{ref}} &= \langle \Phi^{\text{ref}} | \hat{S}_e | \Phi^{\text{ref}} \rangle = -k_B \sum_{i=1}^{\infty} [f_i \ln f_i + (1 - f_i) \ln(1 - f_i)]. \end{aligned} \quad (2.13)$$

Minimizing the free energy with respect to the electron density by performing functional derivatives results in the KS equation for the KS orbitals

$$\left(-\frac{\hbar^2}{2m}\Delta + v_{\text{eff}}(\mathbf{r})\right)\phi_n(\mathbf{r}) = \epsilon_n \phi_n(\mathbf{r}), \quad (2.14)$$

with the effective potential

$$v_{\text{eff}}(\mathbf{r}) = \frac{e^2}{4\pi\epsilon_0} \int d^3r' \frac{n_e(\mathbf{r}')}{|\mathbf{r} - \mathbf{r}'|} - \frac{e^2}{4\pi\epsilon_0} \sum_{I=1}^{N_n} \frac{Z_I}{|\mathbf{r} - \mathbf{R}_I|} + \frac{\delta}{\delta n_e(\mathbf{r})} F_{\text{XC}}[n]. \quad (2.15)$$

The only unknown term in the effective potential is the XC functional, which, therefore, determines the fidelity of the simulation. The different levels of approximations for this quantity can be ordered according to the rungs of a ladder which was proposed by Perdew *et al.* [211]. The lowest rung is the local density approximation (LDA), which, similar to Thomas-Fermi-Dirac theory [212–214], uses homogeneous electron gas expressions for exchange and correlation densities [80, 215, 216] at the local density in each point in space. This can be extended to local inhomogeneities by also considering the density gradient via an enhancement factor within the generalized gradient approximation (GGA) [217–223]. Higher-order derivatives and local kinetic energy densities are considered in Meta-GGAs [224–226]. The exact Hartree-Fock exchange can be included in hybrid functionals [227–232]. In this thesis, the GGA by Perdew, Burke, and Ernzerhof (PBE) [220] is used for most simulations, while the hybrid functional by Heyd, Scuseria, and Ernzerhof (HSE) [227, 228] is used in some cases where very accurate band gaps are required [233].

Equations (2.14), (2.15), and (2.11) have to be solved self-consistently since the electronic density  $n_e(\mathbf{r})$  enters in the effective potential, Eq. (2.15), and  $n_e(\mathbf{r})$  is computed from the KS orbitals, which are the solutions to the KS equation (2.14), which is in turn determined by the effective potential. Once a self-consistent solution is reached, the equation of motion for the nuclei, Eq. (2.7), can be solved to move the nuclei. The density functional framework can be extended to explicitly include a time dependence of the electronic density due to the Runge-Gross theorem [234]. This time-dependent formulation can be used to numerically propagate the electron density in time to explicitly simulate the electron dynamics, which is referred to as RT-TDDFT. Alternatively, in LR-TDDFT, a linear response formalism is applied in this time-dependent framework. In the context of transport properties, this approach is detailed in Sec. 2.3.1.

### Numerical implementation

Several commercial and open-source DFT codes exist, Quantum ESPRESSO [235, 236] and ABINIT [237, 238] being some popular examples. In this thesis, all DFT-MD simulations are performed with the Vienna *ab initio* simulation package (VASP) [239–242]. Some of the static DFT simulations that are subsequently analyzed using LR-TDDFT (see Sec. 2.3.1) are computed with the GPAW code [243–246]. Both frameworks employ periodic boundary conditions and can, therefore, take advantage of Bloch’s theorem [247] to represent the KS orbitals at a given wave vector  $\mathbf{k}$  by

$$\begin{aligned} \phi_{\mathbf{k},n}(\mathbf{r}) &= u_{\mathbf{k},n}(\mathbf{r}) \exp(i\mathbf{k}\cdot\mathbf{r}), \\ u_{\mathbf{k},n}(\mathbf{r}) &= \frac{1}{\sqrt{\Omega}} \sum_{\mathbf{G}} C_{\mathbf{G},\mathbf{k}n} \exp(i\mathbf{G}\cdot\mathbf{r}), \end{aligned} \quad (2.16)$$

where  $\Omega$  is the box volume and  $u_{\mathbf{k},n}(\mathbf{r})$  is a function that exhibits the lattice periodicity and can be expanded in a basis of plane waves using the reciprocal lattice vectors  $\mathbf{G}$ . The plane wave coefficients  $C_{\mathbf{G},\mathbf{k}n}$  are then varied to find the equilibrium electron density. Integrals

over the first Brillouin zone are replaced by the sum over KS orbitals evaluated at representative points, e.g., the Baldereschi mean value point [248] or the Monkhorst-Pack sampling points [249]. Due to numerical limitations, this expansion must be truncated, limiting the spatial resolution. In practice, the reciprocal lattice vectors included in the expansion are given by the inequality

$$\frac{\hbar^2}{2m} |\mathbf{G} + \mathbf{k}|^2 < E_{\text{cut}}, \quad (2.17)$$

which makes the cutoff energy  $E_{\text{cut}}$  an important convergence parameter. To reduce the required spatial resolution, the projector augmented wave method [250] for pseudo-potentials is employed, which replaces the rapidly oscillating wave function near the cores with non-oscillating pseudo wave functions which reproduce the same electron density.

The temperature of the nuclei in the MD simulations is controlled by coupling to a heat bath via the Nosé-Hoover thermostat [251–253] or the more advanced Nosé-Hoover chains [254]. The time propagation of the nuclear positions and velocities according to Eq. (2.7) is usually performed by the Verlet algorithm [255] or the more modern velocity Verlet algorithm [256].

## 2.2 Ion dynamics

The DFT-MD formalism enables the direct simulation of ion dynamics in WDM with an *ab initio* description of the electron density and its interaction with the ions. From the time propagation prescribed in Eq. (2.7), the ion density in time  $n_i(\mathbf{r}, t)$  and its spatial Fourier components  $n_i(\mathbf{k}, t)$  can be computed as

$$n_i(\mathbf{r}, t) = \sum_{I=1}^{N_n} \delta^3(\mathbf{r} - \mathbf{R}_I(t)), \quad n_i(\mathbf{k}, t) = \sum_{I=1}^{N_n} e^{i\mathbf{k} \cdot \mathbf{R}_I(t)}. \quad (2.18)$$

The wave vector  $\mathbf{k}$  indicates the characteristic length scale and orientation at which spatial oscillations in the ion density are studied. Analogously, the ion velocities  $\mathbf{v}_I(t)$  are known and, therefore, the ion current density  $\mathbf{j}_i(\mathbf{r}, t)$  and its spatial Fourier components  $\mathbf{j}_i(\mathbf{k}, t)$ , as well as its longitudinal and transverse components  $j_i^{\parallel/t}(\mathbf{k}, t)$  relative to  $\mathbf{k}$  can be inferred as

$$\mathbf{j}_i(\mathbf{r}, t) = \sum_{I=1}^{N_n} \mathbf{v}_I(t) \delta^3(\mathbf{r} - \mathbf{R}_I(t)), \quad \mathbf{j}_i(\mathbf{k}, t) = \sum_{I=1}^{N_n} \mathbf{v}_I(t) e^{i\mathbf{k} \cdot \mathbf{R}_I(t)}, \quad (2.19)$$

$$j_i^{\parallel}(\mathbf{k}, t) = \sum_{I=1}^{N_n} v_I^{\parallel}(t) e^{i\mathbf{k} \cdot \mathbf{R}_I(t)}, \quad j_i^{\perp}(\mathbf{k}, t) = \sum_{I=1}^{N_n} v_I^{\perp}(t) e^{i\mathbf{k} \cdot \mathbf{R}_I(t)}. \quad (2.20)$$

The parallel and perpendicular components of the ion velocities relative to the wave vector  $\mathbf{k}$  at each point in time are denoted by  $v_I^{\parallel}(t)$  and  $v_I^{\perp}(t)$ , respectively.

The information contained in the trajectories of the ions can be summarized via the autocorrelation function of  $n_i(\mathbf{k}, t)$ , often called the intermediate scattering function

$$F_{ii}(\mathbf{k}, t) := \frac{1}{N_n} \langle n_i(\mathbf{k}, \tau) n_i(-\mathbf{k}, \tau + t) \rangle_{\tau} = \lim_{\Theta \rightarrow \infty} \frac{1}{N_n} \frac{1}{\Theta} \int_0^{\Theta} n_i(\mathbf{k}, \tau) n_i(-\mathbf{k}, \tau + t) d\tau, \quad (2.21)$$

which describes the time evolution of ion density oscillations on a characteristic length scale and orientation given by  $\mathbf{k}$ . Here,  $t$  refers to the correlation time, and  $\tau$  denotes an absolute time over which the average is performed. In practice, the simulation duration  $\Theta$  is finite, and the integral in the second equality must be truncated at a sufficiently long time for which convergence can be established.

Especially for scattering experiments that probe the target in frequency space, see Sec. 1.2.2, the more useful quantity is the temporal Fourier transform of Eq. (2.21), the ion-ion DSF (iDSF)

$$S_{ii}(\mathbf{k}, \omega) := \frac{1}{2\pi} \int_{-\infty}^{\infty} F_{ii}(\mathbf{k}, t) e^{i\omega t} dt = \lim_{\Theta \rightarrow \infty} \frac{1}{2\pi N_n} \frac{1}{\Theta} \left| \int_{-\Theta/2}^{\Theta/2} n_i(\mathbf{k}, t) e^{i\omega t} dt \right|^2, \quad (2.22)$$

where the second equality is due to the Wiener-Khinchin theorem [257, 258]. The angular frequency  $\omega$  determines the temporal frequency at which the density oscillations occur.

An important quantity that integrates over all dynamical effects on a given length scale is the iSSF

$$S_{ii}(\mathbf{k}) := \int_{-\infty}^{\infty} S_{ii}(\mathbf{k}, \omega) d\omega = F_{ii}(\mathbf{k}, t=0) = \frac{1}{N_n} \langle |n_i(\mathbf{k}, \tau)|^2 \rangle_{\tau}, \quad (2.23)$$

which is the time-averaged absolute square of the spatial Fourier components of the ion density per ion. In that sense, it is a generalization of the Laue condition for diffraction in solids introduced in Sec. 1.2.2, and can be applied to diffraction measurements in the liquid and solid state to gain information on structure and ion correlations. It can be easily connected to the iDSF and the intermediate scattering function as demonstrated in Eq. (2.23).

The notion of the iDSF, which defines the power spectrum of  $n_i(\mathbf{r}, \tau)$ , can be extended to the longitudinal and transverse parts of the ion current density  $j_i^{1/t}(\mathbf{k}, t)$  and its power spectrum is defined by

$$J_{ii}^{1/t}(\mathbf{k}, \omega) := \frac{1}{2\pi N_n} \frac{1}{\Theta} \left| \int_{-\Theta/2}^{\Theta/2} j_i^{1/t}(\mathbf{k}, t) e^{i\omega t} dt \right|^2. \quad (2.24)$$

The longitudinal part of the spectrum contains the same information as the iDSF, as these quantities are linked via  $J_{ii}^1(\mathbf{k}, \omega) = \frac{\omega^2}{|\mathbf{k}|^2} S_{ii}(\mathbf{k}, \omega)$ . The transverse part, however, contains valuable information about transverse excitations that cannot be gained from the ion density alone.

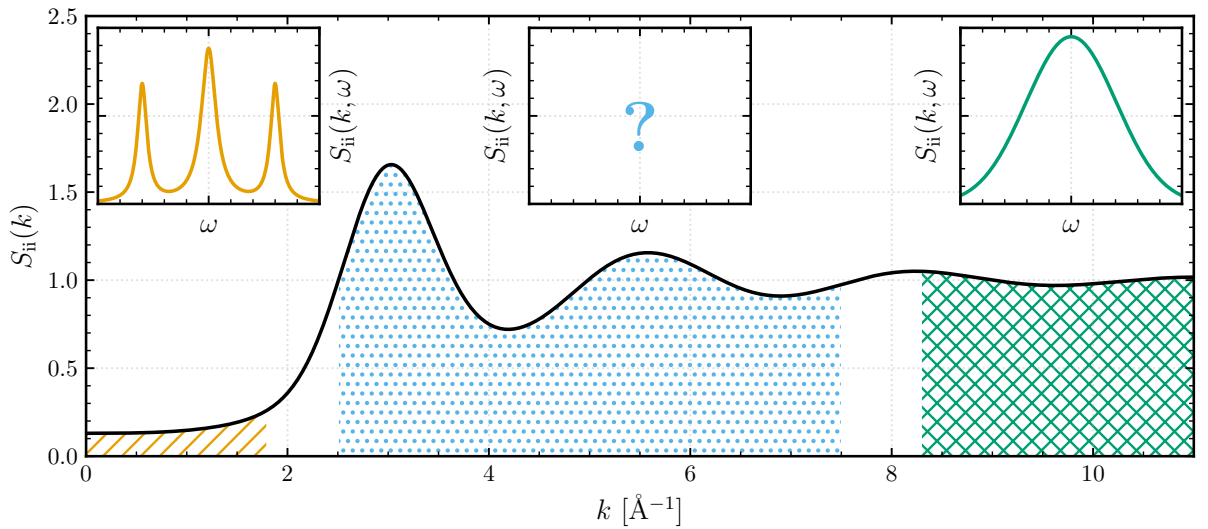


**Figure 2.1:** Schematic representation of the iSSF  $S_{ii}(k)$  for a correlated liquid. The single-particle regime at large  $k$  (green) and the hydrodynamic regime at small  $k$  (yellow) are indicated by shaded areas, and the typical shape of the iDSF in these regimes is shown in the insets. The intermediate scattering regime, where non-hydrodynamic corrections to the hydrodynamic behavior play a vital role and no simple analytic description exists, is given in blue.

In the liquid state, the system becomes isotropic, and the wave vector  $\mathbf{k}$  can be replaced by the wave number  $k$ . For a general quantity  $A(\mathbf{k})$  that depends on the wave vector  $\mathbf{k}$ , a wave-number-dependant analogue can be written as

$$A(k) = \int_{\mathbb{R}^3} \frac{1}{4\pi|\mathbf{k}'|^2} A(\mathbf{k}') \delta(|\mathbf{k}'| - k) d^3k'. \quad (2.25)$$

In this work, the isotropic versions of Eqs. (2.21)-(2.24) are used unless a solid state is considered. For these expressions, different analytically tractable limiting cases exist, which are illustrated in Fig. 2.1 by means of a typical iSSF for a correlated liquid. At short length scales,  $k \gg 1$ , and short time scales,  $\omega \gg 1$ , the ions behave independently of each other and can be treated within the free particle limit. In this limit, the iDSF and iSSF can be derived from an uncorrelated liquid that follows the Maxwell-Boltzmann distribution as

$$\lim_{k \rightarrow \infty} S_{ii}(k, \omega) = \sqrt{\frac{M_I \beta}{2\pi k^2}} \exp\left(-\frac{M_I \beta \omega^2}{2k^2}\right), \quad (2.26)$$

$$\lim_{k \rightarrow \infty} S_{ii}(k) = 1, \quad (2.27)$$

where  $1/\beta = k_B T$  and  $k_B$  is the Boltzmann constant. The second equality holds because, when the definition of  $n_i(\mathbf{k}, t)$  from Eq. (2.18) is plugged into Eq. (2.23), only the exponentials with the same ion positions do not average out. The iDSF in this limit is shown in green in the inset of Fig. 2.1.

Contrarily, in the long-wavelength limit,  $k \ll 1$ , only macroscopic correlations over long distances and long time scales are relevant. Here, the hydrodynamic Navier-Stokes equations [259–261] can accurately describe the liquid. The iDSF in this hydrodynamic regime is discussed further in Sec. 2.2.2 (see the left inset in Fig. 2.1). The iSSF at vanishing wave numbers  $k$  can be computed from thermodynamic relations [262] as

$$\lim_{k \rightarrow 0} S_{ii}(k) = \kappa_T \bar{n}_i k_B T, \quad (2.28)$$

where  $\kappa_T$  is the isothermal compressibility and  $\bar{n}_i$  is the average ion density. The intermediate regime between these limits is dominated by complex interactions on the length scale of inter-atomic distances where the correlations are strongest. In Sec. 2.2.2, an approach to systematically extend the hydrodynamic description to higher wave numbers is introduced.

### 2.2.1 High-dimensional neural network potential

Several schemes for learning the many-body interactions predicted by quantum simulations have been developed since the first application of feed-forward neural networks [263] to PIMC simulations [264]. Some of the most widely used frameworks are Gaussian approximation potentials (GAP) [265, 266], spectral neighbor analysis potentials (SNAP) [267, 268] and deep potential MD [269–271] among others. In this thesis, the high-dimensional neural network potential (HDNNP) architecture proposed by Behler and Parinello is adopted [272] to learn atomic energies and forces from DFT simulations. The trained HDNNP can be used to replace the term  $\nabla_I E_n(\mathbf{R})$  in Eq. (2.7), negating the need to perform the DFT simulation once the training is completed. This leads to speed increases and the ability to significantly scale up the simulation size as most DFT implementations scale as  $\propto N_e^3$ , whereas the neural-network-based MD simulation scales linearly. The combination of HDNNPs with MD simulations is referred to as NN-MD in this work. The main limitations of the direct application of feed-forward neural networks to the Cartesian coordinates of the ions are the lack of explicit consideration of translational invariance and the fixed size of the input layer that prevents the scaling to larger systems.

Behler and Parinello [272] suggested circumventing this by setting up individual neural networks for each atom which learn the atomistic energies and forces from the description of their local surrounding. To this end, the environment of each atom within a given cutoff radius  $R_{\text{cut}}$  is described by a set of atom-centered symmetry functions (ACSFs)  $G$ . A wide variety of ACSFs exists [273–275], but for the fairly simple systems studied in this work, the originally proposed radial and angular ACSFs [272]

$$G_I^{\text{rad}} = \sum_{J \neq I} \exp[-\eta(R_{IJ} - r_s)^2] f_c(R_{IJ}), \quad (2.29)$$

$$G_I^{\text{ang}} = 2^{1-\zeta} \sum_{\substack{J, K \neq I \\ J < K}} (1 + \lambda \cos \theta_{IJK})^\zeta e^{-\eta(R_{IJ}^2 + R_{IK}^2 + R_{JK}^2)} f_c(R_{IJ}) f_c(R_{IK}) f_c(R_{JK}) \quad (2.30)$$

are used. Here,  $R_{IJ} = |\mathbf{R}_I - \mathbf{R}_J|$  is the distance between ions  $I$  and  $J$ , and  $\theta_{IJK}$  is the angle between the vectors connecting ions  $I$  and  $J$  and ions  $K$  and  $J$ . The cutoff function  $f_c$  ensures the ACSF smoothly vanishes at the cutoff radius  $R_{\text{cut}}$ . By varying the characteristic parameters  $\eta$ ,  $r_s$ ,  $\zeta$ , and  $\lambda$ , a set of different ACSFs is constructed, which ought to be sufficiently large and diverse to accurately describe the atomic environment. For a graphical representation of the effect that these parameters have on the shape of the ACSFs, see Refs. [274, 276]. The symmetry functions in this work are chosen according to the schemes presented in Refs. [274, 277].

With a given set of ACSFs, a neural network with a fixed-size input layer can be constructed for each atom. Figure 2.2 illustrates such a neural network if the environment of the atom is described by only two ACSFs. In practice, significantly more ACSFs must be chosen to ensure an accurate description. The weights of the connections between the neurons, given in light orange in Fig. 2.2, can be adjusted to produce predictions that are more aligned with the reference data. The number and size of the hidden layers determine the degree of complexity that the neural network can learn, where training larger networks is more challenging. In this work, a typical fully connected feed-forward neural network is used, and the output is the atomistic energy and the forces, which can be computed as a derivative of the energy. In the reference data produced by DFT simulations, the forces are available for each individual atom, while only one total energy for the entire simulation box exists. The *ab initio* reference data is split up into a training set that usually comprises 80% of the data, and a test set that makes up the remaining 20% of data. Training is only performed on the training set, while the performance of the HDNNP is evaluated on the test set. As mentioned, the weights of the HDNNP (strength of connections between neurons and an additional bias term) are adjusted in order to achieve a better agreement between the predictions and the reference data. The gradients of the predictions for energies and forces with respect to the weights can be computed via backpropagation [278]. These gradients can then be used to minimize a cost function, for example

$$\Gamma = \frac{1}{N_E} \sum_{i=1}^{N_E} \left( \frac{E_{i,\text{ref}} - E_{i,\text{NN}}}{N_n} \right)^2 + \gamma \frac{1}{N_F} \sum_{i=1}^{N_F} \left( \frac{F_{i,\text{ref}} - F_{i,\text{NN}}}{N_n} \right)^2. \quad (2.31)$$

The total energies of the reference training configuration and the prediction by the neural network are given by  $E_{i,\text{ref}}$  and  $E_{i,\text{NN}}$ , respectively, and  $N_E$  is number of available reference

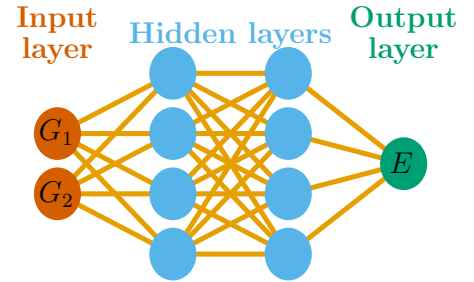


**Figure 2.2:** A schematic representation of a fully connected feed-forward neural network that takes two symmetry functions  $G_1$  and  $G_2$  to compute the energy  $E$  (modeled after Ref. [276]). Bias is omitted for readability.



energies. The quantities  $F_{i,\text{ref}}$  and  $F_{i,\text{NN}}$ , and  $N_F$  are defined analogously, but the forces are available for each atom and in every Cartesian direction. The weighting factor  $\gamma$  can be adjusted to ensure more accurate predictions for energies or forces. Instead of updating the weights after each epoch (one full pass through the training data) with standard methods like gradient descent [279] or the adaptive moment solver [280], in practice, a Kalman filter approach [281, 282] is often chosen, which adjusts the weights every time a prediction is compared to reference data.

In this thesis, the numerical implementation of the HDNNP in the `n2p2` software package is used [283–285] to learn the forces and energies, and the LAMMPS MD simulation code [286] drives the NN-MDs. For a general overview of feed-forward neural networks, see Refs. [287–289], and for a thorough discussion of HDNNPs, including newer generations of networks that also consider long-range electrostatic interactions and non-locality, see Ref. [276].

### 2.2.2 Generalized collective modes

The generalized collective modes (GCM) approach provides a systematic framework to extend the hydrodynamic description to include additional non-hydrodynamic structural or thermal relaxation processes that occur on intermediate length and time scales. In the macroscopic limit, dynamics of the three conserved hydrodynamic variables, the ion density  $n_i(k, t)$ , the current density  $j_i^1(k, t)$  (see Eqs. (2.18) and (2.19)), and the energy density

$$e(\mathbf{k}, t) = \sum_{I=1}^{N_n} \epsilon_I e^{i\mathbf{k}\cdot\mathbf{R}_I(t)} \quad (2.32)$$

are governed by the Navier-Stokes equations [259–261]. It should be noted that the atomistic energies  $\epsilon_I$  in Eq. (2.32) are naturally available in the HDNNPs discussed in Sec. 2.2.1, which is not the case for DFT-MD simulations. With the use of constitutive relations and the application of temporal Laplace transforms, a hydrodynamic matrix equation can be set up, the eigenmodes of which describe the diffusive and propagating modes of the hydrodynamic model [261]. Within this model, the iDSF can be expressed as [261]

$$S_{ii}(k, \omega) = \frac{S_{ii}(k)}{2\pi} \left[ \left( \frac{\gamma - 1}{\gamma} \right) \frac{2D_T k^2}{\omega^2 + (D_T k^2)^2} + \frac{1}{\gamma} \left( \frac{\Gamma k^2}{(\omega - c_s k)^2 + (\Gamma k^2)^2} + \frac{\Gamma k^2}{(\omega + c_s k)^2 + (\Gamma k^2)^2} \right) \right], \quad (2.33)$$

where  $\gamma = C_P/C_V$  is the heat capacity ratio,  $D_T$  is the thermal diffusivity,  $\Gamma$  is the sound attenuation coefficient, and  $c_s$  is the adiabatic speed of sound.

A simple approach to extending this model beyond the hydrodynamic regime, referred to as the generalized hydrodynamic model [290, 291], constitutes of introducing  $k$ -dependent material properties in Eq. (2.33). These quantities can then be determined from fits to scattering experiments at different angles, or MD simulations analyzed at different length scales. This approach, however, provides no pathway to directly compute the corrections to the hydrodynamic model and gives no rationale for at which wave numbers non-hydrodynamic modes contribute noticeably to the iDSF, rendering the hydrodynamic fit not suitable. The GCM approach was first proposed in Refs. [292–294]. It extends the set of three hydrodynamic variables

$$\underline{\mathbf{A}}^{(3\text{-mode})}(k, t) = \{n_i(k, t), j_i^1(k, t), e(k, t)\} \quad (2.34)$$

to include time derivatives of these variables or other non-conserved quantities. In this work, the first corrections to the hydrodynamic model in a 5-mode approximation

$$\underline{\mathbf{A}}^{(5\text{-mode})}(k, t) = \{n_i(k, t), j_i^l(k, t), e(k, t), \dot{j}_i^l(k, t), \dot{e}(k, t)\} \quad (2.35)$$

are considered by additionally including the first time derivatives of the longitudinal current density and the energy density. The relation between these variables, which is established by the Navier-Stokes equations in the hydrodynamic model, is derived via the Memory function formalism [295–297] or the generalized Langevin equation [298, 299]. A Markovian approximation is applied to higher-order memory functions, which allows us to consider memory effects and time correlations on intermediate time scales. The result of this procedure, analogous to the hydrodynamic model, is a matrix equation defined by a generalized hydrodynamic matrix. The eigenvectors  $\mathbf{X}_i$  and eigenvalues  $z_i$  of this matrix, again, characterize the collective modes of the system under investigation. Eigenmodes corresponding to real eigenvalues describe diffusive processes, while a pair of complex conjugate eigenvalues represents a propagating process. In general, all time correlation functions among the variables in the set under consideration (see Eqs. (2.34) and (2.35)) can be computed as a sum of the eigenmodes. The time correlation function for the ion density, introduced as the intermediate scattering function in Eq. (2.21), can be expressed as

$$F_{ii}(k, t) = \sum_i^{N_\nu} G_{n_i n_i}^i(k) e^{-z_i(k)t}, \quad (2.36)$$

where the weight coefficients  $G_{n_i n_i}^i$  for the time correlation function of the ion density can be directly computed through the eigenvectors. The sum runs over all  $N_\nu$  eigenmodes. Other time correlation functions, e.g., the current-current correlation function, can be determined analogously. The iDSF is given by the temporal Fourier transform of Eq. (2.36). A detailed account of the GCM approach is presented in Refs. [300, 301], and some applications ranging from simple Lennard-Jones liquids to complex binary and molecular liquids are detailed in Refs. [302–305]. Some easier-to-implement fitting schemes based on the GCM approach are presented in Refs. [306, 307].

The procedure outlined in this section, as well as the correlation functions Eqs. (2.21)-(2.24), are implemented in the python array programming package `NUMPY` [308]. The eigenvectors and eigenvalues of the generalized hydrodynamic matrix are computed through routines from the `SCIPY` package [309].

## 2.3 Electron dynamics

The dynamics of the electrons occur on significantly shorter time scales than the previously discussed ion dynamics. Equivalently, excitation energies associated with electronic transitions in scattering experiments are notably higher as discussed in Sec. 1.2.2. Furthermore, the electron dynamics are not simulated explicitly within in the DFT-MD framework. The finite temperature DFT formalism determines the average electron density in thermodynamic equilibrium and performs no explicit time propagation. Therefore, static properties like the form factor

$$N(\mathbf{k}) = \lim_{\tau \rightarrow \infty} \frac{1}{\tau} \int_0^\tau dt \frac{n_e(\mathbf{k}, t)}{n_i(\mathbf{k}, t)} \quad (2.37)$$



can be computed easily because the Fourier components of the equilibrium electron density at each point in time,  $n_e(\mathbf{r}, t)$ , can be computed via

$$n_e(\mathbf{k}, t) = \int_{\mathbb{R}^3} d^3r n_e(\mathbf{r}, t) e^{i\mathbf{k}\cdot\mathbf{r}}. \quad (2.38)$$

The form factor determines how, on average, the electrons are statically distributed around the ions, and thereby determines how strongly photons couple to the ions in scattering experiments, see Eq. (1.7) and (1.8).

However, in order to access the electron dynamics, the known equilibrium state can be studied via response theory. Although non-linear contributions to the response have received attention recently [310], this thesis only considers the linear response regime, which is sufficient for typical WDM scattering experiments.

Fundamental quantities relating the response of the system to external perturbations are the dielectric function  $\epsilon(k, \omega)$ , relating the total potential experienced by a test charge to the external potential, and the density-density response function  $\chi(k, \omega)$ , relating a change in electron density to the external potential. For a non-isotropic periodic system, these quantities ought to be written in a tensor form [311, 312] and a general relation between them is given via [313–316]

$$\epsilon_{\mathbf{G}\mathbf{G}'}^{-1}(\mathbf{k}, \omega) = \delta_{\mathbf{G}\mathbf{G}'} + V_{\mathbf{G}\mathbf{G}'}^{\mathbf{C}}(\mathbf{k}) \chi_{\mathbf{G}\mathbf{G}'}(\mathbf{k}, \omega), \quad V_{\mathbf{G}\mathbf{G}'}^{\mathbf{C}}(\mathbf{k}) = \frac{1}{\epsilon_0} \frac{e^2}{|\mathbf{G} + \mathbf{k}| |\mathbf{G}' + \mathbf{k}|}, \quad (2.39)$$

where  $\delta_{\mathbf{G}\mathbf{G}'}$  is the Kronecker delta and  $V_{\mathbf{G}\mathbf{G}'}^{\mathbf{C}}$  is the Coulomb potential in Fourier space, often called the Coulomb kernel. Here, a Bloch representation is assumed (as is suitable because the DFT codes used in this thesis employ a plane wave basis set), and the subscripts indicate that the tensors are expanded in the reciprocal lattice vectors  $\mathbf{G}$ . Equation (2.39) reduces to a scalar relation for homogeneous plasmas. In general, however, the macroscopic dielectric function must be computed by

$$\epsilon_{\mathbf{M}}(\mathbf{k}, \omega) = \frac{1}{\epsilon_{\mathbf{00}}^{-1}(\mathbf{k}, \omega)}, \quad (2.40)$$

where a full inversion of the dielectric tensor must be performed, yielding local field effect (LFE) due to non-diagonal components. These effects are denoted as crystal LFE (C-LFE) according to the classification in Ref. [317] to differentiate these contributions from LFEs due to XC effects discussed in Sec. 2.3.1. Given the electronic response defined by these quantities, the eDSF can be computed through the fluctuation dissipation theorem [318, 319] as

$$S_{ee}(k, \omega) = -\frac{\epsilon_0 \hbar k^2}{\pi e^2 \bar{n}_e} \frac{\text{Im}[\epsilon^{-1}(k, \omega)]}{1 - \exp\left(\frac{-\hbar\omega}{k_{\text{B}}T}\right)} = -\frac{1}{\pi \bar{n}_e} \frac{\text{Im}[\chi(k, \omega)]}{1 - \exp\left(\frac{-\hbar\omega}{k_{\text{B}}T}\right)}, \quad (2.41)$$

where  $\bar{n}_e$  is the average electron density. Whether this relation gives the total eDSF  $S_{ee}^{\text{tot}}$ , the eDSF of the free electrons  $S_{ee}^0$ , or the eDSF due to electronic transitions  $S_{\text{et}}$  (see Eqs. (1.7) and (1.8)) is determined by the dynamics included in the response functions  $\epsilon(k, \omega)$  and  $\chi(k, \omega)$ . If they are derived in a framework that explicitly considers the ionic as well as the electronic response to the external potential, the total eDSF can be computed. If the response functions are determined for an electron gas model,  $S_{ee}^0$  is achieved. In the LR-TDDFT framework discussed in Sec. 2.3.1, the response functions are computed from all possible electronic transitions while the ions are kept stationary. Therefore, this approach yields the eDSF due to electronic transitions  $S_{\text{et}}$  which can be combined with the ion dynamics discussed in Sec. 2.2 via the modified Chihara decomposition, Eq. (1.8).

### 2.3.1 Linear-response time-dependent density functional theory

A natural approach to simulating the electron dynamics is to extend the description of the time-independent Schrödinger equation (2.4) discussed in Sec. 2.1 to its time-dependent variant. The applicability of a density functional approach for the dynamic system is given by the Hohenberg-Kohn-type Runge-Gross theorem [234]. A real-time propagation of the electron density within the density functional description is called RT-TDDFT [76–79], which brings about additional complications as the XC functionals ought to be extended to a time-dependent formulation [320, 321]. Alternatively, the time-dependent DFT framework can be used to introduce a time-dependent external perturbation which can be treated in linear response [322–324] based on the time-independent unperturbed system discussed in Sec. 2.1. As mentioned before, the density-density response  $\chi$  is defined by the change of electron density  $\delta n_e$  due to a change in the external potential  $\delta V_{\text{ext}}$ , i.e.,

$$\chi(\mathbf{r}, \mathbf{r}', t, t') = \left. \frac{\delta n_e[V_{\text{ext}}](\mathbf{r}, t)}{\delta V_{\text{ext}}(\mathbf{r}', t')} \right|_{V_{\text{ext}}=V_{\text{ext}}[n_e^0]}. \quad (2.42)$$

Here,  $V_{\text{ext}}$  is given by the Coulomb potential between electrons and ions ( $V_{\text{ne}}$  in Eq. (2.3)) and an arbitrary external field, which can be varied to produce the perturbation. However, the external potential in DFT cannot be changed independently because the change in  $V_{\text{ext}}$  leads to a different electron density  $n_e$ , which in turn leads to a different effective potential  $v_{\text{eff}}$ , see Eq. (2.15). In other words, the effective potential can be written as  $v_{\text{eff}}[n_e[V_{\text{ext}}]]$ . Since the KS system describes non-interacting electrons in an effective potential, its density-density response can be computed by varying the effective potential as

$$\chi^{\text{KS}}(\mathbf{r}, \mathbf{r}', t, t') = \left. \frac{\delta n_e[v_{\text{eff}}](\mathbf{r}, t)}{\delta v_{\text{eff}}(\mathbf{r}', t')} \right|_{v_{\text{eff}}=v_{\text{eff}}[n_e^0]}. \quad (2.43)$$

Equations (2.42) and (2.43) can then be related to each other by using the chain rule of functional derivatives for Eq. (2.42) to give

$$\chi(\mathbf{r}, \mathbf{r}', t, t') = \int d^3x \int d\tau \left. \frac{\delta n_e(\mathbf{r}, t)}{\delta v_{\text{eff}}(\mathbf{x}, \tau)} \frac{\delta v_{\text{eff}}(\mathbf{x}, \tau)}{\delta V_{\text{ext}}(\mathbf{r}', t')} \right|_{V_{\text{ext}}=V_{\text{ext}}[n_e^0]}. \quad (2.44)$$

Now, Eq. (2.43) and the definition of the effective potential, Eq. (2.15), can be plugged into this expression. This yields a Dyson-like equation, which can be expressed in temporal and spatial Fourier space as

$$\chi_{\mathbf{G}\mathbf{G}'}(\mathbf{k}, \omega) = \frac{\chi_{\mathbf{G}\mathbf{G}'}^{\text{KS}}(\mathbf{k}, \omega)}{1 - [V_{\mathbf{G}\mathbf{G}'}^{\text{C}}(\mathbf{k}) + f_{\text{XC}}(\mathbf{k}, \omega)] \chi_{\mathbf{G}\mathbf{G}'}^{\text{KS}}(\mathbf{k}, \omega)}. \quad (2.45)$$

Here the Coulomb kernel  $V_{\mathbf{G}\mathbf{G}'}^{\text{C}}(\mathbf{k})$  and the XC kernel  $f_{\text{XC}}(\mathbf{k}, \omega)$  enter through the functional derivative of  $v_{\text{eff}}$  in Eq. (2.44), and recover all the correlations which were lost in performing a response calculation on the mean-field system as opposed to the fully interacting system. Setting  $f_{\text{XC}}(\mathbf{k}, \omega) = 0$  achieves a mean field description on the level of the RPA [159–161]. In contrast, not neglecting the XC kernel introduces LFEs due to exchange-correlation contributions, denoted exchange-correlation LFEs (XC-LFEs) [317]. A common choice for  $f_{\text{XC}}(\mathbf{k}, \omega)$  is the adiabatic local density approximation (ALDA) [190, 320]. This approximation, however, has known shortcomings [325] and the formulation of new XC kernels is an active field of research [326–330].

The independent-particle density-density response of a KS system can be written as [311, 312, 331, 332]

$$\chi_{\mathbf{G}\mathbf{G}'}^{\text{KS}}(\mathbf{k}, \omega) = \frac{2}{\Omega} \sum_{\mathbf{g}}^{\text{BZ}} w_{\mathbf{g}} \sum_{i,j} \frac{f(\epsilon_{\mathbf{g},i}) - f(\epsilon_{\mathbf{g}+\mathbf{k},j})}{\hbar\omega + \epsilon_{\mathbf{g},i} - \epsilon_{\mathbf{g}+\mathbf{k},j} + i\eta} \times \langle \phi_{\mathbf{g},i} | e^{-i(\mathbf{k}+\mathbf{G})\cdot\mathbf{r}} | \phi_{\mathbf{g}+\mathbf{k},j} \rangle \langle \phi_{\mathbf{g}+\mathbf{k},j} | e^{i(\mathbf{k}+\mathbf{G}')\cdot\mathbf{r}} | \phi_{\mathbf{g},i} \rangle. \quad (2.46)$$

The indices  $i$  and  $j$  run over the eigenstates,  $\mathbf{g}$  denotes the reciprocal vectors in the Brillouin zone (BZ), and  $\phi_{\mathbf{g},i}$  and  $\epsilon_{\mathbf{g},i}$  are the KS wave functions and eigenenergies from Eq. (2.14). The Fermi-Dirac occupation at a given eigenenergy is described by  $f(\epsilon_{\mathbf{g},i})$ . The normalization volume is denoted by  $\Omega$ , and  $w_{\mathbf{g}}$  is the weighting of each  $k$ -point. The infinitesimal contribution  $\eta$  is introduced to avoid the pole. If the XC kernel is set to zero and the homogeneous case is studied, as is appropriate for WDM (see the appendix of Ref. [167]), Eq. (3.2) can be simplified to

$$\epsilon^{\text{KS,RPA}}(\mathbf{k}, \omega) = 1 - \frac{e^2}{|\mathbf{k}|^2} \chi^{\text{KS}}(\mathbf{k}, \omega), \quad (2.47)$$

which represents the macroscopic value and can be used to compute the response of the electrons in XRTS experiments.

In this thesis, the dielectric functions and density-density response functions in the LR-TDDFT framework are computed with the GPAW code [243–246]. Extensive reviews of LR-TDDFT and TD-TDDFT can be found in Refs. [190, 333, 334].

### 2.3.2 Electrical conductivity

Numerical computations of electrical conductivity in WDM are usually performed within linear response theory [335–339]. Given the dielectric response of the macroscopic system, computed through, e.g., the equations derived in the previous section, Eqs. (2.40) and (2.47), the dynamic electrical conductivity  $\sigma(\omega)$  is defined by

$$\lim_{k \rightarrow 0} \epsilon(k, \omega) = 1 + i \frac{1}{\epsilon_0 \omega} \sigma(\omega). \quad (2.48)$$

The fidelity of the conductivity computed through this approach is determined by the XC functional  $F_{\text{XC}}[n_e]$  in Eq. (2.12), used to compute the KS orbitals and eigenenergies, and the XC kernel  $f_{\text{XC}}(\mathbf{k}, \omega)$  in Eq. (2.45), required to compute the response function.

Alternatively, an expression for  $\sigma(\omega)$  [340] can be derived within the statistical framework developed by Kubo [318]. In fact, a general expression for Onsager coefficients exists, from which  $\sigma(\omega)$  and other quantities such as the thermal electrical conductivity and the Lorenz number can be determined [340, 341]. In a basis of KS orbitals, the conductivity according to the Kubo-Greenwood formula [318, 342] is expressed as [343]

$$\text{Re}[\sigma(\omega)] = \frac{2\pi e^2}{3\omega\Omega} \sum_{\mathbf{g}}^{\text{BZ}} w_{\mathbf{g}} \sum_{i,j} \sum_{\alpha=1}^3 [f(\epsilon_{\mathbf{g},j}) - f(\epsilon_{\mathbf{g},i})] \times |\langle \phi_{\mathbf{g},j} | \hat{v}_{\alpha} | \phi_{\mathbf{g},i} \rangle|^2 \delta(\epsilon_{\mathbf{g},i} - \epsilon_{\mathbf{g},j} - \hbar\omega). \quad (2.49)$$

Here,  $\alpha$  runs over the spatial orientations, and the matrix elements  $\langle \phi_{\mathbf{g},j} | \hat{v}_{\alpha} | \phi_{\mathbf{g},i} \rangle$  can be computed from internal routines of DFT codes which take into consideration the effect of the projector augmented wave method [344]. For practical purposes, due to the finite inter-band energy difference, the delta function in Eq. (2.49) ought to be replaced by a Gaussian with a

broadening parameter [345]. This parameter is considered a convergence parameter and must be carefully chosen.

Various other numerical and analytic approaches exist to treat electron dynamics and compute electrical conductivity. For instance, PIMC, especially in its finite temperature formulation and with its efficient implementation [81, 346, 347], supplies valuable *ab initio* results for the homogeneous electron gas [83, 348–351]. It can provide response functions and structure factors [352–355] beyond the XC approximations in DFT. Analytic expression for the direct current conductivity are available in some limiting cases. In a seminal work, Spitzer and Härm derived a value for non-degenerate ideal plasma limit [356], while the Ziman theory describes the fully degenerate limit [357]. To describe the intermediate regime, various interpolation formulas based on, e.g., a generalized Ziman formula [358, 359], a relaxation time approximation [360], and a generalized linear response theory approach combined with a virial expansion of the conductivity [361] have been proposed. A comparison of the Kubo-Greenwood conductivity in Eq. (2.49) with a virial expansion of the conductivity is presented in Sec. 3.4.

## 2.4 Bayesian inference

Astrophysical modeling or the analysis of WDM experiments often include vastly complex models that combine many correlated or uncorrelated input parameters to compute the quantities of interest. Due to the potentially complicated interaction of these input parameters, strong biases might be introduced by concentrating on a subset of the parameters and keeping the remainder constant at heuristically (or arbitrarily) set values [43].

In a general scenario, a set of observed data of interest  $\mathbf{Y} = \{Y_n, n = 1, \dots, N_{\text{obs}}\}$  is given and a probability distribution for a set of input parameters  $\Theta = \{\Theta_n, n = 1, \dots, N_{\text{par}}\}$ , underlying a model  $\mathcal{M}(\mathbf{X}; \Theta)$  which computes the quantity of interest from independent variables  $\mathbf{X} = \{X_n, n = 1, \dots, N_{\text{ind}}\}$  is sought. Here, the number of observations, input parameters, and independent parameters is given by  $N_{\text{obs}}$ ,  $N_{\text{par}}$ , and  $N_{\text{ind}}$ , respectively. In the example of an XRTS experiment, the observations would be the scattering intensity under a scattering angle at a given frequency shift, where the latter two quantities would represent the independent variables. The model would be any sensible physical model that can describe the quantities in Eq. (1.9) for a given scattering angle (or equivalently wave number  $k$ ) and frequency shift  $\omega$ . The input parameters would be a set of parameters describing the target and the experimental setup. In order to find the most likely underlying input parameters, Bayes' theorem [362]

$$P(\Theta|\mathbf{Y}) = \frac{P(\mathbf{Y}|\Theta)P(\Theta)}{P(\mathbf{Y})} \quad (2.50)$$

can be employed. Here,  $P(\Theta|\mathbf{Y})$  is the posterior probability distribution for the parameters  $\Theta$ , given that  $\mathbf{Y}$  was observed, which is the quantity of interest in this section. The prior probability  $P(\Theta)$  encompasses the prior knowledge about the input parameters, which is available before the observations are performed. This information might be due to prior observations and experimental measurements or general restrictions for sensible values of the parameters. The general probability of the observations is given by  $P(\mathbf{Y})$ . This quantity can often not be practically computed. However, since it does not depend on the input parameters, it can be neglected during the inference of  $\Theta$ . The likelihood function  $P(\mathbf{Y}|\Theta)$  describes the likelihood that the observations  $\mathbf{Y}$  were randomly drawn from a given distribution around the true value computed from the model  $\mathcal{M}$  based on parameters  $\Theta$ . A frequent assumption for the spread of the observations is a normal distribution. However, in some situations, the nature of the observation can be included here. For example, for the single-photon detectors employed in Sec. 3.6.2, the distribution of observations around the true value is expected to be a Poisson distribution.

### Efficient sampling of parameter space

The aim of this consideration is to determine  $P(\Theta|\mathbf{Y})$ . However, Eq. (2.50) must be evaluated for every possible value of the vector  $\Theta$ . The dimension of the parameter space grows linearly with the number of input parameters to the model  $\mathcal{M}(\mathbf{X}; \Theta)$ . Even for moderate-size models, it becomes intractable to sample the full parameter space to determine the posterior probability  $P(\Theta|\mathbf{Y})$ .

Therefore, more advanced sampling methods like importance sampling, or MCMC sampling ought to be used to avoid the regions of parameter space where  $P(\Theta|\mathbf{Y})$  is low. A MCMC sampler navigates through parameter space according to an algorithm, and instead of computing the value of the posterior probability at each point in parameter space, the posterior probability is given by the frequency with which every point in parameter space is visited. A schematic representation of this approach for a one-dimensional parameter space is given in Fig. 2.3. One of the most prominent MCMC samplers is the Metropolis-Hastings algorithm [364, 365]. The central quantities in this algorithm are the proposal probability  $g(\Theta'|\Theta)$ , which determines how new proposal points in parameter space are chosen, and the acceptance probability  $A(\Theta'|\Theta)$  of moving to a new point  $\Theta'$  in parameter space, given the current position  $\Theta$ . The proposal density  $g(\Theta'|\Theta)$  must be chosen broad enough to ensure that the parameter space is explored sufficiently but narrow enough to guarantee an appropriate acceptance rate. The acceptance probability in the Metropolis-Hastings algorithm is given by

$$A(\Theta'|\Theta) = \min\left(1, \frac{P(\mathbf{Y}|\Theta') P(\Theta') g(\Theta|\Theta')}{P(\mathbf{Y}|\Theta) P(\Theta) g(\Theta'|\Theta)}\right). \quad (2.51)$$

Here, the factor  $g(\Theta|\Theta')/g(\Theta'|\Theta)$  accounts for biases introduced via asymmetric proposal distributions. The algorithm can then be performed as follows:

1. Choose initial parameter vector  $\Theta = \Theta_0$ .
2. Generate new sample according to  $g(\Theta'|\Theta)$ .
3. Evaluate the acceptance probability  $A(\Theta'|\Theta)$  via Eq. (2.51).
4. Accept if a random number uniformly drawn from  $[0, 1]$  is smaller or equal to  $A(\Theta'|\Theta)$ . Reject otherwise.

This cycle is performed until convergence in the histogram of sample frequency, shown on the right in Fig. 2.3, is reached.

Although the Metropolis-Hastings algorithm performs well for moderate-size models, it exhibits shortcomings in very high-dimensional cases, e.g., slow burn-in and low acceptance rates. In these cases, more modern sampling approaches such as the Sequential Monte Carlo algorithm [366–368] ought to be used. The Sequential Monte Carlo approach is considered an extension of importance sampling. It produces uncorrelated samples, avoiding being trapped in local minima, and does not require a burn-in period. The Bayesian inference in this thesis is performed within the PyMC3 package [369] and uses the Sequential Monte Carlo algorithm. Although Bayesian analysis has been employed extensively in many fields over the past decades, only recently has it emerged as a powerful tool in the analysis of WDM scattering and

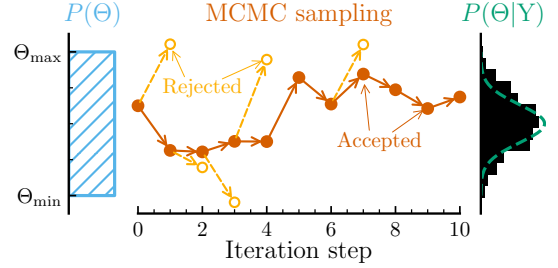


**Figure 2.3:** A schematic representation of Markov-Chain Monte-Carlo (MCMC) sampling of a Gaussian distribution, modeled after Ref. [363].

---

diffraction experiments [42–45]. Further reading regarding Bayesian statistics and sampling techniques can be found in Refs. [289, 370, 371].

### 3 Results

As discussed in Chapter 1, the field of WDM research relies tremendously on the combination of sophisticated theoretical studies, experimental investigations of extreme states of matter in the laboratory, astrophysical observations and accurate modeling of stellar and planetary evolution and interior structure. The close connection of these fields is schematically represented in Fig. 3.1. This thesis presents advances in the theoretical description of ion and electron dynamics based on DFT-MD simulations. These are driven mainly by adopting advanced machine learning techniques and sophisticated many-body theory. The central quantities of interest are electron-electron and ion-ion static and dynamic structure factors (iDSF, eDSF, iSSF & eSSF). From these, material and transport properties relevant to astrophysical modeling, like sound speed, ionic thermal conductivity, electrical conductivity, and others, can be deduced. To ensure sufficient accuracy, the theoretical predictions are compared to experimental data at ambient conditions and known theoretical limiting cases. Additionally, past XRTS experiments at WDM conditions are reanalyzed using more advanced theoretical methods, and the analysis of a new experiment at the NIF is presented. Moreover, the relevance of holistically analyzing experimental results by also considering the experimental setup and free parameters in the theoretical model within a consistent statistical framework is highlighted. Additional contributions to several experimental campaigns are briefly mentioned, and further theoretical support for ongoing analyses of experimental campaigns at GSI and the LCLS are presented. A list of the scientific works to which this author contributed and where the contribution was

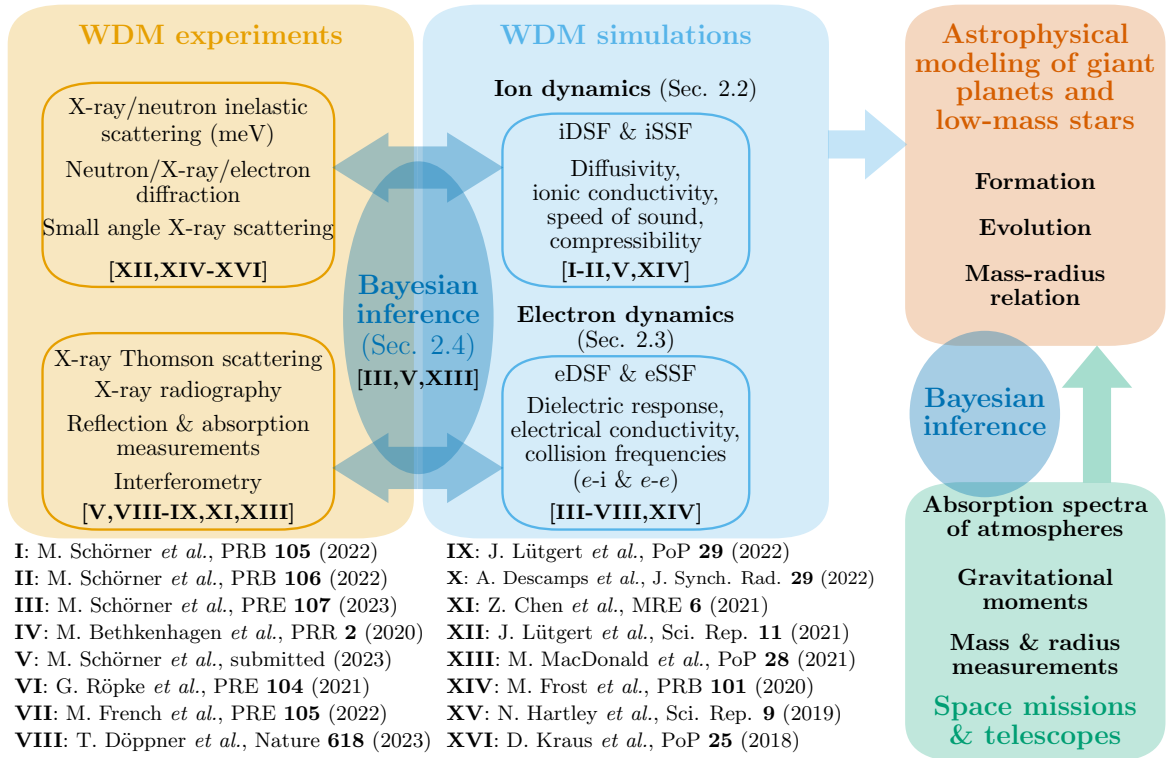


**Figure 3.1:** A schematic overview of the interplay between experiments, simulations, astrophysical modeling, and space missions/telescopes in the context of WDM research. For each field, a few topics of interest are given. The areas of WDM experiments and simulations are shown larger than the other sub-fields to highlight that they are the focus of this thesis. A list of scientific works this author contributed to is shown at the bottom of the figure, and which area of WDM research the respective works contributed to is indicated in the schematic overview by square brackets.



made in the field is shown in Fig. 3.1. This work demonstrates the close interplay of theory and experiment in WDM research.

### 3.1 New insights into ion dynamics at extreme conditions through high-dimensional neural network potentials [Papers I & II]

As described in Sec. 2.2.1, over the past two decades, the advent of HDNNPs has enabled the simulation of large-scale systems with *ab initio* precision. After the first seminal work on the use of neural networks for learning interatomic potentials [263], early applications focused on the simulation of simple molecules [372, 373] and their interaction with metal surfaces [374, 375]. Only recently have these HDNNPs started to be applied in the WDM field [46, 47] and enabled new insights and improved resolution for material properties like the iDSF and intermediate scattering function, which, on a macroscopic scale, could previously only be analyzed for classical MD simulations [376, 377]. For a detailed account of the progress made in HDNNPs, see Ref. [276].

In paper I [378] and paper II [379], the neural network architecture proposed by Behler and Parinello [272] is employed to learn the atomistic energies and forces in aluminum and copper. Paper I [378] considers a wide range of conditions in aluminum ranging from the liquid metal to the warm dense regime and explores to which extent the hydrodynamic regime can be reached and what material properties can be extracted there. The necessary formulas and algorithms for computing the iSSF  $S_{ii}(k)$ , as well as the iDSF  $S_{ii}(k, \omega)$  and intermediate scattering function  $F_{ii}(k, t)$  are presented. The predictions for  $S_{ii}(k)$  and  $S_{ii}(k, \omega)$  are compared to experimental data at liquid metal conditions by Waseda [380] and Scopigno *et al.* [381], respectively, showing good agreement with the diffraction measurement and exhibiting the general trends observed in the inelastic X-ray scattering experiment. Furthermore, it is verified that the NN-MDs reproduce the static and dynamic properties computed from DFT-MD in the  $k$  range accessible to both approaches across all considered conditions so that the presented NN-MD results can be expected to represent *ab initio* precision.

To systematically study the convergence towards the macroscopic limit and the hydrodynamic description, valid at large distances and long time scales, the framework of the GCM approach is used; see Sec. 2.2.2. Additional modes, which go beyond the diffusive heat and the propagating sound mode known from the hydrodynamic model [261], can be accounted for in this framework. However, these non-hydrodynamic modes vanish in the limit of small  $k$  as depicted in Fig. 8 of paper I [378], leaving only one diffusive and one propagating mode. As these modes coincide with the hydrodynamic modes in the limit  $k \rightarrow 0$ , they can be identified as generalized hydrodynamic modes [291] for finite  $k$  as long as non-hydrodynamic modes do not significantly contribute to the dynamics. In the hydrodynamic model, the shape of the iDSF is given by macroscopic material properties, e.g., heat capacity ratio  $\gamma$ , thermal diffusivity  $D_T$ , and adiabatic speed of sound  $c_s$ . For the generalized hydrodynamic modes, these properties become  $k$ -dependent and only converge toward their macroscopic values when the macroscopic limit is reached. This convergence is exemplified in Fig. 3.2 for one of the conditions covered in paper I [378], i.e.,  $T = 1$  eV and  $\rho = 2.356$  g/cm<sup>3</sup>. The  $k$ -dependent generalized heat capacity ratio  $\gamma(k)$  and the generalized ionic thermal conductivity  $\lambda(k)$ , determined through fitting  $S_{ii}(k, \omega)$  and  $F_{ii}(k, t)$  to two generalized hydrodynamic modes, are shown with their respective uncertainties. Both quantities converge to their macroscopic values, which are computed from thermodynamic derivatives [382] for  $\gamma$  and a Green-Kubo relation [383] for  $\lambda$ ; see the dashed lines in Fig. 3.2. The hydrodynamic limit is reached in the NN-MD simulations, whereas in the DFT-MD simulation with 125 atoms (not shown here), wave numbers below  $0.5 \text{ \AA}^{-1}$  are not attainable. Further conditions of liquid aluminum and other quantities, e.g., the adiabatic



speed of sound and the sound attenuation coefficient, are studied in detail, and a comprehensive summary of the obtained values is given in [paper I \[378\]](#). Especially for converting the thermal diffusivity to the ionic thermal conductivity, it is pointed out that great care must be taken in partitioning the heat capacity into electronic and ionic contributions. Only the ionic contribution to the heat capacity should be considered to arrive at the correct value for  $\lambda$ .

The framework presented in [paper I \[378\]](#) for aluminum, in particular the calculation of iSSFs and iDSFs from NN-MDs, is applied to a typical WDM experiment, i.e., a dynamic shock compression (see [Sec. 1.2.1](#)), for copper in [paper II \[379\]](#). Additionally, the study is extended to the solid phase of copper. It considers transverse excitations by decomposing the current-current correlation spectrum  $J_{ii}(k, \omega)$  into its longitudinal and transverse parts as described in [Eq. \(2.24\)](#). For solid copper, the phonon spectrum along high-symmetry orientations in reciprocal space, derived from the peak positions of the longitudinal and transverse parts of  $J_{ii}^{1/t}(k, \omega)$ , is calculated. It is compared to experimental data by Nicklow *et al.* [384] showing excellent agreement. Furthermore, the electrical conductivity is computed

via the Kubo-Greenwood formula, [Eq. \(2.49\)](#), with the PBE [220] and HSE [227, 228] functionals, and via LR-TDDFT, [Eq. \(2.47\)](#). The general agreement to absorption measurements by Henke *et al.* [385] is good for all approaches. However, the first dip in conductivity at approximately 2 eV is underestimated by all theories; see [Fig. 3 in paper II \[379\]](#). For copper in the liquid metal regime, the method is benchmarked by comparing the iSSF to neutron and X-ray diffraction measurements by Waseda and Ohtani [145], and Eder *et al.* [386], respectively, demonstrating good agreement. Additionally, the accuracy of the iDSF is gauged by comparing the peak width of the central thermal mode predicted by the NN-MD simulations with experimental findings by Hagen [387], and Eder *et al.* [386]. It is found that the de Gennes minimum [388] and the behavior at higher  $k$  are reproduced very well. Only at the smallest wave numbers covered experimentally the NN-MD overestimates the width; see [Sec. IV. of paper II \[379\]](#) for more discussion.

Given the good agreement with experimental data, the study is extended to higher temperatures and pressures where experimental observations are very scarce. DFT-MD simulations have proven suitable to predict the states reached during shock compression experiments via the Hugoniot equation [\(1.3\)](#) [18, 114, 115]. Therefore, EOS data up to 60 000 K are computed via DFT-MD simulations and are subsequently used to solve [Eq. \(1.3\)](#) numerically. The resulting principal Hugoniot curve is shown in the density-pressure and pressure-temperature plane in [Figs. 7 and 8 of paper II \[379\]](#), respectively. The results are compared to various experimental data (see [Refs. \[389–396\]](#)), and good agreement is found at relatively low pressures, where the DFT-MD predictions are also comparable to the SESAME EOS table [397]. At higher pressure (approximately above 800 GPa), the principal Hugoniot curve diverges from

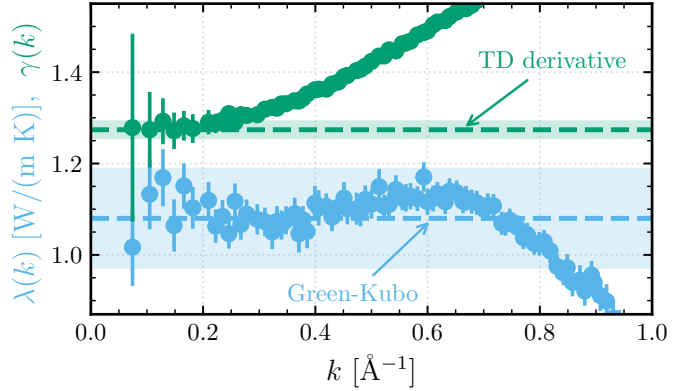


**Figure 3.2:** The generalized heat capacity ratio  $\gamma(k)$  (green filled circles) and generalized ionic thermal conductivity  $\lambda(k)$  (blue filled circles) depending on the wave number  $k$  for liquid aluminum at  $T = 1$  eV and  $\rho = 2.356$  g/cm<sup>3</sup>; see [paper I \[378\]](#) for details. The macroscopic values for the respective quantities are given by the dashed lines, computed from thermodynamic derivatives (TD) [382] and a Green-Kubo relation [383]. The shaded areas represent the uncertainty.

the SESAME predictions. Unfortunately, the experimental uncertainties in this regime are too significant to discriminate between the two approaches. Along the computed principal Hugoniot curve, the evolution of the ion correlations is studied. Up to the melting point, the phonon spectrum is studied, and beyond, the iSSF and iDSF are considered and discussed in detail. The adiabatic speed of sound  $c_s$ , which is connected to the behavior of the propagating sound mode in the iDSF as shown in [paper I \[378\]](#), is compared to VISAR observations in a shock-compression experiment by McCoy *et al.* [394]. The trends with increasing pressure are reproduced well, but the simulations slightly underestimate  $c_s$ . However, the pressure and density observed in the shock-compression experiment align with the predictions of the simulation, indicating that the observed differences are due to a different temperature which was not observed by McCoy *et al.*

In [Fig. 3.3](#), the GCM formalism described in [paper I \[378\]](#) and [Sec. 2.2.2](#) is applied to two conditions beyond the melting point on the principal Hugoniot curve presented in [paper II \[379\]](#). The first condition, shown in the left column, is close to the melting line at  $P = 3.93$  Mbar, and the second condition, depicted in the right column, is at  $P = 9.41$  Mbar, much farther away from the melting line with a temperature of 30 000 K. It is remarkable that, since the GCM formalism requires the knowledge of the energy for each atom (see [Sec. 2.2.2](#)), it cannot be

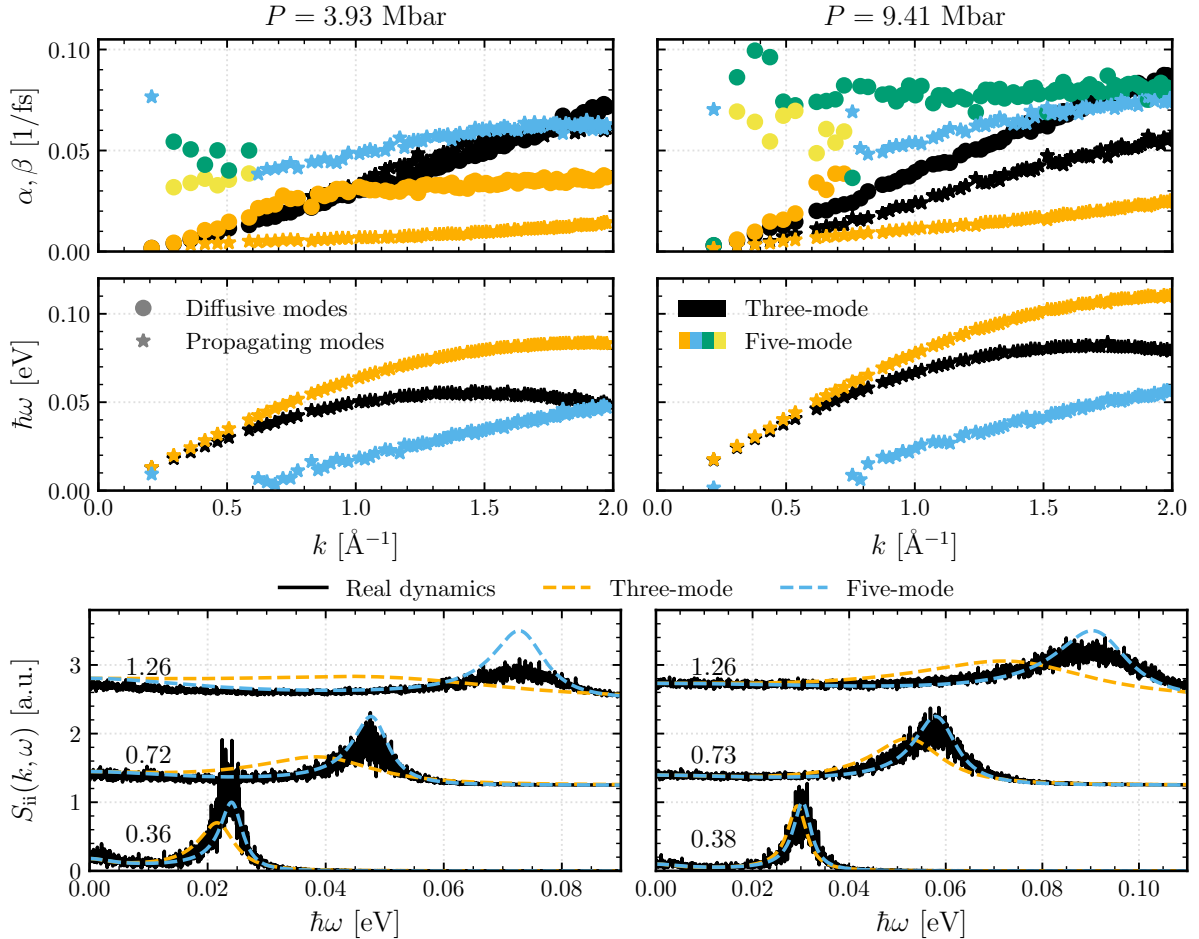


**Figure 3.3:** The GCM description of the iDSF of shock-compressed copper at  $P = 3.93$  Mbar (left column) and  $P = 9.41$  Mbar (right column) on the principal Hugoniot curve; see [paper II \[379\]](#) for the exact conditions. The top row shows the respective decay coefficients  $\alpha$  and  $\beta$  of the diffusive and propagating modes for the three and five-mode approaches. The middle row shows the dispersion relations for the propagating modes. The bottom row shows the predictions of the three and five-mode approaches for three different wave numbers (in units  $\text{\AA}^{-1}$ ), given by the black numbers, compared to the full dynamics observed directly from the MD simulation.

easily applied to DFT-MD simulations because these individual energies are not available due to the many-body nature of DFT. However, because the HDNNPs learn the energies and forces for each particle, this information is naturally accessible when performing NN-MD simulations. For the two conditions along the Hugoniot, the top two rows of Fig. 3.3 display the same analysis as performed on warm dense aluminum in Fig. 8 of paper I [378]. The decay coefficients of the diffusive and propagating modes and the dispersion relations for the propagating modes are computed according to the three and five-mode models; see Sec. 2.2.2. As expected, only the hydrodynamic modes exhibit non-vanishing decay coefficients in the hydrodynamic limit. Two additional diffusive modes with finite decay coefficients appear, as was also observed for aluminum. For  $P = 3.93$  Mbar, these two modes merge at  $0.6 \text{ \AA}^{-1}$  to create a propagating mode. In contrast, at the higher pressure, one of the non-hydrodynamic modes merges with the hydrodynamic diffusive mode to create the new propagating mode. The bottom row of Fig. 3.3 shows the iDSF computed directly from the NN-MD simulations via Eq. (2.22) in black compared to the dynamic predictions from the three and five-mode approaches as dashed lines. For this analysis, the window function discussed in paper I [378] is not applied, which results in the high statistical fluctuations in the iDSF. It is apparent that the three-mode approach quickly deteriorates at wave numbers above  $0.6 \text{ \AA}^{-1}$ , significantly underestimating the mode position of the ion-acoustic mode. Contrarily, the five-mode approach captures its general position well up to the intermediate wave number regime, indicating that the non-hydrodynamic corrections play an essential role in this regime. However, for the Hugoniot state close to the melting line, the magnitude of the ion-acoustic mode is overestimated at  $k = 1.26 \text{ \AA}^{-1}$ . At the same time, the agreement at this wave number is still good for the higher pressure state. Higher-order non-hydrodynamic corrections have a stronger impact in more strongly correlated systems because the strong Coulomb interactions on intermediate length scales are not captured by the hydrodynamic equations. Figure 9 of paper II [379] illustrates the change in the iSSF along the principal Hugoniot which demonstrates the decrease in strong correlations with increasing temperature. This observation is relevant for the execution of meV scattering experiments. The probed wave number can be determined by adjusting the scattering angle accordingly. In order to measure the iDSF in the hydrodynamic regime, the contribution of non-hydrodynamic modes must be negligible at the investigated  $k$  value.

### 3.2 Inelastic electronic dynamic structure factor at extreme conditions [Papers III & IV]

Since the first experimental observation of forward scattering in WDM in 2007 [94], the theoretical methods for describing the light-matter interaction and the collective phenomena probed in forward scattering have improved tremendously. In the early years of this emerging field, the RPA was often used to describe the free electrons [95, 398], which neglects all collisions and includes an average screening mediated through the Coulomb interaction. Due to low experimental signal-to-noise ratios, this approach yielded adequate results at the time. To include electron-ion ( $e$ - $i$ ) collisions, the Mermin formalism, which extends the RPA via a dynamic complex collision frequency [399–401], was combined with a variety of approximate expressions for the  $e$ - $i$  collisions [402]. This was further improved by computing first a static [403] and then a dynamic collision frequency [166] by using the electrical conductivity computed through the Kubo-Greenwood formula, Eq. (2.49), from DFT simulations. However, because these analytic approaches lack a notion of bound states, they can only be applied to the free electrons, while the bound states are traditionally treated within the impulse approximation [163–165]. In WDM, this clear separation into bound and free electrons breaks down due to thermal and pressure ionization [404] and traditional definitions of the ionization state, which enter in the Chihara decomposition of the eDSF as a weighting factor (see Eq. (1.7)), predict unreasonable behavior [405–407]. This can be circumvented by considering all electrons within the same

framework, for example, LR-TDDFT (see Sec. 2.3.1), which has been used more recently in WDM [52, 65, 408]. Although much more computationally expensive than the analytic descriptions, LR-TDDFT simulations allow us to fully consider many-body and quantum mechanical correlation and degeneracy effects. Further theories that are capable of describing bound and free states in WDM are RT-TDDFT [78, 79] and PIMC [80–83] among others, which are beyond the scope of this thesis.

Paper III [167] contains a detailed comparison of the state-of-the-art Mermin-based approach with the dynamic collision frequency computed from Kubo-Greenwood conductivities and the LR-TDDFT formalism, while paper IV [404] explores how the electrical conductivity can be decomposed into contributions from free-free and bound-free transitions, and how this can be used to give a sensible definition of the ionization state in the WDM regime. The decomposition of the electrical conductivity is performed by restricting the sums over initial and final states in the Kubo-Greenwood formula, Eq. (2.49), to specific sets of states that can be identified from the density of states (DOS). In the case of carbon, the DOS shows a band of quasi-bound states to the left of the band gap, which become the well-known 1s states in the limit of an isolated atom. To the right of the band gap, a conduction band can be observed. In Fig. 2 of paper IV [404], the severe broadening of the quasi-bound states and closing of the band gap with increasing density is illustrated. The possible transitions contributing to the electrical conductivity in this case can be summarized as bound-bound (b-b), bound-free (b-f), and free-free (f-f) transitions; see Fig. 1 of paper IV [404] for a visualization. The well-known Thomas-Reiche-Kuhn sum rule [409–412] connects the integral over the dynamic electrical conductivity with the total number of electrons. The idea is now to apply this sum rule to the individual parts of the decomposed electrical conductivity. The number of electrons associated with a specific set of transitions can then be related to the decomposed electrical conductivity via

$$Z^x := \frac{2m_e V}{\pi e^2 N_i} \int_0^\infty d\omega \sigma^x(\omega), \quad x = \{f-f, b-f, b-b\}. \quad (3.1)$$

As a consequence, an average ionization state  $Z^f$  can be connected to the number of electrons per atom contributing to the free-free conductivity  $\sigma^{f-f}(\omega)$  via  $Z^f = Z^{f-f}$ . In contrast, a traditional approach is to integrate the occupied DOS in the conduction band to define the number of free electrons [413–415]. However, this approach neglects the nature of the quasi-bound states to the left of the band gap and cannot account for the delocalization of formerly bound states. The definition in Eq. (3.1) does not suffer from this shortcoming because the sum rule relies on the completeness of the electronic basis set. Therefore, although the integral is performed solely over the free-free part of the conductivity, the ionization state also includes overlap integrals of quasi-bound and free states, which increase as the bound states delocalize. Figure 3.4 shows a comparison of the traditional DOS-based approach to computing the ionization state (left column) and the sum-rule-based approach of Eq. (3.1) (right column) for the conditions of isochorically heated (top row) and compressed (bottom row) beryllium studied in paper III [167]. For the isochorically heated sample at ambient density, the DOS-based approach yields an ionization state  $Z^f = 2$ , suggesting no temperature ionization of the 1s electrons at this temperature. Conversely, the sum-rule-based approach predicts a slight increase in the ionization state due to thermal excitation. However, the shortcomings of the DOS-based approach become especially apparent for highly compressed beryllium. The ionization state  $Z^f = 2.12$  predicted by the DOS-based approach indicates almost no pressure ionization occurs at more than 20-fold compression. In contrast, the definition from Eq. (3.1) considers the significant broadening of the quasi-bound states and the closing of the band gap and accordingly determines the ionization state as  $Z^f = 2.9$ . A more comprehensive study of the sum-rule-based definition of the ionization state for carbon and hydrocarbon and a thorough comparison to analytical models are presented in paper IV [404].

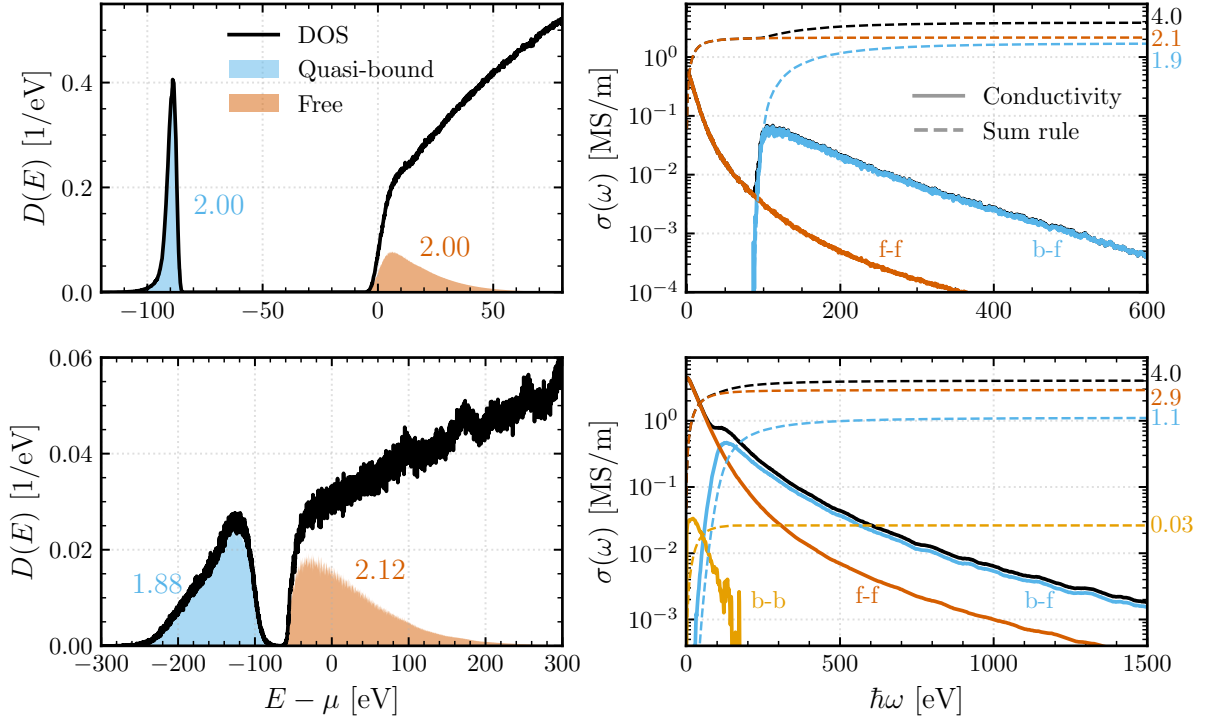


**Figure 3.4:** An illustration of the DOS approach (left column) and the sum-rule-based approach (right column) to determine the ionization state for beryllium at  $\rho = 1.8 \text{ g/cm}^3$  and  $T = 12 \text{ eV}$  (top row) and  $\rho = 40 \text{ g/cm}^3$  and  $T = 50 \text{ eV}$  (bottom row). The black lines in the left column depict the DOS per atom, and the blue and dark orange shaded areas indicate the occupied quasi-bound and free states, respectively. The colored numbers represent the summed-up occupations per atom for the respective shaded areas. The solid lines in the right column depict the full electrical conductivity (black) and the decomposition into contributions from b-f (blue), f-f (dark orange), and b-b (light orange) transitions. The dashed lines depict the values of  $Z^x$  in Eq. (3.1) in dependence of the upper limit of the integral, while the colored numbers specify their converged values.

The dynamic electrical conductivity is intimately connected to the dielectric function, see Eq. (2.48), which can be used to compute the eDSF, as described by the fluctuation-dissipation theorem in Eq. (2.41). Paper III [167] examines how the decomposition of the electrical conductivity shown in the right column of Fig. 3.4 can be used to determine an *ab initio*  $e$ - $i$  collision frequency for the free electrons and how this can be used to compute the eDSF across a range of wave numbers for fully ionized hydrogen, and isochorically heated and compressed beryllium. These results are compared to LR-TDDFT simulations, the state-of-the-art *ab initio* approach for computing the eDSF. The collision frequency is found as the complex collision frequency  $\nu(\omega)$ , which, when plugged into the Mermin dielectric function  $\epsilon^{\text{Mermin}}$ , yields the same result as the dielectric function computed from DFT  $\epsilon^{\text{DFT}}$  in the long wavelength limit:

$$\epsilon^{\text{DFT}}(k=0, \omega) \stackrel{!}{=} \lim_{k \rightarrow 0} \epsilon^{\text{Mermin}}(k, \omega; \nu(\omega)). \quad (3.2)$$

The thus determined  $e$ - $i$  collision frequency,  $\nu^{\text{DFT}}$ , is compared to a variety of analytic approaches [402] for a hydrogen plasma at  $\rho = 2 \text{ g/cm}^3$  and temperatures ranging from  $T = 5 \text{ eV}$  to  $T = 100 \text{ eV}$ ; see Fig. 3 in paper III [167]. In the limit approaching an ideal hydrogen plasma,  $T = 100 \text{ eV}$ , best agreement is observed with the T-Matrix and Gould-DeWitt approach [416–418], indicating that strong collisions must be included in this regime to reach reliable results. Additional consideration of electron-electron ( $e$ - $e$ ) scattering in the Gould-DeWitt scheme results in worse agreement with  $\nu^{\text{DFT}}$  in accordance with the results of paper VI [419] and paper VII [420], which are discussed in Sec. 3.4.



Due to the full ionization of the hydrogen plasma, the total electrical conductivity can be used to determine  $\nu^{\text{DFT}}$ , while for beryllium, special care must be taken of the bound states. Because the Mermin dielectric function is unsuitable to describe bound states, only the f-f contribution to the electrical conductivity shown in the right column of Fig. 3.4 ought to be used to compute the  $e$ -i collision frequency. The b-f contribution to the eDSF can then be approximated by the impulse approximation [163–165] or by assuming that the b-f contribution up to intermediate wave numbers can be well approximated by its result from  $\sigma^{\text{b-f}}$  at  $k = 0 \text{ \AA}^{-1}$ . The latter approach has shown good results in aluminum [166] and is also adopted in paper III [167]. For such a decomposition into b-f and f-f contributions, the correct weighting factors, traditionally assumed to be the ionization states  $Z^{\text{b}}$  and  $Z^{\text{f}}$ , for the b-f and f-f feature in Eq. (1.7) must be chosen. Figure 5 in paper III [167] illustrates that consistent results with LR-TDDFT, which does not perform this separation, can be achieved if the ionization states  $Z^{\text{b}}$  and  $Z^{\text{f}}$  are computed according to the sum rule in Eq. (3.1). Therefore, the definition of ionization state put forward in paper IV [404] not only predicts sensible trends at high temperatures and densities but also is closely connected to one of the premier diagnostic tools available in WDM experiments. Lastly, paper III [167] shows that the collective many-body effects described through the  $e$ -i collision frequency or the LR-TDDFT formalism can have a substantial effect on the inferred plasma conditions in forward scattering experiments. An experiment by Döppner *et al.* [398] is reanalyzed and the initially inferred density of  $1.17 \text{ g/cm}^3$ , found by describing the plasmon through the RPA, is determined to be approximately 35% lower than the  $1.8 \text{ g/cm}^3$  extracted using LR-TDDFT. Conversely, good agreement between LR-TDDFT and the RPA is observed for a backscattering experiment by Kritcher *et al.* [96], which mainly probes the single-particle regime.

### 3.3 Collective X-ray Thomson scattering at the National Ignition Facility [Paper V]

As mentioned in Chapter 1, the accurate modeling of red dwarfs is vital to the understanding of their habitable zone [30]. Simulations of their evolution and magnetic activity rely on fairly simple models for electrical conductivity and opacity. Therefore, it is paramount to perform more advanced many-particle simulations at the conditions present in the interior of these stars, and to establish an experimental platform that can reliably achieve these conditions. Paper V presents the results of the first forward scattering XRTS experiment at the NIF and analyzes it based on an *ab initio* data set for the total eDSF using a Bayesian perspective that takes the impact of the experimental setup into account. While the results of Sec. 3.1 and Sec. 3.2 are focused on ion and electron dynamics, respectively, the results in paper V consider both. The iSSF modulated by the form factor  $|N(k)|^2 S_{\text{ii}}(k)$  gives the magnitude of the ion feature, and the electronic response via the dielectric function represents the inelastic part (plasmon and b-f feature) of the eDSF  $S_{\text{et}}$ . This full *ab initio* description of the eDSF is combined with an accurate parameterization of the instrument and source function [171] for the specific experimental setup shown in Fig. 1 of paper V to analyze the collective XRTS spectra. Due to the close connection of the eDSF to the electrical conductivity outlined in Sec. 3.2, this analysis enables the inference of electrical conductivity at the extreme conditions created at the NIF.

As mentioned in Sec. 1.2.1, the NIF, as the most powerful laser facility in the world, has the unique capability to create matter at the extreme conditions present in the interior of planets and small stars [105, 421]. For the experiment, 184 beams of the NIF were used to drive the compression of a beryllium capsule to extreme densities. An intense X-ray bath, created by irradiating a gold cavity at the center of which the beryllium capsule was located, ablated the capsule's outer layer, resulting in a peak inward velocity of 200 km/s. This implosion was

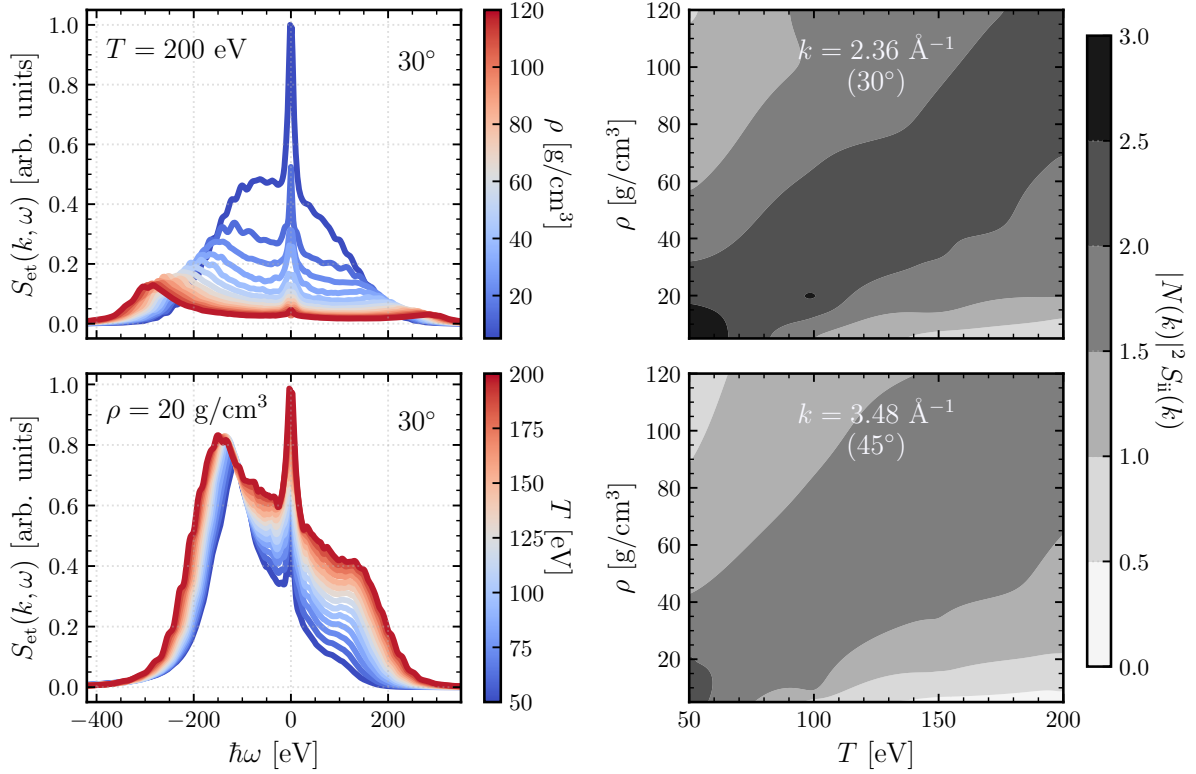


**Figure 3.5:** The left panel shows the interpolated inelastic eDSF due to electronic transitions  $S_{\text{et}}$  for beryllium at  $k = 2.36$   $\text{\AA}^{-1}$  ( $30^\circ$  scattering angle). The top and bottom left panel show  $S_{\text{et}}$  at  $T = 200$  eV and  $\rho = 20$   $\text{g/cm}^3$ , respectively, for the density and temperature ranges covered in [paper V](#). The right panel shows the magnitude of the ion feature given by  $|N(k)|^2 S_{\text{ii}}(k)$  for  $k = 2.36$   $\text{\AA}^{-1}$  ( $30^\circ$  scattering angle) in the top panel and  $k = 3.48$   $\text{\AA}^{-1}$  ( $45^\circ$  scattering angle) in the bottom panel.

observed to stagnate at about 18 ns after the start of the laser drive. For a detailed account of radiation-hydrodynamic simulations of this implosion, see Ref. [422]. An X-ray source for the XRTS measurements was created by irradiating a zinc foil with the eight remaining beams of the NIF. Additionally, the X-rays passed through a copper foil, suppressing the higher energy zinc He- $\alpha$  line, to create a more narrow spectral function as discussed and parameterized in Ref. [171]. After scattering off of the stagnating beryllium shell, the photons are collected in forward direction at  $30^\circ$  and  $45^\circ$  scattering angles.

The total eDSF is computed within the modified Chihara decomposition, Eq. (1.8), on a grid spanning from 50 to 200 eV, and 5 to 120  $\text{g/cm}^3$ , by computing the ion feature and the inelastic feature separately. Although the iDSF  $S_{\text{ii}}(k, \omega)$  appears in the ion feature in Eq. (1.8), its spectral width is vastly more narrow than the spectral function of the zinc foil, and can therefore be replaced by the iSSF  $S_{\text{ii}}(k)$  and a delta distribution in frequency space. As discussed in [paper I](#) [378],  $S_{\text{ii}}(k)$  can be computed from the ion positions during the DFT-MD simulation and the lowest accessible wave number  $k$  is given by the simulation box size. Therefore, between 8 and 128 atoms are used depending on the density to enable access to low enough wave numbers. The total form factor  $N(k)$  can also be computed from snapshots of the DFT-MD simulations using Eq. (2.37). A two-dimensional cubic interpolation between the grid points is performed to achieve a finer resolution in the density-temperature plane. The combined quantity  $|N(k)|^2 S_{\text{ii}}(k)$  is shown in the right panel of Fig. 3.5 for  $k = 2.36$   $\text{\AA}^{-1}$  (top panel) and  $k = 3.48$   $\text{\AA}^{-1}$  (bottom panel), which corresponds to the two scattering angles recorded during the experiment.

The inelastic contribution to the eDSF can be computed for snapshots of the DFT-MD simulation via LR-TDDFT; see the description in Sec. 3.2 and [paper III](#) [167]. Interpolating between

spectra with shifted spectral weights is notoriously difficult [423]. Therefore, an interpolation scheme developed explicitly for interpolating spectra that adhere to sum rules [423] is employed to compute  $S_{\text{et}}$  on a finer density-temperature grid. The result of this interpolation is shown in the left panel of Fig. 3.5 for  $T = 200$  eV (top panel) and  $\rho = 20$  g/cm<sup>3</sup> (bottom panel) at the wave number corresponding to the 30° scattering angle. The shifting of the plasmon feature to higher energies with increasing density can be observed and, especially at low densities, a peak at  $\hbar\omega = 0$  eV arises, which has previously not been observed in analytic theories [71, 166, 403]. A similar peak has also recently been observed in PIMC simulations [424]. Due to its increase at high temperatures and low densities, it is suspected to arise from b-b transitions involving no energy transfer.

Convolving the simulation data in Fig. 3.5 with the parameterized instrument and source function from Ref. [171], the scattering spectrum can be modeled with 12 input parameters, two of which are physical and ten of which are experimental. To analyze the experimental data with such a high-dimensional parameter space, Bayes' theorem is employed (see Sec. 2.4, specifically Eq. (2.50)) to infer the plasma parameters. Including the experimental parameters in this analysis avoids the biasing of the results due to arbitrarily fixed experimental parameters. The sequential Monte Carlo algorithm is employed to sample the parameter space efficiently [367, 368], see Sec. 2.4. The right panel of Fig. 2 in paper V presents the probability distribution  $p(\rho, T|\text{Exp.})$  of the probed mass density and temperature given the observed experimental spectrum. The results of three separate scattering experiments at two different scattering angles are in good agreement with each other, demonstrating the reproducibility

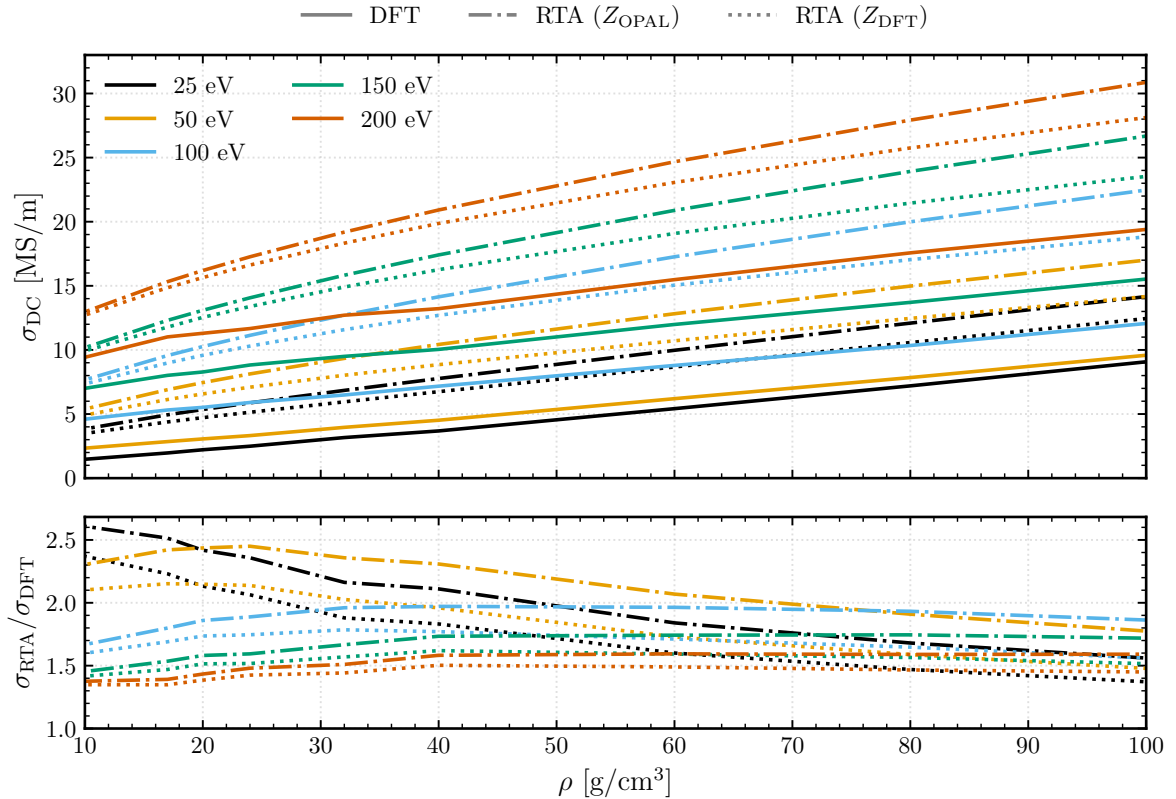


**Figure 3.6:** A comparison of DC conductivities  $\sigma_{\text{DC}}$  in beryllium from DFT, based on the Kubo-Greenwood formula (Eq. (2.49)), and from the relaxation time approximation (RTA) presented in paper VII [420]. The upper panel shows  $\sigma_{\text{DC}}$  for the DFT results (solid lines) and the RTA results with ionization states from the OPAL table [425] (dash-dotted line) and with ionization states computed from DFT via Eq. (3.1) (dotted line). The lower panel shows the ratios of RTA-based conductivities to the DFT data for the two ionization states.



of the experiment. Additionally, the recorded spectra are well reproduced by the posterior predictions of the probability distribution for the input parameters; see the left panel of Fig. 2 in [paper V](#).

Furthermore, the inelastic response of the electrons is intimately connected to the electrical conductivity, enabling inferences about conductivity from collective scattering experiments. The direct current conductivity  $\sigma_{\text{DC}}$  can be computed via the Kubo-Greenwood formula, Eq. (2.49), on the same snapshots used for the prediction of  $S_{\text{et}}$  to infer the electrical conductivity present in the conditions probed during the experiment. A summary of these results in the pressure-temperature regime of interest and the  $P-T$  paths of relevant astrophysical objects are shown in Fig. 3 of [paper V](#), showing that conductivities up to  $8.2_{-0.4}^{+0.8}$  MS/m were observed. To highlight differences between the presented many-body *ab initio* conductivities and relaxation time approximation (RTA) models commonly used in stellar evolution codes [426, 427], the here presented Kubo-Greenwood conductivities along four isotherms are contrasted with results from the RTA presented in [paper VII](#) [420] in Fig. 3.6. The RTA model requires an ionization state  $Z^{\text{f}}$  to compute the conductivity. The upper panel of Fig. 3.6 shows results from the RTA model with ionization states from the widely used OPAL table [425] and ionization states from DFT that are obtained according to the approach outlined in Sec. 3.2. The general trends agree well with the *ab initio* data. However, especially at the lower temperatures, the analytic results overestimate the conductivity by more than 100% compared to the *ab initio* data. To better illustrate the differences, the ratios of the RTA-based conductivities  $\sigma_{\text{RTA}}$  and the DFT conductivities  $\sigma_{\text{DFT}}$  for both investigated ionization states are displayed in the lower panel of Fig. 3.6. DFT-based ionization states yield better agreement with the *ab initio* conductivities across all considered densities and temperatures, although the deviation remains above 30% for all conditions.

### 3.4 Benchmarking density functional theory conductivity in the ideal-plasma limit [Papers VI & VII]

The electrical conductivity computed from the Kubo-Greenwood formula, Eq. (2.49), was used extensively in Secs. 3.2 and 3.3, and was also employed in [paper II](#) [379]. [Paper VI](#) [419] and [paper VII](#) [420] present a more foundational study of the physical processes included in this approach to computing transport properties and propose an approach to benchmark other analytic models and numerical calculation in the limit of ideal plasmas.

As discussed in Chapter 1, accurately describing WDM is notoriously difficult due to non-negligible degeneracy and strong correlations. The best approaches to describing this state of matter, e.g., DFT-MD, RT-TDDFT or PIMC, account for the many-body nature of WDM while also considering quantum mechanical effects via the Schrödinger equation. Although these theories are expected to be best suited to describe WDM, it is paramount to verify their accuracy. As experimental measurements of transport properties are exceedingly difficult at these conditions, it is natural to study predictions in known limiting cases, e.g., the electrical DC conductivity in the low-density limit as presented in the seminal work by Spitzer and Härm [356]. Further principal checks that can be performed are the satisfaction of the Kramers-Kronig relations [428, 429] for response functions and various sum rules, as described in Sec. 3.2.

[Paper VI](#) [419] proposes to use a virial expansion obtained from kinetic theory and generalized linear response theory [54, 430, 431] to study the electrical conductivity in the low-density limit. The expansion can be performed in terms of the dimensionless parameter  $\Gamma/\Theta$ , which

is proportional to the electron density  $n_e$ , resulting in

$$\sigma = \frac{(k_B T)^{3/2} (4\pi\epsilon_0)^2}{m_e^{1/2} e^2} \frac{1}{\underbrace{\tilde{\rho}_1(T) \ln(\Theta/\Gamma) + \tilde{\rho}_2(T) + \tilde{\rho}_3(T) (\Gamma/\Theta)^{1/2} \ln(\Theta/\Gamma) + \dots}_{\rho^*}}, \quad (3.3)$$

where  $\Theta$  and  $\Gamma$  are the degeneracy and coupling parameters; see Eqs. (1.1) and (1.2). This expression can be found from the virial expansion of the inverse dimensionless electrical conductivity, i.e., the dimensionless electrical resistivity  $\rho^*$  (see Eq. (4) in paper VI [419]). The first virial coefficient  $\tilde{\rho}_1(T)$  determines the behavior of the DC conductivity in the low-density limit, whereas the second coefficient  $\tilde{\rho}_2(T)$  predicts the first corrections with rising density. Higher virial coefficients become increasingly important farther away from the low-density limit. Spitzer and Härm computed the exact value for the first virial coefficient as  $\tilde{\rho}_1^{\text{Spitzer}} = 0.846$  [356]. It is independent of the temperature, although, in general, the virial coefficients carry a temperature dependence. An analogous result for a Lorentz plasma where the electrons only interact with the ions via a statically screened Coulomb potential, in that way neglecting  $e$ - $e$  collisions, can be determined as  $\tilde{\rho}_1^{\text{Lorentz}} = 0.492$  [430, 432, 433].

With these known limits, paper VI [419] introduces a new quantity  $\tilde{\rho}(x, T) = \rho^* / \ln[\Theta/\Gamma]$  and contrasts its low-density behavior with various analytical models (see Refs. [438–441]) and numerical calculations (see Refs. [438, 439]) as a function of  $x = 1/\ln[\Theta/\Gamma]$ . Due to the particular choice of  $\tilde{\rho}(x, T)$ , it will take on the value of the first virial coefficient in the low-density limit. As  $x$  is proportional to the electron density, the correct limit, i.e., the virial coefficient by Spitzer and Härm including  $e$ - $e$  collisions, ought to be obtained at  $x = 0$  in the intersection with the y-axis for Figs. 1 and 2 in paper VI [419]. A full discussion of which analytic approaches satisfy the correct low-density limit can be found there. In Fig. 2 of paper VI [419], new DFT-MD results along with orbital-free DFT-MD simulations by Lambert *et al.* [439] and DFT-MD simulations by Desjarlais *et al.* [438] are presented. The results are obtained by computing the dynamic electrical conductivity via the Kubo-Greenwood formula, Eq. (2.49), and extending them to  $\omega \rightarrow 0$  to arrive at the DC conductivity. Subsequently,  $\rho^*$  and  $\tilde{\rho}$  can be computed and displayed as a function of  $x = 1/\ln[\Theta/\Gamma]$ . The new results show a clear trend towards the virial coefficient of the Lorentz plasma, as can be seen from the linear extrapolation shown in Fig. 2 of paper VI [419]. In stark contrast, the results of Desjarlais *et al.* tend towards the quantum Lenard-Balescu (QLB) result by Karakhtanov *et al.* [440]. However, as discussed in paper VII [420], this behavior is due to an under-converged DC conductivity with respect to particle number.

In Eq. (16) of paper VI [419] a temperature dependence of the second virial coefficient  $\tilde{\rho}_2(T)$ , depicted as the dark blue dashed line in Fig. 3.7, is suggested based on an interpolation between the known high-temperature limit of the quantum Lenard-Balescu expression [438, 440] and the Spitzer limit with classical strong collisions at low temperatures in the quasiclassical Wentzel-Kramers-Brillouin approximation [361, 442–445]. The dashed black line indicates the known

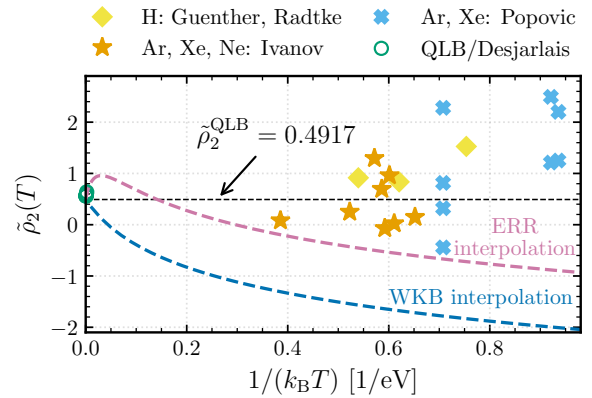


**Figure 3.7:** Second virial coefficient of hydrogen, adapted from the supplemental material of paper VI [419] and Ref. [434]. An interpolation formula by Esser, Redmer, and Röpke (ERR) [361] and Eq. (16) of paper VI [419] are shown as dashed lines, as well as experimental data from Refs. [435–438].

high-temperature QLB limit. Another approximation for  $\tilde{\rho}_2(T)$  is given by an interpolation formula due to Esser, Redmer, and Röpke [361], which is shown as the pink dashed line in Fig 3.7. Additionally, some experimental observations for various elements are presented [435–437], although the only measurements of hydrogen, due to Guenther and Radtke, are given by the yellow diamonds. The remaining observations were obtained in argon and xenon, for which the additional ionic charge is not considered in the theoretical description. The significant spread of experimental data makes it difficult to gauge the accuracy of the presented theories. More accurate low-density measurements or accurate first principal simulation, e.g., PIMC, are needed to make conclusive judgments.

Although paper VI [419] presents strong indications that  $e$ - $e$  scattering is not included in the Kubo-Greenwood conductivities from DFT simulations, it still relies on a linear extrapolation to the low-density limit and the results are influenced by the extension of the dynamic electrical conductivity to the DC conductivity, i.e., whether a Drude extrapolation or a linear extrapolation is used. Paper VII [420] presents a conclusive analysis that shows the lack of  $e$ - $e$  collisions by extending the quantities of interest to other transport properties like the thermopower and the Lorenz number, which are easier to converge in the low-frequency limit; see Fig. 3 in paper VII [420]. These properties can be computed from DFT by evaluating several Onsager coefficients [341], and they show a clear convergence to a constant value in the near-classical plasma limit. This constant value can, once again, be evaluated according to Spitzer and Härm, resulting in 0.7033 and 1.6220 for the thermopower and Lorenz number, respectively, or according to the Lorentz plasma, giving 1.5 and 4.0. Figure 4 of paper VII [420] contrasts these known limits with DFT results along a path through  $\rho - T$  space that most effectively escapes correlation and degeneracy effects. A clear convergence towards the limits of the Lorentz plasma can be observed.

To contrast the many-body description of DFT with an analytic approach which also only considers  $e$ - $i$  collisions, paper VII [420] discusses the RTA [446] proposed by Lee and More [360], but puts forward a different expression for the statically screened Coulomb logarithm [343, 447, 448] that describes the interaction between the electrons and ions. As expected, the expressions for the thermopower and Lorenz number within this approach converge to the limits of the Lorentz plasma in the near-classical limit. Additionally, the RTA can compute dynamic properties, e.g., the dynamic electrical conductivity  $\sigma(\omega)$ . In paper VII [420], it is used to study the lack of convergence in the conductivity calculations at  $\rho = 40 \text{ g/cm}^3$  and  $T = 500 \text{ eV}$  by Desjarlais *et al.* [438]. DFT calculations ranging from 128 to 512 atoms are compared to the RTA result for  $\sigma(\omega)$  in Fig. 2 of that publication. At energies above 5 eV, the conductivity for all atom numbers are in excellent agreement with the RTA result. However, the energy at which the DFT results diverge from the RTA predictions systematically decreases with the number of atoms in the simulation. Even at 512 atoms, a 20% higher DC conductivity than with 256 atoms is observed. The convergence behavior seems to indicate agreement with the RTA, which predicts a more than 10% higher DC conductivity than the DFT results with 512 atoms. Interestingly, despite the good agreement between DFT and RTA at the extreme conditions studied by Desjarlais *et al.*, Fig. 3.8 shows systematic deviation for RTA calcula-

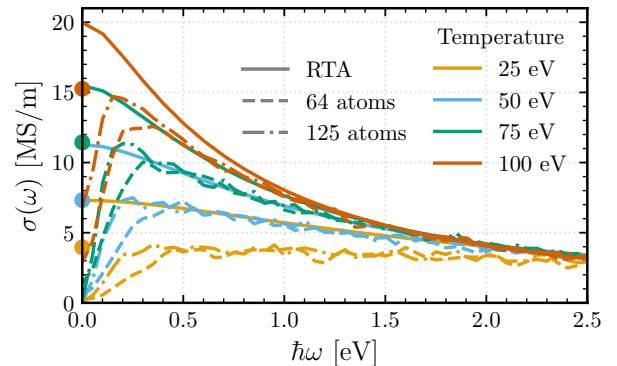


**Figure 3.8:** Dynamic electrical conductivity of hydrogen at  $\rho = 2 \text{ g/cm}^3$  for various temperatures at 64 (dashed) and 125 (dash-dotted) atoms; see paper VI [419] for simulation details. The dots at  $\hbar\omega = 0 \text{ eV}$  denote the inferred DC conductivities. The solid lines represent predictions according to the RTA from paper VII [420].

tions of a hydrogen isochor at  $\rho = 2 \text{ g/cm}^3$  studied in [paper VI \[419\]](#). The RTA overestimates the low-frequency conductivity and, in fact, seems to agree best with the DFT conductivities at 25 eV higher temperatures. This might be explained by the fact that the calculations by Desjarlais *et al.* [438] are closer to the ideal plasma limit than the conditions considered in [Fig. 3.8](#), as can be seen from [Fig. 2 of paper VI \[419\]](#).

### 3.5 Additional publications

The previous sections contain a representative selection of the scientific work performed by this author and aim to give a comprehensive overview of the contributions to WDM research enclosed in this thesis. As indicated in [Fig. 3.1](#), nine additional scientific publications are not explicitly included in this thesis. A short summary of their content and the author's contribution is given below.

[Section 3.3](#) details the analysis of forward XRTS at the NIF. In a related campaign, backward XRTS spectra were collected to study the single-particle regime of the imploding beryllium capsule. From these observations, it was possible to deduce the onset of pressure-driven K-shell delocalization, which was reported in [paper VIII \[449\]](#). For the discussion of the K-shell delocalization, this author analyzed changes in electron density and DOS upon extreme compression in several DFT-MD simulations. Many insights gained about delocalization and the interesting high-pressure behavior of beryllium are currently being prepared for a separate publication.

In [paper IX \[61\]](#), the experimental setup and theoretical considerations for an opacity measurement of hydrogen at the NIF is presented. DFT and average-atom models are used to study the contribution of free-free absorption, which is the dominating process in the region of interest, to the opacity. This author contributed to the comparison of the numerical approaches to the analytical model and the discussion of relevant processes for the total opacity.

While [Sec. 3.1](#) details computational advances in the simulation of ion dynamics, [paper X \[450\]](#) concerns the experimental establishment of an meV inelastic scattering setup at the LCLS and EuXFEL to measure ion dynamics. Measurements on iron and gold recorded at the LCLS are presented to support the discussion. This author was involved in discussing the feasibility of simulating and observing the ion dynamics with the given spectral resolution. The ongoing work detailed in [Sec. 3.6.2](#) represents the combination of the computational and experimental advances described in [Sec. 3.1](#) and [paper X \[450\]](#).

[Paper XI \[451\]](#) describes the observation of a highly conductive state in warm dense water at the Free Electron LASer Hamburg (FLASH). This result is derived from transmission and reflectivity measurements on a planar liquid water jet. This author was part of the experimental team and was specifically tasked with the alignment of interferometry on a planar jet. Furthermore, on-the-fly interferometry calculations were performed to gauge the thickness and homogeneity of the jet.

In order to perform the forward XRTS measurements at the NIF presented in [Sec. 3.3](#), improvements to the spectral width of the X-ray source and a better understanding of the instrument response function were required. [Paper XIII \[171\]](#) uses a physics-based model to parameterize the influence of the X-ray backlighter and XRTS setup at the NIF on recorded spectra. It includes the copper filter that provides improved spectral resolution and models its temperature dependence. This author contributed to discussions concerning the coupling of this parameterization with various scattering codes, as well as ray-tracing codes to model the interaction with the target.

A novel high-pressure phase of sodium and potassium is reported in paper XIV [452]. A phase formed of interpenetrating sodium and potassium diamond lattices is found in powder X-ray diffraction above 5.9 GPa at a temperature of 295 K. This author computed pressure-volume curves using DFT, which aligned well with experimental results, and showed dynamic stability via the phonon spectrum. The electron localization function was also computed, showing electron localization between nearest-neighbor sodium atoms.

Papers XII [453], XV [454], and XVI [455] are the result of a shock-compression experiment on polystyrene, polyethylene, and polyethylene terephthalate at the LCLS. They present EOS data collected on all materials. It was shown that polyethylene does not form diamonds up to pressures of 200 GPa, contrasting earlier results on polystyrene [64]. A wide variety of diagnostics was used in this experiment, i.e., X-ray diffraction, XRTS in forward and backward orientation, small angle X-ray scattering, and VISAR. This author was part of the experimental team executing the measurements. Specifically, the tasks included keeping a log book of the used targets and experimental parameters, remotely aligning the targets in the X-ray beam, and triggering the laser.

### 3.6 Ongoing work at high-energy-density facilities

The previous sections present results that have been published or are currently under review. In this section, additional work is presented, which was performed in preparation and during ongoing analyses of experiments. XFEL facilities have played a significant role in the emergence of the WDM research field. With the recent upgrade to the LCLS and the full operation of the HIBEF facility at the EuXFEL ramping up over the past years, new experimental capabilities open up new avenues to study matter in extreme conditions with unprecedented accuracy. However, also particle accelerators like the GSI Helmholtz Centre for Heavy Ion Research [100], and the FAIR facility [21, 101–103], which is currently under construction, offer unique opportunities to create extreme states of matter by bombarding the samples with particles. In Sec. 3.6.1, current efforts to develop a temperature diagnostic for targets heated by heavy ion beams at GSI are described. To benchmark the performed simulations, XRTS predictions are compared to a recent experiment at the EuXFEL, which employed the high spectral resolution of the new generation of XFELs. In Sec. 3.6.2, calculations of phonons and iDSFs in a cryogenically cooled argon jet are presented. These simulations are currently used for the analysis of the first high-resolution measurements of ion dynamics at LCLS.

#### 3.6.1 GSI facility & European X-ray free electron laser

A single-crystal diamond target is heated by a heavy-ion beam at GSI to observe graphitization via X-ray diffraction measurements. The X-ray source in this experimental setup is a titanium foil irradiated by a long-pulse laser to create a backlighter. To infer the temperature of the sample, a temperature diagnostic via XRTS is developed at GSI. Although the electron temperature at very high temperatures can be determined via the detailed balance relation, as demonstrated in Sec. 3.2, this is not feasible for the temperatures achieved at GSI. The up-shifted scattering signal is not detectable due to the strong suppression given by the detailed balance. Furthermore, temperature inference through the Debye-Waller factor [175–178] for diamond is problematic due to its high Debye temperature [456]. Alternatively, the temperature in an equilibrated system can be inferred from the iSSF  $S_{ii}(k)$  by measuring the magnitude of the ion feature in Eq. (1.8). Its magnitude is determined by the iSSF and the form factor. The form factor is unchanged at the relatively low temperatures achieved at this facility and can, therefore, be approximated by its ambient value. Additionally, at the low temperatures reached in this experiment, the inelastic contribution to the scattering is not



affected. Therefore, changes in the magnitude of the ion feature can be directly related to  $S_{ii}(k)$ .

To reliably infer the temperature from the measured ion feature, accurate calculations of  $S_{ii}(k)$  at various temperatures ought to be performed. The approach outlined in Sec. 3.1 is adopted here to achieve DFT-level accuracy at a sufficient simulation box size that affords the required resolution in reciprocal space. A summary of  $S_{ii}(k)$  for five different temperatures, ranging from ambient temperature to the highest expected temperature, 3000 K, is shown in Fig. 3.9. The upper panel shows  $S_{ii}(k)$  on a log scale over a wide  $k$  range. Clear trends with temperatures are apparent, enabling a reliable temperature inference from measurements of the ion feature. However, relatively large statistical fluctuations can be observed, especially at large  $k$  and higher temperatures. In experiments, due to the finite size of the detector, the scattering signal is recorded over a range of angles. To model this, an effective iSSF

$$S_{ii}^{\text{eff}}(k; w) = \frac{1}{w} \int_{k-w/2}^{k+w/2} S_{ii}(k') dk' \quad (3.4)$$

is introduced, which represents a sliding average over  $S_{ii}(k)$  with a given window size  $w$ . The bottom panels of Fig. 3.9 display this quantity with a window size of  $0.05 \text{ \AA}^{-1}$ . The lower left panel zooms in on the  $k$  range between the two Laue peaks surrounding the wave number at which the XRTS spectrum was recorded. The values at  $k = 4.447 \text{ \AA}^{-1}$ , indicated by the vertical dashed line, are the basis for the temperature diagnostic. The bottom right panel of Fig. 3.9

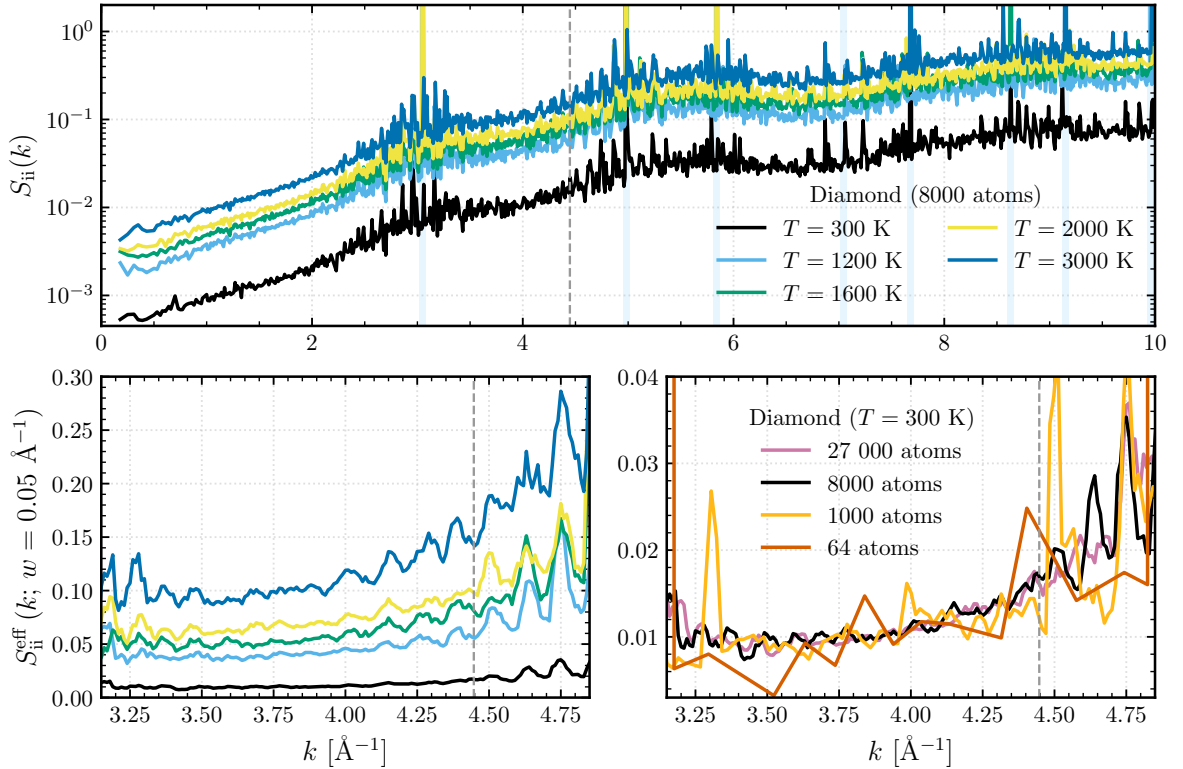


**Figure 3.9:** An overview of the iSSF  $S_{ii}(k)$  of diamond for various temperatures and atom numbers used to infer the temperature in the heated diamond. The upper panel shows  $S_{ii}(k)$  on a logarithmic scale for all considered temperatures with 8000 atoms in the simulation box and indicates the Laue peaks by the blue shaded areas. The bottom panels show  $S_{ii}^{\text{eff}}(k; w)$  from Eq. (3.4) for a window size of  $0.05 \text{ \AA}^{-1}$ . The lower left panel zooms in on the  $k$  range of interest for the experiment. The lower right panel shows the convergence with respect to atom numbers for the simulation at  $T = 300 \text{ K}$ . For all panels, the vertical dashed line indicates the wave number  $k = 4.447 \text{ \AA}^{-1}$  at which the XRTS spectrum was recorded.

shows the convergence behavior with respect to particle number at ambient temperature in the range of  $k$  values considered for the experiment. The smallest particle number, 64 atoms in the simulation box, represents typical sizes for DFT-MD simulations. Significant fluctuations can be observed, although all simulations were run for 200 000 time steps. At 1000 atoms, pseudo-Laue peaks are still observed close to the wave number of interest. Only for 8000 and 27 000 atoms,  $S_{ii}^{\text{eff}}(k; w)$  exhibits convergence behavior at  $k = 4.447 \text{ \AA}^{-1}$ . Especially for the ambient temperature, which is used as a reference value to gauge the changes to the ion feature caused by heating, reducing fluctuations and obtaining accurate results is of paramount importance.

The inelastic feature in the XRTS spectrum normalizes the total spectrum to extract an absolute value for the magnitude of the elastic feature. Furthermore, it is also used in a ray-tracing code that models the experimental setup at GSI. Very accurate XRTS measurements on ambient diamond from the EuXFEL were recorded by Voigt *et al.* [457], which are used here to test the reliability of the LR-TDDFT calculations for the inelastic feature (see Sec. 3.2). The experimental data by Voigt *et al.* [457] and various LR-TDDFT simulations for the inelastic feature are shown in the left panel of Fig. 3.10. As discussed in Sec. 2.3.1 and the appendix of paper III [167], LFEs can occur as C-LFEs and XC-LFEs [317]. The left panel of Fig. 3.10 shows predictions including no LFEs (light blue), only C-LFEs (green), and with C-LFEs and XC-LFEs in the ALDA (yellow). All predictions agree reasonably with the experiment, although the computation using the ALDA performs worst across the inelastic feature. The inclusion of C-LFEs improves the description of the feature at 5980 eV. The excitation of the 1s electrons around 5710 eV is not included in the LR-TDDFT simulations because a carbon pseudo-potential was employed, which freezes the 1s electrons in the core. However, this feature was discussed in detail in Ref. [457].

The right panel of Fig. 3.10 shows DFT results for the magnitude of the ion feature  $S_{ee}^{\text{eff}}(k)$ , computed from the iSSF  $S_{ii}(k)$  and the form factor  $N(k)$ . The broadening of the diffraction measurement in this experiment was  $0.09 \text{ \AA}^{-1}$ , and it is included analogously to the definition in Eq. (3.4). The black diamond indicates the magnitude of the ion feature determined from the fit in the left panel of Fig. 3.10. The agreement is good within the measurement's error

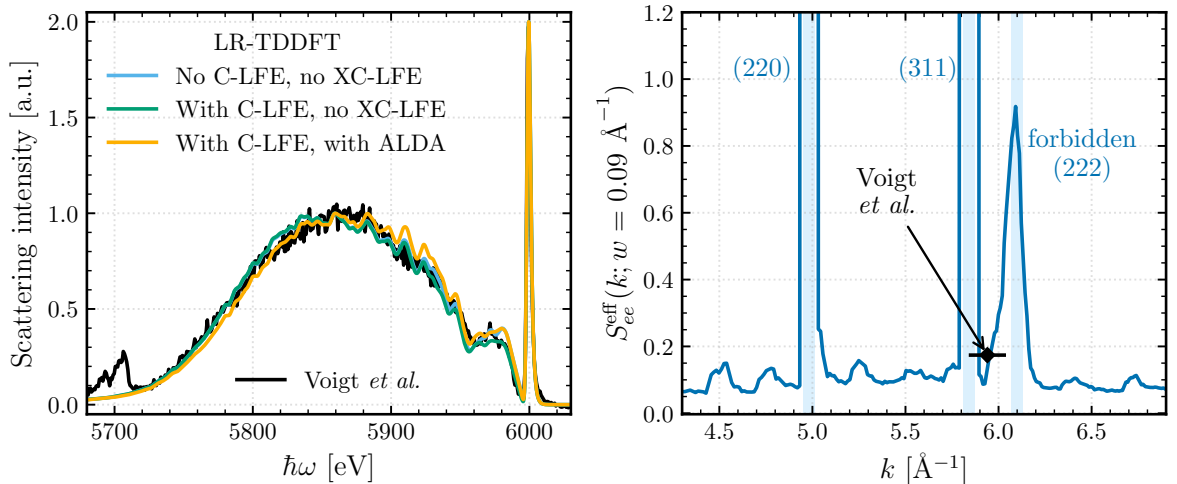


**Figure 3.10:** Analysis of the experiment by Voigt *et al.* [457] at the EuXFEL. The left panel shows the measured XRTS spectrum and LR-TDDFT simulations for the inelastic contribution of ambient diamond that account for C-LFE and XC-LFE at different levels (see Sec. 2.3.1). The magnitude of the ion feature is a fit parameter. The right panel shows the iSSF  $S_{ii}(k)$  modulated by the squared form factor  $|N(k)|^2$  of ambient diamond. The magnitude determined via the free fit parameter in the left panel is indicated at the wave number probed during the experiment.

bars, giving credence to this temperature diagnostic. The forbidden (222) reflection occurs in diamond due to the covalent bonds, which create an asymmetric charge distribution around the atoms [458, 459].

### 3.6.2 Linac Coherent Light Source

Paper I [378] and paper II [379], discussed in Sec. 3.1, demonstrate the capability to reach the hydrodynamic regime with DFT precision using state-of-the-art numerical methods. Over the past years, experimental capabilities have also improved drastically, enabling inelastic scattering measurements with unprecedented spectral resolution at XFEL facilities to measure phonons or ion acoustic modes. Experimental setups for high-resolution measurements have been presented at the LCLS [460] and the EuXFEL [461]; see paper X [450]. In the first application of these new capabilities at the EuXFEL, the phonon modes of single-crystal diamond have been resolved, and the temperature of the diamond was resolved via the detailed balance relation [462].

At the LCLS, this new experimental setup is employed to study shock-compressed argon. A cryogenically cooled liquid argon jet [463–465] serves as a target to enable high rep-rate measurements. A high-intensity short-pulse laser irradiates the jet to induce shock compression, and the jet is subsequently probed by the narrow bandwidth X-rays produced by the self-seeded beam [466] which is passed through a four-bounce channel-cut (533) single crystal silicon monochromator. From this setup, inelastic X-ray scattering in the meV regime is

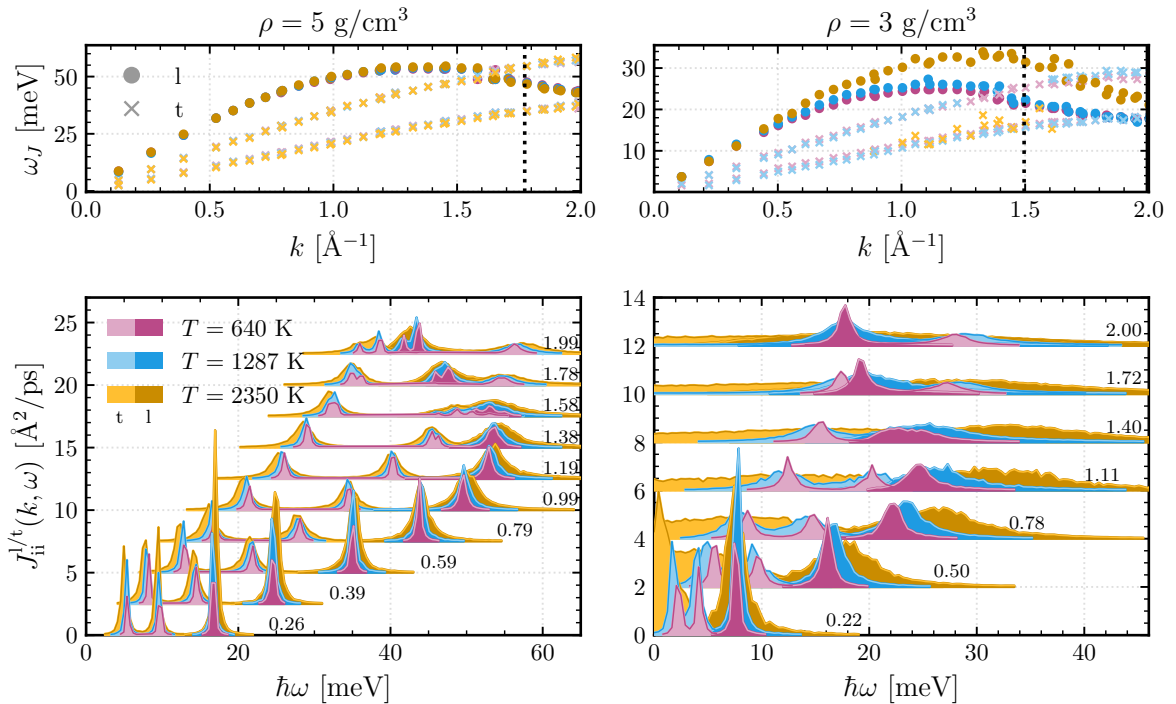


**Figure 3.11:** Overview of longitudinal and transverse current-current correlation spectrum  $J_{ii}^{l/t}(k, \omega)$  of argon along the high symmetry path  $\Gamma - K - X$  in reciprocal space. The left column depicts results for  $\rho = 5 \text{ g/cm}^3$ , while the right panel shows results for  $\rho = 3 \text{ g/cm}^3$ . The upper panels show the phonon spectra, and the bottom panels show  $J_{ii}^{l/t}(k, \omega)$  for various  $k$ , indicated by the small black numbers next to the curves. The three considered temperatures are color-coded, and the transverse and longitudinal modes correspond to the lighter and darker shades, respectively. For visibility,  $J_{ii}^{l/t}(k, \omega)$  is only shown for values larger than  $0.5 \text{ \AA}^2/\text{ps}$ . The vertical black dotted line in the upper panels denotes the position of  $K$  in reciprocal space.



observed at two different scattering angles corresponding to wave numbers of  $1.33 \text{ \AA}^{-1}$  and  $1.98 \text{ \AA}^{-1}$ . The spectra are recorded as a function of delay time after the peak of the laser pulse, and using Bayesian inference, see Sec. 2.4, the temperature of the sample is inferred via the detailed balance relation. For the thus determined temperatures, DFT-MD simulations on a density grid ranging from  $2 \text{ g/cm}^3$  to  $8 \text{ g/cm}^3$  are performed. To ensure a sufficient resolution in reciprocal space, separate HDNNPs are trained for each temperature, see Sec. 3.1, and the simulations are scaled up to approximately 23 000 atoms.

Figure 3.11 depicts the longitudinal (l) and transverse (t) current-current correlation spectrum  $J_{ii}^{l/t}(k, \omega)$  in the high-symmetry orientation  $\Gamma - K - X$ ; see Eq. (2.24) for a definition of  $J_{ii}^{l/t}(k, \omega)$ . The left column shows results for the temperatures of interest at  $\rho = 5 \text{ g/cm}^3$ , which represents more than a 2.5-fold compression, while the right column depicts argon at  $\rho = 3 \text{ g/cm}^3$  for the same temperature. In the bottom panels,  $J_{ii}^{l/t}(k, \omega)$  is depicted for several wave numbers up to  $2 \text{ \AA}^{-1}$ , while the upper panel shows the corresponding phonon spectra; see Fig. 1 in paper II [379] for a comparison in copper. As expected for an fcc lattice along the studied reciprocal orientation, the typical structure of two transverse acoustic and one longitudinal acoustic mode is observed for all cases where solid argon is present. At  $\rho = 5 \text{ g/cm}^3$ , this is the case for all temperatures, whereas for  $\rho = 3 \text{ g/cm}^3$ , melting is detected at  $T = 2350 \text{ K}$ . Furthermore, at  $T = 1287 \text{ K}$ , a solid structure is still present but significant broadening of the phonon modes and slight hardening of the longitudinal mode around  $1 \text{ \AA}^{-1}$  is noted. The data set displayed in Fig. 3.11 and the additional densities not shown here represent the foundation for analyzing the first meV-resolution inelastic scattering experiment on a liquid target at the LCLS.

### 3.7 Summary and outlook

This thesis presents several methodological advances in the simulation of ion and electron dynamics at WDM conditions based on DFT. Especially, for the ion dynamics and the interpretation of scattering experiments, these advances are driven by modern machine-learning approaches. The simulation results are benchmarked by well-understood experiments at more moderate conditions (paper I [378] and paper II [379]) or theoretically known limiting cases (paper VI [419] and paper VII [420]). A new definition of ionization state and methods based on DFT are compared to analytic approaches at extreme conditions, and the differences in inferred plasma parameters in scattering experiments are evaluated (paper III [167] and paper IV [404]). Finally, these simulation methods are used to analyze experiments at some of the leading experimental facilities in the world (paper V, Sec. 3.6.1 and Sec. 3.6.2).

In paper I [378] and paper II [379], the immense potential of HDNNPs [276] is utilized to scale up simulations of WDM to reach the macroscopic regime while maintaining *ab initio* precision. The GCM framework is adopted to study ion dynamics. It serves as a solid theoretical foundation to perform simple fits in the hydrodynamic limit, which allows the extraction of important material and transport properties, e.g., the thermal ionic conductivity, and to study the occurrence of non-hydrodynamic modes at higher wave numbers. As a test case, it is applied to a wide range of conditions in aluminum and a typical WDM experiment, i.e., a dynamic shock compression in copper. With the improvements to the spectral resolution at XFEL facilities like EuXFEL and LCLS, and high rep-rate drive lasers, like the recently commissioned DiPOLE 100-X at the high-energy-density station of the EuXFEL, numerous experimental studies of ion dynamics in compressed solids and liquids will be performed soon. The work presented in this thesis will form the theoretical foundation for a joint DFG project between the EuXFEL and the University of Rostock over the next three years. Furthermore, this author is currently involved in analyzing the first meV-resolution inelastic scattering experiment on a liquid target at the LCLS, as described in Sec. 3.6.2.

The behavior of the electrons under WDM conditions is studied in [paper III](#) [167] and [paper IV](#) [404]. A sensible definition of the ionization degree for matter under extreme conditions, which is based on a sum rule for the electrical conductivity, is given and discussed for the case of warm dense carbon and hydrocarbon. The topic has since been actively discussed in the community and, especially in the context of average atom models [407, 467, 468], new sensible definitions of the ionization degree have been introduced and compared to the results obtained in [paper IV](#) [404]. How this ionization state is established in the inelastic electronic feature of XRTS spectra and how the description of this feature using DFT-based approaches can be connected to widely used collision-frequency-based description is detailed in [paper III](#) [167]. Further work needs to be performed on determining suitable XC kernels for LR-TDDFT [326, 327, 355, 469], especially lifting the adiabaticity limitation, which might allow for the inclusion of  $e$ - $e$  collisions. Additionally, the Chihara decomposition relies on a clear separation of electron and ion dynamics. To what extent the ion dynamics discussed in [Sec. 3.1](#) influence the electron feature of XRTS remains an open question.

The first collective scattering measurements recorded at the NIF are presented and analyzed in [paper V](#). The analysis uses DFT-MD results for the ion and electron dynamics. It describes the influence of the experimental setup via a physics-based parameterization of the X-ray source and instrument. This enables the accurate determination of plasma parameters and the inference of electrical conductivity at the conditions found in the core of a young Proxima Centauri. The NIF offers a unique capability to create the extreme states of matter present in the interior of stars, and this will enable new ground-breaking discoveries in laboratory astrophysics over the coming years, as exemplified by the observation of K-shell delocalization in [paper VIII](#) [449]. Additionally, the measurements proposed by [paper IX](#) [61] were recently performed at the NIF. Ongoing analysis of radiography measurements of hydrogen aims to determine hydrogen's opacity at the conditions found in the deep interiors of red dwarfs. Moreover, the framework of Bayesian inference described in [Sec. 2.4](#) and used in [paper V](#) is currently being applied to a planetary interior structure model [470] by this author, by comparing its predictions to observations of the radius, mass, and temperature of exoplanets.

[Paper VI](#) [419] and [paper VII](#) [420] propose a framework using a virial expansion of the electrical conductivity to inspect analytic and numerical approaches in the near-classical plasma limit and show that the thermopower and Lorenz number are easier to converge quantities that can also clearly indicate the presence of  $e$ - $e$  collisions. Conclusive evidence of their absence in the transport properties computed from Onsager coefficients within the DFT formalism is presented. Currently, ongoing work examines whether  $e$ - $e$  collisions are included in more advanced approaches, such as a finite temperature formulation [471, 472] of the GW approximation [473, 474]. Furthermore, [paper VI](#) [419] studies the virial coefficients of various analytic approaches that were published in the context of the Charged-Particle Transport Coefficient Comparison Workshop [441]. This author has contributed DC thermal and electrical conductivities for aluminum and beryllium at extreme conditions for the next installment of this workshop to also benchmark analytic approaches farther away from the near-classical plasma limit.

# 4 Publications

This chapter contains three peer-reviewed first-author publications [167, 378, 379], one submitted first-author publication and three publication as a co-author [404, 419, 420]. An overview prior to every publication lists the authors and their respective contributions to the publication.

## 4.1 Extending *ab initio* simulations for the ion-ion structure factor of warm dense aluminum to the hydrodynamic limit using neural network potentials

### Author contributions

#### **M. Schörner**

Preparation of the manuscript, update of DFT-MD simulations, training of NN potentials and calculations of NN-MD simulations, implementation of DSF code and GCM code

#### **H.R. Rüter**

Preparation of the manuscript, calculations of original DFT-MD simulations

#### **M. French**

Preparation of the manuscript, calculations of the Green-Kubo thermal ionic conductivities

#### **R. Redmer**

Supervision of the project, preparation of the manuscript

## Extending *ab initio* simulations for the ion-ion structure factor of warm dense aluminum to the hydrodynamic limit using neural network potentials

Maximilian Schörner<sup>1</sup>, Hannes R. Rüter<sup>2</sup>, Martin French<sup>1</sup> and Ronald Redmer<sup>1</sup>

<sup>1</sup>Universität Rostock, Institut für Physik, D-18051 Rostock, Germany

<sup>2</sup>CFisUC, Department of Physics, University of Coimbra, Coimbra, 3004-516, Portugal



(Received 1 March 2022; revised 5 May 2022; accepted 19 May 2022; published 31 May 2022)

We calculate the intermediate scattering function of warm dense aluminum by using density functional theory molecular dynamics simulations. From this data set, we derive the static and dynamic ion-ion structure factors. By applying a generalized collective modes model, we can fit the excitation spectra of the ion system and thereby extract the dispersion for the ion acoustic modes, as well as the decay coefficients for the diffusive and collective modes. The results are discussed and compared with experimental data if available. We show that computational limitations prevent sufficient access to the hydrodynamic limit and demonstrate that this can be circumvented using high-dimensional neural network potentials. We extract the ionic thermal conductivity of aluminum in the hydrodynamic limit and compare to values computed using a Green-Kubo relation. We highlight the importance of partitioning the heat capacity into electronic and ionic contributions and only using the ionic contribution to compute the thermal conductivity of the ions in the hydrodynamic limit.

DOI: [10.1103/PhysRevB.105.174310](https://doi.org/10.1103/PhysRevB.105.174310)

### I. INTRODUCTION

The theoretical description of dense Coulomb systems poses many challenges. The long-range character of the Coulomb interaction leads to many-particle effects such as dynamic screening and self-energy, which modify the effective interactions and, thereby, also the dispersion relations and excitation spectra dramatically compared with dilute, weakly interacting systems. Methods which rely on expansions with respect to small parameters (e.g., virial, activity, fugacity expansions) are not applicable. Furthermore, a quantum treatment has to be applied in order to incorporate Heisenberg's uncertainty principle and Pauli's exclusion principle present in fermionic systems. Such quantum statistical descriptions have been developed successfully for dense plasmas based on, e.g., Green's functions [1,2] and integral equations [3]. Their calculation is, however, complicated since a hierarchy for the equations of motion or the correlation functions follows which has to be truncated on an appropriate level, see Ref. [4].

For the description of warm dense matter (WDM), i.e., plasmas at high densities as typical for condensed matter and temperatures of only few eV, the quantum and correlation effects are dominant. Interestingly, the interior of planets can be mapped to the WDM region and corresponding data for the equation of state and the transport coefficients are crucial for models of their interior structure (e.g., core and mantle for rocky planets [5] or core and fluid envelopes of different composition for giant planets [6,7]), their thermal evolution (cooling behavior) [8,9] and magnetic field generation (dynamo action) [10,11]. However, the determination of equation of state data and, in particular, of transport coefficients of WDM via shock wave or ramp compression experiments is

complicated so that reliable theoretical predictions are indispensable.

Therefore methods of condensed matter physics were transferred successfully to this state, located between conventional condensed matter and high-temperature plasmas. [12] A very efficient method is based on electronic structure calculations using density functional theory (DFT) for a given configuration of nuclei. The results are in turn used to compute the forces on the nuclei via the Hellmann-Feynman theorem so that they can be propagated in a molecular dynamics (MD) step. The repeated cycling through this scheme is known as DFT-MD method, which yields accurate structural properties, equation of state data, and transport coefficients of WDM, see Refs. [12,13].

As the DFT-MD calculations describe the evolution of the system in time, dynamic properties of WDM can also be computed through space- and time-dependent correlation functions. In the limit of large length and time scales it is possible to average out the effects of individual particles, which leads to the hydrodynamic description. A fundamental problem in this context are the large scales that must be realized for a standard hydrodynamic description [14] to remain valid in WDM. One of the most prominent extensions of this description to higher wave numbers is named generalized hydrodynamics [15,16], or the more general generalized collective mode (GCM) approach. [17] Many principal studies on model systems like the Yukawa one-component plasma [18,19] and the generalized Lennard-Jones system [20] developed techniques to analyze MD results in this regime. Early numerical descriptions of real systems used classical MD simulations with respect to effective quantum potentials [21,22]. However, it is an open question whether or not the dynamic properties of a dense, interacting quantum system

can properly be described by effective two-particle potentials. This is no limitation in DFT-MD calculations due to their self-consistent many-body nature.

An orbital-free (OF) formulation of DFT was used to compute the dynamic ion-ion structure factor for warm dense aluminum [23]. Although no effective pair potentials were used, the OF approach lacks the explicit formulation with discrete Kohn-Sham orbitals, which is especially important in dense systems that differ significantly from a free-electron-gas-like system and exhibit condensed matter characteristics. Much more expensive DFT-MD simulations within a full Kohn-Sham treatment were performed in a previous paper for liquid and warm dense aluminum [24], which should emulate the forces on the ions adequately. As a result the ion-acoustic modes were resolved and their dispersion relations given. This approach has also been used successfully for warm dense lithium [25]. Recently, deep potential molecular dynamics simulations [26] and molecular dynamics simulation employing ion-ion potentials constructed from a neutral pseudoatom model [27] were used to study the nonequilibrium effects of two-temperature warm dense aluminum, which was shown to be present in laser-shocked aluminum [28]. The latter two methods are computationally significantly less expensive than DFT-MD simulations and therefore enable large-scale simulations with more than 100 000 atoms, which makes the hydrodynamic regime better accessible. We adopt a similar approach as Ref. [26], in the following called neural network molecular dynamics (NN-MD), to extend our DFT-MD simulations to larger scales by using high-dimensional neural network potentials implemented in the N2P2 software package, [29–31] which employs Behler-Parrinello symmetry functions [32].

In the present paper we apply the method presented in Ref. [24] in order to calculate the dynamic ion-ion structure factor in warm dense aluminum for a wider range of parameters (density, temperature), see Sec. II. We give a brief overview of the error analysis in Sec. III and compare the static and dynamic structure factor with available experimental results in Sec. IV. Furthermore, we fit the numerical data for the dynamic structure factor (DSF) to a generalized hydrodynamic model in Sec. V and derive dispersion relations and the decay coefficients. Here, we compare the capability of extracting thermodynamic and transport properties, in particular, the thermal conductivity of the ions, in the hydrodynamic limit between the NN-MD and the DFT-MD simulations. In principle, highly resolved measurements of the ion-ion DSF for WDM states would enable the determination of these quantities for such extreme condition. Corresponding inelastic x-ray scattering experiments are planned at free electron laser facilities like the European XFEL [33,34] or the LCLS in Stanford [35]. At the end, we give conclusions in Sec. VI.

## II. THEORETICAL METHOD

Although DFT-MD allows access to information on both the electronic and ionic system, all quantities of interest in this paper can be derived from the ion positions at each point in time. From this the ion-ion intermediate scattering function

$$F_{ii}(\vec{k}, t) := \frac{1}{N} \langle n_{\vec{k}}^{(i)}(\tau) n_{-\vec{k}}^{(i)}(\tau + t) \rangle_{\tau}, \quad (1)$$

with

$$\langle \dots \rangle_{\tau} = \lim_{\Theta \rightarrow \infty} \frac{1}{\Theta} \int_0^{\Theta} \dots d\tau \quad (2)$$

can be determined where  $n_{\vec{k}}^{(i)}(t) = \sum_{i=1}^N e^{-i\vec{k} \cdot \vec{r}_i(t)}$  is the Fourier transformed ion number density and  $\vec{k}$  is the wave vector. The number of ions is denoted by  $N$  and  $\Theta$  is the simulation duration, which must approach infinity in the exact relation. We approximate this limit by sufficiently long simulation times.

The dynamic ion-ion structure factor  $S_{ii}(\vec{k}, \omega)$  is given by the Fourier transform of the intermediate scattering function

$$S_{ii}(\vec{k}, \omega) := \frac{1}{2\pi} \int_{-\infty}^{\infty} F_{ii}(\vec{k}, t) e^{i\omega t} dt, \quad (3)$$

with the angular frequency  $\omega$ . By virtue of the Wiener-Khinchin theorem this is equivalent to

$$S_{ii}(\vec{k}, \omega) = \lim_{\Theta \rightarrow \infty} \frac{1}{2\pi N \Theta} \left| \int_{-\Theta/2}^{\Theta/2} n_{\vec{k}}^{(i)}(t) e^{i\omega t} dt \right|^2, \quad (4)$$

which is the formula we employed for the present calculations. The intermediate scattering function  $F_{ii}(\vec{k}, t)$  is then determined by an inverse Fourier transformation of  $S_{ii}(\vec{k}, \omega)$ . Analogously, the longitudinal and transverse current spectra can be determined from

$$J_{ii,l/t}(\vec{k}, \omega) := \lim_{\Theta \rightarrow \infty} \frac{1}{2\pi N \Theta} \left| \int_{-\Theta/2}^{\Theta/2} j_{\vec{k}}^{(i,l/t)}(t) e^{i\omega t} dt \right|^2, \quad (5)$$

and

$$j_{\vec{k}}^{(i,l)}(t) = \sum_{i=1}^N v_i^{\parallel} e^{-i\vec{k} \cdot \vec{r}_i(t)}, \quad (6)$$

$$j_{\vec{k}}^{(i,t)}(t) = \sum_{i=1}^N v_i^{\perp} e^{-i\vec{k} \cdot \vec{r}_i(t)}, \quad (7)$$

where  $v_i^{\parallel}$  is the component of the velocity which is parallel to  $\vec{k}$ , and  $v_i^{\perp}$  is the component which is parallel to a given  $\vec{k}_{\perp}$ , which is perpendicular to  $\vec{k}$ . Velocities are computed from the ion positions via central finite differences. The shape of the simulation box determines the wave vectors  $\vec{k}$  at which  $S_{ii}(\vec{k}, \omega)$  can be evaluated. Only wave vectors that result in complete oscillations within the simulation box are allowed and can be computed from the reciprocal lattice vectors.

The ion dynamics are obtained by performing DFT-MD simulations with the Vienna *ab initio* simulation package (VASP) [36–38]. Within these simulations the Born-Oppenheimer approximation is used to decouple the ion and electron dynamics. For the determination of the electron density the finite temperature DFT approach [39] is used, employing the generalized gradient approximation of Perdew, Burke, and Ernzerhof [40] for the exchange correlation functional. At each time step the electron density is determined self-consistently, which allows the determination of the forces acting on each ion. The ions are moved classically due to the Coulomb interactions with the other ions and the electrons by solving Newton's second law for a given time step  $\Delta t$ . Within the VASP code the electronic wave functions are expanded into plane waves up to a cutoff energy  $E_{\text{cut}}$  and



TABLE I. Overview of the simulation parameters used in this study: temperature  $T$ , mass density  $\rho$ , size of time step  $\Delta t$ , number of ions in DFT-MD simulation  $N_i^{\text{DFT}}$  and number of ions in NN-MD simulation  $N_i^{\text{NN}}$ .

$T$ [K]	$k_B T$ (eV)	$\rho$ (g/cm <sup>3</sup> )	$\Delta t$ (fs)	$N_i^{\text{DFT}}$	$N_i^{\text{NN}}$
1000	0.086	2.356	3.0	125	32 000
5802	0.5	2.356	1.0	125	32 000
5802	0.5	4.712	1.0	125	32 000
11605	1.0	2.356	1.0	125	32 000
11605	1.0	4.712	1.0	125	32 000
58023	5.0	4.712	1.0	125	32 000
58023	5.0	8.1	1.0	125	32 000

projector augmented-wave potentials [41] are used to describe the ion potential. For aluminum we employ the PAW PBE Al 04Jan2001 potential, which treats the ten inner electrons within a frozen core approximation and only considers the three valence electrons within the DFT framework. We use a cutoff energy of 700 eV. For the temperature control the algorithm of Nosé-Hoover [42,43] is used with a mass parameter corresponding to a temperature oscillation period of 40 time steps. The simulation box for aluminum is spanned by vectors that correspond to its solid lattice structure: face centered cubic (fcc). The sampling of the Brillouin zone was carried out at the Baldereschi mean value point [44]. We have carefully checked the convergence of our results with regard to plane wave energy cutoff, length of the time step, number of particles and Brillouin zone sampling.

In order to enable a larger simulation size, we train a high-dimensional neural network potential, implemented in the N2P2 software package [29,30], using the energies and forces predicted by the DFT-MD simulations. Although these simulations are performed at finite electron temperature, we use an extrapolation of the internal energy to its value at zero electron temperature (provided by VASP [45]) to train the neural network. This allows us to exclude the contributions from electronic excitations to the internal energy, and, by extension, the electronic contributions to the heat capacity which we compute in Sec. V C. The neural network uses Behler-Parrinello symmetry functions [32] to describe the surrounding of each ion and employs a Kalman filter to update the network during the training procedure. We employ the default neural network configuration with a cutoff radius ranging from 4 Å for the simulations at 8.1 g/cm<sup>3</sup> to 6 Å at 2.356 g/cm<sup>3</sup>. The surrounding of the ions is described by ten radial symmetry functions and twelve narrow angular symmetry functions, with parameters chosen according to Ref. [46]. The neural network potential is then used in conjunction with the classical molecular dynamics simulation code LAMMPS [47] to generate the NN-MD simulations. We train a separate neural network for each condition to ensure the highest accuracy in reproducing the DFT-MD results. The networks are trained on 10 000 configurations, which are randomly sampled from the 20 000 time steps of the DFT-MD simulation and additional 5000 time steps at slightly higher and lower temperature and density. We give the specific parameters used in the simulations in Table I. For  $k_B T = 0.5$  eV and  $\rho =$

4.712 g/cm<sup>3</sup>, aluminum froze into an fcc lattice, while at all other conditions it remained a liquid.

### III. FITTING PROCEDURE AND ERROR ANALYSIS

#### A. Fit to generalized collective modes

For the DSF of liquids and plasmas, there exists a well known limiting case at long wavelength  $k \rightarrow 0$  and low frequencies  $\omega \rightarrow 0$ , the hydrodynamic limit [21]. In this limit, the DSF consists of a zero-centered Lorentzian peak, which is called the diffusive mode, and two Lorentzian shaped side peaks, which are called propagating collective modes, centered at finite frequencies [14].

The diffusive mode is mainly determined by the thermal diffusivity, while for the collective modes also the adiabatic speed of sound and the viscosity of the medium play a role. This limiting case can be extended to a generalized hydrodynamic model, in which the general shape of the DSF is kept the same but the transport coefficients become dependent on the wave number  $|\vec{k}|$ . While this approach shows good results at small wave numbers, [18] especially beyond the first correlation peak, nonhydrodynamic thermal modes and structural relaxation modes also contribute to the DSF [48]. Theoretical models for the description of the DSF at a wide range of wave vectors have been developed, with the generalized collective mode (GCM) approach being one of the most successful [49]. It extends the set of considered dynamic variables from the three hydrodynamic variables particle density, energy density, and momentum density to include their derivatives or other nonconserved variables, resulting in additional mode contributions to the correlation functions. However, since these microscopic variables cannot be observed in experiments and access to the local energy density in *ab initio* simulations is restricted, several fitting as well as fit-free methods [48] have been developed.

In this paper, we adopt the fitting scheme of Wax and Bryk [50]. Within this scheme the intermediate scattering function is modeled according to a GCM approach with one propagating and one diffusive mode

$$F_{ii}^{\text{GCM}}(\vec{k}, t) = A e^{-\alpha|t|} + (B_1 \cos(\omega_0|t|) + B_2 \sin(\omega_0|t|)) e^{-\beta|t|} \\ = A e^{-\alpha|t|} + C \cos(\omega_0|t| + \phi) e^{-\beta|t|}, \quad (8)$$

with the relation

$$C = \sqrt{B_1^2 + B_2^2}, \quad \phi = \arctan\left(-\frac{B_2}{B_1}\right), \quad (9)$$

leading, via the Fourier transform (3), to the DSF

$$S_{ii}^{\text{GCM}}(\vec{k}, \omega) = \frac{1}{2\pi} \left( \frac{2A\alpha}{\alpha^2 + \omega^2} + \frac{B_1\beta}{\beta^2 + (\omega_0 + \omega)^2} + \frac{B_1\beta}{\beta^2 + (\omega_0 - \omega)^2} + \frac{B_2(\omega_0 + \omega)}{\beta^2 + (\omega_0 + \omega)^2} + \frac{B_2(\omega_0 - \omega)}{\beta^2 + (\omega_0 - \omega)^2} \right). \quad (10)$$

The zero-centered Lorentzian in Eq. (10) corresponds to a diffusive process, while the remaining Lorentzians at finite

frequencies correspond to propagating processes. These two modes are not necessarily the hydrodynamic modes, although they will coincide with them in the limit  $k \rightarrow 0$ . In the GCM scheme, modes correspond to either real or imaginary eigenvalues of the generalized hydrodynamic matrix, with real eigenvalues leading to diffusive modes and imaginary eigenvalues corresponding to propagating processes. Therefore, in this fitting scheme, it is assumed that the behavior of the system can be described by the two (hydrodynamic or nonhydrodynamic) modes of Eqs. (8) and (10). Similar to Ref. [50], we find that the inclusion of an additional mode does not improve the results enough to justify the addition of further fitting parameters. The parameters  $A$ ,  $B_1$ ,  $B_2$ ,  $\alpha$ ,  $\beta$ , and  $\omega_0$  are unknown functions of the wave number  $k$ , but we omit the index  $k$  for brevity. Following the fitting scheme of Ref. [50],  $A$ ,  $B_1$ , and  $B_2$  can be eliminated as independent parameters by constraining the model function to obey the zeroth, first, and second frequency moments:

$$\int_{-\infty}^{\infty} S_{ii}(k, \omega) d\omega = S_{ii}(k), \quad (11)$$

$$\int_{-\infty}^{\infty} S_{ii}(k, \omega) \omega d\omega = 0, \quad (12)$$

$$\int_{-\infty}^{\infty} S_{ii}(k, \omega) \omega^2 d\omega = -\partial_t^2 F_{ii}(k, t)|_{t=0}. \quad (13)$$

The first frequency moment is constrained to be zero, therefore this model avoids the unphysical cusp in  $F_{ii}(\vec{k}, t)$  at  $t = 0$  that is present in the hydrodynamic model. In contrast to Ref. [50] for the second frequency moment, we do not use the one component plasma (OCP) value, but the value directly obtained from the intermediate scattering function  $F_{ii}(\vec{k}, t)$  by finite differences.

For curve fitting we seek to minimize the least-square merit function of the form:

$$\chi(\vec{k}) = \sum_{i=0}^{N_d} w_i (f^{\text{model}}(i) - f^{\text{data}}(i))^2, \quad (14)$$

where  $f^{\text{model}}$  is a model function one tries to fit to the dataset  $f^{\text{data}}$ ,  $N_d$  is the number of data points and  $w_i$  is the weight for the  $i$ th data point, which is usually chosen to be the inverse variance  $1/\sigma_{f(i)}^2$ . Following the scheme of Ref. [50], the parameters  $\alpha$ ,  $\beta$  and  $\omega_0$  are obtained by fitting Eqs. (8) and (10) to  $F_{ii}$  and  $S_{ii}$  obtained from the DFT-MD and NN-MD simulations. The standard deviation of each data point is determined through the error analysis described in the next section. From the Jacobian of the fitting problem (14) with respect to the fitting parameters, it is possible to estimate a standard error for these parameters. It should be pointed out that this error merely describes how sensitive the fit to the simulation data is to small changes in the respective fitting parameter. It includes no information on the physical validity of the given model function, which has to be discussed separately.

For fitting we employ a standard Marquardt-Levenberg fitting algorithm (as implemented in the SCIPY library for scientific computing in PYTHON [51]) obtaining first the parameters  $\beta$  and  $\omega_0$  by fitting to  $S_{ii}$  keeping  $\alpha$  fixed. Then  $\alpha$  is obtained by fitting to  $F_{ii}$  with  $\beta$  and  $\omega_0$  fixed. This procedure

is then repeated until all parameters converge to an accuracy of 0.001%.

## B. Error analysis

For the estimation of the errors we report the confidence intervals calculated for a confidence level of 68% (i.e., one standard deviation). Here, we follow the error estimation of Welch for the use of the Fast Fourier Transform in power spectra calculations [52]. A DSF calculated by Eq. (4) has a standard deviation of  $\sigma_{S(\vec{k}, \omega)} = S(\vec{k}, \omega)$ . By splitting the duration of the simulation into  $N_I$  intervals and averaging over all individual power spectra, the standard deviation of  $S_{ii}^{\text{GCM}}(\vec{k}, \omega)$  is reduced by  $\sqrt{N_I}$ . Because the systems under investigation are isotropic we report only on quantities depending on the magnitude of the wave vector  $|\vec{k}|$  and averages over the  $N_k$  wave vectors with magnitude  $|\vec{k}|$  can be performed. In addition, since the ions are treated classically in our simulations, we expect the intermediate scattering function  $F(\vec{k}, t)$  to be symmetric and real-valued, corresponding to a real and symmetric DSF with respect to  $\omega$ . Therefore an average of the positive and negative frequency part is taken which results in a further reduction of the error leading to the error approximation

$$\sigma_{S_{ii}(\vec{k}, \omega)} \approx \frac{S_{ii}(\vec{k}, \omega)}{\sqrt{2N_k N_I}}. \quad (15)$$

While the number of intervals stays constant during the analysis, the number of wave vectors corresponding to a given magnitude increases with  $|\vec{k}|$ , causing lower relative errors at larger wave vectors.

In our calculations, we arrive at the intermediate scattering function via the Fast Fourier Transform from the DSF  $S_{ii}(\vec{k}, \omega)$ . Using quadratic error propagation on the formulation of the fast Fourier transform leads to a constant error

$$\begin{aligned} \sigma_{F_{ii}(\vec{k}, t)} &= \sqrt{\sum_j \sigma_{S_{ii}(\vec{k}, \omega_j)}^2 \Delta\omega} \\ &\approx \sqrt{\sum_j \frac{S_{ii}(\vec{k}, \omega_j)^2}{2N_k N_I} \Delta\omega}, \end{aligned} \quad (16)$$

where  $\omega_j$  are the discrete frequencies available from the Fourier transform and  $\Delta\omega$  is their spacing. Using Eqs. (15) and (16) for the weight  $w_i$  in (14) allows us to extract an estimated error on the fit parameters  $\alpha$ ,  $\beta$ ,  $\omega$ , and, using error propagation on the equations given by the sum rules, also for the remaining parameters.

In order to further reduce noise in the simulation data, a window function  $g_{\vec{k}}(t)$  is applied to the intermediate scattering function to suppress statistical oscillations at large times  $t$ .

## IV. RESULTS FOR THE STATIC AND DYNAMIC STRUCTURE FACTOR

### A. The static ion-ion structure factor

To validate the accuracy of our simulation approach, we compare with experimental x-ray diffraction data [53] available for small temperatures in Fig. 1.

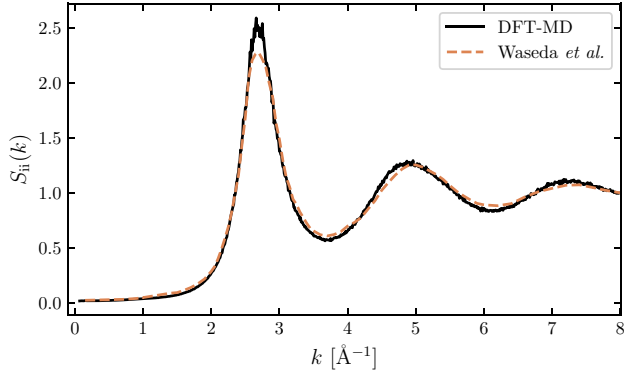


FIG. 1. Comparison of DFT-MD calculations and experimental results [53] for liquid aluminum at 2.356 g/cm<sup>3</sup> and  $T = 1000$  K.

Very good agreement is found except for values around the first peak, where a sharp cusp is observed. A similar behavior has also been observed in earlier MD simulations, which can be explained by the periodic boundary conditions that induce additional order. Furthermore, the statistical error in this region is comparatively large because of the especially large correlation times that are present there. Additionally, we show a comparison of the static ion-ion structure factor generated from the DFT-MD and NN-MD simulations in Fig. 2. It can be observed that the static structure is reproduced well by the NN-MD simulations. For the lowest considered temperature  $T = 1000$  K, the first correlation peak of the NN-MD is slightly lower than that of the original DFT-MD simulation. This is due to the diminishing impact of the periodic boundary conditions in the larger simulation box of the NN-MD simulations. The agreement for the other liquid conditions not shown in Fig. 2 is equally good, while the static structure factor of solid aluminum exhibits a strong particle number dependence.

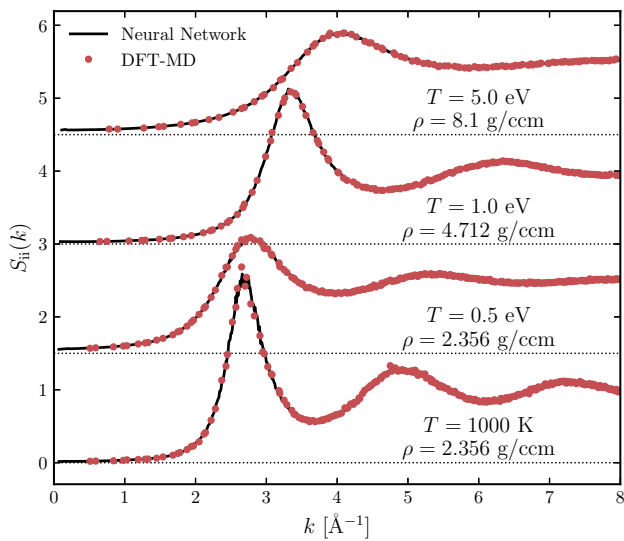


FIG. 2. Comparison of results for the static ion-ion structure factor from DFT-MD simulations and NN-MD for liquid aluminum at various conditions.

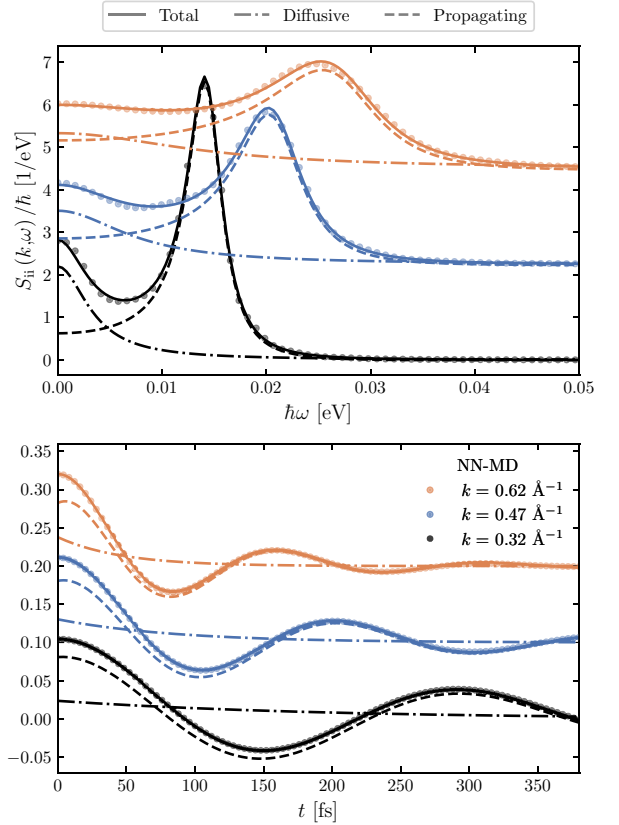


FIG. 3. Comparison of the DSF (top panel) and the intermediate scattering function (bottom panel) and the fit to the GCM model [described in Eqs. (8) and (10)] for a NN-MD simulation of aluminum at 2.356 g/cm<sup>3</sup> and  $T = 1.0$  eV. The diffusive and propagating part of the fit are indicated separately. The curves are shifted by 2.25 eV<sup>-1</sup> for the DSF and 0.1 for the intermediate scattering function with respect to each other for clarity.

## B. The dynamic ion-ion structure factor

In Fig. 3, the block averaged DSF for aluminum is compared with the curves obtained by the fitting procedure at 11605 K. Very good agreement between the NN-MD data and the GCM model is found even at high wave numbers (see upper panel in Fig. 3), far from the collective region. The same observations can be made for all other conditions under investigation in this paper (Table I).

As expected, very good agreement is also found for the intermediate scattering function (see lower panel in Fig. 3). However, after the decay of the correlations,  $F_{ii}(\vec{k}, t)$  exhibits statistical fluctuations at long times  $t$ . To reduce the effect of these unphysical fluctuations from the DSF and to reduce truncation effects we use a window function  $g_{\vec{k}}(t)$  that is defined in terms of a decay time  $\theta_{\vec{k}}$  by

$$g_{\vec{k}}(t) = \begin{cases} 1, & \text{if } |t| < \theta_{\vec{k}}/2 \\ \exp\left(-16 \frac{(t - \theta_{\vec{k}}/2)^2}{\theta_{\vec{k}}^2}\right), & \text{if } |t| > \theta_{\vec{k}}/2. \end{cases} \quad (17)$$

$S_{ii}(\vec{k}, \omega)$  is then obtained by Fourier transformation of  $g_{\vec{k}}(t)F_{ii}(\vec{k}, t)$ . The use of a window function as in Eq. (17) leaves the intermediate scattering function unchanged at



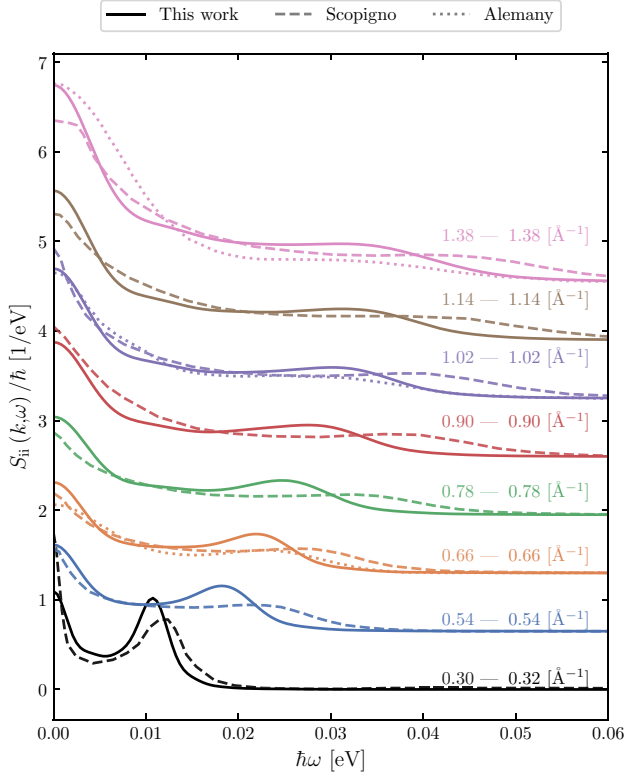


FIG. 4. DSF  $S_{ii}(\vec{k}, \omega)$  of liquid aluminum at  $\rho = 2.356 \text{ g/cm}^3$  and  $T = 1000 \text{ K}$ . Dashed lines: experimental x-ray scattering results [54]. Dotted lines: DFT-MD of Alemany *et al.* [55]. Solid lines: present NN-MD simulations. The right wave numbers correspond to the present NN-MD results, while the left ones correspond to Refs. [54,55]. For clarity, each set of curves is shifted by an offset of  $0.6 \text{ eV}^{-1}$  with respect to the lower one.

times, where static fluctuations play a minor role, and damps the statistical fluctuations where they dominate the signal. To avoid bias in the choice of  $\theta_{\vec{k}}$ , it is determined from the results of the fitting procedure. We define  $\theta_{\vec{k}}$  as the time after which the intermediate scattering function has decayed to 0.1% of its initial value, i.e., we use the  $\theta_{\vec{k}}$  that fulfills

$$|A|e^{-\alpha\theta_{\vec{k}}} + |C|e^{-\beta\theta_{\vec{k}}} = 0.001 F_{ii}(\vec{k}, 0) \quad (18)$$

$$= 0.001 (|A| + |C|). \quad (19)$$

Note again that the fitting parameters  $A$ ,  $C$ ,  $\alpha$ , and  $\beta$  are all wave number dependent, but the index  $\vec{k}$  has been omitted. With this specific choice for the window function there are still small statistical artifacts visible in the DSF but a more important feature is that it leaves the height and form of the peaks practically unchanged.

In Fig. 4, we compare the DSF of liquid aluminum at 1000 K to several measurements of Scopigno *et al.* [54] and to earlier DFT-MD simulations [55] that used the LDA for the exchange-correlation functional. The normalization of the experimental data could not be determined from the experiment, but has been determined from fitting procedures. We found that static structure factors from this procedure are, on average, by a factor 1.52 lower than our NN-MD results

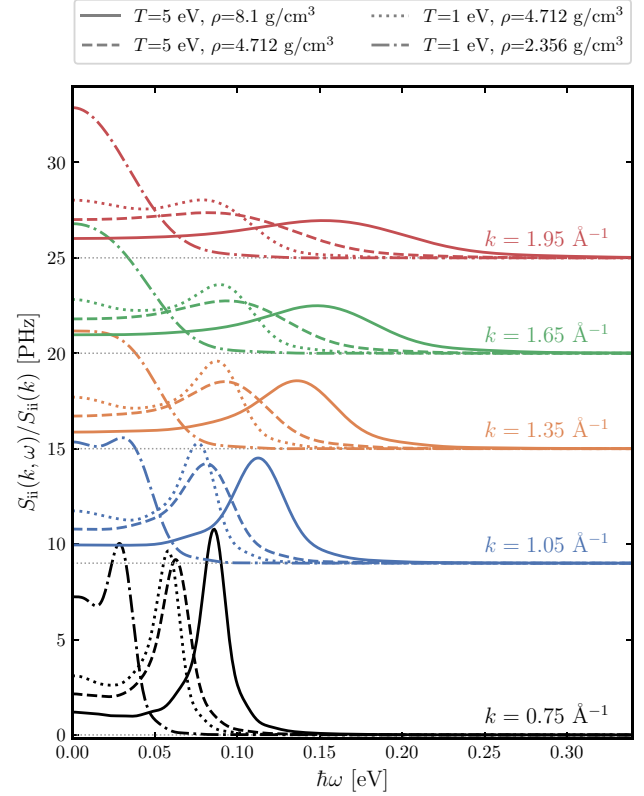


FIG. 5. DSF  $S_{ii}(\vec{k}, \omega)$  of warm dense aluminum at different densities and temperatures. For clarity each set of curves is shifted by an offset with respect to the lower one. The dotted lines represent the baseline for each set.

and thus in Fig. 4 scaled the data of Scopigno *et al.* [54] by this factor. Alemany *et al.* [55] report on a normalized DSF  $S_{ii}(\vec{k}, \omega)/S_{ii}(\vec{k})$ . Therefore, in Fig. 4, we scaled their data according to our  $S_{ii}(\vec{k})$  for comparison. Since the calculation of the structure factor can only be carried out on the reciprocal lattice corresponding to the periodic boundary conditions, the comparison is done at those wave numbers that are closest to the ones in the experiment. Good agreement is found between our simulations and the experiment. Compared to the experiment the peaks and shoulders are located at slightly lower frequencies in our simulation and the peaks are more pronounced. Compared to the *ab initio* calculation of Alemany *et al.* [55] our simulation uses a larger energy cutoff, a larger number of ions, a smaller time step and has a longer simulation time. They used the LDA for the XC contribution, while we use the GGA by Perdew, Burke, and Ernzerhof [40]. Furthermore, due to numerical limitations at the time, the previous DFT study was performed with 205 atoms for 850 time steps, which in our experience is far too few to properly converge the width and height of the side and central peak.

Figure 5 shows the DSF  $S_{ii}(\vec{k}, \omega)$  of warm dense aluminum at four different conditions for various wave vectors inside the first Brillouin zone, illustrating its trends with temperature and density. With increasing densities, a shift of the propagating mode to higher frequencies and a clear separation from the diffusive mode can be observed. Additionally, the

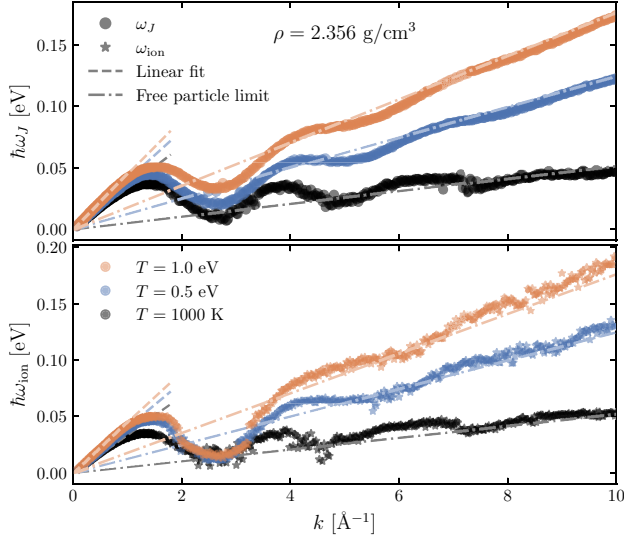


FIG. 6. Peak position  $\omega_J$  of the longitudinal current-current spectral function  $J_{ii}(k, \omega)$  (top) and the frequency of the ion acoustic mode  $\omega_{\text{ion}}$  (bottom), extracted by fitting to  $S_{ii}(k, \omega)$ , as a function of the wave number  $k$  for aluminum at various temperatures for the mass density  $\rho = 2.356 \text{ g/cm}^3$ . The linear behavior of  $\omega_{\text{ion}}$  for small  $k$ , predicted by the hydrodynamic model, is indicated by dashed lines. The free particle limit of  $\omega_J$  for large  $k$  is depicted by dash-dotted lines.

higher densities suppress the diffusive mode due to the higher collision rates. At constant density, a higher temperature leads to a broadening and a slight shift to higher frequencies of the propagating mode, indicating a faster sound transport in heated materials (see Sec V A).

## V. MATERIAL PROPERTIES

### A. Dispersion relation

The frequency  $\omega_{\text{ion}}$  of the ion acoustic waves can be determined from the fitting procedure, giving reliable data in the long-wavelength regime. A general quantity that does not rely on fitting is the peak position of the longitudinal current-current spectrum [see Eq. (5)], which will coincide with the hydrodynamic behavior for  $k \rightarrow 0$ , see Fig. 6. All investigated cases exhibit a linear dispersion at small  $k$ . At relatively low temperatures, local maxima in the peak position are observed followed by a de Gennes minimum [56] located at the position of the first correlation peak of the static structure factor  $S_{ii}(\vec{k})$ . Analogous to the reciprocal space in solids, where the first Brillouin zone is repeated infinitely beyond its boundaries, a periodicity, albeit faster decaying, occurs in liquids due to the near-field order. At length scales characteristic of this near-field order, described by the first correlation peak, the dispersion tends back to its value at  $k = 0$ , similar to the dispersion of phonons going to zero at the center of neighboring Brillouin zones. This minimum becomes less pronounced for higher temperatures as the near-field order of the system decreases. Instead, the curves reach an intermediate plateau and then go over to a positive dispersion. For large  $k$ , the peak position of the longitudinal current-current spectral function

TABLE II. Adiabatic speed of sound  $c_{s,\text{HD}}$ , extracted from the fit to the hydrodynamic model in (8) and (10) and adiabatic speed of sound  $c_{s,\text{TD}}$  computed from the thermodynamic relation in (22) for aluminum at given temperatures  $T$  and mass densities  $\rho$ .

$T$ (K)	$\rho$ (g/cm <sup>3</sup> )	$c_{s,\text{HD}}$ (km/s)	$c_{s,\text{TD}}$ (km/s)
1000	2.356	$5.087 \pm 0.025$	$4.73 \pm 0.12$
5802	2.356	$6.029 \pm 0.016$	$6.02 \pm 0.05$
11 600	2.356	$6.736 \pm 0.018$	$6.73 \pm 0.04$
11 600	4.712	$11.579 \pm 0.024$	$11.349 \pm 0.025$
58 020	4.712	$13.049 \pm 0.017$	$12.908 \pm 0.020$
58 020	8.1	$17.406 \pm 0.017$	$17.451 \pm 0.003$

can be described by the classical free particle limit of a non-interacting system

$$\omega_J(\vec{k}) = \sqrt{\frac{2}{m_i \beta}} |\vec{k}| \quad (20)$$

with the ion mass  $m_i$  and  $1/\beta = k_B T_i$ , where  $k_B$  is the Boltzmann constant. This peak at finite frequencies occurs because the zero-centered Gaussian DSF of a noninteracting system is multiplied by  $\omega^2/k^2$  to arrive at the longitudinal current-current spectral function. We suspect the rise of  $\omega_{\text{ion}}$  at high  $k$ , where the DSF is close to a perfect Gaussian, is due to our choice of fit function. Because a Gaussian cannot be approximated by a Lorentzian, a second contribution at finite frequency is necessary. This highlights the inadequacy of this fit function beyond the first correlation peak, and in the following, we will therefore not apply it there.

By fitting

$$\omega_{\text{ion}}(\vec{k}) = c_s |\vec{k}| \quad (21)$$

to the small  $k$  dispersion relation of  $\omega_{\text{ion}}$  extracted from the fit, the adiabatic velocity of sound  $c_s$  is determined, see Table II. The dashed lines in Fig. 7 indicate the linear fit for the liquid conditions considered in this work. We use the first eight oscillation frequencies  $\omega_{\text{ion}}$  at each condition for the linear fit. It can be shown that the inclusion of more or less data points does not significantly impact the extracted value for the adiabatic velocity of sound. The speed of sound at 1000 K can be compared to experimental data by using the suggested best fit from Ref. [57]. For a temperature of 1000 K, one obtains a speed of sound of 4648 m/s, which is in reasonable agreement with our value of 5087 m/s. Remarkably, the experimental speed of sound is not recovered by the x-ray scattering study of Scopigno *et al.* on liquid aluminum, [54] either, from which an adiabatic speed of sound of  $\sim 5700$  m/s can be derived. Additionally, following Ref. [58] and the supplemental material of Ref. [20], we compute the adiabatic speed of sound directly from the thermodynamic relations

$$c_{s,\text{TD}}^2 = \frac{1}{\rho \chi_S} = \frac{\gamma}{\rho \chi_T}, \quad (22)$$

$$\chi_T = \frac{1}{\rho} \left( \frac{\partial \rho}{\partial P} \right)_T, \quad (23)$$

with the heat capacity ratio  $\gamma = C_p/C_v$ , the mass density  $\rho$ , the pressure  $P$  and the adiabatic and isothermal compress-

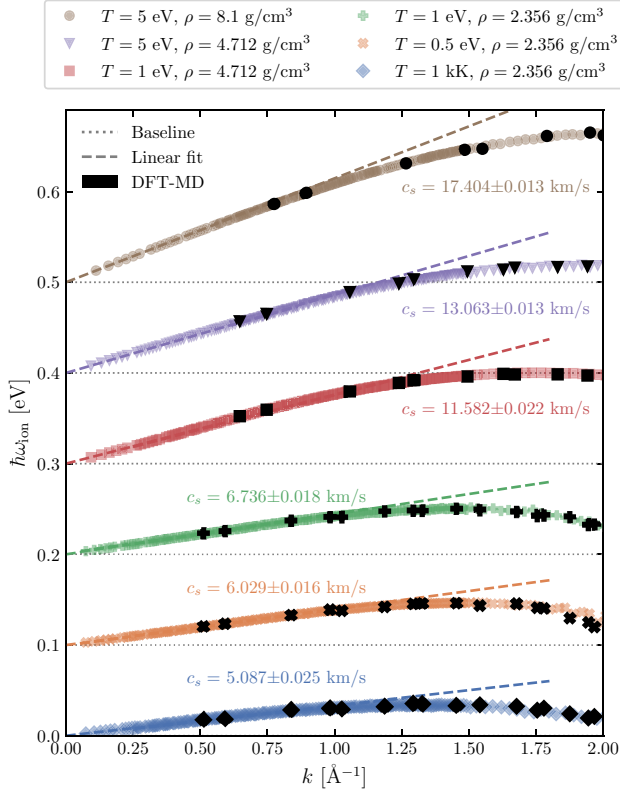


FIG. 7. Long-wavelength behavior of the oscillation frequency of the ion acoustic waves  $\omega_{\text{ion}}$  as a function of the wave number  $k$  for aluminum at various conditions. The linear behavior for small  $k$ , predicted by the hydrodynamic model, is indicated by dashed lines and the inferred speed of sound is shown. The extracted peak position from the underlying DFT-MD simulations are also indicated by the black symbols. For clarity each set of curves is shifted by an offset of 0.1 eV with respect to the lower one. The dotted lines represent the baseline for each set.

ibilities  $\chi_S$  and  $\chi_T$ . In order to evaluate these expressions, we perform additional simulations at 5% to 10% below and above the desired density and temperature and evaluate the derivatives using central finite differences. The results are summarized in Table II. The agreement between both methods is good for all conditions that are hotter than 1000 K. At these conditions, the results for the direct calculation via (22) deviate less than 5% from the value extracted from the fit to the GCM model. However, just above the melting line at 1000 K, the direct calculation results in a prediction for the adiabatic speed of sound which is  $\sim 10\%$  lower than the result extracted from the fit. This speed of sound lines up better with the experimentally observed value, indicating that the hydrodynamic limit at this condition might require even smaller wave numbers than accessible in this work.

In Fig. 7, we also indicate the frequencies that we determined directly from the DFT-MD simulations (black symbols). Due to the significantly smaller simulation size, the available wave vectors cover the  $k$  axis more sparsely and the smallest available wave vectors are at least seven times larger than the smallest wave vectors from the NN-MD. The

dispersion is reproduced well by the NN-MD in all cases. For the simulations at  $\rho = 2.356 \text{ g/cm}^3$ , the lowest five  $k$  values of our DFT-MD results lie within the linear behavior of the dispersion, while the denser conditions have at most two  $k$  values in the linear regime. Therefore it would be difficult to justify a linear fit to the available DFT-MD data at these conditions.

### B. Mode contributions

While fitting the DSF with one propagating and one diffusive mode is justified in the hydrodynamic limit, contributions from additional kinetic modes will become relevant at higher wave numbers. The GCM framework enables us to include arbitrary amounts of additional modes. However, the shape of the DSF is generally not discriminative enough to achieve reliable results from fitting procedures. Furthermore, statistical noise prohibits us from identifying the onset of small corrections beyond the hydrodynamic limit. In order to circumvent this limitation, we adopt the scheme laid out in Refs. [17,49,59], which uses the memory-function formalism to construct a generalized hydrodynamic matrix on an extended set of hydrodynamic variables. We employ the five-mode approach by including the first time derivatives of the longitudinal current and energy, on top of the three hydrodynamic variables. This approach does not rely on fitting to the DSF and, therefore, does not suffer from the shortcomings mentioned earlier when examining the transition to the nonhydrodynamic regime. Due to the higher memory storage demand, we only use 4000 atoms for this analysis.

In Fig. 8, we show the results of the five-mode approach compared to the three-mode approach, which can only describe generalized hydrodynamic modes, for the most extreme condition considered in this study at  $T = 5 \text{ eV}$  and  $\rho = 8.1 \text{ g/cm}^3$ . The other conditions show similar trends regarding the onset of nonhydrodynamic corrections. The top panel of Fig. 8 shows the decay coefficients of the various modes. In the low- $k$  limit, only two modes tend toward zero, which identifies them as the hydrodynamic modes which will survive on long time scales. The remaining modes are two quickly decaying diffusive modes, which do not contribute in the hydrodynamic limit. At  $\sim 0.8 \text{ \AA}^{-1}$ , the hydrodynamic and one nonhydrodynamic diffusive mode merge to create an additional propagating mode, which is the typical behavior of a damped wave equation (see Fig. 1 in Ref. [17]). The oscillation frequency of this additional mode is displayed in the bottom panel of Fig. 8. It follows the same trend as the hydrodynamic sound wave, but at a significantly lower frequency. It is apparent that these nonhydrodynamic corrections only occur for wave numbers above  $0.5 \text{ \AA}^{-1}$ , but contribute significantly above  $1 \text{ \AA}^{-1}$ . For smaller wave numbers, the three- and five-mode approaches give virtually the same predictions, giving credence to our fit functions (8) and (10). We, therefore, conclude that fitting to these functions at small  $k$  will in fact reveal the thermodynamic and transport properties that describe the hydrodynamic model [14].

### C. Ionic transport

As mentioned in Sec. III A, the general diffusive and propagating modes from Eqs. (8) and (10) can be identified as the

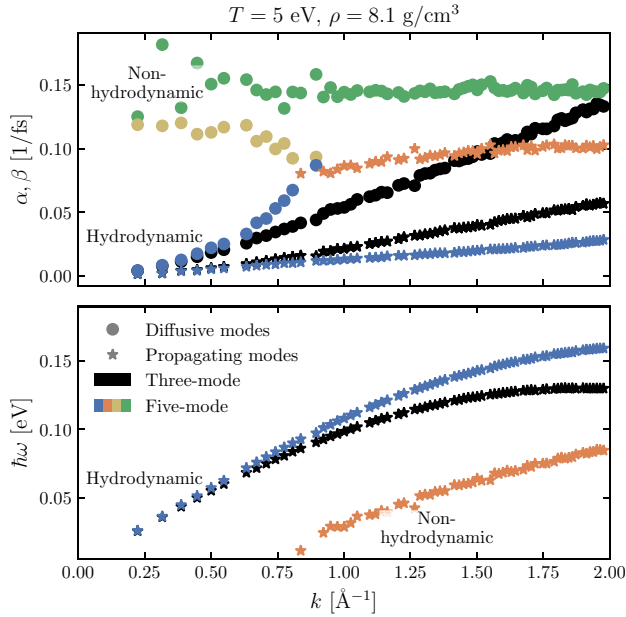


FIG. 8. Decay coefficients according to the five-mode and three-mode GCM approach (top) and frequencies of the propagating modes (bottom). Propagating modes are denoted by stars and diffusive modes by full circles, colors enumerate the different modes of the five-mode approach, while black symbols denote the generalized hydrodynamic modes of the three-mode approach.

well known hydrodynamic modes [21] in the limit of  $k \rightarrow 0$  and  $\omega \rightarrow 0$ . In this limit, the diffusive mode is connected to the thermal diffusivity  $D_T$  via  $\alpha = D_T k^2$  and the propagating mode becomes symmetric, i.e.,  $B_2$  vanishes, while  $\beta = \Gamma k^2$ , where  $\Gamma$  is the sound attenuation coefficient. Therefore the behavior of the decay coefficients in equation (8), which describe how fast diffusive and collective processes decay with time, can be connected to well known material properties. As these coefficients also determine the full width at half maximum (FWHM) of the peaks in the DSF [see Eq. (10)], this allows both experiment and theory to access these properties of interest, provided that the hydrodynamic regime of wave numbers is reached.

In Fig. 9, we show the FWHM of the zero-centered diffusive peak in the DSF for the considered liquid conditions. The FWHM is given by  $2\alpha$ , and  $\alpha$  is found by fitting to the DSF and intermediate scattering function of the NN-MD simulations. The results that were found by fitting to the underlying DFT-MD simulations are also shown by the black symbols in Fig. 9. It is apparent that the hydrodynamic regime for this quantity is reached at lower wave numbers than for the dispersion relation in Fig. 7. None of the considered cases have more than two DFT-MD data points in the region that matches the indicated limiting behavior. Additionally, the FWHM of the central mode is sensitive to statistical fluctuations and requires a large number of time steps in order to reach converged results. Due to computational limitations, we perform 40 000 or fewer time steps for all DFT-MD simulations, while we perform between 150 000 and 600 000 time steps for the

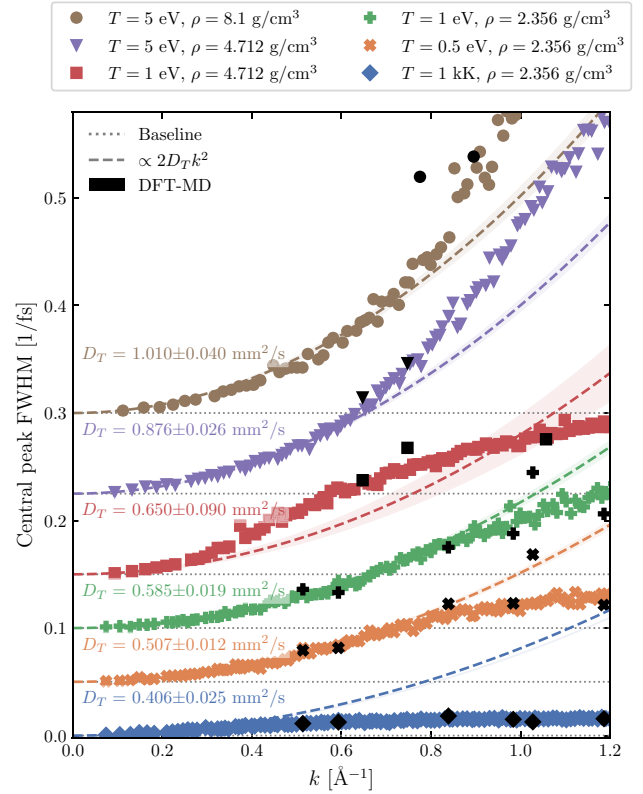


FIG. 9. FWHM of the central, diffusive peak of the DSF in equation (10), which is given by  $2\alpha$ , dependent on the wave number  $k$ . A fit to  $2D_T k^2$  is indicated and the best fit result for the thermal diffusivity  $D_T$  is given. The extracted FWHM from the underlying DFT-MD simulations are also indicated by black symbols. For clarity, each set of curves is shifted by an offset with respect to the lower one. The dotted lines represent the baseline for each set.

NN-MD simulations. The statistical fluctuations induced by the shorter simulations can be observed in Fig. 9.

Additionally, the lowest available wave numbers correspond to only a few wave vectors. For a cubic simulation box, only three wave vectors are averaged to compute the smallest  $k$ . For the DFT-MD simulations, only the smallest  $k$  approach the hydrodynamic limit, where only very few  $k$  vectors correspond to each  $k$  value, leading to worse statistical averages compared to the NN-MD simulations.

We follow the approach outlined in Ref. [20] to compute the thermal conductivity of the ions  $\lambda_{ii}$  from the thermal diffusivity  $D_T$ . We employ the thermodynamic derivatives

$$C_{m,v} = \left( \frac{\partial U_m}{\partial T} \right)_V, \quad (24)$$

$$C_{m,p} - C_{m,v} = V_m T \left( \frac{\partial P}{\partial T} \right)_V^2 \left( \frac{\partial V_m}{\partial P} \right)_T \quad (25)$$

to determine the molar heat capacities at constant volume  $C_{m,v}$  and at constant pressure  $C_{m,p}$ . The internal energy per mol is given by  $U_m$  and the molar volume is  $V_m$ . Note that if  $U_m$  is taken from the DFT-MD simulations, the molar heat capacities contain contributions from thermal electronic



TABLE III. Molar total heat capacity at constant volume  $C_{m,v}$  and at constant pressure  $C_{m,p}$  computed via thermodynamic derivatives from DFT-MD simulations for various temperatures and densities. These values include the electronic contribution. The corresponding adiabatic coefficient is also given.

$T$ (K)	$\rho$ (g/cm <sup>3</sup> )	$C_{m,v}$ [J/(K mol)]	$C_{m,p}$ [J/(K mol)]	$\gamma$
1000	2.356	25.9 ± 1.9	34.2 ± 2.8	1.32 ± 0.04
5802	2.356	24.9 ± 1.0	31.4 ± 1.5	1.263 ± 0.026
11 600	2.356	29 ± 4	38 ± 5	1.30 ± 0.07
11 600	4.712	31.6 ± 3.3	35 ± 4	1.093 ± 0.017
58 020	4.712	44 ± 11	53 ± 15	1.22 ± 0.08
58 020	8.1	44 ± 8	48 ± 10	1.103 ± 0.029

excitations. These contributions can be removed by subtracting the electronic heat capacity via  $C_{v,e} = T \left( \frac{\partial S_e}{\partial T} \right)_V$ , with the electronic entropy  $S_e$ . However, removing the contributions of electronic excitations from the pressure, which influences  $C_{m,p}$ , is not easily possible. Therefore we compute the heat capacity from the NN-MD simulations which were consistently trained on DFT-MD energies excluding the electronic excitation energy. Both procedures yield heat capacities at constant volume within 5% for the densities and temperatures considered here. We summarize the heat capacities computed from the DFT-MD simulations without the subtraction of the electronic contribution in Table III and the heat capacities computed from the NN-MD in Table IV.

The thermal conductivity of the ionic subsystem  $\lambda_{ii}$  can now be computed via

$$\lambda = D_T \frac{C_{m,p}}{V_m}, \quad (26)$$

results are given in Table V. In order to compare the ionic thermal conductivity extracted from the hydrodynamic limit to another approach based on the same DFT-MD simulations, we compare with the linear response treatment of the thermal conductivity as described in Ref. [60]. We have parametrized radial force fields between the ions with Eq. (6) from Ref. [60], setting the potential cutoff parameter to  $C = 6$ , which was sufficient to produce converged thermal conductivities. The generated force fields between the aluminum ions are purely repulsive. The ionic thermal conductivity  $\lambda_{ii,GK}$  was then calculated with the Green-Kubo formula using the

TABLE IV. Molar ionic heat capacity at constant volume  $C_{m,v}$  and at constant pressure  $C_{m,p}$  computed via thermodynamic derivatives from NN-MD simulations for various temperatures and densities. The corresponding adiabatic coefficient is also given.

$T$ (K)	$\rho$ (g/cm <sup>3</sup> )	$C_{m,v}$ [J/(K mol)]	$C_{m,p}$ [J/(K mol)]	$\gamma$
1000	2.356	24.62 ± 0.20	31.69 ± 0.29	1.287 ± 0.004
5802	2.356	18.719 ± 0.027	23.64 ± 0.04	1.2631 ± 0.0008
11 600	2.356	17.36 ± 0.09	22.11 ± 0.13	1.274 ± 0.003
11 600	4.712	23.61 ± 0.12	25.92 ± 0.14	1.0976 ± 0.0008
58 020	4.712	17.61 ± 0.15	20.67 ± 0.19	1.1736 ± 0.0027
58 020	8.1	19.83 ± 0.17	21.09 ± 0.18	1.0637 ± 0.0009

TABLE V. The thermal conductivity  $\lambda_{ii,HD}$ , computed from  $D_T$  in Fig. 9 via Eq. (26), and the thermal conductivity  $\lambda_{ii,GK}$  computed from the Green-Kubo relation as described in Ref. [60] for aluminum at given temperatures  $T$  and mass densities  $\rho$ .

$T$ (K)	$\rho$ (g/cm <sup>3</sup> )	$\lambda_{ii,HD}$ [W/(m K)]	$\lambda_{ii,GK}$ [W/(m K)]
1000	2.356	1.12 ± 0.07	0.93 ± 0.10
5802	2.356	1.05 ± 0.03	1.01 ± 0.11
11 600	2.356	1.13 ± 0.04	1.08 ± 0.11
11 600	4.712	2.9 ± 0.4	3.4 ± 0.4
58 020	4.712	3.16 ± 0.09	2.5 ± 0.6
58 020	8.1	6.40 ± 0.25	5 ± 1

ionic trajectories from the DFT-MD simulations as described in Ref. [60]. Table V contains the results, which are in good agreement with those derived from the dynamic structure factor.

For completeness, note that the total thermal conductivity of liquid metals is usually dominated by the electronic part, e.g., the experimentally observed value for liquid aluminum at 1000 K [61] is two orders of magnitude larger than the value we determined for the ionic thermal conductivity. This prevents a direct comparison of our calculated ionic thermal conductivities with experiments.

In Fig. 10, we show the FWHM of the propagating mode, which appears at the finite excitation frequency indicated in Fig. 6. From fitting to the low- $k$  behavior of the FWHM, the longitudinal sound attenuation coefficient  $\Gamma$  can be determined. The statistical fluctuations in this mode are significantly smaller than in the diffusive mode, making it easier to determine where the hydrodynamic regime begins. Especially at the lowest available density  $\rho = 2.356$  g/cm<sup>3</sup>, higher temperatures lead to an extension of the hydrodynamic regime to higher wave numbers. Due to these smaller statistical fluctuations, the agreement with the significantly shorter DFT-MD simulations is also better than in the diffusive mode.

## VI. CONCLUSIONS

In this work, we gave an extensive overview of the computation of the ionic DSF and intermediate scattering function and some relevant practical considerations for its application in the WDM regime. We introduced a simple GCM model with one diffusive and one propagating mode which can be matched to the dynamic behavior of liquid aluminum via a fitting procedure. We showed that liquid aluminum from the melting line up to the WDM regime can be approximated well by this simple model across all length scales apart from the distances corresponding to the first correlation peak in the static ion-ion structure factor, where the description breaks down. Good agreement with experimental data for the static and dynamic ion-ion structure factor was observed for liquid aluminum at 1000 K. We demonstrated how information about the  $k$  and  $\omega$  dispersion can be extracted from the fitting procedure and highlighted the convergence to the hydrodynamic model in the limit of long wave lengths. The inability of DFT-MD simulations to reach statistically converged results in the hydrodynamic regime, due to computational limitations, was demonstrated. This shortcoming can be circumvented by

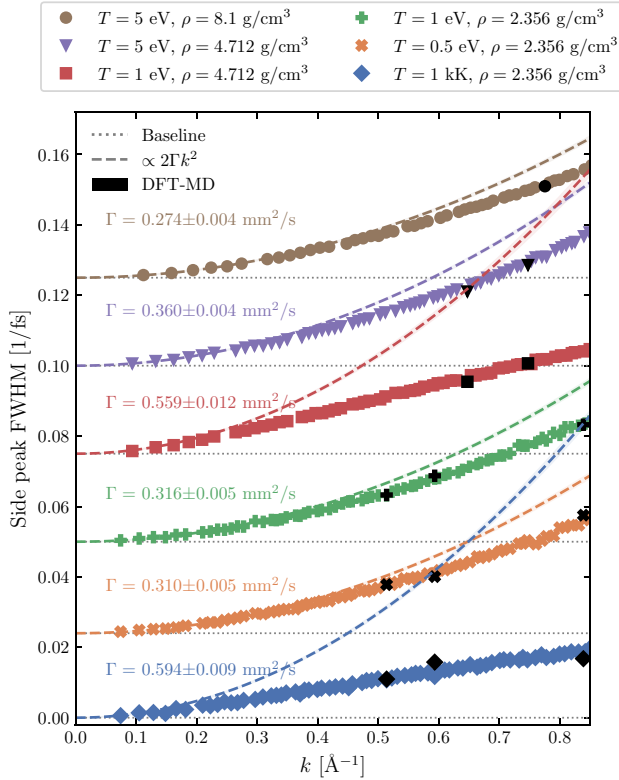


FIG. 10. FWHM of the propagating side peaks of the DSF in equation (10), which is given by  $2\beta$ , dependent on the wave number  $k$ . A fit to  $2\Gamma k^2$  is indicated and the best fit result for the sound attenuation coefficient  $\Gamma$  is given. The extracted FWHM from the underlying DFT-MD simulations are also indicated by black symbols. For clarity each set of curves is shifted by an offset with respect to the lower one. The dotted lines represent the baseline for each set.

using molecular dynamics simulations powered by a neural network trained on Behler-Parrinello symmetry functions. We showed that this procedure can be used to perform simulations with 32 000 atoms and up to 600 000 time steps. Thus this enabled us to extract thermal conductivities of the ions in the hydrodynamic limit and we compared these results with

ionic thermal conductivities computed from a Green-Kubo relation. Reasonable agreement between the two approaches was observed for the considered conditions. We emphasize the importance of using only the ionic heat capacity, as opposed to the total heat capacity, to compute the ionic thermal conductivity from the ionic thermal diffusivity. We demonstrated that additional nonhydrodynamic modes do not contribute in the  $k$  range of interest, by computing a five- and three-mode GCM model and showing that they converge to the same result in the hydrodynamic limit.

The approach presented here for warm dense aluminum can be applied to other single-component materials like iron, water or hydrogen as relevant in geophysics or planetary physics. Based on corresponding simulation results for the dynamic ion-ion structure factor, combining DFT calculations and neural networks, reasonable predictions for the sound velocity, thermal diffusivity or thermal conductivity can be made for matter under extreme conditions. Perspectively, these properties will be probed experimentally using inelastic x-ray scattering (IXS) experiments at free electron laser facilities. High-resolution IXS platforms with meV-monochromators are currently implemented at the European XFEL [33,34] and the LCLS in Stanford [35]. The corresponding spectra can then be compared to, e.g., GCM models as outlined here and, if the resolution of the measured spectra is sufficient, thermal and transport properties can be extracted from the dynamical properties of WDM. Such combined efforts would improve the so far rather scarce data basis for WDM considerably and thereby enable upgraded models for the interior structure and thermal evolution of solar and extrasolar planets.

#### ACKNOWLEDGMENTS

We thank Th. Bornath, S. H. Glenzer, G. Gregori, W. Lorenzen, P. Neumayer, K.-U. Plagemann, T. G. White, and U. Zastrau for helpful discussions and T. G. White for providing data. We thank the anonymous referees for helpful comments. This work was supported by the North German Supercomputing Alliance (HLRN) and the ITMZ of the University of Rostock. We thank the Deutsche Forschungsgemeinschaft (DFG) for support within the Research Unit FOR 2440.

- [1] W. D. Kraeft, D. Kremp, W. Ebeling, and G. Röpke, *Quantum Statistics of Charged Particle Systems* (Akademie-Verlag, Berlin, 1986).
- [2] D. Kremp, M. Schlanges, and W. D. Kraeft, *Quantum Statistics of Nonideal Plasmas* (Springer, Berlin, 2004).
- [3] S. Ichimaru, *Statistical Plasma Physics, Vol. II: Condensed Plasmas* (Addison Wesley, Reading, 1994).
- [4] *Introduction to Computational Methods in many Body Physics*, edited by M. Bonitz and D. Semkat (Rinton Press, Berlin, 2006).
- [5] T. Duffy, N. Madhusudhan, and K. K. M. Lee, in *Treatise on Geophysics*, 2nd ed., edited by G. Schubert (Elsevier, Oxford, 2015), Vol. 2, Chap. 2.07, pp. 149–178.
- [6] Y. Miguel, T. Guillot, and L. Fayon, *Astron. Astrophys.* **596**, A114 (2016).
- [7] R. Helled, G. Mazzola, and R. Redmer, *Nat. Rev. Phys.* **2**, 562 (2020).
- [8] J. J. Fortney, M. Ikoma, N. Nettelmann, T. Guillot, and M. S. Marley, *Astrophys. J.* **729**, 32 (2011).
- [9] J. Leconte and G. Chabrier, *Astron. Astrophys.* **540**, A20 (2012).
- [10] G. Schubert and K. M. Söderlund, *Phys. Earth Planet. Inter.* **187**, 92 (2011).
- [11] J. Wicht, M. French, S. Stellmach, N. Nettelmann, T. Gastine, L. Duarte, and R. Redmer, in *Magnetic Fields in the Solar System*, edited by H. Lüher, J. Wicht, S. A. Gilder, and M. Holschneider (Springer, Cham, 2018), Chap. 2, pp. 7–81.
- [12] F. Graziani, M. P. Desjarlais, R. Redmer, and S. B. Trickey (editors), *Frontiers and Challenges in Warm Dense Matter* (Springer, Cham, 2014).



- [13] J. M. McMahon, M. A. Morales, C. Pierleoni, and D. M. Ceperley, *Rev. Mod. Phys.* **84**, 1607 (2012).
- [14] J. P. Hansen and I. R. McDonald, *Theory of simple liquids*, 3rd ed. (Elsevier Academic Press, London, 2006).
- [15] I. M. de Schepper and E. G. D. Cohen, *Phys. Rev. A* **22**, 287 (1980).
- [16] W. E. Alley and B. J. Alder, *Phys. Rev. A* **27**, 3158 (1983).
- [17] I. Mryglod, *Condens. Matter Phys.* **1**, 753 (1998).
- [18] J. P. Mithen, J. Daligault, and G. Gregori, *Phys. Rev. E* **83**, 015401(R) (2011).
- [19] J. P. Mithen, *Phys. Rev. E* **89**, 013101 (2014).
- [20] B. Cheng and D. Frenkel, *Phys. Rev. Lett.* **125**, 130602 (2020).
- [21] J. P. Hansen, I. R. McDonald, and E. L. Pollock, *Phys. Rev. A* **11**, 1025 (1975).
- [22] I. Morozov, H. Reinholz, G. Röpke, A. Wierling, and G. Zwicknagel, *Phys. Rev. E* **71**, 066408 (2005).
- [23] T. G. White, S. Richardson, B. J. B. Crowley, L. K. Pattison, J. W. O. Harris, and G. Gregori, *Phys. Rev. Lett.* **111**, 175002 (2013).
- [24] H. R. Rüter and R. Redmer, *Phys. Rev. Lett.* **112**, 145007 (2014).
- [25] B. B. L. Witte, M. Shihab, S. H. Glenzer, and R. Redmer, *Phys. Rev. B* **95**, 144105 (2017).
- [26] Q. Zeng, X. Yu, Y. Yao, T. Gao, B. Chen, S. Zhang, D. Kang, H. Wang, and J. Dai, *Phys. Rev. Research* **3**, 033116 (2021).
- [27] L. Harbour, G. D. Förster, M. W. C. Dharma-wardana, and L. J. Lewis, *Phys. Rev. E* **97**, 043210 (2018).
- [28] J. Clérouin, N. Desbiens, V. Dubois, and P. Arnault, *Phys. Rev. E* **94**, 061202(R) (2016).
- [29] T. Morawietz, A. Singraber, C. Dellago, and J. Behler, *Proc. Natl. Acad. Sci. USA* **113**, 8368 (2016).
- [30] A. Singraber, T. Morawietz, J. Behler, and C. Dellago, *J. Chem. Theory Comput.* **15**, 3075 (2019).
- [31] A. Singraber, n2p2 - a neural network potential package, <https://zenodo.org/record/4750573>.
- [32] J. Behler and M. Parrinello, *Phys. Rev. Lett.* **98**, 146401 (2007).
- [33] A. Descamps, B. K. Ofori-Okai, K. Appel, V. Cerantola, A. Comley, J. H. Eggert, L. B. Fletcher, D. O. Gericke, S. Göde, O. Humphries, O. Karnbach, A. Lazicki, R. Loetzsch, D. McGonegle, C. A. J. Palmer, C. Plueckthun, T. R. Preston, R. Redmer, D. G. Senesky, C. Strohm *et al.*, *Sci. Rep.* **10**, 14564 (2020).
- [34] L. Wollenweber, T. R. Preston, A. Descamps, V. Cerantola, A. Comley, J. H. Eggert, L. B. Fletcher, G. Geloni, D. O. Gericke, S. H. Glenzer, S. Göde, J. Hastings, O. S. Humphries, A. Jenei, O. Karnbach, Z. Konopkova, R. Loetzsch, B. Marx-Glowna, E. E. McBride, D. McGonegle *et al.*, *Rev. Sci. Instrum.* **92**, 013101 (2021).
- [35] E. E. McBride, T. G. White, A. Descamps, L. B. Fletcher, K. Appel, F. P. Condamine, C. B. Curry, F. Dallari, S. Funk, E. Galtier, M. Gauthier, S. Goede, J. B. Kim, H. J. Lee, B. K. Ofori-Okai, M. Oliver, A. Rigby, C. Schoenwaelder, P. Sun, T. Tschentscher *et al.*, *Rev. Sci. Instrum.* **89**, 10F104 (2018).
- [36] G. Kresse and J. Hafner, *Phys. Rev. B* **47**, 558 (1993).
- [37] G. Kresse and J. Hafner, *Phys. Rev. B* **49**, 14251 (1994).
- [38] G. Kresse and J. Furthmüller, *Phys. Rev. B* **54**, 11169 (1996).
- [39] N. D. Mermin, *Phys. Rev.* **137**, A1441 (1965).
- [40] J. P. Perdew, K. Burke, and M. Ernzerhof, *Phys. Rev. Lett.* **77**, 3865 (1996).
- [41] P. E. Blöchl, *Phys. Rev. B* **50**, 17953 (1994).
- [42] S. Nosé, *J. Chem. Phys.* **81**, 511 (1984).
- [43] W. G. Hoover, *Phys. Rev. A* **31**, 1695 (1985).
- [44] A. Baldereschi, *Phys. Rev. B* **7**, 5212 (1973).
- [45] G. Kresse and J. Furthmüller, *Comput. Mater. Sci.* **6**, 15 (1996).
- [46] M. Gastegger, L. Schwiedrzik, M. Bittermann, F. Berzsenyi, and P. Marquetand, *J. Chem. Phys.* **148**, 241709 (2018).
- [47] A. P. Thompson, H. M. Aktulga, R. Berger, D. S. Bolintineanu, W. M. Brown, P. S. Crozier, P. J. in 't Veld, A. Kohlmeyer, S. G. Moore, T. D. Nguyen, R. Shan, M. J. Stevens, J. Tranchida, C. Trott, and S. J. Plimpton, *Comput. Phys. Commun.* **271**, 108171 (2022).
- [48] T. Bryk and A. B. Belonoshko, *Phys. Rev. B* **86**, 024202 (2012).
- [49] T. Bryk, *Eur. Phys. J. Spec. Top.* **196**, 65 (2011).
- [50] J.-F. Wax and T. Bryk, *J. Phys.: Condens. Matter* **25**, 325104 (2013).
- [51] P. Virtanen *et al.*, *Nature Methods* **17**, 261 (2020).
- [52] P. D. Welch, *IEEE Trans. Audio Electroacoust.* **15**, 70 (1967).
- [53] Y. Waseda, *The Structure of Non-Crystalline Materials* (McGraw-Hill, New York, 1980).
- [54] T. Scopigno, U. Balucani, G. Ruocco, and F. Sette, *Phys. Rev. E* **63**, 011210 (2000).
- [55] M. M. G. Alemany, L. J. Gallego, and D. J. González, *Phys. Rev. B* **70**, 134206 (2004).
- [56] P. G. De Gennes, *Physica* **25**, 825 (1959).
- [57] S. Blairs, *Int. Mater. Rev.* **52**, 321 (2007).
- [58] J. Schnakenberg, *Thermodynamik und Statistische Physik*, 1st ed. (Wiley, Hoboken, NJ, 1998).
- [59] I. Mryglod, I. Omelyan, and M. Tokarchuk, *Mol. Phys.* **84**, 235 (1995).
- [60] M. French, *New J. Phys.* **21**, 023007 (2019).
- [61] M. Leitner, T. Leitner, A. Schmon, K. Aziz, and G. Pottlacher, *Metall. Mater. Trans. A* **48**, 3036 (2017).

## 4.2 *Ab initio* study of shock-compressed copper

### Author contributions

#### **M. Schörner**

Preparation of the manuscript, DFT-MD simulations, training of NN potentials and NN-MD simulations, interpretation

#### **B.B.L. Witte**

Supervision of the project, preparation of the manuscript

#### **A.D. Baczewski**

Preparation of the manuscript, interpretation of the simulations

#### **A. Cangi**

Preparation of the manuscript, LR-TDDFT simulations, and interpretation

#### **R. Redmer**

Supervision of the project, preparation of the manuscript

***Ab initio* study of shock-compressed copper**Maximilian Schörner<sup>1</sup>,<sup>1</sup> Bastian B. L. Witte,<sup>1</sup> Andrew D. Baczewski<sup>2</sup>,<sup>2</sup> Attila Cangi<sup>3</sup>,<sup>3</sup> and Ronald Redmer<sup>1</sup><sup>1</sup>University of Rostock, Institute of Physics, D-18051 Rostock, Germany<sup>2</sup>Center for Computing Research, Sandia National Laboratories, Albuquerque, New Mexico 87185, USA<sup>3</sup>Center for Advanced Systems Understanding (CASUS), Helmholtz-Zentrum Dresden-Rossendorf, D-02826 Görlitz, Germany

(Received 13 May 2022; revised 8 July 2022; accepted 26 July 2022; published 11 August 2022)

We investigate shock-compressed copper in the warm dense matter regime by means of density functional theory molecular dynamics simulations. We use neural-network-driven interatomic potentials to increase the size of the simulation box and extract thermodynamic properties in the hydrodynamic limit. We show the agreement of our simulation results with experimental data for solid copper at ambient conditions and liquid copper near the melting point under ambient pressure. Furthermore, a thorough analysis of the dynamic ion-ion structure factor in shock-compressed copper is performed and the adiabatic speed of sound is extracted and compared with experimental data.

DOI: [10.1103/PhysRevB.106.054304](https://doi.org/10.1103/PhysRevB.106.054304)**I. INTRODUCTION**

Understanding matter in extreme conditions is challenging. Especially warm dense matter (WDM), which is characterized by temperatures above a few electronvolt (eV) and solid densities exhibits non-negligible degeneracy and strong correlations that must be treated in a quantum mechanical many-body framework [1,2]. Experimentally, due to their high energy density, these states can only be created transiently, and therefore, must be probed on short time scales using intense short-wavelength radiation. Shock-compression experiments are among the premier ways extreme conditions can be reached in the laboratory. They have been used to study the high-pressure phase diagram of various geological materials [3], metals like silver, gold and platinum [4–6], iron at super-Earth conditions [7], and hydrocarbons [8–10], even revealing novel phenomena like the formation of diamonds in the interior of Neptune [11]. In shock and ramp compression studies, copper itself is often used as a resistivity gauge [12], and its behavior under extreme conditions has been the target of several theoretical and experimental studies over the past decades. The conductivity of expanded liquid copper has been studied in rapid wire evaporation experiments [13] and isochoric heating experiments using a closed vessel apparatus [14], while the effects of femtosecond irradiation has been studied using first-principles calculations [15]. Melting curves over a wide pressure range have been predicted theoretically and measured [16–20]. Recently, Baty *et al.* [21] have used *ab initio* simulations to study the melting line of copper up to pressures relevant for shock compression, while accounting for the experimentally and theoretically predicted metastable bcc phase [22–25]. Furthermore, a plethora of shock wave measurements in the Mbar regime are available, although the uncertainties for measurements beyond 5 Mbar increase significantly. Notoriously, it is challenging to extract reliable information on structural or transport properties at these extreme conditions. However, with novel improvements to the

spectral resolution at high-brilliance x-ray free electron laser facilities, it is now becoming possible to measure the ion dynamics of transient WDM states through inelastic x-ray scattering [26–28], as well as structural changes via x-ray diffraction [8–10]. While a lot of theoretical work regarding copper has been performed on phase transitions and the energy transfer from the electrons to ions, we focus, here, on the ion dynamics that can be accessed in scattering experiments.

The dynamic structure factor (DSF) is vital for accurately describing the dynamics of matter under extreme conditions. There has been a lot of work on the DSF in the context of molecular dynamics (MD) simulations, ranging from the direct observation from ion trajectories [29,30] to fits to analytical expressions [31–33]. Large-scale classical simulations have been employed to reach the hydrodynamic regime [34–36] and to study structural properties and propagation in glasses and disordered solids via the dispersion of the longitudinal and transverse DSF [37–39]. Furthermore, MD simulations have been coupled to density functional theory [40,41] (DFT-MD) to reach *ab initio* accuracy in the description of the DSF [42]. This allows us to probe the ion dynamics of dynamically compressed targets, requiring sophisticated many-body simulations, that take into account the quantum mechanical nature of WDM states, to compare with the experimental observations. These DFT-MD simulations have proven successful at describing the principal shock Hugoniot [43–45] and the ion-ion DSF of various materials [46–49]. Recently, the use of neural network potentials has emerged, combining the benefits of the large-scale classical simulations with the *ab initio* accuracy of the forces in DFT. Several studies have shown the application of this technique to the DSF [36,50,51] and studied the extent of the hydrodynamic regime and the accessibility of various transport and thermodynamic properties.

Here, we apply these state-of-the-art methods to shock-compressed copper at experimentally reachable conditions and we make predictions for experimentally observable

quantities like the static and dynamic ion-ion structure factor. First, we benchmark our results against experimental results for solid and liquid copper, and then compute the principal Hugoniot curve and study the change of the ion dynamics. A brief summary of the relevant equations and the details of the simulation methods are given in Sec. II. In Sec. III, we determine the phonon spectrum of solid copper at ambient conditions from the ion-ion DSF and compute the dynamic electrical conductivity. For liquid copper at ambient pressure near the melting point, we compute the static and dynamic structure factor and compare to experimental results, see Sec. IV. Subsequently, we compute the principal Hugoniot curve in Sec. V and compare to shock compression experiments, and experimental and theoretical predictions for the melting line. Finally, in Sec. VI, we study the evolution of the static and dynamic ion-ion structure factor during shock compression and extract the adiabatic speed of sound, which we compare to recent measurements by McCoy *et al.* [52].

## II. THEORETICAL METHOD

Through DFT-MD simulations, we gain access to the time-dependent ion positions  $\vec{r}_i(t)$  and velocities  $\vec{v}_i(t)$ . By virtue of the Wiener-Khinchin theorem [53,54], the dynamic ion-ion structure factor

$$S_{ii}(\vec{k}, \omega) = \frac{1}{2\pi N} \int_{-\infty}^{\infty} dt \langle n_{\vec{k}}(\tau) n_{-\vec{k}}(\tau + t) \rangle_{\tau} e^{i\omega t}, \quad (1)$$

which contains all information on the dynamics of the ion system, can be defined. Here  $N$  is the number of ions in the system,  $\vec{k}$  is the wave vector,  $\omega$  is the frequency, and the spatial Fourier component of the ion density  $n(\vec{r}, t)$  is given as

$$n_{\vec{k}}(t) = \int_{\mathbb{R}^3} d^3r n(\vec{r}, t) e^{i\vec{k}\cdot\vec{r}} = \sum_{i=1}^N e^{i\vec{k}\cdot\vec{r}_i(t)}, \quad (2)$$

$$n(\vec{r}, t) = \sum_{i=1}^N \delta^3(\vec{r} - \vec{r}_i(t)), \quad (3)$$

with the time-dependent ion positions  $\vec{r}_i(t)$ . In Eq. (1),  $\tau$  denotes an absolute time relative to the time delay  $t$ . The ensemble average, denoted by subscript  $\tau$ , is taken to be the sample average for independent configurations with different values of  $\tau$  but the same value of  $t$ .

According to the hydrodynamic model [33], the dispersion of the collective side peak of  $S_{ii}(\vec{k}, \omega)$ , called the sound mode in the hydrodynamic limit, is connected to the adiabatic speed of sound  $c_s$  via

$$\omega_{\text{sound}}(\vec{k}) = c_s |\vec{k}|. \quad (4)$$

The position of the sound mode  $\omega_{\text{sound}}$  can be extracted from the DSF via a fitting scheme (for details, see Refs. [46,47,51]).

The dispersion of the longitudinal current-current correlation spectrum  $J(\vec{k}, \omega)$ , which is closely related to the DSF via

$$J(\vec{k}, \omega) = \frac{\omega^2}{k^2} S_{ii}(\vec{k}, \omega), \quad (5)$$

defines the apparent sound speed  $c_1$ .

The long-wavelength limit of the static ion-ion structure factor, which is defined as the frequency integrated ion-ion

DSF  $S_{ii}(k) = \int_{-\infty}^{\infty} S_{ii}(k, \omega) d\omega$ , can also be determined from

$$\lim_{k \rightarrow 0} S_{ii}(k) = \kappa_T n_i k_B T \quad (6)$$

via thermodynamic relations [55]. Here,  $n_i$  is the ion density,  $T$  is the temperature and  $\kappa_T$  is the isothermal compressibility which is also accessible via the thermodynamic relation

$$\kappa_T = -\frac{1}{V} \left( \frac{\partial V}{\partial P} \right)_T, \quad (7)$$

where  $V$  is the volume of the simulation box and  $P$  is the pressure.

In order to analyze shock compression experiments, we employ the Hugoniot equation [56–59]

$$\epsilon_1 - \epsilon_0 = \frac{1}{2} (P_1 + P_0) (V_0 - V_1), \quad (8)$$

$$\epsilon_a = \frac{E_a}{m_a}, \quad a = 0, 1, \quad (9)$$

which can be derived from the conservation of energy  $E$ , momentum  $p$ , and mass  $m$  at a propagating shock front. Here, the subscript 0 indicates the conditions of the unshocked material while subscript 1 indicates the conditions of the shocked material.

The DFT-MD simulations in this work were performed within the Vienna *ab initio* Simulation Package (VASP) [60–62]. The electron density at each time step is computed according to the finite-temperature DFT approach [63], using the generalized gradient approximation of Perdew, Burke and Ernzerhof (PBE) [64] for the exchange correlation functional (XC functional). The MD is carried out using the Born-Oppenheimer approximation by solving Newton's equations of motion for the ion positions. The forces are determined by the electronic charge density, where the electrons always remain in an instantaneous, thermal equilibrium defined by the ion positions.

Within VASP the Kohn-Sham orbitals are expanded in a plane wave basis set up to a cutoff energy  $E_{\text{cut}}$ , which we set at 800 eV. For the ion potential of copper a projector augmented-wave potential [65] is used (PAW PBE Cu GW 19May2006), which treats the outer 11 electrons explicitly in the DFT framework, with the remaining electrons frozen in the core. For temperature control, the algorithm of Nosé-Hoover [66,67] is used with a mass parameter corresponding to a temperature oscillation period of 40 time steps. To allow for melting and freezing along the principal Hugoniot curve, the simulation box for copper is spanned by lattice vectors of the face-centered cubic (fcc) structure. For the simulations at ambient pressure, 125 copper atoms were used, while for all conditions along the Hugoniot curve 64 copper atoms were placed in the simulation box. The sampling of the Brillouin zone was carried out at the Baldereschi mean-value point [68] for all DFT-MD simulations. For the conductivity calculations, at least ten uncorrelated snapshots are taken from the DFT-MD simulation and reevaluated using a more accurate energy convergence criterion and a 2 x 2 x 2 Monkhorst-Pack grid [69]. Additionally, these snapshots were evaluated using the hybrid XC functional of Heyd, Scuseria and Ernzerhof (HSE) [70,71]. For these calculations, however, only the Baldereschi mean-value point was considered due to the

higher computational demand of HSE calculations. The electrical conductivity is computed from these simulations via the Kubo-Greenwood formula [72,73], using the eigenstates and eigenenergies of the Kohn-Sham orbitals (for details, see Ref. [74]). We employ a complex shift of 0.1 in the Kramers-Kronig transformation. We have carefully checked the convergence of our results with regard to plane wave energy cutoff, length of the time step, number of particles and Brillouin zone sampling. Additionally, we compute electronic transport properties using time-dependent DFT (TD-DFT) in the linear response regime [75], which is based on the linear density-density response of the electronic system to an external, time-dependent perturbation.

Furthermore, we train high-dimensional neural network (NN) interatomic potentials to reproduce the DFT forces and energies, enabling us to perform neural-network-driven molecular dynamics (NN-MD) simulations with up to 32 000 copper atoms. Separate neural network potentials are trained for each condition due to the large temperature range covered in this study. Each neural network is trained on at least 4000 configurations randomly sampled from DFT-MD simulations that span at least 40 000 time steps. These simulations include a long (at least 20 000 time steps) simulation at the desired conditions and shorter (at least 5000 time steps) simulations at slightly higher and lower density and temperature than the considered conditions. The higher particle number improves the resolution of the phonon dispersion in the solid due to the larger number of available wave vectors, and it enables access to the hydrodynamic limit in the liquid regime. We use the implementation in the n2p2 software package [76–78], which employs Behler-Parrinello symmetry functions to describe the environment of each copper atom and subsequently passes these symmetry functions to the input layer of the neural network. A Kalman filter is used to adjust the weights and biases of the neural network during training. We use two hidden layers with 40 nodes each, and set the cutoff radius between 6 Å at ambient conditions and 4 Å at the highest pressure condition along the Hugoniot. The environment of each atom is described by 13 radial symmetry functions and 12 narrow angular symmetry functions chosen according to the scheme described in Ref. [79]. The remaining parameters are set to their default values. The trained potential is subsequently used in conjunction with the LAMMPS molecular dynamics simulation code [80] to produce the MD simulations. The temperature in the NN-MD simulations is also controlled using a Nosé-Hoover thermostat.

### III. RESULTS FOR SOLID COPPER AT AMBIENT CONDITIONS

First, we test our simulations against known results for ambient solid copper at the density  $\rho = 8.94 \text{ g/cm}^3$  and temperature  $T = 303 \text{ K}$ . While the DSF described in Eq. (1) can be averaged over all wave vectors with equal magnitude in liquid and warm dense copper, the orientation of  $\vec{k}$  relative to the crystallographic axes is relevant in the solid phase. In Fig. 1, we show the phonon dispersion of solid copper at ambient conditions along a high-symmetry path through the first Brillouin zone. The phonon positions are determined from the transverse and longitudinal current-current correlation spec-

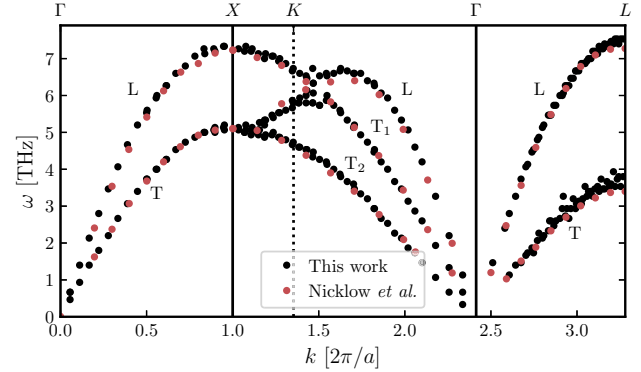


FIG. 1. The phonon dispersion of solid copper at  $\rho = 8.94 \text{ g/cm}^3$  and  $T = 303 \text{ K}$  extracted from the longitudinal and transverse current-current correlation spectrum. The  $x$  axis is scaled by the lattice constant  $a$  of ambient copper. Experimental data from Nicklow *et al.* is given as a reference [82].

trum  $J_i(k, \omega)$  and  $J_1(k, \omega)$  (see Ref. [51] for details) of the NN-MD simulations by the peak finding routine *find\_peaks* implemented in the SciPy library for scientific computing in python [81]. This analysis of phonon modes is fully dynamic and does not require a harmonic or quasiharmonic oscillator model.

The observed agreement with experimental data by Nicklow *et al.* [82] is very good, indicating that the lattice dynamics in solid copper are well described by our simulations. We show an example of the transverse and longitudinal current-current correlation spectrum along the high-symmetry path  $\Gamma - K - X$  in Fig. 2. The contributions due to longitudinal density oscillations are colored green and the correlation spectrum of transverse currents is colored red.

Furthermore, we investigate the dynamic electrical conductivity using the Kubo-Greenwood formula [72,73]. Results for PBE and HSE calculations are shown in Fig. 3 compared to an experimental result by Henke *et al.* [83] and predictions from TD-DFT linear response calculations. Experimentally, Henke *et al.* measured the absorption coefficient  $\alpha(\omega)$  of

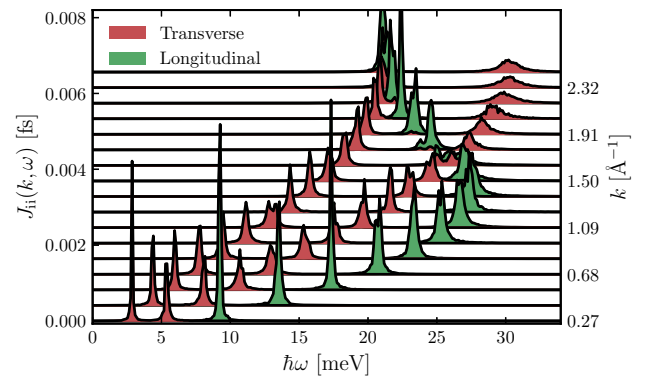


FIG. 2. The current-current correlation spectrum of solid copper at  $\rho = 8.94 \text{ g/cm}^3$  and  $T = 303 \text{ K}$  along the high-symmetry path  $\Gamma - K - X$ . The transverse part is colored red, while the longitudinal part is colored green.



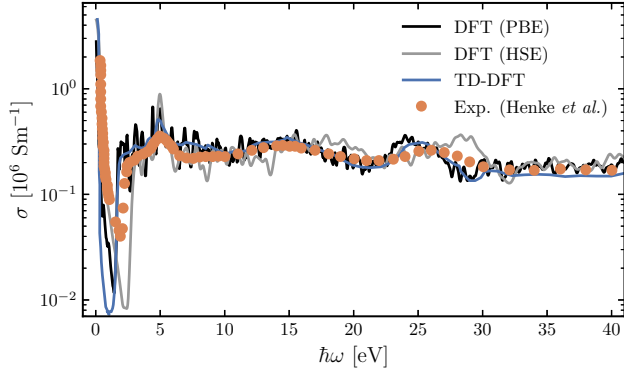


FIG. 3. Dynamic electrical conductivity of solid copper at ambient conditions computed from a DFT simulation with 125 atoms using the Kubo-Greenwood formula and results of TD-DFT linear response calculations with four atoms and the adiabatic local density approximation. The black line indicates results achieved with the PBE XC functional, while the grey line represents results using the HSE XC functional. Measurements of Henke *et al.* [83] are given as reference.

ambient copper which can be translated to the real part of the dynamic electrical conductivity by Kramers-Kronig relations. We also compute the dynamic electrical conductivity using linear response TD-DFT. Here, we compute the density-density response function due to an external perturbation potential within a simulation cell containing four atoms. The effect of electron-electron interactions is incorporated using the random-phase approximation, which accounts for local-field effects from the Coulomb interaction but neglects exchange-correlation. From the response function, transport properties, such as the electrical conductivity or the DSF, are extracted by aid of the fluctuation-dissipation theorem. TD-DFT has been used to compute XRTS spectra using both the real-time [84] and linear response formalisms [85]. The agreement in Fig. 3 is good, while the theoretical models predict a significantly lower conductivity at  $\approx 2$  eV. Also, the measurements are lower than the theory predictions at  $\approx 7$  eV and the feature at  $\approx 25$  eV, which is observed by theory and experiment, occurs at lower frequencies in the simulations. This shift corresponds to shifted energy states relative to the continuum of states. The DFT-MD simulation predicts the energy states responsible for the observed feature at higher energies than the experiment indicates. This underestimation of energy gaps is a well known problem of DFT with commonly used XC functionals like PBE [64]. Better agreement with experimental observations can be achieved using the hybrid functional HSE [70,71] as shown, e.g., for aluminum [86]. However, in this case, the HSE calculations overestimate the position of the feature, shifting it to  $\approx 28$  eV.

#### IV. RESULTS FOR LIQUID COPPER AT AMBIENT PRESSURE

As another test of the method we perform simulations of liquid copper at  $\rho = 7.69$  g/cm<sup>3</sup> and  $T = 1773$  K in order to compare to experimental data by Waseda and Ohtani [87] who performed x-ray diffraction experiments at these conditions.

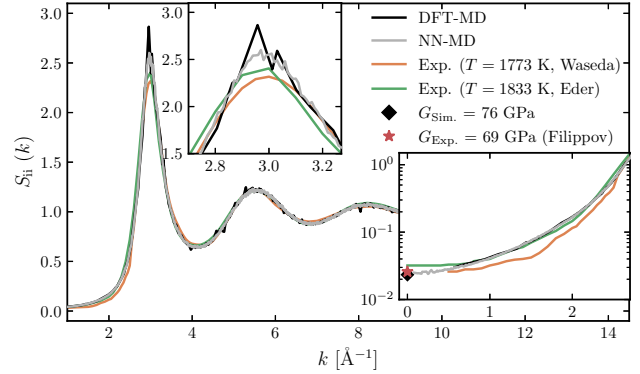


FIG. 4. Static structure factor of liquid copper at  $\rho = 7.69$  g/cm<sup>3</sup> and  $T = 1773$  K computed from a DFT-MD simulation with 125 atoms and a NN-MD simulation with 32 000 atoms. Two experimental results from x-ray diffraction (Waseda and Ohtani [87]) and neutron diffraction (Eder *et al.* [88]) are shown as reference. The right inset zooms in on the long-wavelength behavior and shows the  $k \rightarrow 0$  prediction by DFT-MD and an experimental result of liquid copper near the melting point by Filippov [91]. The top inset zooms in on the behavior around the first correlation peak.

We additionally compare to neutron diffraction data by Eder *et al.* [88]. The atomic form factor must be regarded if the ion dynamics are to be extracted from x-ray scattering. Waseda and Ohtani used form factors computed from relativistic Dirac-Slater wave functions [89] with anomalous dispersion corrections [90], while for neutron diffraction merely the multiple scattering in the sample must be accounted for [88]. Figure 4 shows static ion structure factors calculated from a DFT-MD simulation with 125 atoms and a NN-MD simulation with 32 000 atoms.

The static structure factors inferred from Waseda and Ohtani ( $T = 1773$  K) and from the diffraction experiments of Eder *et al.* ( $T = 1833$  K) are displayed for comparison. The general agreement is good while there are noticeable differences in the first correlation peak at around  $3 \text{ \AA}^{-1}$  and for the low- $k$  limit, displayed in the insets of Fig. 4. The first correlation peak is characterized by the length scale at which the minimum of the interatomic potential occurs. Here, longer simulations lead to better statistics, which better resolves the dynamics in this area, leading to a lowering of the peaks. Additionally, smaller simulation boxes artificially enhance the near-field order that is induced by the minimum of the interatomic potential. Experimentally, it is influenced by the angular resolution of the detector and spectral width of the light/neutron source. Remarkably, the first correlation peak of Eder *et al.* lies higher than that of Waseda and Ohtani, although higher temperatures generally lead to diminishing correlations, corresponding to a lower correlation peak.

The low- $k$  limit is of interest because the value for  $k \rightarrow 0$  can be determined by the isothermal compressibility via Eq. (6) which is accessible through DFT-MD simulations via Eq. (7). We perform additional simulations at 5% higher and lower densities in order to evaluate the derivative. The limit determined this way is indicated by the black diamond in the inset, while the violet asterisk is determined from inserting an experimental compressibility (inferred from the speed of



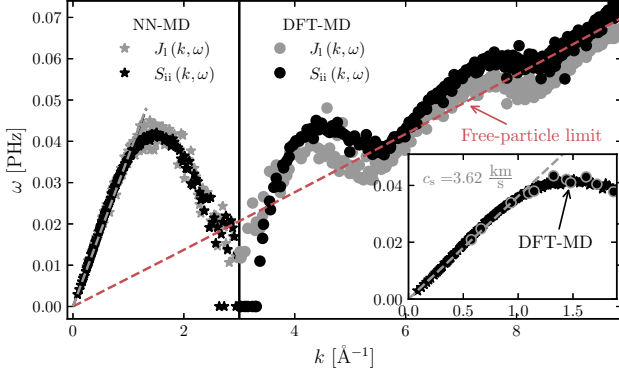


FIG. 5. Peak position of the ion acoustic mode taken from the DSF and from the longitudinal current-current correlation  $J_1(k, \omega)$  [see Eq. (5)] dependent on the  $k$  value. For wave numbers below the first correlation peak results from the NN-MD simulation are shown, while all other results are taken from the DFT-MD simulation. A best linear fit for the low  $k$  limit of the ion acoustic mode of the DSF is indicated and the corresponding adiabatic speed of sound is presented. The inset shows a comparison between DFT-MD and NN-MD results for small  $k$ .

sound) [91] into Eq. (6). Eder *et al.* artificially extended their structure factor for  $k$  values smaller than  $0.5 \text{ \AA}^{-1}$  to match the value computed from the compressibility near the melting point by Filippov *et al.* [91], also used for the violet asterisk, and a density determined by Cahill and Kirshenbaum [92]. It approaches a higher value than the two indicated limits due to the higher temperature of the experiment [see Eq. (6)]. The DFT-MD simulation with 125 atoms allows access to  $k$  values down to  $0.57 \text{ \AA}^{-1}$ , which indicates that the trend of  $S_{ii}(k)$  agrees qualitatively with the known limit at  $k \rightarrow 0$ , while no definite conclusion on the agreement can be made without further investigation with more atoms. With the larger NN-MD simulations, it is apparent that  $S_{ii}(k)$  also agrees quantitatively with the limit computed through (6). For wave vectors  $k$  between  $0.8 \text{ \AA}^{-1}$  and  $2.5 \text{ \AA}^{-1}$ , observations differ between Eder *et al.* and Waseda and Ohtani. The DFT-MD simulations agree well with the former while the latter is significantly lower in that region (see inset in the lower right corner of Fig. 4). A reason for this difference could be the form factor which must be additionally considered for x-ray diffraction experiments.

Furthermore, we compute the DSF  $S_{ii}(k, \omega)$  and the closely related longitudinal current-current correlation spectrum  $J_1(k, \omega)$ . We extract various properties of the different contributing modes by fitting to a generalized collective modes approach [93,94] with one diffusive and one propagating mode, see Ref. [51] for details. Figure 5 shows the peak positions of the ion acoustic mode extracted from the DSF as a function of the wave vector  $k$ . This can be considered as the dispersion relation of the ion acoustic mode. Also shown in this figure are the peak positions of the longitudinal current correlation given by Eq. (5) which describes collective excitations via currents [95] and determines the apparent speed of sound  $c_1$  [96]. The DSF, on the other hand, can be used to extract the adiabatic speed of sound  $c_s$  in the hydrodynamic

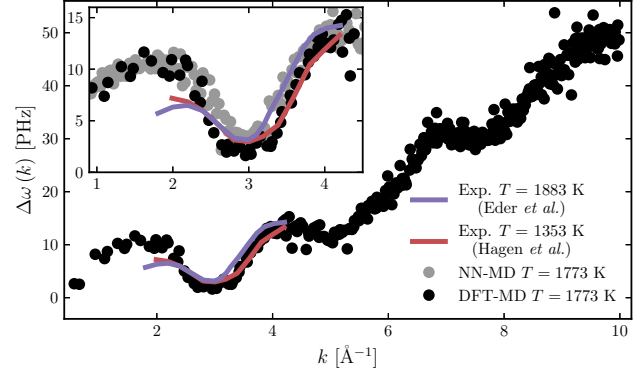


FIG. 6. Peak width of the thermal mode of the ion-ion DSF dependent on the  $k$  value. Experimental results from Hagen *et al.* [98] and data calculated from experimentally determined static ion structure factors by Eder *et al.* [88] are given as comparison. The inset shows a comparison between the results of the DFT-MD (125 atoms) and NN-MD (32 000 atoms) simulations in the region where experimental data is available.

limit [33]. Both of these quantities are indicated in Fig. 5, as well as the free-particle limit of a noninteracting classical system. In this limit, the peak position of  $J_1$  is determined by the noncollective mode which is described by

$$\omega_J(\vec{k}) = \sqrt{\frac{2}{m_i \beta}} |\vec{k}|, \quad (10)$$

see Ref. [97]. The different physical regimes that correspond to low- and high- $k$  values were discussed in detail recently in Ref. [51] for warm dense aluminum. As the ions behave like free particles in the high- $k$  limit, their dispersion is described by the free-particle limit, as can be seen from Fig. 5.

Another feature that can be extracted from the DSF is the width of the diffusive thermal mode represented in Fig. 6. It corresponds to the random thermal movement of the ions and its shape is connected to how much energy can be coupled to this mode. The wider the peak, the higher the energy transfer to an individual ion can be. The magnitude of the peak is determined by the static structure factor which accounts for how many ions are present on the length scale defined by  $k$ . Therefore, the width and the height of the peak determine the energy that can be transferred to the thermal mode. In Fig. 6, the widths for DFT-MD simulations with 125 atoms and NN-MD simulations with 32 000 atoms are shown and compared to an experimental result from inelastic neutron scattering by Hagen *et al.* [98] and a result inferred from neutron scattering by Eder *et al.* [88]. While the former represents a direct measurement, the results by Eder *et al.* are calculated from the static structure factor in Fig. 4. They use a simple model [99] with one free parameter to artificially introduce the dynamics. The *ab initio* DFT-MD approach describes the dynamics in a more consistent way than the model chosen by Eder *et al.* Since their static structure factor agreed well with DFT-MD simulations (see Fig. 4), the observed deviations are attributed to the artificially introduced dynamics.

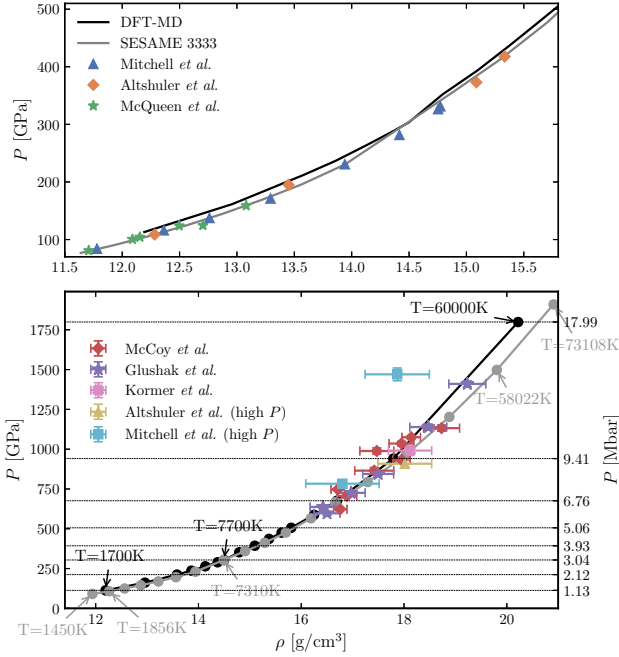


FIG. 7. Lower panel: Hugoniot curve for copper in the  $P$ - $\rho$  plane inferred from isotherms calculated using DFT-MD (black) and isotherms from the SESAME 3333 table [100] (grey). The temperatures for some data points are annotated. High pressure experimental values by McCoy *et al.* [52], Glushak *et al.* [101], Kormer *et al.* [102], Altschuler *et al.* [103], and Mitchell *et al.* [104] are shown. The dotted horizontal lines indicate the conditions we choose for further investigation. More information on the conditions is given in Table I. Upper panel: Zoomed in view of the low pressure range, where experimental data by Mitchell *et al.* [105], Altschuler *et al.* [106], and McQueen *et al.* [107] are shown.

## V. THE PRINCIPAL HUGONIOT CURVE

The Hugoniot equation (8) is dependent on pressure  $P$ , density  $\rho$ , and specific internal energy  $\epsilon$ . For a given temperature, the equation of state (EOS) defines the values for  $P$ ,  $\rho$ , and  $\epsilon$  that satisfy the Hugoniot equation. We compute 16 isotherms ranging from 1700 K upto 60 000 K, with four to five different densities per isotherm.

The pressure and internal energy are interpolated using cubic splines, and Eq. (8) is solved numerically to give the principal Hugoniot curve depicted in Fig. 7. The EOS data along the principal Hugoniot curve is listed in Table I. As a comparison, we compute the principal Hugoniot curve from the standard SESAME 3333 EOS table [100]. Figure 7 illustrates the results obtained from DFT-MD isotherms and from SESAME isotherms in the pressure-density plane. Experimentally, the Hugoniot curve of copper in the pressure-density plane has been constrained well for pressures up to 4 Mbar (see Fig. 7). For higher pressures, the spread of experimental results is significantly larger [52] and experimental uncertainties increase.

The SESAME EOS predicts consistently higher temperatures during the compression process. While the temperature difference at  $\approx 1$  Mbar at roughly similar conditions is  $\approx 150$  K, the difference becomes  $\approx 3200$  K around 6.7 Mbar.

TABLE I. Conditions for compressed copper predicted from DFT-MD isotherms.

$P$ (GPa)	$T$ (K)	$\rho$ (g/cm <sup>3</sup> )	$u$ (kJ/g)
113	1700	12.193	-3.9774
162	3000	12.959	-2.8628
212	4600	13.583	-1.6052
237	5400	13.862	-0.9597
264	6300	14.134	-0.2339
289	7200	14.373	0.4534
304	7700	14.499	0.8458
352	8200	14.793	2.1275
393	9500	15.095	3.3089
436	10900	15.373	4.5471
476	12400	15.617	5.7083
506	13500	15.805	6.6302
586	16600	16.249	9.1182
676	20000	16.694	11.8969
941	30000	17.792	20.5124
1799	60000	20.220	50.4514

While the deviation in the pressure-density plane is small and difficult to assess experimentally, the temperature difference is significant and could be used to test the respective EOS. The agreement in Fig. 7 is best between 2.5 and 3.5 Mbar which is the region in which both EOS predict the melting point as can be seen in Fig. 8.

Experimental results by Mitchell *et al.* [105], Altschuler *et al.* [106], and McQueen *et al.* [107] are indicated in the upper panel of Fig. 7 and show better agreement with the SESAME data while the DFT-MD Hugoniot lies slightly higher in the pressure-density-plane. The lower panel of Fig. 7 shows the available high-pressure Hugoniot compression data by McCoy *et al.* [52], Glushak *et al.* [101], Kormer *et al.* [102], Altschuler *et al.* [103], and Mitchell *et al.* [104]. In this regime,

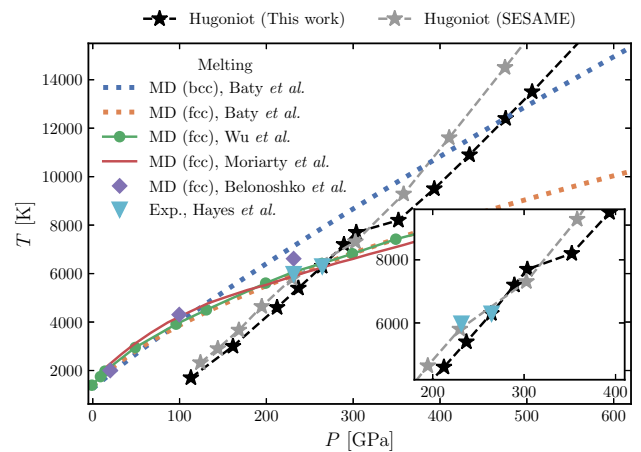


FIG. 8. Hugoniot curve for copper in the  $T$ - $P$ -plane inferred from isotherms calculated using DFT-MD (black) and isotherms from the SESAME 3333 table (grey). Melting lines determined by Wu *et al.* [18], Moriarty *et al.* [19], and Belonoshko *et al.* [20] using different variations of MD simulations as well as experimental results by Hayes *et al.* [17] are indicated.

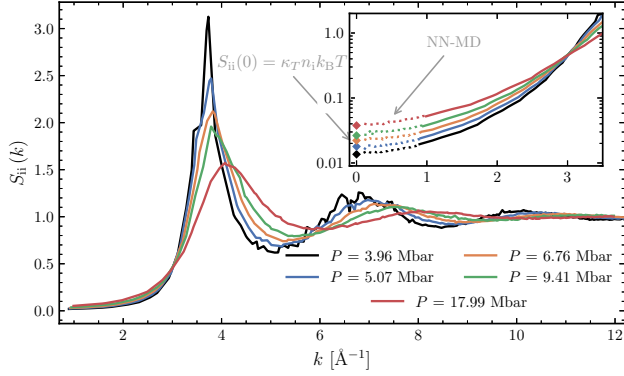


FIG. 9. DFT-MD results of the static structure factor of liquid copper along the Hugoniot curve. In the inset the low  $k$  behavior is shown on a log scale and the NN-MD results are shown for wave numbers that are not accessible to the DFT-MD results. The limits for  $k \rightarrow 0$  are also indicated [see Eq. (6)]. Further information on the conditions is given in Fig. 7 and Table I.

both EOS studied here are compatible with the experimental data due to their large experimental uncertainties. The only exception is the high-pressure point by Mitchell *et al.* around 1500 GPa, which agrees with neither of the theoretical predictions.

In the temperature-pressure plane, the melting point along the Hugoniot is easily identifiable by a kink which is due to the latent heat needed for the phase transition. From the inset in Fig. 8, the melting point as predicted by SESAME lies between 2.3 and 3 Mbar, and the melting point predicted by DFT-MD calculations lies between 3 and 3.5 Mbar. While the MD simulations by Wu *et al.* [18] and Moriarty *et al.* [19], as well as experiments by Hayes *et al.* [17] agree roughly with the SESAME results, the two-phase MD simulations by Belonoshko *et al.* [20] display a trend that tends towards the melting point predicted by DFT-MD simulations. However, their calculations did not cover the pressure range in question. A recent study by Baty *et al.* [21] considers the melting line for the fcc structure of copper, as well as the melting line of the experimentally observed bcc phase, which lies above the fcc melting point along the Hugoniot. For the subsequent examination of the material along the principal Hugoniot curve, the conditions indicated by horizontal dashed lines in the upper panel of Fig. 7 were used to perform extended simulations.

## VI. ION DYNAMICS OF SHOCK-COMPRESSED COPPER

The static ion structure factors in the liquid phase are displayed in Fig. 9. The correlation peaks exhibit a shift to higher- $k$  values for increasing density. Shifts for constant pressure differences along the Hugoniot are expected to become smaller, as the density  $\rho$  is a convex function of the pressure  $P$  (as seen in Fig. 7). A smoothing and lowering of the correlation peaks is also observable due to the lowering of the coupling parameter, caused by a combination of higher temperatures, higher densities and ionization. The limits for  $k \rightarrow 0$  are also indicated by diamonds in the inset of Fig. 9. The limits are computed via the compressibility using Eqs. (7)

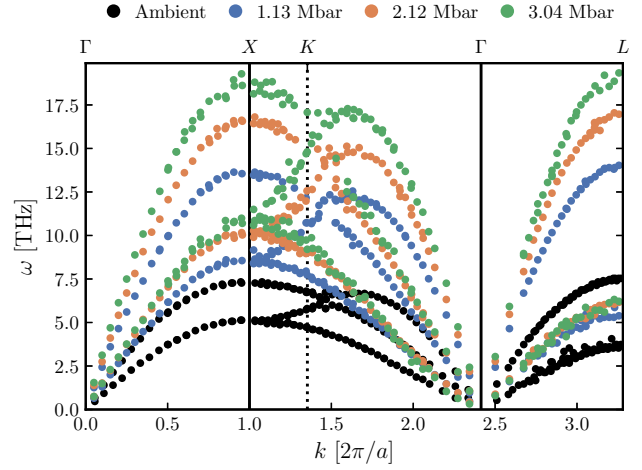


FIG. 10. Phonon dispersion of solid copper along the principal Hugoniot curve along high-symmetry direction in the Brillouin zone. The  $x$  axis is normalized by the lattice constant  $a$  to make the results at different densities comparable. Further information on the conditions is given in Fig. 7 and Table I.

and (6), analogous to Sec. IV. The lowest wave number available through the DFT-MD simulations is  $0.9 \text{ \AA}^{-1}$ , observed for the lowest density at  $15.095 \text{ g/cm}^3$ , due to the small simulation boxes with 64 atoms.

In order to test the computed limits, we perform NN-MD simulations with 32 000 atoms, enabling access to wave numbers down to  $0.1 \text{ \AA}^{-1}$ . The static structure factor at the additionally accessible wave numbers is given by the dashed lines in the inset of Fig. 9, demonstrating good agreement with the DFT-MD data and the thermodynamically determined limit. The determined compressibilities will be used to compute the adiabatic speed of sound in the following.

We study three points along the principal Hugoniot curve, where we expect solid conditions of copper according to Fig. 7 and Fig. 8. The phonon dispersion of copper for ambient conditions and the Hugoniot conditions at 1.13, 2.12, and 3.04 Mbar are shown in Fig. 10. While we only show the peak position here, a systematic broadening of the phonon modes is also observed, as expected due to the increasing temperature. Furthermore, a systematic hardening for most of the phonon branches and orientations can be observed. Along the  $\Gamma - L$  direction, we observe a strong hardening of the longitudinal mode, while the transverse branch hardens significantly less than along the other shown orientations.

Once the copper melts, the effect of further compression on the ion acoustic mode can be investigated. Figure 11 shows the change of the dynamic ion structure factor at different  $k$  values along the Hugoniot computed from the NN-MD simulations.

Since the simulations are performed at different densities, but with the same number of atoms, the size of the simulation box varies which leads to slightly different  $k$  values in each case. However, the large-scale NN-MD simulations with 32 000 atoms permit access to a dense  $k$  grid in the considered range. Therefore, the  $k$  values at all conditions are within 1% of the numbers given in Fig. 11. A similar study on aluminum [51] has shown that increased temperature

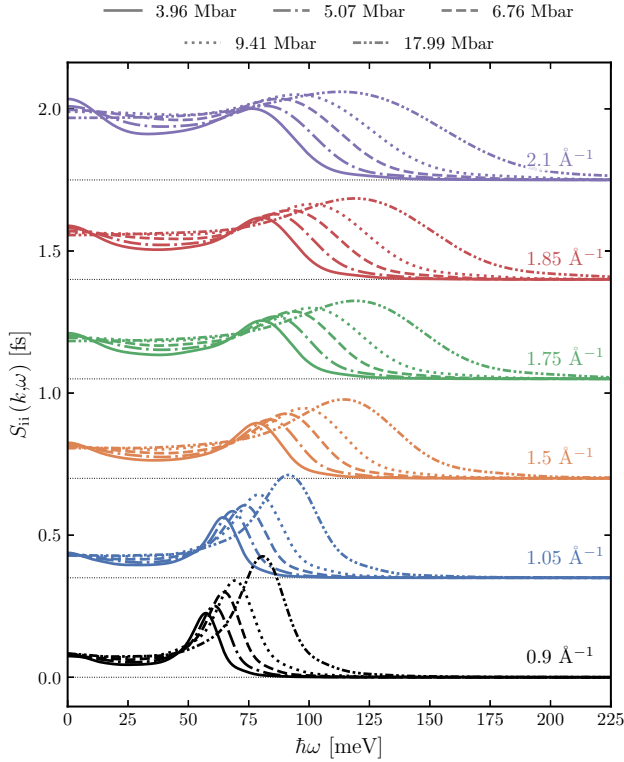


FIG. 11. DSF of liquid copper along the principal Hugoniot curve computed from the NN-MD simulations. The curves are shifted by 0.35 fs with respect to the next lower  $k$  value for readability. Further information on the conditions is given in Fig. 7 and Table I.

leads to a more pronounced ion acoustic mode, but does not shift it to higher  $\omega$ . This effect is, therefore, attributed to the density increase along the principal Hugoniot curve. The more pronounced ion acoustic mode, as well as the generally elevated course of  $S_{ii}(k, \omega)$  for higher temperatures is in accord with the observation in Fig. 9 that the static structure factor  $S_{ii}(k)$  is greater at high temperatures than at low temperatures for  $k$  values smaller than  $2.8 \text{ \AA}^{-1}$ .

The adiabatic speed of sound can be computed from the thermodynamic relation

$$c_s = \sqrt{\frac{\gamma}{\kappa_T \rho}}, \quad (11)$$

with the isothermal compressibilities  $\kappa_T$  computed in Fig. 9. The upper panel of Fig. 12 shows the linear trends computed from Eq. (11), as well as the dispersion of the ion acoustic mode taken from the DSF shown in Fig. 11. It is apparent that the observed peak positions converge to the linear behavior for all conditions, while for the more extreme conditions, the hydrodynamic regime is reached at smaller  $k$  values. The bottom panel of Fig. 11 shows the peak position of the longitudinal current-current correlation spectrum across a wide range of wave numbers. The free-particle limit of a noninteracting system [see Eq. (10)] is given as a reference. The dispersion above  $10 \text{ \AA}^{-1}$  for all conditions is well approximated by this limiting behavior.

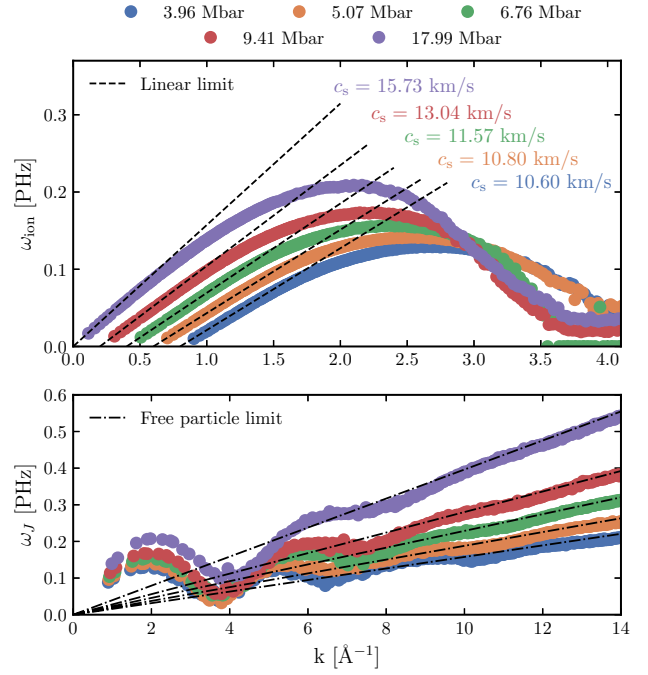


FIG. 12. The upper panel shows the peak position of the ion acoustic mode  $\omega_{\text{ion}}$  taken from the DSF's in Fig. 11 dependent on the  $k$  value and a linear dispersion computed from Eq. (11). The corresponding adiabatic speeds of sound are presented. The lower panel shows the dispersion of the longitudinal current-current correlation spectrum  $J_l$  extracted from the NN-MD simulations and the free-particle behavior. For readability, the curves in the upper panel are shifted by  $0.2 \text{ \AA}^{-1}$  to the right with respect to the next lower pressure condition.

The adiabatic speed of sound is also accessible during shock wave experiments via VISAR measurements [108,109], where the time it takes the shock wave to travel through the target is recorded. First measurements of the speed of sound in copper for this pressure region were observed by McCoy *et al.* [52] during a shock compression experiment. The inferred pressure-density conditions, amongst others, are

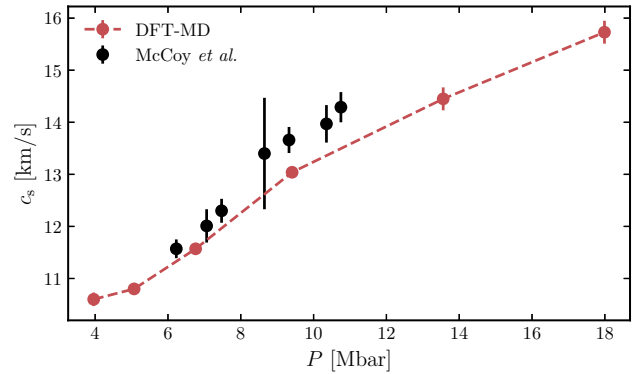


FIG. 13. Adiabatic speed of sound computed from the thermodynamic relation (11) compared to experimental VISAR measurements by McCoy *et al.* [52] for shock-compressed copper.



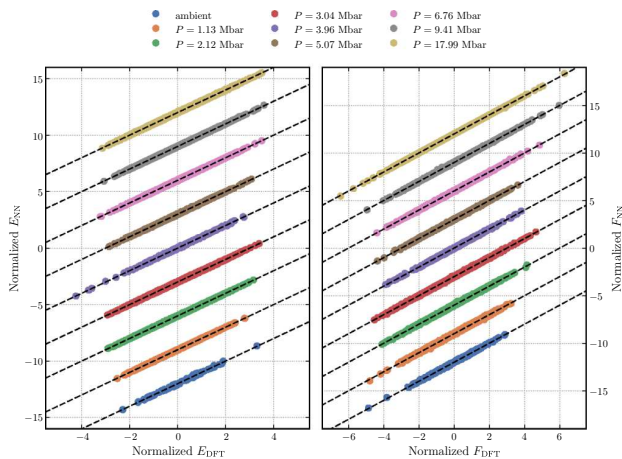


FIG. 14. Validation sets of the NN potentials for energies and forces computed by DFT. As a reference, the black dashed lines show perfect correspondence between the NN potential and DFT.

shown in Fig. 7 and agree within error bars with our simulations. In Fig. 13, we show the experimentally determined adiabatic speed of sound compared to the values computed through Eq. (11). All of the simulation data points lie slightly below the experimentally observed results. As the principal Hugoniot becomes steeper in the  $P - \rho$  plane, the adiabatic speed of sound appears to flatten out towards higher pressures. Unfortunately, the experimental data does not extend to these pressure to verify this trend.

## VII. CONCLUSION

In this work, we performed an extensive analysis of shock-compressed copper using DFT-MD simulations and MD simulations driven by high-dimensional neural network potentials. By analyzing the ion-ion structure factor, we showed that our DFT-MD simulations are able to accurately describe the phonon spectrum of solid copper. Likewise, our analysis of the dynamic electrical conductivity in terms of the Kubo-Greenwood formula and linear response TD-DFT yielded close agreement with existing experimental data. Furthermore, we computed the static and dynamic ion-ion structure factor of liquid copper near the melting line. The agreement with diffraction data was observed to be excellent and the width of the thermal mode agreed well with experiments at wave numbers around the first correlation peak.

The Hugoniot curve was computed from several isotherms up to 60 000 K and 18 Mbar and compared to predictions by the SESAME EOS. Good agreement in the pressure-density plane was achieved between DFT-MD, SESAME and experiments upto 4 Mbar. Differences in the temperature between

DFT-MD and SESAME along the Hugoniot were identified, and the resulting shift of the melting point to higher pressures was highlighted. We observed the hardening of phonon spectra in the solid regime of the Hugoniot compression and, analogously, studied the shift of ion acoustic modes to higher excitation energies. Phonon hardening is currently lively debated and recent work has shown that phonons can be resolved at free electron laser facilities [26–28,110], enabling future direct observations of phonon hardening in shock compression experiments. We found the adiabatic speed of sound along the Hugoniot to be slightly underestimated by DFT-MD relative to recent experimental results. We provided *ab initio* predictions for the evolution of phonon and ion acoustic modes during shock compression of copper, as well as adiabatic speeds of sound for pressures beyond those previously reached by McCoy *et al.* [52]. We hope this inspires further high-pressure shock compression studies, coupled with high resolution x-ray scattering to resolve the ion dynamics of copper under these conditions.

## ACKNOWLEDGMENTS

We thank E. McBride, L. Fletcher, and S. Glenzer for helpful discussions. The DFT-MD and NN-MD simulations and further analysis were performed at the North-German Supercomputing Alliance (HLRN) and the ITMZ of the University of Rostock. M.S. and R.R. thank the Deutsche Forschungsgemeinschaft (DFG) for support within the Research Unit FOR 2440. This work was partially supported by the Center of Advanced Systems Understanding (CASUS) which is financed by Germany’s Federal Ministry of Education and Research (BMBF) and by the Saxon State Government out of the state budget approved by the Saxon State Parliament. Sandia National Laboratories is a multi-mission laboratory managed and operated by National Technology & Engineering Solutions of Sandia, LLC, a wholly owned subsidiary of Honeywell International, Inc., for the US Department of Energy’s National Nuclear Security Administration under Contract No. DE-NA0003525.

## APPENDIX: VALIDATION SETS OF NN POTENTIALS

We show the validation sets of forces and energies computed via DFT for all the conditions treated in this work in Fig. 14. Perfect predictions by the NN potential, corresponding to the straight lines  $E_{NN} = E_{DFT}$  and  $F_{NN} = F_{DFT}$ , are indicated by the black dashed lines. Here,  $E_{DFT}$  and  $F_{DFT}$  are the energies and forces computed through DFT, where  $F_{DFT}$  can be any cartesian component of the force vector. Analogously,  $E_{NN}$  and  $F_{NN}$  are the energies and forces predicted by the NN potential.

- [1] F. Graziani, M. P. Desjarlais, R. Redmer, and S. B. Trickey, *Frontiers and Challenges in Warm Dense Matter* (Springer, Cham, 2014)
- [2] S. H. Glenzer and R. Redmer, *Rev. Mod. Phys.* **81**, 1625 (2009).

- [3] T. S. Duffy and R. F. Smith, *Front. Earth Sci.* **7**, 23 (2019).
- [4] R. Briggs, F. Coppari, M. G. Gorman, R. F. Smith, S. J. Tracy, A. L. Coleman, A. Fernandez-Pañella, M. Millot, J. H. Eggert, and D. E. Fratanduono, *Phys. Rev. Lett.* **123**, 045701 (2019).

- [5] S. M. Sharma, S. J. Turneaure, J. M. Winey, Y. Li, P. Rigg, A. Schuman, N. Sinclair, Y. Toyoda, X. Wang, N. Weir, J. Zhang, and Y. M. Gupta, *Phys. Rev. Lett.* **123**, 045702 (2019).
- [6] S. M. Sharma, S. J. Turneaure, J. M. Winey, and Y. M. Gupta, *Phys. Rev. Lett.* **124**, 235701 (2020).
- [7] R. G. Kraus, R. J. Hemley, S. J. Ali, J. L. Belof, L. X. Benedict, J. Bernier, D. Braun, R. E. Cohen, G. W. Collins, F. Coppari, M. P. Desjarlais, D. Fratanduono, S. Hamel, A. Krygier, A. Lazicki, J. Mcnaney, M. Millot, P. C. Myint, M. G. Newman, J. R. Rygg, D. M. Sterbentz, S. T. Stewart, L. Stixrude, D. C. Swift, C. Wehrenberg, and J. H. Eggert, *Science* **375**, 202 (2022).
- [8] D. Kraus, N. J. Hartley, S. Frydrych, A. K. Schuster, K. Rohatsch, M. Rödel, T. E. Cowan, S. Brown, E. Cunningham, T. van Driel, L. B. Fletcher, E. Galtier, E. J. Gamboa, A. Laso Garcia, D. O. Gericke, E. Granados, P. A. Heimann, H. J. Lee, M. J. MacDonald, A. J. MacKinnon, E. E. McBride, I. Nam, P. Neumayer, A. Pak, A. Pelka, I. Prencipe, A. Ravasio, R. Redmer, A. M. Saunders, M. Schölmerich, M. Schörner, P. Sun, S. J. Turner, A. Zettl, R. W. Falcone, S. H. Glenzer, T. Döppner, and J. Vorberger, *Phys. Plasmas* **25**, 056313 (2018).
- [9] N. J. Hartley, S. Brown, T. E. Cowan, E. Cunningham, T. Döppner, R. W. Falcone, L. B. Fletcher, S. Frydrych, E. Galtier, E. J. Gamboa, A. Laso Garcia, D. O. Gericke, S. H. Glenzer, E. Granados, P. A. Heimann, H. J. Lee, M. J. MacDonald, A. J. MacKinnon, E. E. McBride, I. Nam, P. Neumayer, A. Pak, A. Pelka, I. Prencipe, A. Ravasio, M. Rödel, K. Rohatsch, A. M. Saunders, M. Schölmerich, M. Schörner, A. K. Schuster, P. Sun, T. van Driel, J. Vorberger, and D. Kraus, *Sci. Rep.* **9**, 4196 (2019).
- [10] J. Lüttger, J. Vorberger, N. J. Hartley, K. Voigt, M. Rödel, A. K. Schuster, A. Benuzzi-Mounaix, S. Brown, T. E. Cowan, E. Cunningham, T. Döppner, R. W. Falcone, L. B. Fletcher, E. Galtier, S. H. Glenzer, A. Laso Garcia, D. O. Gericke, P. A. Heimann, H. J. Lee, E. E. McBride, A. Pelka, I. Prencipe, A. M. Saunders, M. Schölmerich, M. Schörner, P. Sun, T. Vinci, A. Ravasio, and D. Kraus, *Sci. Rep.* **11**, 12883 (2021).
- [11] D. Kraus, J. Vorberger, A. Pak, N. J. Hartley, L. B. Fletcher, S. Frydrych, E. Galtier, E. J. Gamboa, D. O. Gericke, S. H. Glenzer, E. Granados, M. J. MacDonald, A. J. MacKinnon, E. E. McBride, I. Nam, P. Neumayer, M. Roth, A. M. Saunders, A. K. Schuster, P. Sun, T. van Driel, T. Döppner, and R. W. Falcone, *Nat. Astron.* **1**, 606 (2017).
- [12] A. A. Golyshev, D. V. Shakh-ray, V. V. Kim, A. M. Molodets, and V. E. Fortov, *Phys. Rev. B* **83**, 094114 (2011).
- [13] A. W. DeSilva and J. D. Katsourous, *Phys. Rev. E* **57**, 5945 (1998).
- [14] J. Clerouin, P. Noiret, P. Blottiau, V. Recoules, B. Siberchicot, and P. Renaudin, *Phys. Plasmas* **19**, 082702 (2012).
- [15] N. A. Smirnov, *Phys. Rev. B* **101**, 094103 (2020).
- [16] D. Errandonea, *Phys. Rev. B* **87**, 054108 (2013).
- [17] D. Hayes, H. Hixson, and R. McQueen, in *Shock Compression of Condensed Matter*, edited by M. Furnish, L. Chhabildas, and H. Hixson (AIP, New York, 2000), pp. 483–488.
- [18] Y. N. Wu, L. P. Wang, Y. S. Huang, and D. M. Wang, *Chem. Phys. Lett.* **515**, 217 (2011).
- [19] J. Moriarty, in *Shock Waves in Condensed Matter*, edited by S. Schmidt and N. Holmes (North-Holland, Amsterdam, 1987), pp. 101–106.
- [20] A. B. Belonoshko, R. Ahuja, O. Eriksson, and B. Johansson, *Phys. Rev. B* **61**, 3838 (2000).
- [21] S. R. Baty, L. Burakovsky, and D. Errandonea, *Crystals* **11**, 537 (2021).
- [22] A. V. Bolesta and V. M. Fomin, *AIP Conf. Proc.* **1893**, 020008 (2017).
- [23] M. Sims, R. Briggs, F. Coppari, A. Coleman, M. Gorman, A. Panella-Fernandez, R. Smith, J. Eggert, and J. Wicks, in *Proceedings of the 2019 COMPRES Annual Meeting* (Big Sky Resort, Big Sky, Montana, 2019).
- [24] S. M. Sharma, S. J. Turneaure, J. M. Winey, and Y. M. Gupta, *Phys. Rev. B* **102**, 020103(R) (2020).
- [25] N. A. Smirnov, *Phys. Rev. B* **103**, 064107 (2021).
- [26] E. E. McBride, T. G. White, A. Descamps, L. B. Fletcher, K. Appel, F. P. Condamine, C. B. Curry, F. Dallari, S. Funk, E. Galtier, M. Gauthier, S. Goede, J. B. Kim, H. J. Lee, B. K. Ofori-Okai, M. Oliver, A. Rigby, C. Schoenwaelder, P. Sun, T. Tschentscher, B. B. L. Witte, U. Zastrau, G. Gregori, B. Nagler, J. Hastings, S. H. Glenzer, and G. Monaco, *Rev. Sci. Instrum.* **89**, 10F104 (2018).
- [27] A. Descamps, B. K. Ofori-Okai, K. Appel, V. Cerantola, A. Comley, J. H. Eggert, L. B. Fletcher, D. O. Gericke, S. Göde, O. Humphries, O. Karnbach, A. Lazicki, R. Loetzsch, D. McGonegle, C. A. J. Palmer, C. Plueckthun, T. R. Preston, R. Redmer, D. G. Senesky, C. Strohm, I. Uschmann, T. G. White, L. Wollenweber, G. Monaco, J. S. Wark, J. B. Hastings, U. Zastrau, G. Gregori, S. H. Glenzer, and E. E. McBride, *Sci. Rep.* **10**, 14564 (2020).
- [28] L. Wollenweber, T. R. Preston, A. Descamps, V. Cerantola, A. Comley, J. H. Eggert, L. B. Fletcher, G. Geloni, D. O. Gericke, S. H. Glenzer, S. Göde, J. Hastings, O. S. Humphries, A. Jenei, O. Karnbach, Z. Konopkova, R. Loetzsch, B. Marx-Glowna, E. E. McBride, D. McGonegle, G. Monaco, B. K. Ofori-Okai, C. A. J. Palmer, C. Plückthun, R. Redmer, C. Strohm, I. Thorpe, T. Tschentscher, I. Uschmann, J. S. Wark, T. G. White, K. Appel, G. Gregori, and U. Zastrau, *Rev. Sci. Instrum.* **92**, 013101 (2021).
- [29] M. Allen and D. Tildesley, *Computer Simulation of Liquids* (Clarendon Press, Oxford, 1989).
- [30] M. M. G. Alemany, O. Diéguez, C. Rey, and L. J. Gallego, *Phys. Rev. B* **60**, 9208 (1999).
- [31] I. Mryglod, *Condens. Matter Phys.* **1**, 753 (1998).
- [32] T. Bryk, *Eur. Phys. J.: Spec. Top.* **196**, 65 (2011).
- [33] J. P. Hansen and I. R. McDonald, *Theory of Simple Liquids*, 3rd ed. (Elsevier Academic Press, London, 2006).
- [34] J. P. Mithen, J. Daligault, and G. Gregori, *Phys. Rev. E* **83**, 015401(R) (2011).
- [35] J. P. Mithen, *Phys. Rev. E* **89**, 013101 (2014).
- [36] B. Cheng and D. Frenkel, *Phys. Rev. Lett.* **125**, 130602 (2020).
- [37] G. Monaco and S. Mossa, *Proc. Natl. Acad. Sci. USA* **106**, 16907 (2009).
- [38] H. Mizuno, S. Mossa, and J.-L. Barrat, *Proc. Natl. Acad. Sci. USA* **111**, 11949 (2014).
- [39] N. Oyama, H. Mizuno, and A. Ikeda, *Phys. Rev. E* **104**, 015002 (2021).
- [40] P. Hohenberg and W. Kohn, *Phys. Rev.* **136**, B864 (1964).
- [41] W. Kohn and L. J. Sham, *Phys. Rev.* **140**, A1133 (1965).
- [42] M. M. G. Alemany, L. J. Gallego, and D. J. González, *Phys. Rev. B* **70**, 134206 (2004).



- [43] M. D. Knudson, M. P. Desjarlais, A. Becker, R. W. Lemke, K. R. Cochrane, M. E. Savage, D. E. Bliss, T. R. Mattsson, and R. Redmer, *Science* **348**, 1455 (2015).
- [44] M. Millot, S. Hamel, J. R. Rygg, P. M. Celliers, G. W. Collins, F. Coppari, D. E. Fratanduono, R. Jeanloz, D. C. Swift, and J. H. Eggert, *Nat. Phys.* **14**, 297 (2018).
- [45] A. Ravasio, M. Bethkenhagen, J.-A. Hernandez, A. Benuzzi-Mounaix, F. Datchi, M. French, M. Guarguaglini, F. Lefevre, S. Ninet, R. Redmer, and T. Vinci, *Phys. Rev. Lett.* **126**, 025003 (2021).
- [46] B. B. L. Witte, M. Shihab, S. H. Glenzer, and R. Redmer, *Phys. Rev. B* **95**, 144105 (2017).
- [47] H. R. Rüter and R. Redmer, *Phys. Rev. Lett.* **112**, 145007 (2014).
- [48] T. G. White, S. Richardson, B. J. B. Crowley, L. K. Pattison, J. W. O. Harris, and G. Gregori, *Phys. Rev. Lett.* **111**, 175002 (2013).
- [49] N. M. Gill, R. A. Heinonen, C. E. Starrett, and D. Saumon, *Phys. Rev. E* **91**, 063109 (2015).
- [50] Q. Zeng, X. Yu, Y. Yao, T. Gao, B. Chen, S. Zhang, D. Kang, H. Wang, and J. Dai, *Phys. Rev. Res.* **3**, 033116 (2021).
- [51] M. Schörner, H. R. Rüter, M. French, and R. Redmer, *Phys. Rev. B* **105**, 174310 (2022).
- [52] C. A. McCoy, M. D. Knudson, and S. Root, *Phys. Rev. B* **96**, 174109 (2017).
- [53] N. Wiener, *Acta Math.* **55**, 117 (1930).
- [54] A. Khintchine, *Math. Ann.* **109**, 604 (1934).
- [55] D. Chaturvedi, M. Rovere, G. Senatore, and M. Tosi, *Physica B+C* **111**, 11 (1981).
- [56] P. Hugoniot, *J. École Polytech* **57**, 3 (1887).
- [57] P. Hugoniot, *J. École Polytech* **58**, 1 (1889).
- [58] W. J. M. Rankine, *Lond. Edinb. Dublin Philos. Mag. J. Sci.* **1**, 225 (1851).
- [59] W. J. M. Rankine, *Philos. Trans. Royal Soc.* **160**, 277 (1870).
- [60] G. Kresse and J. Hafner, *Phys. Rev. B* **47**, 558 (1993).
- [61] G. Kresse and J. Hafner, *Phys. Rev. B* **49**, 14251 (1994).
- [62] G. Kresse and J. Furthmüller, *Phys. Rev. B* **54**, 11169 (1996).
- [63] N. Mermin, *Phys. Rev.* **137**, A1441 (1965).
- [64] J. P. Perdew, K. Burke, and M. Ernzerhof, *Phys. Rev. Lett.* **77**, 3865 (1996).
- [65] P. E. Blöchl, *Phys. Rev. B* **50**, 17953 (1994).
- [66] S. Nosé, *J. Chem. Phys.* **81**, 511 (1984).
- [67] W. G. Hoover, *Phys. Rev. A* **31**, 1695 (1985).
- [68] A. Baldereschi, *Phys. Rev. B* **7**, 5212 (1973).
- [69] H. J. Monkhorst and J. D. Pack, *Phys. Rev. B* **13**, 5188 (1976).
- [70] J. Heyd, G. E. Scuseria, and M. Ernzerhof, *J. Chem. Phys.* **118**, 8207 (2003).
- [71] J. Heyd, G. E. Scuseria, and M. Ernzerhof, *J. Chem. Phys.* **124**, 219906 (2006).
- [72] R. Kubo, *J. Phys. Soc. Jpn.* **12**, 570 (1957).
- [73] D. A. Greenwood, *Proc. Phys. Soc. London* **71**, 585 (1958).
- [74] B. Holst, M. French, and R. Redmer, *Phys. Rev. B* **83**, 235120 (2011).
- [75] E. K. U. Gross and W. Kohn, *Phys. Rev. Lett.* **55**, 2850 (1985).
- [76] A. Singraber, “n2p2 - a neural network potential package,” (2021), computer software, version 2.1.4, <https://zenodo.org/record/4750573>.
- [77] T. Morawietz, A. Singraber, C. Dellago, and J. Behler, *Proc. Natl. Acad. Sci. USA* **113**, 8368 (2016).
- [78] A. Singraber, T. Morawietz, J. Behler, and C. Dellago, *J. Chem. Theory Comput.* **15**, 3075 (2019).
- [79] M. Gastegger, L. Schwiedrzik, M. Bittermann, F. Berzsenyi, and P. Marquetand, *J. Chem. Phys.* **148**, 241709 (2018).
- [80] A. P. Thompson, H. M. Aktulga, R. Berger, D. S. Bolintineanu, W. M. Brown, P. S. Crozier, P. J. in 't Veld, A. Kohlmeyer, S. G. Moore, T. D. Nguyen, R. Shan, M. J. Stevens, J. Tranchida, C. Trott, and S. J. Plimpton, *Comput. Phys. Commun.* **271**, 108171 (2022).
- [81] P. Virtanen, R. Gommers, T. E. Oliphant, M. Haberland, T. Reddy, D. Cournapeau, E. Burovski, P. Peterson, W. Weckesser, J. Bright, S. J. van der Walt, M. Brett, J. Wilson, K. J. Millman, N. Mayorov, A. R. J. Nelson, E. Jones, R. Kern, E. Larson, C. J. Carey, Í. Polat, Y. Feng, E. W. Moore, J. VanderPlas, D. Laxalde, J. Perktold, R. Cimrman, I. Henriksen, E. A. Quintero, C. R. Harris, A. M. Archibald, A. H. Ribeiro, F. Pedregosa, P. van Mulbregt, A. Vijaykumar, A. P. Bardelli, A. Rothberg, A. Hilboll, A. Kloeckner, A. Scopatz, A. Lee, A. Rokem, C. N. Woods, C. Fulton, C. Masson, C. Häggström, C. Fitzgerald, D. A. Nicholson, D. R. Hagen, D. V. Pasechnik, E. Olivetti, E. Martin, E. Wieser, F. Silva, F. Lenders, F. Wilhelm, G. Young, G. A. Price, G.-L. Ingold, G. E. Allen, G. R. Lee, H. Audren, I. Probst, J. P. Dietrich, J. Silterra, J. T. Webber, J. Slavič, J. Nothman, J. Buchner, J. Kulick, J. L. Schönberger, J. V. de Miranda Cardoso, J. Reimer, J. Harrington, J. L. C. Rodríguez, J. Nunez-Iglesias, J. Kuczynski, K. Tritz, M. Thoma, M. Newville, M. Kümmerer, M. Bolingbroke, M. Tartre, M. Pak, N. J. Smith, N. Nowaczyk, N. Shebanov, O. Pavlyk, P. A. Brodtkorb, P. Lee, R. T. McGibbon, R. Feldbauer, S. Lewis, S. Tygier, S. Sievert, S. Vigna, S. Peterson, S. More, T. Pudlik, T. Oshima, T. J. Pingel, T. P. Robitaille, T. Spura, T. R. Jones, T. Cera, T. Leslie, T. Zito, T. Krauss, U. Upadhyay, Y. O. Halchenko, Y. Vázquez-Baeza, and S. I.0 Contributors, *Nat. Methods* **17**, 261 (2020).
- [82] R. M. Nicklow, G. Gilat, H. G. Smith, L. J. Raubenheimer, and M. K. Wilkinson, *Phys. Rev.* **164**, 922 (1967).
- [83] B. Henke, E. Gullikson, and J. Davis, *At. Data Nucl. Data Tables* **54**, 181 (1993).
- [84] A. D. Baczewski, L. Shulenburg, M. P. Desjarlais, S. B. Hansen, and R. J. Magyar, *Phys. Rev. Lett.* **116**, 115004 (2016).
- [85] K. Ramakrishna, A. Cangi, T. Dornheim, A. Baczewski, and J. Vorberger, *Phys. Rev. B* **103**, 125118 (2021).
- [86] B. B. L. Witte, P. Sperling, M. French, V. Recoules, S. H. Glenzer, and R. Redmer, *Phys. Plasmas* **25**, 056901 (2018).
- [87] Y. Waseda and M. Ohtani, *Philos. Mag.* **32**, 273 (1975).
- [88] O. J. Eder, B. Kunsch, M. Suda, E. Erdpresser, and H. Stiller, *J. Phys. F* **10**, 183 (1980).
- [89] D. Cromer and J. Waber, *Acta Crystallogr.* **18**, 104 (1965).
- [90] D. Cromer, *Acta Crystallogr.* **18**, 17 (1965).
- [91] S. Filippov, N. Kazakov, and L. Pronin, *Ultrasound Velocity and Compressibility of Liquid Metals in Relation to Different Physical Properties*, 3rd ed. (Izv. Vyssh. Uchebn. Zaved. Chern Metall, 1966), pp. 8–14.
- [92] J. Cahill and A. Kirshenbaum, *J. Phys. Chem.* **66**, 1080 (1962).
- [93] T. Bryk and A. B. Belonoshko, *Phys. Rev. B* **86**, 024202 (2012).

- [94] J.-F. Wax and T. Bryk, *J. Phys.: Condens. Matter* **25**, 325104 (2013).
- [95] R. Zwanzig, *Phys. Rev.* **156**, 190 (1967).
- [96] U. Balucani and M. Zoppi, *Dynamics of the Liquid State* (Oxford Science Publishers, Oxford, 1994).
- [97] T. Scopigno, U. Balucani, G. Ruocco, and F. Sette, *J. Phys.: Condens. Matter* **12**, 8009 (2000).
- [98] S. Hagen, Untersuchung der kollektiven Bewegungen im polykristallinen und fluessigen Kupfer durch inelastische Neutronenstreuung, Ph.D. thesis, University of Karlsruhe, Germany, 1973.
- [99] J. Copley and S. Lovesey, *Rep. Prog. Phys.* **38**, 461 (1975).
- [100] K. S. Trainor, *J. Appl. Phys.* **54**, 2372 (1983).
- [101] B. L. Glushak, A. P. Zharkov, M. V. Zhernokletov, V. Ya. Ternovoi, A. S. Filimonov, and V. E. Fortov, *Zh. Eksp. Teor. Fiz.* **96**, 1301 (1989) [*Sov. Phys. JETP* **69**, 739 (1989)].
- [102] S. B. Kormer, A. I. Funtikov, V. D. Urlin, and A. N. Kolesnikova, *Zh. Eksp. Teor. Fiz.* **42**, 686 (1962) [*Sov. Phys. JETP* **15**, 477 (1962)].
- [103] L. V. Al'tshuler, A. A. Bakanova, and R. F. Trunin, *Zh. Eksp. Teor. Fiz.* **42**, 91 (1962) [*Sov. Phys. JETP* **15**, 65 (1962)].
- [104] A. C. Mitchell, W. J. Nellis, J. A. Moriarty, R. A. Heinle, N. C. Holmes, R. E. Tipton, and G. W. Repp, *J. Appl. Phys.* **69**, 2981 (1991).
- [105] A. Mitchell and W. Nellis, *J. Appl. Phys.* **52**, 3363 (1981).
- [106] L. Altshuler, S. Kormer, A. Bakanova, and R. Trunin, *Zh. Eksp. Teor. Fiz.* **38**, 790 (1960) [*Sov. Phys. JETP* **11**, 573 (1960)].
- [107] R. McQueen, S. Marsh, J. Taylor, J. Fritz, and W. Carter, in *High-Velocity Impact Phenomena*, edited by R. Kinslow (Academic, New York, 1970).
- [108] L. M. Barker, *Exp. Mech.* **12**, 209 (1972).
- [109] M. Li, S. Zhang, H. Zhang, G. Zhang, F. Wang, J. Zhao, C. Sun, and R. Jeanloz, *Phys. Rev. Lett.* **120**, 215703 (2018).
- [110] A. Descamps, B. K. Ofori-Okai, J. K. Baldwin, Z. Chen, L. B. Fletcher, S. H. Glenzer, N. J. Hartley, J. B. Hasting, D. Khaghani, M. Mo, B. Nagler, V. Recoules, R. Redmer, M. Schörner, P. Sun, Y. Q. Wang, T. G. White, and E. E. McBride, *J. Synchrotron Radiat.* **29**, 931 (2022).

### 4.3 X-ray Thomson scattering spectra from density functional theory molecular dynamics simulations based on a modified Chihara formula

#### Author contributions

**M. Schörner**

Preparation of the manuscript, implementation of Mermin dielectric function and *ab initio* collision frequency code, DFT-MD and LR-TDDFT simulations and interpretation

**M. Bethkenhagen**

Preparation of the manuscript, DFT-MD simulations and interpretation

**T. Döppner**

Preparation of the manuscript, interpretation of simulations and experiments

**D. Kraus**

Interpretation of simulations and experiments

**L.B. Fletcher**

Computation of bound-free spectra in impulse approximation, interpretation of simulations and experiments




**S.H. Glenzer**

Preparation of the manuscript, interpretation of simulations and experiments

**R. Redmer**

Supervision of the project, interpretation of simulations, preparation of the manuscript

## X-ray Thomson scattering spectra from density functional theory molecular dynamics simulations based on a modified Chihara formula

Maximilian Schörner <sup>1,\*</sup> Mandy Bethkenhagen <sup>2,3</sup> Tilo Döppner<sup>4</sup> Dominik Kraus,<sup>1,5</sup> Luke B. Fletcher,<sup>6</sup> Siegfried H. Glenzer,<sup>6</sup> and Ronald Redmer <sup>1</sup>

<sup>1</sup>University of Rostock, Institute of Physics, 18051 Rostock, Germany

<sup>2</sup>École Normale Supérieure de Lyon, Laboratoire de Géologie de Lyon, CNRS UMR 5276, 69364 Lyon, Cedex 07, France

<sup>3</sup>Institute of Science and Technology Austria, Am Campus 1, 3400 Klosterneuburg, Austria

<sup>4</sup>Lawrence Livermore National Laboratory, Livermore, California 94551, USA

<sup>5</sup>Helmholtz-Zentrum Dresden-Rossendorf, 01328 Dresden, Germany

<sup>6</sup>SLAC National Accelerator Laboratory, Menlo Park, California 94025, USA



(Received 4 January 2023; revised 29 March 2023; accepted 10 May 2023; published 14 June 2023)

We study *ab initio* approaches for calculating x-ray Thomson scattering spectra from density functional theory molecular dynamics simulations based on a modified Chihara formula that expresses the inelastic contribution in terms of the dielectric function. We study the electronic dynamic structure factor computed from the Mermin dielectric function using an *ab initio* electron-ion collision frequency in comparison to computations using a linear-response time-dependent density functional theory (LR-TDDFT) framework for hydrogen and beryllium and investigate the dispersion of free-free and bound-free contributions to the scattering signal. A separate treatment of these contributions, where only the free-free part follows the Mermin dispersion, shows good agreement with LR-TDDFT results for ambient-density beryllium, but breaks down for highly compressed matter where the bound states become pressure ionized. LR-TDDFT is used to reanalyze x-ray Thomson scattering experiments on beryllium demonstrating strong deviations from the plasma conditions inferred with traditional analytic models at small scattering angles.

DOI: [10.1103/PhysRevE.107.065207](https://doi.org/10.1103/PhysRevE.107.065207)

### I. INTRODUCTION

X-ray Thomson scattering (XRTS) has been one of the premier diagnostic tools for warm dense matter (WDM) experiments, enabling measurements of the electron density, temperature, and ionization state [1–3]. The states reached in these experiments are characterized by temperatures of a few electron volts (eV) and around solid densities, which constitutes strongly correlated plasmas with non-negligible degeneracy. This prevents the application of ideal plasma theory for the analysis of these experiments, and rather requires a quantum mechanical treatment in a many-body framework. Knowledge of equation of state data as well as thermal and electrical transport properties for warm dense hydrogen and beryllium is essential for modeling astrophysical objects [4,5] and inertial confinement fusion [6], where hydrogen is used as fuel while beryllium often serves as ablator material [7,8]. Furthermore, hydrogen and beryllium are excellent test cases for new theoretical approaches. The analytical behavior in many limiting cases for fully ionized hydrogen plasmas are known and beryllium can be used to test the treatment of bound states in a simple low- $Z$  material. WDM is typically opaque in the optical regime, as the light frequency is smaller than the plasma frequency  $\omega_{\text{pl}}$  of these plasmas. Therefore, it is indispensable to have diagnostic tools at experiments that

are well understood, both experimentally and theoretically. XRTS has proven to overcome many of the experimental challenges of probing WDM. The high-energy x-ray photons can penetrate dense plasmas, and since the advent of free-electron lasers (FELs), rep-rated x-ray sources with sufficient brilliance for probing short-lived transient states are available in addition to laser-plasma sources which only allow a limited number of experiments and require complex sample assemblies. New FEL techniques like self-seeding [9,10] have also resulted in much narrower bandwidths of the x-ray source, enabling the measurement of phonons and ion acoustic modes [11,12] and a better resolution of density and temperature-sensitive regions in the XRTS spectrum.

Due to the steadily improving quality of collected spectra, it is vital to have accurate theoretical modeling of the scattering. While in the past, the resolution of XRTS spectra often did not allow for discrimination between different theoretical approaches, now, fitting experimental spectra to theoretical models has allowed predictions of electron temperature and density to within a few percent uncertainty [13–15]. As a result, the fidelity of the theoretical model used is now the limiting factor in determining the correct plasma parameters in experiments that employ XRTS as a diagnostic tool. Most approaches rely on the semiclassical Chihara decomposition [16,17] of the spectrum into three distinct contributions which originates from distinguishing between free and bound electrons in a chemical picture. An analogous fully quantum-mechanical description has also been proposed [18]. The

\*maximilian.schoerner@uni-rostock.de

standard approach for modeling XRTS spectra in the Chihara description is a combination of theories to describe each component individually [19]. The ion dynamics are usually described by the hypernetted-chain approximation with different expressions for the interaction potential while the form factors are described by a screened hydrogenic approximation to the wave functions [20] and the Debye-Hückel approximation for the screening cloud. The plasmon can be described by the random phase approximation (RPA) or the Mermin dielectric function in order to also include electron-ion collisions which can also be approximated to different degrees [21]. Further electron correlations can be accounted for by local field corrections [22]. Contributions that are related to bound-free transitions are treated within the impulse approximation [23] which is sometimes modified by the ionization potential depression and normalized according to different sum rules.

In recent years, this approach has been partially replaced by *ab initio* descriptions like density functional theory molecular dynamics (DFT-MD) simulations and real-time or linear-response time-dependent DFT (RT/LR-TDDFT) computations. Witte *et al.* successfully used electron-ion collision frequencies determined by DFT to accurately model the plasmon of an aluminum plasma [24]. This approach was subsequently compared to LR-TDDFT and other theoretical models by Ramakrishna *et al.* for ambient and extreme conditions in aluminum [25] and carbon [26], which was then used to discern miscibility in an XRTS experiment [13]. Mo *et al.* also used LR-TDDFT to study isochorically heated aluminum [27]. Baczewski *et al.* went beyond the Chihara decomposition by simulating the real-time propagation of the electronic density using RT-TDDFT [28]. Path integral Monte Carlo simulations have delivered approximation-free results for the uniform electron gas [29] and hydrogen plasmas [30], but are currently unable to describe heavier elements.

The capability of DFT-MD to compute ion dynamics and the form factors was already demonstrated and tested in previous publications [31–33]. Therefore, in this work, we focus on the inelastic contribution to the scattering spectrum, i.e., the plasmon and bound-free contribution. Although the *ab initio* approaches offer a better description of the many-body nature involved in the scattering process, they incur substantial computational cost and take a long time to perform, which is especially troubling if the conditions reached in an experiment cannot easily be constrained. Therefore, the much faster analytic approach of using the Mermin dielectric function is still widely used in the field of WDM research [14,34,35]. To test the validity of the Mermin description, we connect the DFT and Mermin approach in the macroscopic limit ( $k \rightarrow 0$ ) by introducing an *ab initio* electron-ion collision frequency, as first described in Ref. [24], and examine differences of the predicted scattering spectra at finite scattering angles.

In Secs. II A and II B, we give an overview of the theoretical foundation for computing the electronic dynamic structure factor from the Mermin dielectric function with a dynamic complex collision frequency and apply this framework to extract a DFT-based collision frequency. In Sec. II C, a short summary and the relevant equations for LR-TDDFT is given. In Sec. II D we give the details of the simulation method. We compute DFT-based collision frequencies for a hydrogen plasma and compare them to several analytic approaches in

Sec. III and we study the impact of these collision frequencies on dynamic structure factors (DSFs) for hydrogen and beryllium plasmas in Secs. IV A, IV B, and IV C. In Sec. V, we apply the full *ab initio* description of LR-TDDFT to interpret XRTS experiments on beryllium, which were previously analyzed using analytic approaches. We evaluate the impact on the inferred plasma parameters for XRTS experiments at small and large scattering angles, showing good agreement in the backscattering and significant deviations in the forward scattering.

## II. THEORETICAL BACKGROUND

### A. Dynamic structure factor

The electronic DSF [1]

$$S_{ee}^{\text{tot}}(\vec{k}, \omega) = \frac{1}{2\pi N_e} \int_{-\infty}^{\infty} dt \langle n_{\vec{k}}^e(\tau) n_{-\vec{k}}^e(\tau + t) \rangle_{\tau} e^{i\omega t} \quad (1)$$

is the central quantity representing the spatially resolved power spectrum of an electronic system, describing its dynamics at given temporal and spatial periodicities given by the frequency  $\omega$  and the wave vector  $\vec{k}$ , respectively. The number of considered electrons is  $N_e$  and the spatial Fourier components of the electron density are given by  $n_{\vec{k}}^e$ . The time is described by  $t$  and  $\tau$ , where  $\langle \dots \rangle_{\tau}$  describes a time average over  $\tau$ . Experimentally,  $S_{ee}^{\text{tot}}(\vec{k}, \omega)$  can be used to identify how strong a photon will couple to density fluctuations at a given energy transfer and scattering angle [1]. In this work we will use a slight modification of the common decomposition of Eq. (1) introduced by Chihara [16,17]:

$$S_{ee}^{\text{tot}}(\vec{k}, \omega) = |f_i(\vec{k}) + q(\vec{k})|^2 S_{ii}(\vec{k}, \omega) + \underbrace{Z_f S_{ee}^0(\vec{k}, \omega) + Z_b S_{bf}(\vec{k}, \omega)}_{Z S_{et}(\vec{k}, \omega)}. \quad (2)$$

The first term refers to the elastic response of the electrons which follow the ion motion described by the ion-ion structure factor  $S_{ii}(\vec{k}, \omega)$ . Here,  $f_i(\vec{k})$  describes the contribution of tightly bound electrons and  $q(\vec{k})$  represents the loosely bound screening cloud around the ions. The second term, called the electron feature, arises from the collective behavior of the free electrons in the system undergoing transitions to different free-electron states. The number of free electrons per atom is labeled  $Z_f$  and their DSF is denoted by  $S_{ee}^0(\vec{k}, \omega)$ . The last term in Eq. (2) is the bound-free contribution. In the original work, Chihara clearly separates free and bound electrons and describes this term as a convolution of the DSF of the core electrons with the self-part of the ionic DSF [17]. We treat the bound-free contribution on the same footing as the free-electron contribution and introduce the bound-free DSF  $S_{bf}(\vec{k}, \omega)$  and the number of bound electrons per atom  $Z_b$ . Both the free-electron and bound-free contributions arise due to inelastic transitions of the electrons and can, therefore, be combined into one DSF  $S_{et}(\vec{k}, \omega)$  that accounts for all electronic transitions. This avoids the artificial separation into bound and free electrons for both the charge state  $Z$  and the DSF. According to the fluctuation-dissipation theorem [36], this combined DSF can be related to the dielectric response



described by the dielectric function  $\epsilon(\vec{k}, \omega)$  via

$$S_{\text{ct}}(\vec{k}, \omega) = -\frac{\epsilon_0 \hbar \vec{k}^2 \text{Im}[\epsilon^{-1}(\vec{k}, \omega)]}{\pi e^2 n_e 1 - \exp\left(\frac{-\hbar\omega}{k_B T_e}\right)}. \quad (3)$$

The vacuum permittivity is denoted by  $\epsilon_0$ , the reduced Planck constant is  $\hbar$ , and  $e$  is the elementary charge. The electron density is given by  $n_e$ , the electron temperature is  $T_e$ , and the Boltzmann constant is  $k_B$ . At which conditions the separation into free and bound-free parts in Eq. (2) is justified and yields the same results as the combined approach discussed in Secs. IV B and IV C.

### B. Dielectric function with electron-ion collisions

The dielectric function  $\epsilon(\vec{k}, \omega)$  is a central material property that is connected to other material properties, like the electrical conductivity  $\sigma(\omega)$  in the long-wavelength limit or the DSF via the fluctuation-dissipation theorem from Eq. (3). One of the first approaches that produced collective features of the electron system, such as plasmons, is the Lindhard dielectric function [37]

$$\epsilon^{\text{RPA}}(\vec{k}, \omega) = \lim_{\eta \rightarrow 0} \left[ 1 - \frac{2e^2}{\epsilon_0 k^2} \int \frac{d^3q}{(2\pi)^3} \frac{f_{\vec{q}-\vec{k}/2} - f_{\vec{q}+\vec{k}/2}}{\hbar(\omega + i\eta) + E_{\vec{q}-\vec{k}/2} - E_{\vec{q}+\vec{k}/2}} \right], \quad (4)$$

which accounts for electric field screening in the RPA. The arguments  $\vec{k}$  and  $\omega$  are the wave vector and the angular frequency, respectively.  $E_{\vec{q}}$  and  $f_{\vec{q}}$  are the kinetic energy and the Fermi occupation of an electron with wave vector  $\vec{q}$  in the unperturbed free-electron gas. The small imaginary contribution to the frequency  $\eta$  is introduced to avoid the pole in the integration and approaches zero thereafter. However, for degenerate, strongly correlated systems, electron-ion interactions, which are neglected in Eq. (4), have to be accounted for in order to accurately describe the dielectric function.

It was shown that electron-ion collisions can be included via a dynamic collision frequency  $\nu(\omega)$  in the framework of the Mermin dielectric function [38–41]

$$\epsilon^{\text{Mermin}}[\vec{k}, \omega; \nu(\omega)] = 1 + \frac{(1 + i\frac{\nu(\omega)}{\omega})(\epsilon^{\text{RPA}}[\vec{k}, \omega + i\nu(\omega)] - 1)}{1 + i\frac{\nu(\omega)}{\omega} \frac{\epsilon^{\text{RPA}}[\vec{k}, \omega + i\nu(\omega)] - 1}{\epsilon^{\text{RPA}}(\vec{k}, 0) - 1}}. \quad (5)$$

This collision frequency is defined as the difference to the RPA in the macroscopic limit due to the interaction of electrons and ions [21]. Further correlations between the electrons can be included via local field corrections by going beyond the RPA and replacing  $\epsilon^{\text{RPA}}$  in Eq. (5) by the dielectric function of the one-component plasma [22,42,43]. Extensive work has been performed on the evaluation of different analytic collision frequencies and local field corrections [21,22,44], as well as first attempts to incorporate *ab initio* results to determine collision frequencies [45].

We present the derivation of the RPA dielectric function in the presence of a dynamic complex collision frequency in Appendix A. Equations (5), (A7), and (A8) are the basis for calculating the Mermin dielectric function for a given

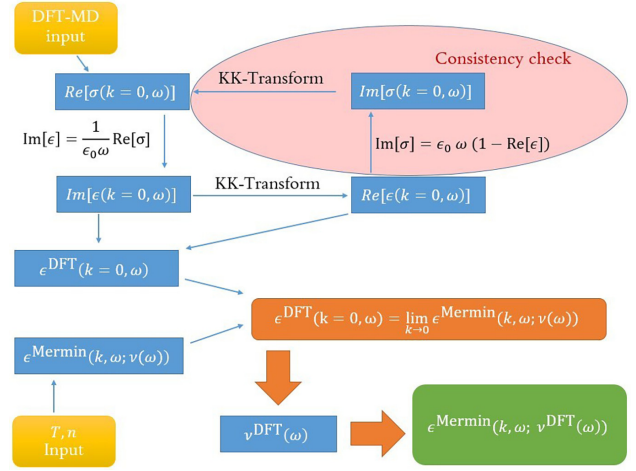


FIG. 1. Schematic work flow for determining the dynamic collision frequency and  $k$ -dependent dielectric function via DFT.

dynamic collision frequency  $\nu(\omega)$ . In the following, because we are dealing with isotropic systems, we will only consider the magnitude of wave vector  $\vec{k}$  and drop the vector notation.

One of the most prominent approximations for the collision frequency is the Born collision frequency [21], the combination of which with the Mermin dielectric function in Eq. (5) is called the Born-Mermin approximation. It is widely used in the analysis of XRTS spectra in the WDM field. We give the exact equations used in this work in Appendix B. However, complex many-particle effects, as they are considered in *ab initio* simulations, cannot be accounted for by this approach.

In Fig. 1, we show the schematic procedure to compute a DFT-based collision frequency from an electrical conductivity in the optical limit. In essence, we construct a complex collision frequency for which the Mermin dielectric function coincides with the *ab initio* dielectric function in the optical limit. As input, the temperature and electron density of the plasma are needed for the Mermin dielectric function and the real part of the electrical conductivity is needed from the simulation. According to the Kubo-Greenwood formula [46,47] the conductivity is

$$\begin{aligned} \text{Re}[\sigma(k=0, \omega)] &= \frac{2\pi e^2}{3\omega\Omega} \sum_{\vec{g}} w_{\vec{g}} \sum_{j=1}^N \sum_{i=1}^N \sum_{\alpha=1}^3 [f(\epsilon_{j,\vec{g}}) - f(\epsilon_{i,\vec{g}})] \\ &\times \langle \psi_{j,\vec{g}} | \hat{v}_{\alpha} | \psi_{i,\vec{g}} \rangle^2 \delta(\epsilon_{i,\vec{g}} - \epsilon_{j,\vec{g}} - \hbar\omega). \end{aligned} \quad (6)$$

The indices  $i$  and  $j$  run over the eigenstates,  $\alpha$  runs over the spatial orientations, and  $\vec{g}$  denotes the reciprocal vectors in the Brillouin zone where the wave functions  $\psi_{i,\vec{g}}$  are evaluated. The Fermi-Dirac occupation at a given eigenenergy  $\epsilon_{j,\vec{g}}$  is described by  $f(\epsilon_{j,\vec{g}})$  and  $\hat{v}_{\alpha}$  is the velocity operator in the direction  $\alpha$ . The normalization volume is denoted by  $\Omega$  and  $w_{\vec{g}}$  is the weighting of each  $k$  point. We translate the electrical conductivity to the imaginary dielectric function via

$$\text{Im}[\epsilon(k=0, \omega)] = \frac{1}{\epsilon_0\omega} \text{Re}[\sigma(k=0, \omega)] \quad (7)$$



and use the Kramers-Kronig transformation to compute the corresponding real part, leading to a complex dielectric function  $\epsilon^{\text{DFT}}(k=0, \omega)$ . If we require an equivalence between the DFT result and the Mermin dielectric function in the optical limit

$$\epsilon^{\text{DFT}}(k=0, \omega) \stackrel{!}{=} \lim_{k \rightarrow 0} \epsilon^{\text{Mermin}}(k, \omega; \nu(\omega)), \quad (8)$$

the real and imaginary parts must be equal simultaneously. This can be achieved by adjusting the real and imaginary parts of the dynamic collision frequency which feeds into the Mermin dielectric function, leading to a two-dimensional optimization problem. The result of this optimization is a collision frequency  $\nu^{\text{DFT}}(\omega)$  for which the analytic Mermin dielectric function yields the same results as DFT in the macroscopic limit. Because there is no notion of bound states in the theoretical framework of the Mermin dielectric function, the electrical conductivity must only originate from free or quasi-free states. For this purpose, the conductivity in Eq. (6) can be split into different contributions (see Ref. [48] for details).

Figure 2 shows the convergence of the Mermin dielectric function and DSF to the DFT result in the optical limit for a beryllium plasma at  $\rho = 5 \text{ g/cm}^3$  and  $T = 100 \text{ eV}$ . Due to the presence of bound states in beryllium at these conditions, only the electrical conductivity due to free electrons can be used as an input to the workflow depicted in Fig. 1 and all quantities in Fig. 2 are free-electron contributions. The DFT results for the dielectric function  $\epsilon^{\text{DFT}}(k, \omega)$  and the connected DSF  $S^{\text{DFT}}(k, \omega)$  are only available at  $k=0$  and are shown as a constant reference for the various  $k$  depicted in Fig. 2. In both panels, it is apparent that, with the correct collision frequency  $\nu^{\text{DFT}}(\omega)$ , the Mermin result converges to the optical limit described by DFT. In practice, the limit  $k \rightarrow 0$  is reached at wave numbers that correspond to length scales that are significantly larger than any characteristic length scales of the studied system. For beryllium at these conditions, the convergence is reached for wave numbers smaller or equal to  $10^{-4} \text{ \AA}^{-1}$  as depicted in Fig. 2. The dielectric functions in the upper panel are connected to the DSF in the lower panel by Eq. (3). However, it is apparent that the dynamic dielectric function in the upper panel of Fig. 2 is more sensitive to changes in the wave number than the DSF shown in the bottom panel, which is dominated by the pole in  $\epsilon^{-1}(k, \omega)$ .

### C. Linear-response time-dependent density functional theory

In the framework of LR-TDDFT the density response of the noninteracting homogeneous Kohn-Sham system can be evaluated at a finite momentum transfer as [49,50]

$$\chi_{\text{KS}}(\vec{k}, \omega) = \frac{1}{\Omega} \sum_{\vec{g}, i, j} \frac{f(\epsilon_{i, \vec{g}}) - f(\epsilon_{j, \vec{g} + \vec{k}})}{\omega + \epsilon_{i, \vec{g}} - \epsilon_{j, \vec{g} + \vec{k}} + i\eta} \times \langle \psi_{i, \vec{g}} | e^{-i\vec{k}\vec{r}} | \psi_{j, \vec{g} + \vec{k}} \rangle \langle \psi_{i, \vec{g}} | e^{i\vec{k}\vec{r}} | \psi_{j, \vec{g} + \vec{k}} \rangle. \quad (9)$$

The quantities in this equation are defined analogously to the Kubo-Greenwood formula in Eq. (6). This response function can be related to the full density response  $\chi$  via a Dyson equation [49], with different levels of approximation for the exchange-correlation kernel  $f_{\text{XC}}$ . A closed expression can be

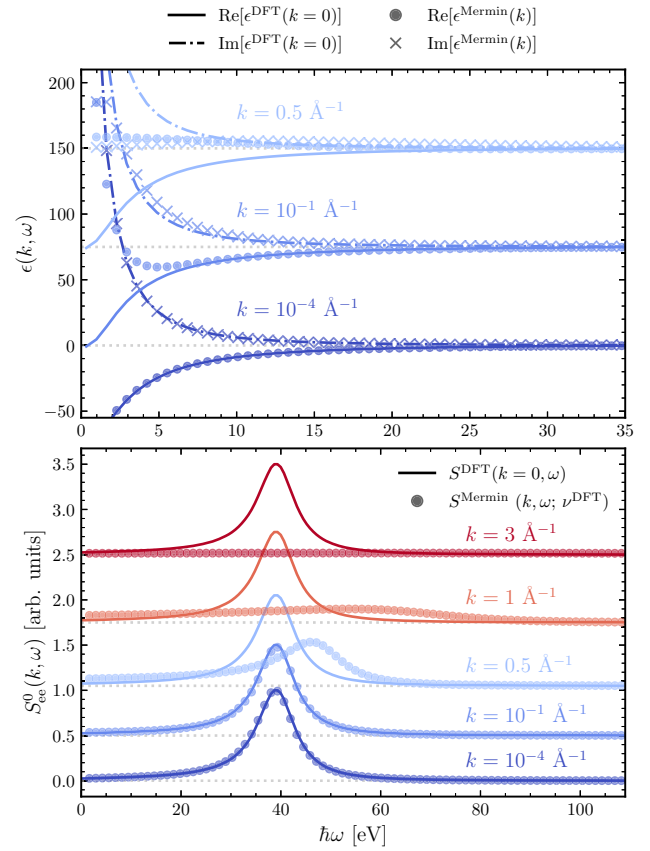


FIG. 2. The top panel shows the free-electron part of the dielectric function  $\epsilon(k, \omega)$  in a beryllium plasma at  $\rho = 5 \text{ g/cm}^3$  and  $T = 100 \text{ eV}$ . The DFT results are given at  $k=0$ , where the solid lines are the real part and the dash-dotted lines are the imaginary part. The Mermin dielectric function from Eq. (5) is calculated with the DFT collision frequency  $\nu^{\text{DFT}}$ . The colors represent different values for  $k$ , while the real and imaginary parts are given by the circles and crosses, respectively. The bottom panel shows the free-electron DSF  $S_{ee}^0(k, \omega)$  computed from DFT (solid lines) at  $k=0$  and from the Mermin dielectric function (circles) at various  $k$ . The DSFs are scaled to the same magnitude and the dielectric function and DSFs are shifted by 75 and 0.5 arb. units, respectively, with respect to the next lowest wave number for readability.

written as

$$\chi(\vec{k}, \omega) = \frac{\chi_{\text{KS}}(\vec{k}, \omega)}{1 - [v(\vec{k}) + f_{\text{XC}}(\vec{k}, \omega)]\chi_{\text{KS}}(\vec{k}, \omega)}, \quad (10)$$

where  $v(\vec{k})$  is the Fourier transform of the Coulomb potential. The exchange-correlation kernel in Eq. (10) is closely connected to the local field corrections mentioned in Sec. II B [42,51,52]. The level of the RPA is achieved for  $f_{\text{XC}} = 0$ , for which the dielectric function can be computed as

$$\epsilon_{\text{KS}}^{\text{RPA}}(\vec{k}, \omega) = 1 - \frac{4\pi}{|\vec{k}|^2} \chi_{\text{KS}}(\vec{k}, \omega). \quad (11)$$

In this framework, the electron-ion coupling is considered, on the one hand, through the snapshots taken from the DFT-MD simulation, which effectively account for static screening via

the static ion-ion structure factor, and on the other hand, through the Kohn-Sham orbitals  $\psi_{i,\vec{g}}$  in Eq. (9), which are the result of a DFT calculation that considers the Coulomb interaction between the electrons and ions.

Because the Mermin dielectric function accounts for electron interactions on the level of the RPA, we set  $f_{XC} = 0$  and use Eq. (11) in Secs. IV A, IV B, and IV C to facilitate comparisons. In Sec. V, we use the adiabatic local density approximation [49,53].

#### D. Computational details

All DFT-MD simulations for this work were performed with the Vienna *ab initio* simulation package (VASP) [54–56]. The electronic and ionic parts are decoupled by the Born-Oppenheimer approximation and, for fixed ion positions, the electronic problem is solved in the finite-temperature DFT approach [57]. In VASP, the electronic wave functions are expanded in a plane-wave basis set up to an energy cutoff  $E_{\text{cut}}$ . After the electronic ground state density is determined self-consistently at every time step, the forces on the ions via Coulomb interactions with other ions and the electron cloud are computed and the ions are moved according to Newton's second law. The temperature control in the MD simulation is performed via the Nosé-Hoover algorithm [58,59] with a mass parameter corresponding to a temperature oscillation period of 40 time steps. All simulations are performed using the exchange-correlation functional of Perdew, Burke, and Ernzerhof (PBE) [60]. For beryllium, we use the PAW\_PBE Be\_sv\_GW 31Mar2010 potential with an energy cutoff of 800 eV for all simulations apart from the compressed case in Sec. IV C for which we use a Coulomb potential with a cutoff of 10000 eV. For further details on the hydrogen simulation parameters, see Ref. [61].

The dynamic electrical conductivity, which is the input for the scheme presented in Fig. 1, was computed from the eigenfunctions and eigenenergies of separate DFT cycles with a more precise energy convergence criterion via the Kubo-Greenwood formula (6). These simulations were performed on at least five snapshots taken at equidistant time steps from the DFT-MD simulation. The scheme described in Sec. II B was implemented using the NUMPY software package [62] for arrays to store the dynamic properties and for the evaluation of simple numerical integration. More elaborate integrals, such as in Eqs. (A7) and (A8), were evaluated using Gaussian quadrature from the SCIPY software package [63]. The Kramers-Kronig transformation between the real and imaginary parts of the dynamic dielectric function and the electrical conductivity was performed according to Maclaurin's formula from Ref. [64].

The LR-TDDFT calculations were performed in the GPAW code [50,65–67]. The same snapshots as for the Kubo-Greenwood calculations were used and a  $2 \times 2 \times 2$  or  $4 \times 4 \times 4$  Monkhorst-Pack grid [68] was employed for calculations of  $k$ -dependent dielectric functions. For the considered conditions, already the Baldereschi mean value point [69] yields converged optical conductivities for the Kubo-Greenwood calculations. For hydrogen, the dielectric function was computed with a plane-wave energy cutoff of at least 50 eV, while for beryllium at least 250 eV were used.

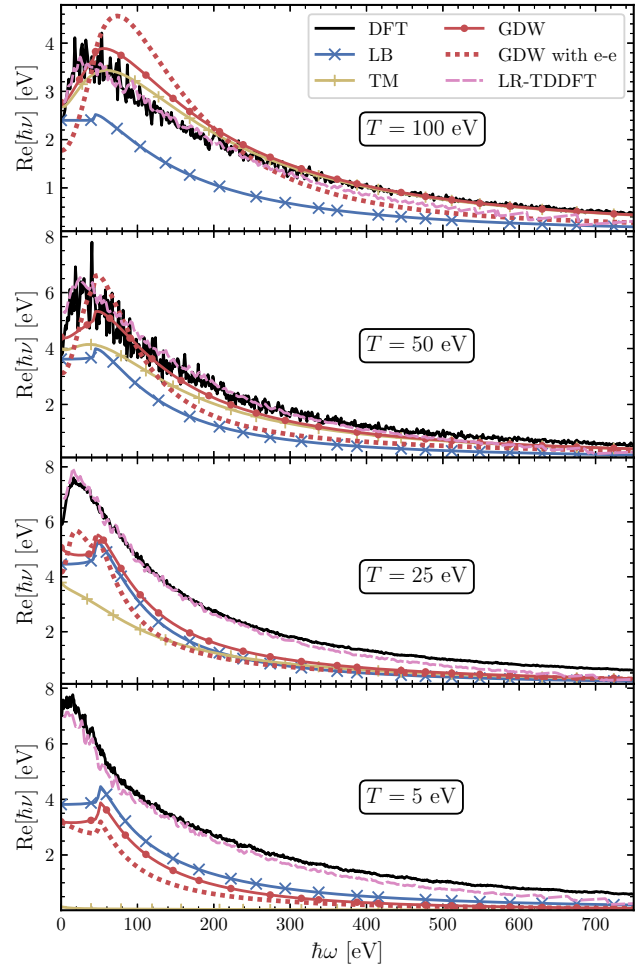


FIG. 3. The real part of the dynamic collision frequency of hydrogen plasmas at  $\rho = 2 \text{ g/cm}^3$  for temperatures ranging from 5 to 100 eV. The DFT and LR-TDDFT collision frequencies determined via Eq. (8) from their respective electrical conductivities are shown in black and pink, respectively. The LB collision frequency is shown in blue with crosses and the  $T$ -matrix approach is shown in yellow with plus symbols. The GDW collision frequencies with and without electron-electron collisions are depicted in red as a dotted line and as a solid line with filled circles, respectively.

### III. DYNAMIC COLLISION FREQUENCY

The workflow presented in Fig. 1 results in a complex dynamic collision frequency  $\nu^{\text{DFT}}(\omega)$ . To study how this collision frequency compares to different levels of analytic approximations, we determine the real part of  $\nu^{\text{DFT}}$  for a hydrogen isochore at  $\rho = 2 \text{ g/cm}^3$  from 5 to 100 eV (see Ref. [61] for numerical details). This temperature range was chosen to illustrate the transition from the WDM regime to the ideal plasma regime. In Fig. 3 we compare these collision frequencies to the Lenard-Balescu (LB) collision frequency, the  $T$ -matrix (TM) approach, and the Gould-DeWitt (GDW) approach. The LB approach goes beyond the Born collision frequency by including dynamic screening, while the TM approach accounts for strong binary collisions by summing up ladder diagrams in the perturbation expansion [70]. The GDW

scheme combines the dynamic screening of the LB approach with the strong collisions of the TM treatment and should, in principle, give the most accurate results. For further details on the analytic approaches, see Refs. [21,70–73]. The aforementioned approaches solely describe electron-ion collisions, but electron-electron (e-e) collisions can be included by modulating the collision frequency with a renormalization factor [21]. The GDW collision frequency including e-e collisions is also indicated in Fig. 3 by the red dotted lines. It is apparent that although the DFT predictions agree well with the TM and GDW approaches at high temperatures, it deviates significantly at lower temperatures where complex many-body and quantum effects contribute strongly. At  $T = 100$  eV, the collision frequency is dominated by strong collisions between ions and electrons. However, the inclusion of e-e collisions via the renormalization factor leads to worse agreement with the DFT results, which is in agreement with recent observations that the Kubo-Greenwood formula applied to DFT lacks e-e collisions [61,74]. Furthermore, we apply the workflow presented in Fig. 1 to the electrical conductivity in the optical limit computed by LR-TDDFT to extract a collision frequency which we show as the pink dashed lines in Fig. 3. At all temperatures, its behavior is very similar to the Kubo-Greenwood results, which indicates that electron-electron collisions are also not included in this description of transport properties. It is remarkable that at high frequencies the LR-TDDFT collision frequency lies significantly below the Kubo-Greenwood results for all considered temperatures. In our tests, this could not be attributed to a lack of convergence in the number of bands or cutoff energy.

#### IV. DYNAMIC STRUCTURE FACTOR

##### A. Hydrogen

Given a dynamic collision frequency  $\nu(\omega)$ , Eqs. (3) and (5) can be used to compute the electronic DSF  $S_{ee}(k, \omega)$  where the  $k$  dependence only enters through the Mermin dielectric function. The LR-TDDFT approach allows direct access to the dielectric function at finite  $k$  by computing transition matrix elements between Kohn-Sham states at different  $k$  points [50]. In Fig. 4, we show the electronic DSF of a hydrogen plasma at  $\rho = 2$  g/cm<sup>3</sup> and  $T = 50$  eV (lower panel) and  $T = 5$  eV (upper panel). The direct computations through LR-TDDFT are shown as solid lines, while we also present DSFs computed via the Mermin dielectric function in conjunction with the DFT and GDW collision frequencies shown in Fig. 3 as dashed and dash-dotted lines, respectively. Additionally, we show the results from the Mermin dielectric function with the Born collision frequency [see Eq. (B1)], which constitutes the often used Born-Mermin approach, as dotted lines. At the lowest wave number shown in Fig. 4,  $k = 0.67$  Å<sup>-1</sup>, we are considering the collective behavior where collisions are important, as can be seen from the dimensionless scattering parameter  $\alpha$  (see Ref. [1] for definition), which is 4.17 and 2.84 for  $T = 5$  and  $T = 50$  eV, respectively.

As expected for a fully ionized hydrogen plasma, the  $k$  dependence encoded by the Mermin dielectric function agrees well with the direct computation via LR-TDDFT for all considered collision frequencies at both conditions.

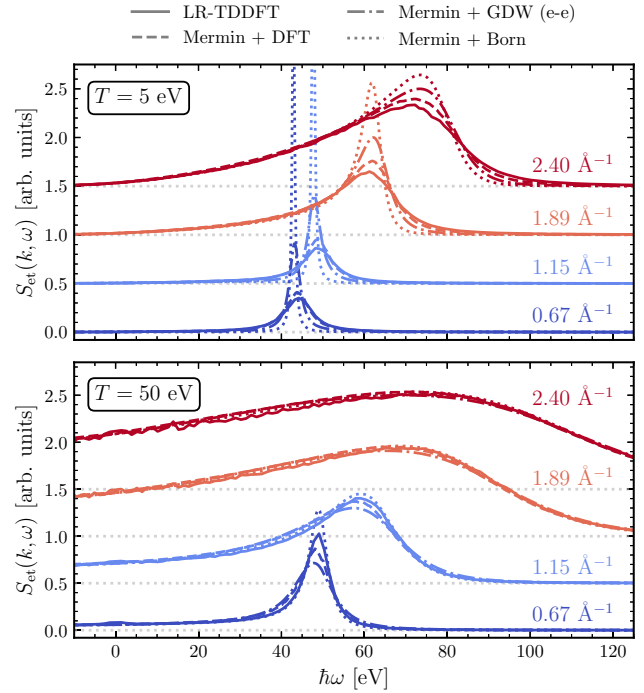


FIG. 4. The inelastic electronic DSF  $S_{ee}(k, \omega)$  of a hydrogen plasma at  $\rho = 2$  g/cm<sup>3</sup> and  $T = 5$  eV (upper panel) and  $T = 50$  eV (lower panel) from  $k = 0.67$  to  $k = 2.40$  Å<sup>-1</sup>. The solid line denotes the direct computation from LR-TDDFT at the respective wave numbers, while the other lines denote DSFs computed from the Mermin dielectric function with the DFT collision frequency (dashed lines), the GDW collision frequency including electron-electron collisions (dash-dotted lines), and the Born collision frequency (dotted lines). The DSFs are shifted by 0.5 arb. units with respect to the next lowest wave number for readability.

However, at  $T = 5$  eV, the damping of the plasmon predicted by LR-TDDFT can only be captured with the DFT collision frequency, especially at small  $k$ . The Born collision frequency leads to a vast overestimation of the plasmon magnitude for  $k$  below  $2.4$  Å<sup>-1</sup> and also the GDW approach with renormalization overestimates the magnitude by a factor of 2 for  $k$  below  $1.15$  Å<sup>-1</sup>. With increasing wave numbers, the collisions become less significant, and the DSFs for all collision frequencies start to converge to the same result. At  $T = 50$  eV, the collisions play a smaller role, which is demonstrated by the largely identical predictions from all collision frequencies for  $k$  above  $1.15$  Å<sup>-1</sup>. It is notable that although the inclusion of electron-electron collisions leads to significant discrepancies between the dynamic collision frequencies in Fig. 3, these differences cannot be observed in the DSF, given the numerical noise. In the LR-TDDFT data, a small additional contribution at  $\hbar\omega = 0$  eV appears, which has also recently been seen in path-integral Monte Carlo simulations [75]. This bump is not included in the Mermin formalism and appears more pronounced at higher temperatures and lower densities (also see Secs. IV B and IV C), leading us to propose that it is connected to bound-bound transitions without energy transfer.

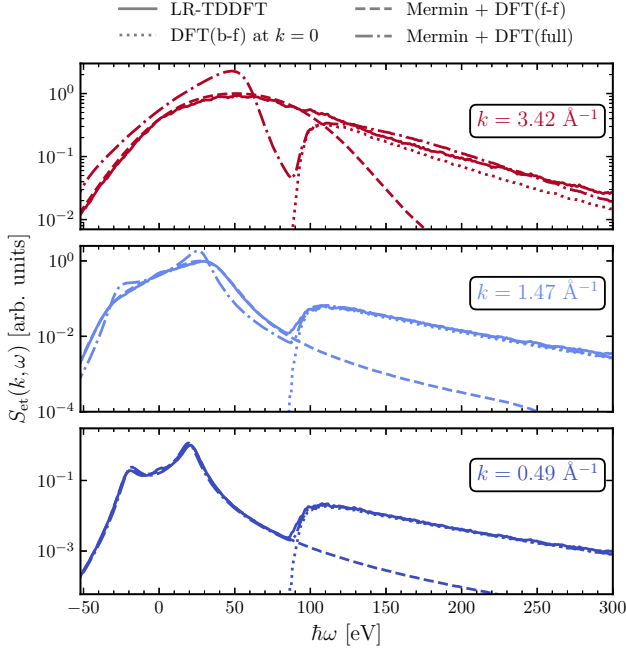


FIG. 5. The inelastic electronic DSF  $S_{\text{et}}(k, \omega)$  of a beryllium plasma at  $\rho = 1.8 \text{ g/cm}^3$  and  $T = 12 \text{ eV}$  for various  $k$  values on a logarithmic scale. The solid lines are direct computations at the given  $k$  using LR-TDDFT. The dash-dotted and the dashed lines denote DSFs computed from the Mermin dielectric function with the full DFT collision frequency, determined from the electrical conductivity including bound-free transitions, and the free-free collision frequency, determined from the electrical conductivity including only free-free transitions, respectively. The dotted lines denote the DSF computed directly from the bound-free conductivity at  $k = 0 \text{ \AA}^{-1}$ .

### B. Isochorically heated beryllium

To investigate the impact of tightly bound states on the presented procedure, we study a beryllium plasma at  $\rho = 1.8 \text{ g/cm}^3$  and  $T = 12 \text{ eV}$ , for which the approach of Ref. [48] predicts a charge state  $Z = 2.1$ . The bound  $1s$  states are energetically clearly separated from the free electrons. The collision frequency can either be determined from the full dynamic electrical conductivity that includes the transitions from the bound  $1s$  states to the conduction band, or from the free-free electrical conductivity by restricting the transition matrix elements in Eq. (6) to transitions originating and ending in the conduction band (for details on this decomposition, see Ref. [48]). In the latter case, only the free-free contribution to the DSF is considered within the Mermin dielectric function, while the bound-free contribution must be approximated by its behavior at  $k \rightarrow 0$ . In Fig. 5, we show the comparison of these two approaches to the direct computation of the electronic DSF using LR-TDDFT. At the lowest wave number  $k = 0.49 \text{ \AA}^{-1}$ , shown in the upper panel, all approaches agree well, as expected due to the construction of the collision frequency which requires equivalence in the limit of small  $k$  [see Eq. (8)]. The separation of the conductivity into a free-free and a bound-free contribution allows us to clearly identify the different terms of the Chihara formula (2) in the DSF.

The dotted line represents the bound-free contribution, which agrees exactly with the LR-TDDFT data above  $\sim 90 \text{ eV}$ , and the dashed line represents the free-free contribution (plasmon), which matches the LR-TDDFT results below  $\sim 90 \text{ eV}$ . Remarkably, the prefactors  $Z_f$  and  $Z_b$  in Eq. (2) which give the respective weighting of these two features come out of the definition of the charge state described in Ref. [48] and agree virtually exactly with the direct computation including all transitions in LR-TDDFT.

At  $k = 1.47 \text{ \AA}^{-1}$  in the middle panel of Fig. 5, the deviation of the approach using the full collision frequency to the other approaches becomes apparent. The bound-free dominated DSF above  $\sim 90 \text{ eV}$  is still well approximated by both the full collision frequency and the bound-free feature at  $k \rightarrow 0$ . Below  $\sim 90 \text{ eV}$ , however, the approach using the full collision frequency, denoted by the dash-dotted line, deviates strongly (note the logarithmic scale) from the LR-TDDFT result. The free-free feature computed solely from the collision frequency based on free-free transitions, denoted by the dashed line, still agrees very well with the LR-TDDFT calculation in this energy regime.

The bottom panel of Fig. 5, showing the DSF at  $k = 3.42 \text{ \AA}^{-1}$ , highlights the complete breakdown of the approach using the full collision frequency. While the DSF is still described adequately above  $\sim 90 \text{ eV}$ , its shape is very different from the LR-TDDFT result below that energy. On the other hand, the separate description of free-free and bound-free contributions again describes the DSF accurately compared to the LR-TDDFT data. However, the approximation of the bound-free feature by its  $k \rightarrow 0$  limit starts to deteriorate at this wave number. At the highest energy shift shown in Fig. 5, this approximation underestimates the LR-TDDFT value by a factor of almost 2. Additionally, at the onset of the bound-free feature around  $100 \text{ eV}$ , it overestimates the DSF compared to the LR-TDDFT as can be seen in Fig. 6 which shows the DSF on a linear scale. The fast deterioration beyond the  $k \rightarrow 0$  limit of the approach using the full collision frequency is expected because the framework of the Mermin dielectric function, which encodes the  $k$  dependence, does not include the existence of bound states. Therefore, any such states that are artificially introduced via the collision frequency cannot be handled correctly in the  $k$  dependence.

Furthermore, in Fig. 6, we show the DSFs computed from the Mermin dielectric function with Born collision frequencies for a plasma with a charge state  $Z = 2$  and  $Z = 4$ . The position of the plasmon peak for  $Z = 2$  agrees well with the DFT spectra, while the position of the  $Z = 4$  plasma is consistently at too high energies, as expected due to the higher free-electron density. However, at low  $k$ , the dampening of the plasmon peak due to the Born collision frequency is too low compared to the DFT data, similar as observed for hydrogen in Fig. 4. At the higher wave numbers, the plasmon-peak position of the DFT results agrees well with the Mermin function using the Born collision frequency at  $Z = 2$ , clearly indicating that the bound  $1s$  states do not contribute to this feature. The inset in Fig. 6 shows the density of states (DOS) of the beryllium plasma, which shows a clear separation between the narrow  $1s$  band, which is fully occupied, and the



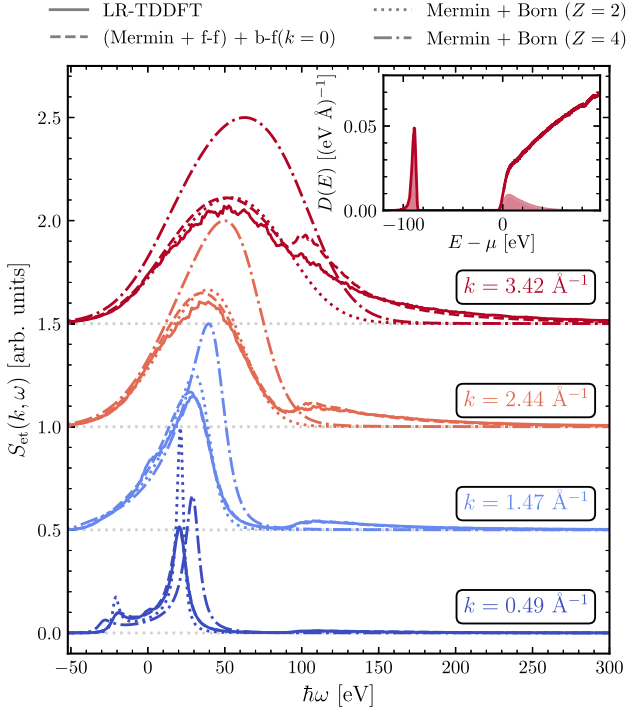


FIG. 6. The inelastic electronic DSF  $S_{\text{et}}(k, \omega)$  of a beryllium plasma at  $\rho = 1.8 \text{ g/cm}^3$  and  $T = 12 \text{ eV}$  for various  $k$  values. The solid lines are direct computations at the given  $k$  using LR-TDDFT, while the dotted and dash-dotted lines denote DSFs computed from the Mermin dielectric function with the Born collision frequency for a plasma with a charge state of  $Z = 2$  and  $Z = 4$ , respectively. The dashed lines represent the sum of the DSF computed through the Mermin dielectric function using the free-free collision frequency and the bound-free DSF at  $k = 0 \text{ \AA}^{-1}$ . The DSFs are shifted by 0.5 arb. units with respect to the next lowest wave number for readability. In the inset, the solid line shows the density of states, while the shaded area denotes the occupied density of states.

conduction band. This clear distinction is the reason why the separate treatment of free-free and bound-free contributions is successful. The bound-free feature does not exhibit a strong  $k$  dependence up to high  $k$  values [23,76], and the plasmon occurs energetically separated in the DSF.

### C. Compressed beryllium

With increasing density and temperature the notion of bound states becomes ill-defined in WDM. The inset in Fig. 7 shows the DOS of a beryllium plasma at  $T = 50 \text{ eV}$  and  $\rho = 40 \text{ g/cm}^3$ , which demonstrates the closing of the band gap compared to the inset in Fig. 6. Furthermore, the former  $1s$  states broaden significantly into a band and the DOS converges towards the  $\sqrt{E}$  behavior of a free-electron gas. Because the band gap is still clearly identifiable, the separate treatment of bound-free and free-free contributions to the DSF presented in the previous section can also be applied to these conditions. Figure 7 shows the results of this separate treatment, as well as the direct computation using LR-TDDFT and the DSF from the Mermin dielectric function using the full collision frequency. While the separate treatment of

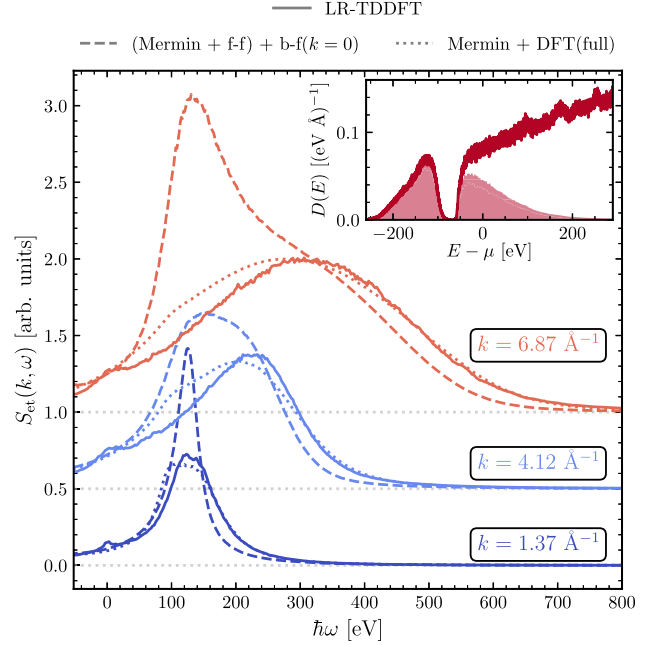


FIG. 7. The inelastic electronic DSF  $S_{\text{et}}(k, \omega)$  of a beryllium plasma at  $\rho = 40 \text{ g/cm}^3$  and  $T = 50 \text{ eV}$  for various  $k$  values. The solid lines are direct computations at the given  $k$  using LR-TDDFT, while the dashed lines represent the sum of the DSF computed through the Mermin dielectric function using the free-free collision frequency and the bound-free DSF at  $k = 0 \text{ \AA}^{-1}$ . The dotted lines denote the DSF computed through the Mermin dielectric function with the full collision frequency. The DSFs are shifted by 0.5 arb. units with respect to the next lowest wave number for readability. In the inset, the solid line shows the density of states, while the shaded area denotes the occupied density of states.

bound-free and free-free contributions yields excellent results for the near-ambient density case in Fig. 5, it poorly approximates the LR-TDDFT results in strongly compressed beryllium shown in Fig. 7. The plasmon peak at  $k = 1.37 \text{ \AA}^{-1}$  is severely underdamped due to the missing bound-free transitions in the collision frequency, which occur in the same energy range as the free-free transitions at these conditions. The use of the Born collision frequency in lieu of the free-free DFT collision frequency leads to an increase of the plasmon-peak magnitude by a factor of 2 (not shown in Fig. 7). The broader peak arising around  $\sim 130 \text{ eV}$  for  $k = 4.12$  and  $k = 6.87 \text{ \AA}^{-1}$  is due to the insufficient approximation of the bound-free feature by its value at  $k = 0 \text{ \AA}^{-1}$ . As can be seen from the LR-TDDFT data, the bound-free features merge with the free-free feature to form one homogeneous feature. At these conditions, using the full collision frequency in the Mermin dielectric function gives better results, which is expected as the former  $1s$  states lose their bound character due to the higher compression and higher temperature. For all considered wave numbers, this approach yields good agreement with the LR-TDDFT data above  $\sim 200 \text{ eV}$ , and approximates the trends below that energy fairly well. Solely at  $\sim 100 \text{ eV}$  this approach predicts a feature that is not visible in the LR-TDDFT results across the considered  $k$  range.

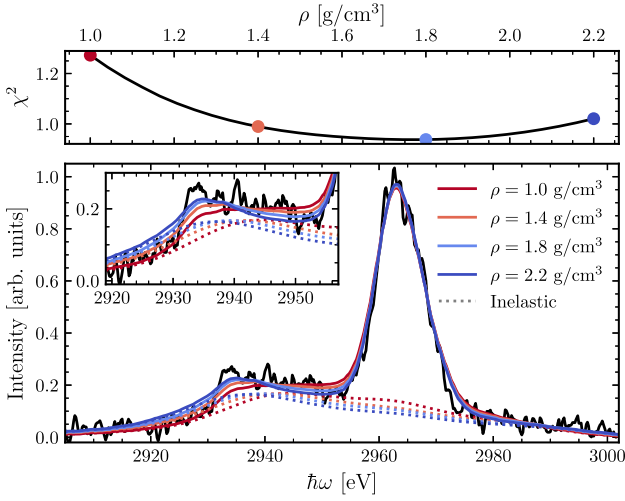


FIG. 8. The lower panel shows the scattering intensity of an isochorically heated beryllium target at  $T = 18$  eV from Ref. [77]. The colors of the solid lines encode different densities used in the LR-TDDFT simulations. The dotted lines denote the inelastic contributions. The upper panel shows the  $\chi^2$  deviation depending on the density used in the simulation where the colored dots correspond to the spectra shown in the lower panel and the black curve is achieved by interpolating to 40 evenly spaced densities between these spectra.

## V. APPLICATION TO EXPERIMENTS

We reanalyze previous XRTS experiments by Döppner *et al.* [77] and Kritcher *et al.* [78] using LR-TDDFT to evaluate the influence of advanced methods on the initially inferred plasma parameters. In general, temperature and density of the target must be considered simultaneously. However, since Döppner *et al.* used detailed balance in their forward-scattering experiment to determine the temperature as  $T = 18$  eV, we use this value and vary the density to find the best agreement with the experimental data. To justify this approach we show the results of a recently suggested model-free temperature diagnostic [79] in Appendix C. For the other experiment, we include the temperature in the analysis.

Firstly, in Fig. 8, we show simulated XRTS spectra with densities ranging from 1.0 to 2.2 g/cm<sup>3</sup> at  $T = 18$  eV together with the forward XRTS spectrum recorded by Döppner *et al.* [77], which was collected at the Omega laser facility at the Laboratory for Laser Energetics at the University of Rochester. The experiment probed a scattering vector of approximately  $k = 1 \text{ \AA}^{-1}$ , enabling access to collective behavior of the plasma. In the original analysis of the experiment a density of 1.17 g/cm<sup>3</sup> was determined by Döppner *et al.* [77]. The electron feature was treated on the level of the RPA without including electron-ion collisions and the ionization was assumed to be  $Z_f = 2.3$ . We compute the electron feature for various densities from LR-TDDFT while including local field corrections via the adiabatic local density approximation [49,53]. The magnitude of the ion feature is left as a free parameter in the  $\chi^2$  minimization. Although none of the computed spectra capture the plasmon at 2930 eV perfectly, the spectrum at  $\rho = 1.8 \text{ g/cm}^3$  yields a 5% lower  $\chi^2$  deviation than any of the other considered densities. The ionization

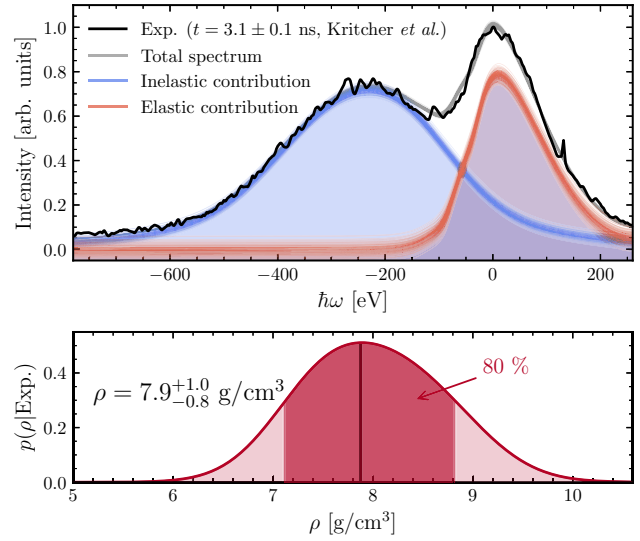


FIG. 9. Scattering intensity of imploding beryllium shells from Ref. [78]. The upper panel shows the experimental data at a delay  $t = 3.1 \pm 0.1$  ns and the posterior prediction for the elastic and inelastic contributions based on LR-TDDFT simulations. The thin lines are 100 spectra computed from parameters randomly sampled from the posterior probability distribution. The shaded areas show the region below the average posterior predictions. The lower panel shows the reduced posterior probability distribution in the density parameter  $\rho$  where the dark shaded area under the curve indicates the 80% highest posterior density interval.

state at this density is  $Z = 2.14$ , determined via the Thomas-Reiche-Kuhn sum rule [48], which is approximately 7% lower than the value used by Döppner *et al.* [77]. Furthermore, the originally determined density is approximately 35% smaller than the here computed density. The remaining disagreement in the shape of the plasmon could be explained by uncertainty in the instrument function or, potentially, local field corrections caused by a more sophisticated exchange-correlation kernel. However, the general spectral position of the plasmon is captured well by our fit and the difference in inferred density highlights the importance of considering many-body physics in the collective scattering regime.

For the experiment by Kritcher *et al.* [78], the temperature cannot reliably be inferred from the detailed balance relation and the temperature must, therefore, be included in the analysis. Furthermore, the instrument and source functions were not available and must be modeled explicitly in the analysis. To analyze the experiments, we simulate spectra on a sufficiently large temperature and density grid and interpolate between them [80] to model arbitrary  $\rho$ - $T$  combinations in this range. Due to the high number of parameters involved in this sort of analysis, we employ Bayesian inference [81] implemented in the PYMC3 software package [82] and use the sequential Monte Carlo algorithm [83,84] for sampling the parameter space. In Fig. 9, we consider the backward XRTS experiment at  $k = 8.42 \text{ \AA}^{-1}$  on imploding beryllium shells by Kritcher *et al.* [78], which was also performed at the Omega laser facility. To analyze the experiment, we simulate spectra on a grid ranging from 2 to 32 g/cm<sup>3</sup> and from 0.1 to 25 eV.



No instrument or source function was supplied in Ref. [78]. We, therefore, use the parametrization of a zinc source given in Ref. [14] and include all the parameters of the instrument response function in the Bayesian analysis. We also replace the Gaussian describing the source broadening by a skewed Gaussian to account for the asymmetry observed in the ion feature. Thus, ten parameters determine the shape of the spectrum, including the physical parameters describing the density and temperature of the sample and the magnitude of the ion feature, and seven parameters describing the experimental setup. The upper panel of Fig. 9 shows an XRTS spectrum collected from an imploding beryllium shell at a delay of  $t = 3.1 \pm 0.1$  ns and the posterior prediction for the elastic and inelastic contribution to the simulated scattering spectrum. The posterior predictions are obtained by sampling parameters according to the posterior probability distribution and using these parameters to simulate the spectrum. The agreement between the simulated spectrum and the experimental data is excellent. The bottom panel of Fig. 9 shows the reduced posterior probability distribution in the density parameter  $\rho$ , which is the full probability distribution integrated over all other parameters. The inferred density  $\rho = 7.9_{-0.8}^{+1.0}$  g/cm<sup>3</sup> corresponds to the maximum *a posteriori* probability and the uncertainties are determined from the 80% highest posterior density interval. With an assumed ionization state  $Z = 2$ , the original analysis by Kritcher *et al.* [78] resulted in estimates of  $\rho = 8.23 \pm 2.24$  g/cm<sup>3</sup> and  $T = 14 \pm 3$  eV. The density, which is the most sensitive plasma parameter with respect to the Compton feature at these conditions, agrees very well with our current study. However, Kritcher *et al.* also used a temperature-dependent model for the ion feature, while we keep the ion feature as a free parameter. Therefore, the inferred temperature is mainly determined from the relative magnitude of the ion feature and the Compton feature. Because the shape of the Compton feature is not very sensitive to the temperature at these conditions, we cannot reliably determine the electron temperature.

## VI. CONCLUSION

In this work, we presented the theoretical basis for computation of DSFs using the Mermin dielectric function with a dynamic complex collision frequency and showed how this framework can be used to extract collision frequencies from DFT simulations. We compared these collision frequencies to several analytic approaches for hydrogen plasmas at  $\rho = 2$  g/cm<sup>3</sup> and, for temperatures approaching the ideal plasma limit, found good agreement with models that incorporate strong collisions. Furthermore, we studied how different collision frequencies impact the DSF calculated from the Mermin dielectric function and compared these results to the direct computation of the DSF at the given wave numbers using LR-TDDFT. For hydrogen, we find good agreement for all collision frequencies at high  $k$ , while at small  $k$ , especially the frequently used Born approximation leads to underdamped plasmon peaks. For beryllium, we showed that a separate treatment of free-free and bound-free contributions to the

DSF yields excellent agreement with the LR-TDDFT for near-ambient densities up to moderate wave numbers ( $k = 3.42$  Å<sup>-1</sup>), while it disagrees significantly for highly compressed beryllium because bound-free transitions interact with the free-free transitions to dampen the plasmon. Therefore, in order to get accurate DSFs over a wide range of wave numbers in extreme conditions, it is imperative to employ *ab initio* approaches like LR-TDDFT or path integral Monte Carlo simulations. Analytic approaches that are based on electron-ion collision frequencies should only be used for the free-free part if free and bound states are clearly separated, and even at these conditions standard descriptions like the Born collision frequency significantly underdampen the plasmon in the collective regime. We applied LR-TDDFT to XRTS experiments on beryllium and found significant differences of roughly 35% in inferred density for small  $k$  for Döppner *et al.* [77] and found good agreement with analytical approaches for backscattering with large  $k$  for Kritcher *et al.* [78].

## ACKNOWLEDGMENTS

We want to thank P. Sperling, B. Witte, M. French, G. Röpke, H. J. Lee, and A. Cangi for many helpful discussions. M.S. and R.R. acknowledge support by the Deutsche Forschungsgemeinschaft (DFG) within the Research Unit FOR 2440. All simulations and analyses were performed at the North-German Supercomputing Alliance (HLRN) and the ITMZ of the University of Rostock. M.B. gratefully acknowledges support by the European Horizon 2020 programme within the Marie Skłodowska-Curie actions (xICE Grant No. 894725) and the NOMIS Foundation. The work of T.D. was performed under the auspices of the U.S. Department of Energy by Lawrence Livermore National Laboratory under Contract No. DE-AC52-07NA27344. D.K. was supported by the Helmholtz Association under VH-NG-1141 and by Deutsche Forschungsgemeinschaft (DFG-German Research Foundation) Project No. 495324226. The work by L.F. and S.G. is supported by DOE Office of Science Fusion Energy Sciences under FWP100182.

## APPENDIX A: DERIVATION OF REAL AND IMAGINARY PARTS OF RPA DIELECTRIC FUNCTION

The collision frequency is generally a complex number

$$\nu(\omega) = \nu_1(\omega) + i\nu_2(\omega), \quad (\text{A1})$$

meaning that its imaginary part acts as a shift of the frequency that enters into  $\epsilon^{\text{RPA}}$  in Eq. (5) and its real part takes on the role of the artificial damping  $\eta$  that was introduced in Eq. (4). However, in this case, the damping is not set to zero after the integration.

Now, we will split Eq. (4) into its real and imaginary parts and consider the modulation of the input frequency  $\omega$  by the complex frequency from Eq. (A1) where the argument of  $\nu$  is

dropped for readability:

$$\text{Re}[\epsilon^{\text{RPA}}(\vec{k}, \omega + iv)] = 1 - \frac{2e^2}{\epsilon_0 k^2} \int \frac{d^3 q}{(2\pi)^3} \frac{(f_{\vec{q}-\vec{k}/2} - f_{\vec{q}+\vec{k}/2})(\hbar\tilde{\omega} - [E_{\vec{q}+\vec{k}/2} - E_{\vec{q}-\vec{k}/2}])}{(\hbar\tilde{\omega} - [E_{\vec{q}+\vec{k}/2} - E_{\vec{q}-\vec{k}/2}])^2 + \hbar^2 v_1^2}, \quad (\text{A2})$$

$$\text{Im}[\epsilon^{\text{RPA}}(\vec{k}, \omega + iv)] = \frac{2e^2}{\epsilon_0 k^2} \int \frac{d^3 q}{(2\pi)^3} \hbar v_1 \frac{f_{\vec{q}-\vec{k}/2} - f_{\vec{q}+\vec{k}/2}}{(\hbar\tilde{\omega} - [E_{\vec{q}+\vec{k}/2} - E_{\vec{q}-\vec{k}/2}])^2 + \hbar^2 v_1^2}. \quad (\text{A3})$$

The shifted frequency  $\tilde{\omega} = \omega - v_2$  is introduced here.

These integrals are performed across the entire momentum space and can therefore be shifted by an arbitrary vector  $\vec{y}$  because for an integral of a function  $G(\vec{x})$ , which goes to 0 as  $|\vec{x}| \rightarrow \infty$ , it holds that

$$\int_{\mathbb{R}^3} d^3 x G(\vec{x}) = \int_{\mathbb{R}^3} d^3 x G(\vec{x} - \vec{y}), \quad \text{with } |\vec{y}| < \infty. \quad (\text{A4})$$

Therefore, we can separate the integrand in Eqs. (A2) and (A3) into two summands with the Fermi occupation of the up- and down-shifted momentum, respectively. We further use Eq. (A4) to shift the momenta in the argument of the Fermi occupation to  $\vec{q}$  in order to get  $f_{\vec{q}}$  as a common prefactor for both summands. The momenta in the subscripts of the energy have to be shifted accordingly. This gives

$$\text{Re}[\epsilon^{\text{RPA}}(\vec{k}, \omega + iv)] = 1 - \frac{2e^2}{\epsilon_0 k^2} 2\pi \int_0^\infty \frac{dq}{(2\pi)^3} q^2 f_q \frac{m_e}{\hbar^2 k} \int_{-1}^1 dz \left( \frac{\kappa - \frac{1}{2}(k + 2qz)}{[\kappa - \frac{1}{2}(k + 2qz)]^2 + \Delta^2} - \frac{\kappa - \frac{1}{2}(-k + 2qz)}{[\kappa - \frac{1}{2}(-k + 2qz)]^2 + \Delta^2} \right) \quad (\text{A5})$$

for the real part and

$$\text{Im}[\epsilon^{\text{RPA}}(\vec{k}, \omega + iv)] = 4\pi \frac{e^2}{\epsilon_0 k^2} \int_0^\infty \frac{dq}{(2\pi)^3} \frac{v_1 m_e^2}{\hbar^3 k^2} q^2 f_q \int_{-1}^1 dz \left( \frac{1}{[\kappa - \frac{1}{2}(k + 2qz)]^2 + \Delta^2} - \frac{1}{[\kappa - \frac{1}{2}(-k + 2qz)]^2 + \Delta^2} \right) \quad (\text{A6})$$

for the imaginary part. Here,  $\vec{k}$  was fixed in the  $q_3$  direction and  $z = \cos \theta$  where  $\theta$  is the angle between  $\vec{q}$  and  $\vec{k}$ . The shorthands  $\kappa = \frac{\tilde{\omega} m_e}{\hbar k}$  and  $\Delta = \frac{m_e v_1}{\hbar k}$  with the electron mass  $m_e$  are introduced. The Fermi occupation can be pulled out of the angle integration as it only depends on the magnitude of the momentum. The integral over the angle can be performed analytically in Eqs. (A5) and (A6), giving

$$\text{Re}[\epsilon^{\text{RPA}}(\vec{k}, \omega + iv)] = 1 + 2\pi \frac{m_e e^2}{\epsilon_0 \hbar^2 k^3} \int_0^\infty \frac{dq}{(2\pi)^3} q f_q \ln \frac{(\Delta^2 + (\kappa - \frac{k}{2} - q)^2)(\Delta^2 + (\kappa + \frac{k}{2} + q)^2)}{(\Delta^2 + (\kappa - \frac{k}{2} + q)^2)(\Delta^2 + (\kappa + \frac{k}{2} - q)^2)} \quad (\text{A7})$$

for the real part, and

$$\begin{aligned} \text{Im}[\epsilon^{\text{RPA}}(\vec{k}, \omega + iv)] &= -4\pi \frac{m_e e^2}{\epsilon_0 \hbar^2 k^3} \int_0^\infty \frac{dq}{(2\pi)^3} q f_q \\ &\times \left[ \arctan \left( \frac{\kappa - \frac{k}{2} - q}{\Delta} \right) + \arctan \left( \frac{\kappa + \frac{k}{2} + q}{\Delta} \right) \right. \\ &\left. - \arctan \left( \frac{\kappa - \frac{k}{2} + q}{\Delta} \right) - \arctan \left( \frac{\kappa + \frac{k}{2} - q}{\Delta} \right) \right] \quad (\text{A8}) \end{aligned}$$

for the imaginary part of the RPA dielectric function modulated by a complex frequency. The remaining integration over  $q$  has to be performed numerically.

## APPENDIX B: EXPRESSIONS FOR THE BORN COLLISION FREQUENCY

One of the most prominent approximations for the collision frequency is the Born collision frequency [21]

$$\begin{aligned} \nu^{\text{Born}}(\omega) &= -i \frac{\epsilon_0 n_i \Omega^2}{6\pi^2 e^2 n_e m_e} \int_0^\infty dq q^6 V_{ei}^2(q) S_{ii}(q) \frac{1}{\omega} \\ &\times [\epsilon^{\text{RPA}}(q, \omega) - \epsilon^{\text{RPA}}(q, 0)], \quad (\text{B1}) \end{aligned}$$

with the ion density  $n_i$ , the electron density  $n_e$ , and the normalization volume  $\Omega$ . There are different approximations for the electron-ion potential  $V_{ei}$  and the static structure factor  $S_{ii}$ . The potential can be approximated by the screened Coulomb potential with the Debye-Hückel or Thomas-Fermi screening parameter depending on the density and temperature regime considered.

Approaches to the structure factor range from the assumption of a homogeneous electron gas [ $S_{ii}(q) = 1$ ] or analytic models like the Debye-Hückel theory to more sophisticated methods like the hypernetted-chain equation or MD simulations. Here, we use the potential

$$V_{ei}(q) = \frac{V_{ei}^{\text{Coulomb}}(q)}{\epsilon^{\text{RPA}}(q, 0)} = -\frac{e_e e_i}{\epsilon_0 \Omega} \frac{1}{q^2 \epsilon^{\text{RPA}}(q, 0)} \quad (\text{B2})$$

and the static structure factor we calculate from our DFT-MD simulations. Equation (B1) is computed by directly calculating its real part and subsequently performing the Kramers-Kronig [85,86] transformation to arrive at the imaginary part.

## APPENDIX C: TEMPERATURE DETERMINATION VIA LAPLACE TRANSFORM

We employ the recently proposed temperature diagnostic based on a two-sided Laplace transform [79] to infer the

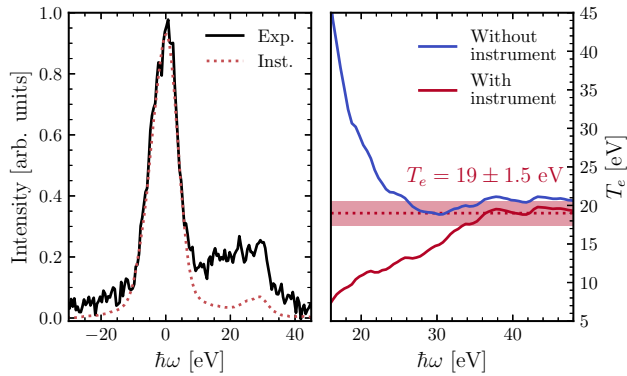


FIG. 10. The left panel shows the scattering intensity and the instrument function from Ref. [77]. The right panel shows the inferred electron temperature according to Ref. [79].

temperature from experiment performed by Döppner *et al.* The left panel of Fig. 10 shows the scattering data and the instrument function, while the right panel shows the inferred temperature according to the procedure described in Ref. [79]. The  $x$  axis denotes the energy up to which the two-sided Laplace transform is performed. A convergence is observed beyond 40 eV and the electron temperature is determined to be  $19 \pm 1.5$  eV. This value agrees within error bars with the electron temperature of 18 eV, originally determined by Döppner *et al.* We, therefore, exclude the electron temperature from the fitting procedure for this experiment.

#### APPENDIX D: CRYSTAL LOCAL FIELD EFFECTS

The expression for LR-TDDFT in Eq. (9) is only valid for homogeneous systems. For a heterogeneous system, the formula is expressed in a basis of reciprocal lattice vectors [87,88]. To get macroscopic information on the dielectric function, the dielectric matrix in the basis of reciprocal lattice vectors must be inverted leading to additional local field

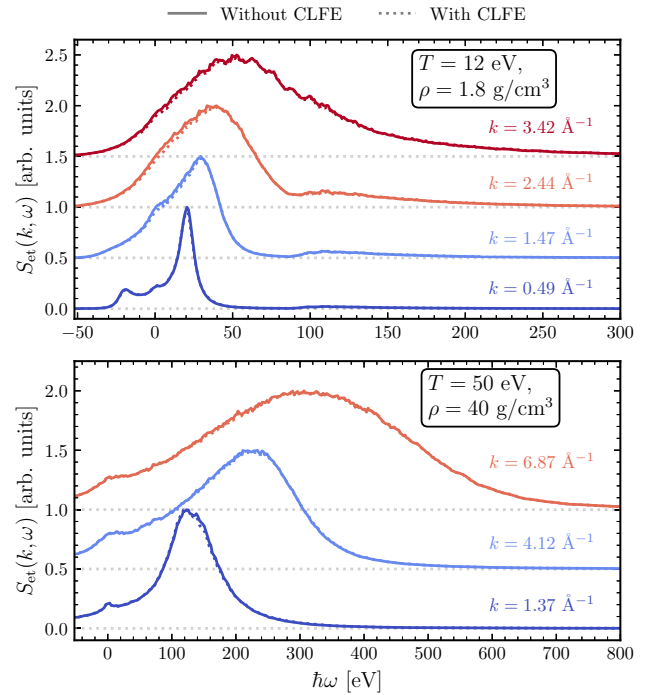


FIG. 11. The upper and lower panels show the DSFs computed from LR-TDDFT shown in Figs. 6 and 7, respectively. The solid lines denote the results without inclusion of CLFE, while the dotted lines represent calculations including CLFE.

effects. These contributions are referred to as crystal local field effects (CLFEs) [89] which are not connected to the local field corrections discussed in Secs. II B and II C. In Fig. 11, we show the DSFs without CLFEs from Secs. IV B and IV C compared to the corresponding results with CLFEs. It is apparent that these effects are negligible in the regime considered in this work.

- [1] S. H. Glenzer and R. Redmer, *Rev. Mod. Phys.* **81**, 1625 (2009).
- [2] L. B. Fletcher, H. J. Lee, T. Döppner, E. Galtier, B. Nagler, P. Heimann, C. Fortmann, S. LePape, T. Ma, M. Millot, A. Pak, D. Turnbull, D. A. Chapman, D. O. Gericke, J. Vorberger, T. White, G. Gregori, M. Wei, B. Barbrel, R. W. Falcone *et al.*, *Nat. Photonics* **9**, 274 (2015).
- [3] R. R. Fäustlin, T. Bornath, T. Döppner, S. Düsterer, E. Förster, C. Fortmann, S. H. Glenzer, S. Göde, G. Gregori, R. Irsig, T. Laarmann, H. J. Lee, B. Li, K.-H. Meiwes-Broer, J. Mithen, B. Nagler, A. Przystawik, H. Redlin, R. Redmer, H. Reinholz *et al.*, *Phys. Rev. Lett.* **104**, 125002 (2010).
- [4] T. Guillot, *Annu. Rev. Earth Planet. Sci.* **33**, 493 (2005).
- [5] R. Helled, J. D. Anderson, M. Podolak, and G. Schubert, *Astrophys. J.* **726**, 15 (2011).
- [6] J. D. Lindl, P. Amendt, R. L. Berger, S. G. Glendinning, S. H. Glenzer, S. W. Haan, R. L. Kauffman, O. L. Landen, and L. J. Suter, *Phys. Plasmas* **11**, 339 (2004).
- [7] H. W. Xu, C. S. Alford, J. C. Cooley, L. A. Dixon, R. E. Hackenberg, S. A. Letts, K. A. Moreno, A. Nikroo, J. R. Wall, and K. P. Youngblood, *Fusion Sci. Technol.* **51**, 547 (2007).
- [8] A. N. Simakov, D. C. Wilson, S. A. Yi, J. L. Kline, D. S. Clark, J. L. Milovich, J. D. Salmonson, and S. H. Batha, *Phys. Plasmas* **21**, 022701 (2014).
- [9] J. Amann, W. Berg, V. Blank, F. J. Decker, Y. Ding, P. Emma, Y. Feng, J. Frisch, D. Fritz, J. Hastings, Z. Huang, J. Krzywinski, R. Lindberg, H. Loos, A. Lutman, H. D. Nuhn, D. Ratner, J. Rzepiela, D. Shu, Y. Shvyd'Ko *et al.*, *Nat. Photonics* **6**, 693 (2012).
- [10] E. E. McBride, T. G. White, A. Descamps, L. B. Fletcher, K. Appel, F. P. Condamine, C. B. Curry, F. Dallari, S. Funk, E. Galtier, M. Gauthier, S. Goede, J. B. Kim, H. J. Lee, B. K. Ofori-Okai, M. Oliver, A. Rigby, C. Schoenwaelder, P. Sun, T. Tschentscher *et al.*, *Rev. Sci. Instrum.* **89**, 10F104 (2018).
- [11] A. Descamps, B. K. Ofori-Okai, K. Appel, V. Cerantola, A. Comley, J. H. Eggert, L. B. Fletcher, D. O. Gericke, S. Göde,

- O. Humphries, O. Karnbach, A. Lazicki, R. Loetzsch, D. McGonegle, C. A. J. Palmer, C. Plueckthun, T. R. Preston, R. Redmer, D. G. Senesky, C. Strohm *et al.*, *Sci. Rep.* **10**, 14564 (2020).
- [12] L. Wollenweber, T. R. Preston, A. Descamps, V. Cerantola, A. Comley, J. H. Eggert, L. B. Fletcher, G. Geloni, D. O. Gericke, S. H. Glenzer, S. Göde, J. Hastings, O. S. Humphries, A. Jenei, O. Karnbach, Z. Konopkova, R. Loetzsch, B. Marx-Glowna, E. E. McBride, D. McGonegle *et al.*, *Rev. Sci. Instrum.* **92**, 013101 (2021).
- [13] S. Frydrych, J. Vorberger, N. J. Hartley, A. K. Schuster, K. Ramakrishna, A. M. Saunders, T. van Driel, R. W. Falcone, L. B. Fletcher, E. Galtier, E. J. Gamboa, S. H. Glenzer, E. Granados, M. J. MacDonald, A. J. MacKinnon, E. E. McBride, I. Nam, P. Neumayer, A. Pak, K. Voigt *et al.*, *Nat. Commun.* **11**, 2620 (2020).
- [14] M. J. MacDonald, A. M. Saunders, B. Bachmann, M. Bethkenhagen, L. Divol, M. D. Doyle, L. B. Fletcher, S. H. Glenzer, D. Kraus, O. L. Landen, H. J. LeFevre, S. R. Klein, P. Neumayer, R. Redmer, M. Schörner, N. Whiting, R. W. Falcone, and T. Döppner, *Phys. Plasmas* **28**, 032708 (2021).
- [15] L. B. Fletcher, J. Vorberger, W. Schumaker, C. Ruyer, S. Goede, E. Galtier, U. Zastrau, E. P. Alves, S. D. Baalrud, R. A. Baggott, B. Barbrel, Z. Chen, T. Döppner, M. Gauthier, E. Granados, J. B. Kim, D. Kraus, H. J. Lee, M. J. MacDonald, R. Mishra *et al.*, *Front. Phys.* **10**, 838524 (2022).
- [16] J. Chihara, *J. Phys. F: Met. Phys.* **17**, 295 (1987).
- [17] J. Chihara, *J. Phys.: Condens. Matter* **12**, 231 (2000).
- [18] B. Crowley and G. Gregori, *High Energy Density Phys.* **13**, 55 (2014).
- [19] D. A. Chapman, D. Kraus, A. L. Kritcher, B. Bachmann, G. W. Collins, R. W. Falcone, J. A. Gaffney, D. O. Gericke, S. H. Glenzer, T. M. Guymier, J. A. Hawrelia, O. L. Landen, S. Le Pape, T. Ma, P. Neumayer, J. Nilsen, A. Pak, R. Redmer, D. C. Swift, J. Vorberger *et al.*, *Phys. Plasmas* **21**, 082709 (2014).
- [20] L. Pauling and J. Sherman, *Z. Kristallograp. - Cryst. Mater.* **81**, 1 (1932).
- [21] H. Reinholz, R. Redmer, G. Röpke, and A. Wierling, *Phys. Rev. E* **62**, 5648 (2000).
- [22] C. Fortmann, A. Wierling, and G. Röpke, *Phys. Rev. E* **81**, 026405 (2010).
- [23] P. Eisenberger and P. M. Platzman, *Phys. Rev. A* **2**, 415 (1970).
- [24] B. B. L. Witte, L. B. Fletcher, E. Galtier, E. Gamboa, H. J. Lee, U. Zastrau, R. Redmer, S. H. Glenzer, and P. Sperling, *Phys. Rev. Lett.* **118**, 225001 (2017).
- [25] K. Ramakrishna, A. Cangi, T. Dornheim, A. Baczewski, and J. Vorberger, *Phys. Rev. B* **103**, 125118 (2021).
- [26] K. Ramakrishna and J. Vorberger, *J. Phys.: Condens. Matter* **32**, 095401 (2020).
- [27] C. Mo, Z. Fu, W. Kang, P. Zhang, and X. T. He, *Phys. Rev. Lett.* **120**, 205002 (2018).
- [28] A. D. Baczewski, L. Shulenburg, M. P. Desjarlais, S. B. Hansen, and R. J. Magyar, *Phys. Rev. Lett.* **116**, 115004 (2016).
- [29] T. Dornheim, S. Groth, and M. Bonitz, *Phys. Rep.* **744**, 1 (2018).
- [30] M. Böhme, Z. A. Moldabekov, J. Vorberger, and T. Dornheim, *Phys. Rev. Lett.* **129**, 066402 (2022).
- [31] H. R. Rüter and R. Redmer, *Phys. Rev. Lett.* **112**, 145007 (2014).
- [32] K.-U. Plagemann, H. R. Rüter, T. Bornath, M. Shihab, M. P. Desjarlais, C. Fortmann, S. H. Glenzer, and R. Redmer, *Phys. Rev. E* **92**, 013103 (2015).
- [33] B. B. L. Witte, M. Shihab, S. H. Glenzer, and R. Redmer, *Phys. Rev. B* **95**, 144105 (2017).
- [34] D. Kraus, B. Bachmann, B. Barbrel, R. W. Falcone, L. B. Fletcher, S. Frydrych, E. J. Gamboa, M. Gauthier, D. O. Gericke, S. H. Glenzer, S. Göde, E. Granados, N. J. Hartley, J. Helfrich, H. J. Lee, B. Nagler, A. Ravasio, W. Schumaker, J. Vorberger, and T. Döppner, *Plasma Phys. Controlled Fusion* **61**, 014015 (2019).
- [35] H. Poole, D. Cao, R. Epstein, I. Golovkin, T. Walton, S. X. Hu, M. Kasim, S. M. Vinko, J. R. Rygg, V. N. Goncharov, G. Gregori, and S. P. Regan, *Phys. Plasmas* **29**, 072703 (2022).
- [36] R. Kubo, *Rep. Prog. Phys.* **29**, 255 (1966).
- [37] J. Lindhard, *Kgl. Danske Videnskab. Selskab Mat.-fys. Medd.* **28**, 1 (1954).
- [38] N. D. Mermin, *Phys. Rev. B* **1**, 2362 (1970).
- [39] A. Selchow and K. Morawetz, *Phys. Rev. E* **59**, 1015 (1999).
- [40] G. Röpke, A. Selchow, A. Wierling, and H. Reinholz, *Phys. Lett. A* **260**, 365 (1999).
- [41] T. Millat, A. Selchow, A. Wierling, H. Reinholz, R. Redmer, and G. Röpke, *J. Phys. A: Math. Gen.* **36**, 6259 (2003).
- [42] A. A. Kugler, *J. Stat. Phys.* **12**, 35 (1975).
- [43] S. Moroni, D. M. Ceperley, and G. Senatore, *Phys. Rev. Lett.* **75**, 689 (1995).
- [44] R. Thiele, T. Bornath, C. Fortmann, A. Höll, R. Redmer, H. Reinholz, G. Röpke, A. Wierling, S. H. Glenzer, and G. Gregori, *Phys. Rev. E* **78**, 026411 (2008).
- [45] K.-U. Plagemann, P. Sperling, R. Thiele, M. P. Desjarlais, C. Fortmann, T. Döppner, H. J. Lee, S. H. Glenzer, and R. Redmer, *New J. Phys.* **14**, 055020 (2012).
- [46] M. French and R. Redmer, *Phys. Plasmas* **24**, 092306 (2017).
- [47] M. Gajdoš, K. Hummer, G. Kresse, J. Furthmüller, and F. Bechstedt, *Phys. Rev. B* **73**, 045112 (2006).
- [48] M. Bethkenhagen, B. B. L. Witte, M. Schörner, G. Röpke, T. Döppner, D. Kraus, S. H. Glenzer, P. A. Sterne, and R. Redmer, *Phys. Rev. Res.* **2**, 023260 (2020).
- [49] E. Engel and R. M. Dreizler, *Density Functional Theory* (Springer Berlin, Heidelberg, 2011).
- [50] J. Yan, J. J. Mortensen, K. W. Jacobsen, and K. S. Thygesen, *Phys. Rev. B* **83**, 245122 (2011).
- [51] M. Petersilka, U. J. Gossmann, and E. K. U. Gross, *Phys. Rev. Lett.* **76**, 1212 (1996).
- [52] Z. Moldabekov, M. Böhme, J. Vorberger, D. Blaschke, and T. Dornheim, *J. Chem. Theory Comput.* **19**, 1286 (2023).
- [53] A. Zangwill and P. Soven, *Phys. Rev. A* **21**, 1561 (1980).
- [54] G. Kresse and J. Hafner, *Phys. Rev. B* **47**, 558 (1993).
- [55] G. Kresse and J. Hafner, *Phys. Rev. B* **49**, 14251 (1994).
- [56] G. Kresse and J. Furthmüller, *Phys. Rev. B* **54**, 11169 (1996).
- [57] N. D. Mermin, *Phys. Rev.* **137**, A1441 (1965).
- [58] S. Nosé, *J. Chem. Phys.* **81**, 511 (1984).
- [59] W. G. Hoover, *Phys. Rev. A* **31**, 1695 (1985).
- [60] J. P. Perdew, K. Burke, and M. Ernzerhof, *Phys. Rev. Lett.* **77**, 3865 (1996).
- [61] G. Röpke, M. Schörner, R. Redmer, and M. Bethkenhagen, *Phys. Rev. E* **104**, 045204 (2021).
- [62] C. R. Harris, K. J. Millman, S. J. van der Walt, R. Gommers, P. Virtanen, D. Cournapeau, E. Wieser, J. Taylor, S. Berg, N. J. Smith, R. Kern, M. Picus, S. Hoyer, M. H. van Kerkwijk,

- M. Brett, A. Haldane, J. Fernández del Río, M. Wiebe, P. Peterson, P. Gérard-Marchant *et al.*, *Nature (London)* **585**, 357 (2020).
- [63] P. Virtanen, R. Gommers, T. E. Oliphant, M. Haberland, T. Reddy, D. Cournapeau, E. Burovski, P. Peterson, W. Weckesser, J. Bright, S. J. van der Walt, M. Brett, J. Wilson, K. J. Millman, N. Mayorov, A. R. J. Nelson, E. Jones, R. Kern, E. Larson, C. J. Carey *et al.*, *Nat. Methods* **17**, 261 (2020).
- [64] K. Ohta and H. Ishida, *Appl. Spectrosc.* **42**, 952 (1988).
- [65] J. J. Mortensen, L. B. Hansen, and K. W. Jacobsen, *Phys. Rev. B* **71**, 035109 (2005).
- [66] J. Enkovaara, C. Rostgaard, J. J. Mortensen, J. Chen, M. Duřak, L. Ferrighi, J. Gavnholt, C. Glinsvad, V. Haikola, H. A. Hansen, H. H. Kristoffersen, M. Kuisma, A. H. Larsen, L. Lehtovaara, M. Ljungberg, O. Lopez-Acevedo, P. G. Moses, J. Ojanen, T. Olsen, V. Petzold *et al.*, *J. Phys.: Condens. Matter* **22**, 253202 (2010).
- [67] A. H. Larsen, J. J. Mortensen, J. Blomqvist, I. E. Castelli, R. Christensen, M. Duřak, J. Friis, M. N. Groves, B. Hammer, C. Hargus, E. D. Hermes, P. C. Jennings, P. B. Jensen, J. Kermode, J. R. Kitchin, E. L. Kolsbjerg, J. Kubal, K. Kaasbjerg, S. Lysgaard, J. B. Maronsson *et al.*, *J. Phys.: Condens. Matter* **29**, 273002 (2017).
- [68] H. J. Monkhorst and J. D. Pack, *Phys. Rev. B* **13**, 5188 (1976).
- [69] A. Baldereschi, *Phys. Rev. B* **7**, 5212 (1973).
- [70] H. Reinholz, *Ann. Phys. (Paris, Fr.)* **30**, 1 (2005).
- [71] R. Thiele, R. Redmer, H. Reinholz, and G. Röpke, *J. Phys. A: Math. Gen.* **39**, 4365 (2006).
- [72] H. A. Gould and H. E. DeWitt, *Phys. Rev.* **155**, 68 (1967).
- [73] G. Röpke and R. Redmer, *Phys. Rev. A* **39**, 907 (1989).
- [74] M. French, G. Röpke, M. Schörner, M. Bethkenhagen, M. P. Desjarlais, and R. Redmer, *Phys. Rev. E* **105**, 065204 (2022).
- [75] T. Dornheim, Z. A. Moldabekov, J. Vorberger, and B. Militzer, *Sci. Rep.* **12**, 708 (2022).
- [76] B. A. Mattern and G. T. Seidler, *Phys. Plasmas* **20**, 022706 (2013).
- [77] T. Döppner, O. Landen, H. Lee, P. Neumayer, S. Regan, and S. Glenzer, *High Energy Density Phys.* **5**, 182 (2009).
- [78] A. L. Kritcher, T. Döppner, C. Fortmann, T. Ma, O. L. Landen, R. Wallace, and S. H. Glenzer, *Phys. Rev. Lett.* **107**, 015002 (2011).
- [79] T. Dornheim, M. Böhme, D. Kraus, T. Döppner, T. R. Preston, Z. A. Moldabekov, and J. Vorberger, *Nat. Commun.* **13**, 7911 (2022).
- [80] H.-C. Weissker, R. Hambach, V. Olevano, and L. Reining, *Phys. Rev. B* **79**, 094102 (2009).
- [81] M. F. Kasim, T. P. Galligan, J. Topp-Mugglestone, G. Gregori, and S. M. Vinko, *Phys. Plasmas* **26**, 112706 (2019).
- [82] J. Salvatier, T. V. Wiecki, and C. Fannesbeck, *PeerJ Comput. Sci.* **2**, e55 (2016).
- [83] P. Del Moral, A. Doucet, and A. Jasra, *J. R. Stat. Soc. B* **68**, 411 (2006).
- [84] S. A. Sisson, Y. Fan, and M. M. Tanaka, *Proc. Natl. Acad. Sci. USA* **104**, 1760 (2007).
- [85] R. de L. Kronig, *J. Opt. Soc. Am.* **12**, 547 (1926).
- [86] H. A. Kramers, *Atti Cong. Intern. Fisici* **2**, 545 (1927).
- [87] S. L. Adler, *Phys. Rev.* **126**, 413 (1962).
- [88] N. Wisner, *Phys. Rev.* **129**, 62 (1963).
- [89] S. Waidmann, M. Knupfer, B. Arnold, J. Fink, A. Fleszar, and W. Hanke, *Phys. Rev. B* **61**, 10149 (2000).

#### 4.4 Carbon ionization at gigabar pressures: An *ab initio* perspective on astrophysical high-density plasmas

**M. Bethkenhagen**

Preparation of the manuscript, creation of new method, DFT-MD simulations and interpretation

**B.B.L. Witte**

Preparation of the manuscript, creation of new method

**M. Schörner**

Preparation of the manuscript, development of new method, interpretation of simulations

**G. Röpke**

Preparation of the manuscript, interpretation of simulations and analytic models

**T. Döppner**

Preparation of the manuscript, interpretation of simulations

**D. Kraus**

Preparation of the manuscript, interpretation of simulations

**S.H. Glenzer**

Preparation of the manuscript, interpretation of simulations

**P.A. Sterne**



Preparation of the manuscript, average atom calculations

**R. Redmer**

Supervision of the project, interpretation of simulations, preparation of the manuscript



## Carbon ionization at gigabar pressures: An *ab initio* perspective on astrophysical high-density plasmas

Mandy Bethkenhagen <sup>1,2</sup> Bastian B. L. Witte,<sup>1,3</sup> Maximilian Schörner,<sup>1,3</sup> Gerd Röpke,<sup>1</sup> Tilo Döppner,<sup>4</sup> Dominik Kraus,<sup>5,6</sup> Siegfried H. Glenzer,<sup>3</sup> Philip A. Sterne,<sup>4</sup> and Ronald Redmer <sup>1</sup>

<sup>1</sup>*Institut für Physik, Universität Rostock, 18051 Rostock, Germany*

<sup>2</sup>*CNRS, École Normale Supérieure de Lyon, Laboratoire de Géologie de Lyon LGLTPE UMR 5276, Centre Blaise Pascal, 46 allée d'Italie Lyon 69364, France*

<sup>3</sup>*SLAC National Accelerator Laboratory, 2575 Sand Hill Road, MS 72, Menlo Park, California 94025, USA*

<sup>4</sup>*Lawrence Livermore National Laboratory, Livermore, California 94550, USA*

<sup>5</sup>*Helmholtz-Zentrum Dresden-Rossendorf, 01328 Dresden, Germany*

<sup>6</sup>*Institute of Solid State and Materials Physics, Technische Universität Dresden, 01069 Dresden, Germany*



(Received 7 December 2019; accepted 28 April 2020; published 1 June 2020)

A realistic description of partially ionized matter in extreme thermodynamic states is critical to model the interior and evolution of the multiplicity of high-density astrophysical objects. Current predictions of its essential property, the ionization degree, rely widely on analytical approximations that have been challenged recently by a series of experiments. Here, we propose an *ab initio* approach to calculate the ionization degree directly from the dynamic electrical conductivity using the Thomas-Reiche-Kuhn sum rule. This density functional theory framework captures genuinely the condensed-matter nature and quantum effects typical for strongly correlated plasmas. We demonstrate this capability for carbon and hydrocarbon, which most notably serve as ablator materials in inertial confinement fusion experiments aiming at recreating stellar conditions. We find a significantly higher carbon ionization degree than predicted by commonly used models, yet validating the qualitative behavior of the average atom model PURGATORIO. Additionally, we find the carbon ionization state to remain unchanged in the environment of fully ionized hydrogen. Our results will not only serve as benchmark for traditional models, but more importantly provide an experimentally accessible quantity in the form of the electrical conductivity.

DOI: [10.1103/PhysRevResearch.2.023260](https://doi.org/10.1103/PhysRevResearch.2.023260)

### I. INTRODUCTION

Modeling the internal structure and thermal evolution of low-mass stars, brown dwarfs, and massive giant planets requires accurate equation-of-state data and even more importantly reliable transport properties of warm dense matter [1,2]. For example, the interplay of convective and radiative transport in low-mass stars is reflected by key plasma quantities such as opacity, electrical conductivity, and absorption coefficients. All those properties can be directly linked to the ionization degree, which is defined as the ratio between the number of free electrons and the sum of all electrons.

The ionization degree can be obtained directly from the Saha equations for the limiting case of the low-density plasma in thermodynamic equilibrium. In this framework, the corresponding ionization energies are defined as the difference between the ground-state energy and its continuum of free states. Generally, the ionization energies crucially depend on

the temperature and density of a plasma. For example, an increase of the density results in a lowering of the ionization energies with respect to their well-known values for isolated atoms due to correlation effects such as screening of the Coulomb interaction, self-energy, strong ion-ion interactions, and Pauli blocking [3,4]. This effect is known as ionization potential depression (IPD) and is inherent to any theory aiming at predicting the ionization degree, which has been subject of many-particle physics for decades [4–7]. For instance, the simple Debye-Hückel theory for static screening has been combined with the ion sphere model by Ecker and Kröll (EK) [8] and later improved by Stewart and Pyatt (SP) [9]. The predictions of both models differ considerably for high-density plasmas as encountered in the deep interior of astrophysical objects, which are characterized by pressures up to the gigabar range and temperatures of several eV to keV.

Matter under such extreme conditions is notoriously challenging to produce and probe. However, great advances in x-ray techniques have been made over the last decade and have been implemented at high-power laser facilities and free electron lasers (FELs), which are now available for the experimental study of high-density plasmas. For instance, the ionization state of isochorically heated solid aluminum was extracted at temperatures in the range 10–100 eV by measuring the *K* edge threshold at the Linac Coherent Light Source

*Published by the American Physical Society under the terms of the Creative Commons Attribution 4.0 International license. Further distribution of this work must maintain attribution to the author(s) and the published article's title, journal citation, and DOI.*

(LCLS) [10–12]. Additionally, the ionization of hot dense aluminum plasmas in the range 1–10 g/cm<sup>3</sup> and 500–700 eV was determined using the ORION laser [13]. Experiments performed at the Omega laser facility and National Ignition Facility compressed hydrocarbon (CH) up to 100 Mbar, and obtained the ionization state via x-ray Thomson scattering (XRTS) [14,15]. The same technique was applied at the LCLS to measure the IPD in carbon plasma [16]. Furthermore, the total intensity of plasma emission in Al and Fe driven by narrow-bandwidth x-ray pulses across a range of wavelengths was utilized to determine the IPD [17]. Generally, the results of those experiments indicate that rather simple models including IPD based on the EK or SP approaches fail to describe the ionization degree correctly [7].

Therefore, novel theoretical concepts for the prediction of the ionization degree are imperatively required and first improvements have been made. For example, a two-step Hartree-Fock-Slater (HFS) approach has been proposed recently [18]. It is a combined atomic-solid-plasma model that permits ionization potential depression studies also for single and multiple core hole states [19], or the dynamic ion-ion structure factor [20]. The latter approach has been generalized to include Pauli blocking effects which are important at high densities [21]. Another route is to characterize ionization by applying molecular dynamics simulations for the ions in combination with electronic structure calculations using density functional theory (DFT-MD) [22–24], which is especially well suited for dense plasmas. So far, all DFT-MD works relied widely on the density of states (DOS), which was used to analyze the evolution of the ionization degree with density and temperature [22–24]. However, none of these works provided a consistent picture of the ionization degree resolving the recent discussion on IPD in high-density plasmas (see Refs. [21,23,25], the comment of Iglesias and Sterne [26], and the reply by Hu [27]). This debate is fundamentally related to the question of how to define the ionization degree properly for warm dense matter, which is characterized by densities beyond the applicability range of the Saha equations and its underlying chemical picture.

In this work, we meet this challenge by calculating the ionization degree directly from an experimentally accessible quantity: the dynamic electrical conductivity. This DFT-MD method takes into account the electronic and ionic correlations in a self-consistent way and, in particular, reflects essential features of high-density plasmas such as the existence of energy bands instead of sharp atomic levels and their occupation according to Fermi-Dirac statistics. In contrast to a definition relying entirely on the DOS, our approach is based on the Thomas-Reiche-Kuhn (TRK) sum rule and the evaluation of electronic transitions originating solely from electrons within the conduction band. This method, which has, to our knowledge, never been used before, is a step toward precisely modeling matter at high energy densities as occurring, e.g., in inertially confined fusion experiments [28] or in low-mass stars [1], brown dwarfs, and massive giant planets [2]. Carbon and CH are chosen as exemplary materials relevant to the afore-mentioned applications.

## II. METHODS

### A. Deriving ionization from the dynamic conductivity and the sum rule

The dynamic electrical conductivity, also referred to as optical conductivity, is calculated from the Kubo-Greenwood formula,

$$\sigma^{\text{tot}}(\omega) = \frac{2\pi e^2}{3V\omega} \sum_{\mathbf{k}\nu\mu} (f_{\mathbf{k}\nu} - f_{\mathbf{k}\mu}) |\langle \mathbf{k}\nu | \hat{v} | \mathbf{k}\mu \rangle|^2 \times \delta(E_{\mathbf{k}\mu} - E_{\mathbf{k}\nu} - \hbar\omega), \quad (1)$$

which can be derived from linear response theory [29–32]. In the above equation, the transition matrix elements  $|\langle \mathbf{k}\nu | \hat{v} | \mathbf{k}\mu \rangle|^2$  with the velocity operator  $\hat{v}$  are the key components. They reflect the transition probability between the initial eigenstate associated with band  $\nu$  and the final eigenstate in band  $\mu$  at a particular  $\mathbf{k}$  point in the Brillouin zone of the simulation box of volume  $V$ . For a given frequency  $\omega$ , only states with a positive difference between eigenenergies  $E_{\mathbf{k}\mu}$  and  $E_{\mathbf{k}\nu}$  contribute to the conductivity. The occupation of initial and final states is weighted with the Fermi-Dirac function  $f_{\mathbf{k}\nu} = [\exp((E_{\mathbf{k}\nu} - \mu_e)/k_B T) + 1]^{-1}$ , whereas  $T$  and  $\mu_e$  denote the temperature and the chemical potential of the electrons, respectively. Additionally,  $e$  and  $\hbar$  represent the elementary charge and the reduced Planck constant in Eq. (1).

The resulting dynamical electrical conductivity has to fulfill the well-known TRK sum rule for dipole transitions [33–37],

$$Z^{\text{tot}} = \frac{N_e^{\text{tot}}}{N_i} = \frac{2m_e V}{\pi e^2 N_i} \int_0^\infty d\omega \sigma^{\text{tot}}(\omega). \quad (2)$$

It yields the ratio between the total number of electrons,  $N_e^{\text{tot}}$ , and the number of ionic centers in the system,  $N_i$ , and establishes an important convergence criterion for the numerical computation of the dynamic electrical conductivity. For the examples chosen in this work, we require charge state values of  $Z^{\text{tot}} = 6$  for carbon and  $Z^{\text{tot}} = 7$  for CH in order to fulfill the TRK sum rule exactly. The number of ionic centers is in both cases  $N_i = N_C = N_{\text{CH}} = 32$ .

Our approach separates the dynamic electrical conductivity  $\sigma^{\text{tot}}$  into three individual parts based on the different nature of electronic transitions in the energy spectrum. Hence, the transition matrix elements for a given  $\mathbf{k}$  point of the sum in Eq. (1) are divided into contributions attributed to intraband transitions in the conduction (c-c) and valence (v-v) bands as well as interband transitions between the valence and conduction bands (v-c):

$$\sigma^{\text{tot}}(\omega) = \sigma^{\text{c-c}}(\omega) + \sigma^{\text{v-c}}(\omega) + \sigma^{\text{v-v}}(\omega), \quad (3)$$

whereas each contribution  $x = \{\text{c-c}, \text{v-c}, \text{v-v}\}$  is required to fulfill the partial TRK sum rule,

$$Z^x \equiv \frac{2m_e V}{\pi e^2 N_i} \int_0^\infty d\omega \sigma^x(\omega). \quad (4)$$

The individual conductivity contributions can be simply identified by choosing an energy within the energy gap between the valence and conduction bands, which is chosen naturally

as the center of the gap between the states of interest. For our carbon and CH examples, the gap is always chosen between the clearly identifiable  $1s$  valence and the continuum as conduction states, which already comprise the  $2s$  and  $2p$  states at the considered conditions.

The electrons effectively contributing to the conductivity in the conduction band are the free electrons  $N_e^{\text{free}}$ , so that we can identify  $\sigma^x(\omega) = \sigma^{c-c}(\omega)$  in Eq. (4) and define the ionization state as

$$Z^{\text{free}} = \frac{N_e^{\text{free}}}{N_i} \equiv Z^{c-c}, \quad (5)$$

which we propose as a new and suitable measure for this quantity in high-density plasmas.

Finally, we calculate the ionization degree,

$$\alpha = \frac{Z^{\text{free}}}{Z^{\text{tot}}} = \frac{N_e^{\text{free}}}{N_e^{\text{tot}}}, \quad (6)$$

which is consequently defined as the ratio between the number of free and total charge carriers per number of ionic centers,  $N_i$ .

### B. Computational details

The DFT-MD simulations for carbon and CH were performed with the Vienna Ab initio Simulation Package (VASP) [38–40]. We considered densities between 20 and 400 g/cm<sup>3</sup> at a temperature of 100 eV resulting in a pressure range between 0.8 and 65 Gbar. These conditions correspond to a maximum compression ratio of more than 100 and, thus, it was crucial to treat all electrons explicitly using the Coulomb potential with a cutoff energy of 15 keV. We considered 32 carbon atoms up to 150 g/cm<sup>3</sup> and 64 carbon atoms for the three highest densities starting at 200 g/cm<sup>3</sup>. For the CH calculations, we added 32 and 64 hydrogen atoms to the respective pure carbon simulations. Additionally, a large number of bands, i.e., typically 800–5000 bands, was required to describe the 192 electrons for carbon and respectively the 224 electrons for CH adequately at the high temperature considered here. Each DFT-MD simulation was run for at least 20 000 time steps with a step size of 50 as for carbon and 10 as for CH in order to reflect the ion dynamics properly. A Nosé-Hoover thermostat [41] was used to control the ion temperature, the Brillouin zone was evaluated at the Baldereschi mean value point [42], and we employed the exchange-correlation (XC) functional of Perdew, Burke, and Ernzerhof (PBE) [43].

The electrical conductivity was determined from an average over 20 snapshots taken from the DFT-MD simulation per condition, and a Monkhorst-Pack  $2 \times 2 \times 2$  grid was used to evaluate the Kubo-Greenwood formula, Eq. (1). We performed extensive convergence tests of the DFT-MD simulations with respect to the energy cutoff, number of bands,  $\mathbf{k}$  point sets, and the number of atoms. Furthermore, we tested the influence of the XC functional used in the DFT cycles by carrying out additional calculations with the local density approximation (LDA) and strongly constrained and appropriately normed (SCAN) [44] functionals. All parameters were chosen such that the TRK sum rule is always fulfilled within 2%, which depends most significantly on the number of explicitly considered bands.

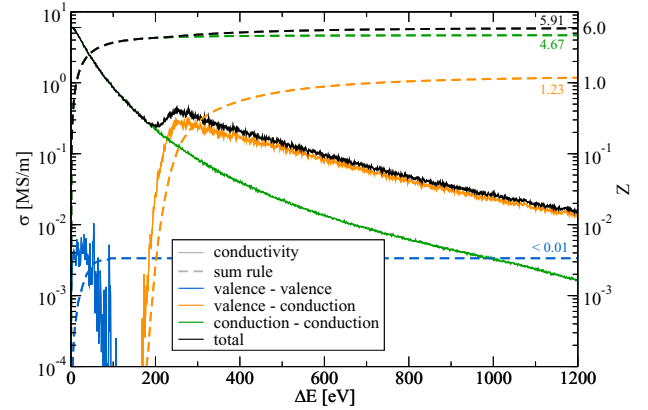


FIG. 1. Electrical conductivity (solid lines) and TRK sum rule values (dashed lines) for a carbon simulation snapshot at 50 g/cm<sup>3</sup> and  $T = 100$  eV. The different colors indicate the total value and the individual components of both quantities according to Eqs. (3) and (4). The final TRK sum rule values are given as colored numbers.

## III. RESULTS

### A. Dynamic electrical conductivity and sum rule

In the following, we demonstrate our method for an exemplary single snapshot of a carbon plasma at 50 g/cm<sup>3</sup> and 100 eV. In Fig. 1, the total dynamic electrical conductivity obtained with the Kubo-Greenwood approach is shown as a solid black line. The curve spans three orders of magnitude over the entire considered energy range and exhibits a pronounced local maximum at about 250 eV, which results from the strong v-c conductivity contribution as becomes apparent upon breaking up the total conductivity into its individual contributions associated with c-c, v-c, and v-v transitions according to Eq. (3). While the c-c contribution dominates the total conductivity at energies below 225 eV, the v-c contribution shows a pronounced threshold behavior at about 175 eV and starts to prevail at energies above 225 eV. At the same time, the v-v transition contribution is almost negligible and can be associated with hopping processes. These can occur as a result of the partial filling of the  $1s$  states at the extreme densities and temperatures investigated here. This behavior is contrary to the known 0 K concept for solids, where the v-v conductivity has to be zero, since the full occupation of the  $1s$  states leads to a vanishing transition probability due to selection rules.

Evaluation of the TRK sum rule for the total conductivity according to Eq. (2) yields a value of 5.91, which agrees with the exact sum rule value of 6 within 2%. The same procedure applied to the v-c contribution results in a value of 1.23, which makes up about 21% of the total sum rule at these conditions. Additionally, the sum rule for the v-v transitions yields a value less than 0.01, which translates to about 0.2% of the total value, and contributes the most at low energies. Finally, the largest total sum rule contribution of the remaining 79% is attributed to the sum rule value applied to the c-c conductivity contribution. The resulting c-c value is 4.67 and will be identified as the ionization state later in this work. Note that all sum rule values given in the following sections are

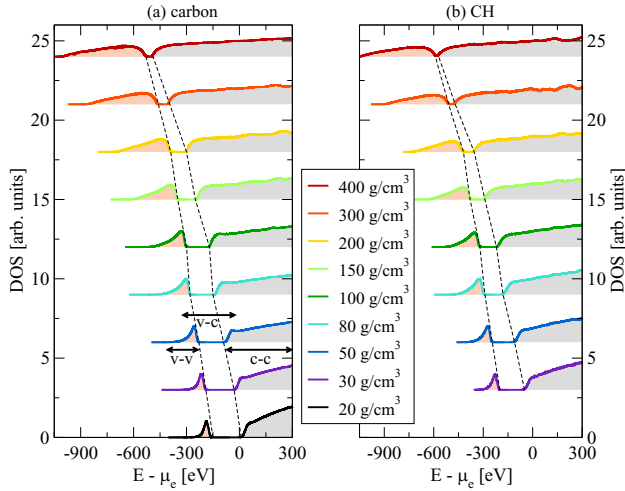


FIG. 2. Density of states of (a) carbon and (b) CH for different densities at  $T = 100$  eV. The pink areas indicate states in the 1s valence band, while states in the conduction band are colored in grey. The black arrows show exemplarily at  $50 \text{ g/cm}^3$  the regions associated with intraband (v-v, c-c) and interband (v-c) transitions. The dashed lines serve as a guide to the eye for the valence-conduction gap.

corrected by a factor  $Z^{\text{exact}}/Z^{\text{tot}}$  that accounts for the numerical uncertainty.

### B. Density of states

In Fig. 2, we show our results for the DOS for carbon and CH for all considered densities at 100 eV. Each DOS shows a pronounced valence band corresponding to the 1s states at small energies and the continuum of conduction states at high energies. Note that all energies are plotted with respect to the chemical potential  $\mu_e$ .

For both materials, we observe the valence bands to broaden and shift towards smaller energies with increasing density. At the same time, the edge of the conduction states moves as well towards smaller energies and the gap between valence and conduction bands narrows with rising density. However, the gap never completely vanishes for the considered conditions and can be still clearly identified at the highest considered density of  $400 \text{ g/cm}^3$ .

The center of the gap between valence and conduction bands serves as input for our method to calculate the different conductivity contributions. In principle, any energy in the gap can be used to separate valence from conduction states. In this work, the gap was determined for every snapshot individually via the smallest energy difference between a state in the valence band and one in the conduction state. This approach is formally equivalent to the highest occupied molecular orbital–lowest unoccupied molecular orbital method, which is applied at  $T = 0$  K to obtain the energy difference between highest occupied and lowest unoccupied molecular orbital.

### C. Conductivity-based ionization

In Fig. 3 we present our DFT-MD results for the ionization state of dense carbon for a temperature of 100 eV as a function

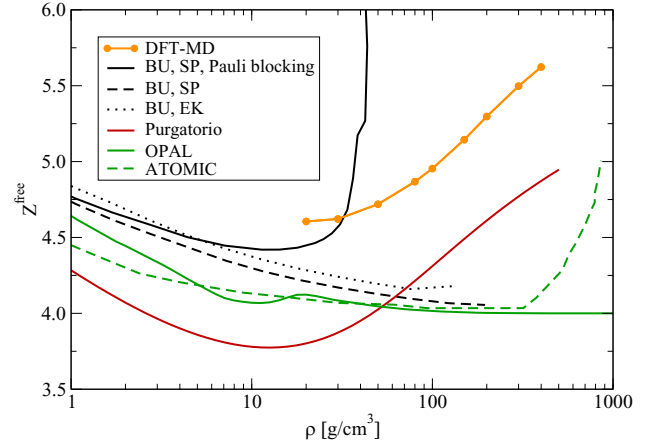


FIG. 3. Ionization state of carbon,  $Z^{\text{free}}$ , derived from DFT-MD simulations (orange line) according to Eq. (5) compared to predictions of PURGATORIO (red line), OPAL (green solid line) [5], ATMOIC (green dashed line) [45], and Beth-Uhlenbeck (BU) calculations (black lines) [21]. The BU results incorporate the two different IPD models by Ecker and Kröll (EK) and Stewart and Pyatt (SP), respectively, and the solid line additionally takes into account Pauli blocking effects.

of density compared to ionization models that are commonly used for modeling astrophysical or inertial confinement fusion (ICF) capsule implosions.

For the lowest densities considered here, the predictions for the carbon ionization state of PURGATORIO [46], ATMOIC [45], OPAL [5], and the different Beth-Uhlenbeck (BU) models [21] agree qualitatively and predict a decreasing ionization state with increasing density. However, two classes of models can be identified for the high-density regime. On one hand, OPAL and both BU models without Pauli blocking generally continue that trend at densities above  $10 \text{ g/cm}^3$ . Among the three models, OPAL predicts the smallest ionization state and converges towards a constant value of 4. The BU curve including IPD based on the SP model gives slightly higher ionization states, but leads to no essential change in the general behavior compared to the BU approach using the EK description instead. On the other hand, the second class of curves, namely, PURGATORIO, ATMOIC, the BU model including Pauli blocking, as well as our DFT-MD results, is characterized by a steep rise at high densities, which is associated with pressure ionization expected under those conditions [47]. However, the slope and onset of this rise in ionization state vary vastly depending on the approach. The steepest slopes are predicted by ATMOIC and the BU model including Pauli blocking, which in contrast to the other two BU models includes electron degeneracy. While ATMOIC suggests the onset of the increase at about  $300 \text{ g/cm}^3$ , the BU model including Pauli blocking predicts this effect at a density an order of magnitude lower. The DFT-MD results confirm the increase, but the slope of our DFT-MD curve is not as steep. Furthermore, our calculations capture the slope of the average atom model PURGATORIO, which evaluates the effective charge at the Wigner-Seitz radius [46]. However, our *ab initio* calculations yield systematically about 0.5 higher ionization states than PURGATORIO, indicating that



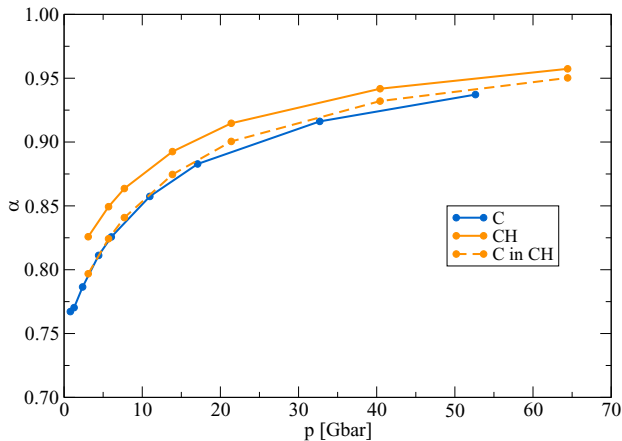


FIG. 4. Ionization degree  $\alpha$  of pure carbon (blue line), CH (solid orange line), and carbon in CH assuming hydrogen to be fully ionized (dashed orange line).

this effective one-particle model is not capturing all important correlation effects treated via our many-body method.

The ionization degree derived according to Eq. (6) is shown as a function of pressure for carbon and CH as solid lines in Fig. 4. For both materials, we find a steady increase of the ionization degree in the range of 0.76 to 0.96. Both curves have a very similar slope, while CH yields slightly higher ionization degrees than carbon. Additionally, we plot the ionization degree of the carbon in CH as a dashed curve, which agrees remarkably well with the values found for pure carbon indicating that the ionization degree of carbon is not changed by adding hydrogen. Note that this curve was calculated under the assumption that all hydrogen atoms are fully ionized. This assumption was tested for pure hydrogen at  $80 \text{ g/cm}^3$ , where we find an ionization degree of 1.00 as a result of the conductivity showing only a c-c contribution and of the vanished gap in the DOS.

#### IV. CONCLUSION

Our presented method to derive the ionization state and ionization degree entirely from *ab initio* simulations by applying the exact TRK sum rule for the dynamic electrical conductivity is entirely self-consistent. This approach naturally takes into account the electronic and ionic correlations; in particular, it reflects essential features of high-density plasmas such as the existence of energy bands instead of sharp

atomic levels and their occupation according to Fermi-Dirac statistics. Our DFT-MD results for the carbon ionization state predict a gradually increasing pressure ionization and strongly disagree with commonly used models such as BU [21], OPAL [5], and ATOMIC [45] in high-density plasmas, yet we confirm the slope of the average atom model PURGATORIO [46]. This indicates that the degeneracy and many-body effects contained in our DFT-MD treatment are crucial to incorporate in any description of the ionization degree and that assumptions based on atomic physics are not valid to treat the ionization balance in high-density plasmas properly. Our conductivity-based method directly exploits knowledge of possible electronic transitions taking into account the nature of the wave functions of different states, which cannot be captured by a method that solely relies on the evaluation of the density of states, and additionally provides an experimentally accessible quantity. Hence, the presented data will be useful for analyzing and predicting conditions in inertial confinement fusion experiments using, e.g., the National Ignition Facility. In particular, these data will guide the understanding of XRTS spectra (see Refs. [48,49]).

Finally, the conditions considered in this work are typically found in high-density astrophysical objects. For instance, densities of  $100 \text{ g/cm}^3$  and temperatures of 100 eV are expected in the interior of M dwarf stars with a mass of  $0.1 M_{\odot}$  (in units of the solar mass). Our results for the ionization degree of carbon and CH can be directly used as input for interior structure models, whose underlying radiation transport models and the nuclear reaction rates crucially rely on ionization models and opacities.

#### ACKNOWLEDGMENTS

We thank Luke B. Fletcher, Martin French, Dirk O. Gericke, Clemens Kellermann, Laurent Masse, and Martin Preising for helpful discussions. M.B., B.B.L.W., M.S., and R.R. acknowledge support by the Deutsche Forschungsgemeinschaft (DFG) within the FOR 2440. B.B.L.W., M.S., and S.H.G. were supported by the DOE Office of Science, Fusion Energy Science under FWP 100182. The work of T.D. and P.A.S. was performed under the auspices of the U.S. Department of Energy by Lawrence Livermore National Laboratory under Contract No. DE-AC52-07NA27344 and supported by Laboratory Directed Research and Development (LDRD) Grant No. 18-ERD-033. D.K. was supported by the Helmholtz Association under VH-NG-1141. The DFT-MD calculations were performed at the North-German Supercomputing Alliance (HLRN) facilities and the computing cluster Titan hosted at the ITMZ at University of Rostock.

- [1] G. Chabrier and I. Baraffe, Structure and evolution of low-mass stars, *Astron. Astrophys.* **327**, 1039 (1997).
- [2] A. Becker, M. Bethkenhagen, C. Kellermann, J. Wicht, and R. Redmer, Material properties for the interiors of massive giant planets and brown dwarfs, *Astron. J.* **156**, 149 (2018).
- [3] R. Zimmermann, K. Kilimann, W.-D. Kraeft, D. Kremp, and G. Röpke, Dynamical screening and self-energy of excitons in the electron-hole plasma, *Phys. Status Solidi B* **90**, 175 (1978).

- [4] W.-D. Kraeft, D. Kremp, W. Ebeling, and G. Röpke, *Quantum Statistics of Charged Particle Systems* (Akademie-Verlag, Berlin, 1986).
- [5] F. J. Rogers, F. J. Swenson, and C. A. Iglesias, OPAL equation-of-state tables for astrophysical applications, *Astrophys. J.* **456**, 902 (1996).
- [6] M. S. Murillo and J. C. Weisheit, Dense plasmas, screened interactions, and atomic ionization, *Phys. Rep.* **302**, 1 (1998).



- [7] B. J. B. Crowley, Continuum lowering—a new perspective, *High Energy Density Phys.* **13**, 84 (2014).
- [8] G. Ecker and Kröll, Lowering of the ionization energy for a plasma in thermodynamic equilibrium, *Phys. Fluids* **6**, 62 (1963).
- [9] J. C. Stewart and K. D. Pyatt, Jr., Lowering of ionization potentials in plasmas, *Astrophys. J.* **144**, 1203 (1966).
- [10] S. M. Vinko, O. Ciricosta, B. I. Cho, K. Engelhorn, H.-K. Chung, C. R. D. Brown, T. Burian, J. Chalupsky, R. Falcone, C. Graves, V. Hajkova, A. Higginbotham, L. Juha, J. Krzywinski, H. J. Lee, M. Messerschmidt, C. D. Murphy, Y. Ping, A. Scherz, W. Schlotter, S. Toleikis, J. Turner, L. Vysin, T. Wang, B. Wu, U. Zastra, D. Zhu, R. W. Lee, P. A. Heimann, B. Nagler, and J. S. Wark, Creation and diagnosis of a solid-density plasma with an x-ray free electron laser, *Nature* **482**, 59 (2012).
- [11] O. Ciricosta, S. M. Vinko, H.-K. Chung, B.-I. Cho, C. R. D. Brown, T. Burian, J. Chalupsky, K. Engelhorn, R. W. Falcone, C. Graves, V. Hajkova, A. Higginbotham, L. Juha, J. Krzywinski, H. J. Lee, M. Messerschmidt, C. D. Murphy, Y. Ping, D. S. Rackstraw, A. Scherz, W. Schlotter, S. Toleikis, J. J. Turner, L. Vysin, T. Wang, B. Wu, U. Zastra, D. Zhu, R. W. Lee, P. Heimann, B. Nagler, and J. S. Wark, Direct Measurements of the Ionization Potential Depression in a Dense Plasma, *Phys. Rev. Lett.* **109**, 065002 (2012).
- [12] B. I. Cho, K. Engelhorn, S. M. Vinko, H.-K. Chung, O. Ciricosta, D. S. Rackstraw, R. W. Falcone, C. R. D. Brown, T. Burian, J. Chalupský, C. Graves, V. Hájková, A. Higginbotham, L. Juha, J. Krzywinski, H. J. Lee, M. Messerschmidt, C. Murphy, Y. Ping, N. Rohringer, A. Scherz, W. Schlotter, S. Toleikis, J. J. Turner, L. Vysin, T. Wang, B. Wu, U. Zastra, D. Zhu, R. W. Lee, B. Nagler, J. S. Wark, and P. A. Heimann, Resonant  $K\alpha$  Spectroscopy of Solid-Density Aluminum Plasmas, *Phys. Rev. Lett.* **109**, 245003 (2012).
- [13] D. J. Hoarty, P. Allan, S. F. James, C. R. D. Brown, L. M. R. Hobbs, M. P. Hill, J. W. O. Harris, J. Morton, M. G. Brookes, R. Shepherd, J. Dunn, H. Chen, E. Von Marley, P. Beiersdorfer, H.-K. Chung, R. W. Lee, G. Brown, and J. Emig, Observations of the Effect of Ionization-Potential Depression in Hot Dense Plasma, *Phys. Rev. Lett.* **110**, 265003 (2013).
- [14] L. B. Fletcher, A. L. Kritcher, A. Pak, T. Ma, T. Döppner, C. Fortmann, L. Divol, O. S. Jones, O. L. Landen, H. A. Scott, J. Vorberger, D. A. Chapman, D. O. Gericke, B. A. Mattern, G. T. Seidler, G. Gregori, R. W. Falcone, and S. H. Glenzer, Observations of Continuum Depression in Warm Dense Matter with X-Ray Thomson Scattering, *Phys. Rev. Lett.* **112**, 145004 (2014).
- [15] D. Kraus, D. A. Chapman, A. L. Kritcher, R. A. Baggott, B. Bachmann, G. W. Collins, S. H. Glenzer, J. A. Hawreliak, D. H. Kalantar, O. L. Landen, T. Ma, S. LePape, J. Nilsen, D. C. Swift, P. Neumayer, R. W. Falcone, D. O. Gericke, and T. Döppner, X-ray scattering measurements on imploding CH spheres at the National Ignition Facility, *Phys. Rev. E* **94**, 011202(R) (2016).
- [16] D. Kraus, B. Bachmann, B. Barbrel, R. W. Falcone, L. B. Fletcher, S. Frydrych, E. J. Gamboa, M. Gauthier, D. O. Gericke, S. H. Glenzer, S. Göde, E. Granados, N. J. Hartley, J. Helfrich, H. J. Lee, B. Nagler, A. Ravasio, W. Schumaker, J. Vorberger, and T. Döppner, Characterizing the ionization potential depression in dense carbon plasmas with high-precision spectrally resolved x-ray scattering, *Plasma Phys. Controlled Fusion* **61**, 014015 (2018).
- [17] M. F. Kasim, J. S. Wark, and S. M. Vinko, Validating continuum lowering models via multi-wavelength measurements of integrated x-ray emission, *Sci. Rep.* **8**, 6276 (2018).
- [18] S.-K. Son, R. Thiele, Z. Jurek, B. Ziaja, and R. Santra, Quantum-Mechanical Calculation of Ionization-Potential Lowering in Dense Plasmas, *Phys. Rev. X* **4**, 031004 (2014).
- [19] F. B. Rosmej, Ionization potential depression in an atomic-solid-plasma picture, *J. Phys. B: At. Mol. Opt. Phys.* **51**, 09LT01 (2018).
- [20] C. L. Lin, G. Röpke, H. Reinholz, and W. D. Kraeft, Ionization potential depression and optical spectra in a Debye plasma model, *Contrib. Plasma Phys.* **57**, 518 (2017).
- [21] G. Röpke, D. Blaschke, T. Döppner, C. Lin, W. D. Kraeft, R. Redmer, and H. Reinholz, Ionization potential depression and Pauli blocking in degenerate plasmas at extreme densities, *Phys. Rev. E* **99**, 033201 (2019).
- [22] S. M. Vinko, O. Ciricosta, and J. S. Wark, Density functional theory calculations of continuum lowering in strongly coupled plasmas, *Nat. Commun.* **5**, 3533 (2014).
- [23] S. X. Hu, Continuum Lowering and Fermi-Surface Rising in Strongly Coupled and Degenerate Plasmas, *Phys. Rev. Lett.* **119**, 065001 (2017).
- [24] K. P. Driver, F. Soubiran, and B. Militzer, Path integral Monte Carlo simulations of warm dense aluminum, *Phys. Rev. E* **97**, 063207 (2018).
- [25] C. A. Iglesias, A plea for a reexamination of ionization potential depression measurements, *High Energy Density Phys.* **12**, 5 (2014).
- [26] Carlos A. Iglesias and Philip A. Sterne, Comment on “Continuum Lowering and Fermi-Surface Rising in Strongly Coupled and Degenerate Plasmas”, *Phys. Rev. Lett.* **120**, 119501 (2018).
- [27] S. X. Hu, Reply, *Phys. Rev. Lett.* **120**, 119502 (2018).
- [28] S. H. Glenzer *et al.*, Cryogenic thermonuclear fuel implosions on the National Ignition Facility, *Phys. Plasmas* **19**, 056318 (2012).
- [29] R. Kubo, Statistical-mechanical theory of irreversible processes. I. General theory and simple applications to magnetic and conduction problems, *J. Phys. Soc. Jpn.* **12**, 570 (1957).
- [30] D. A. Greenwood, The Boltzmann equation in the theory of electrical conduction in metals, *Proc. Phys. Soc.* **71**, 585 (1958).
- [31] V. Recoules and J.-P. Crocombette, Ab initio determination of electrical and thermal conductivity of liquid aluminum, *Phys. Rev. B* **72**, 104202 (2005).
- [32] B. Holst, M. French, and R. Redmer, Electronic transport coefficients from ab initio simulations and application to dense liquid hydrogen, *Phys. Rev. B* **83**, 235120 (2011).
- [33] W. Thomas, Über die Zahl der Dispersionselektronen, die einem stationären Zustände zugeordnet sind. (Vorläufige Mitteilung), *Naturwissenschaften* **13**, 627 (1925).
- [34] F. Reiche and W. Thomas, Über die Zahl der Dispersionselektronen, die einem stationären Zustand zugeordnet sind, *Z. Phys.* **34**, 510 (1925).
- [35] W. Kuhn, Über die Gesamtstärke der von einem Zustände ausgehenden Absorptionslinien, *Z. Phys.* **33**, 408 (1925).
- [36] G. D. Mahan, *Many-Particle Physics* (Plenum Publishers, New York, 2000).

- [37] M. P. Desjarlais, J. D. Kress, and L. A. Collins, Electrical conductivity for warm, dense aluminum plasmas and liquids, *Phys. Rev. E* **66**, 025401(R) (2002).
- [38] G. Kresse and J. Hafner, Ab initio molecular-dynamics for liquid-metals, *Phys. Rev. B* **47**, 558 (1993).
- [39] G. Kresse and J. Hafner, Ab initio molecular-dynamics simulation of the liquid-metal–amorphous-semiconductor transition in germanium, *Phys. Rev. B* **49**, 14251 (1994).
- [40] G. Kresse and J. Furthmüller, Efficient iterative schemes for *ab initio* total-energy calculations using a plane-wave basis set, *Phys. Rev. B* **54**, 11169 (1996).
- [41] S. Nosé, A unified formulation of the constant temperature molecular dynamics methods, *J. Chem. Phys.* **81**, 511 (1984).
- [42] A. Baldereschi, Mean-value point in the Brillouin zone, *Phys. Rev. B* **7**, 5212 (1973).
- [43] J. P. Perdew, K. Burke, and M. Ernzerhof, Generalized Gradient Approximation Made Simple, *Phys. Rev. Lett.* **77**, 3865 (1996).
- [44] J. Sun, A. Ruzsinszky, and J. P. Perdew, Strongly Constrained and Appropriately Normed Semilocal Density Functional, *Phys. Rev. Lett.* **115**, 036402 (2015).
- [45] P. Hakel, M. E. Sherill, S. Mazevet, J. Abdallah, Jr., J. anf Colgan, D. P. Kilcrease, N. H. Magee, C. J. Fontes, and H. L. Zhang, The new Los Alamos opacity code ATOMIC, *J. Quantum Spectrosc. Radiat. Transf.* **99**, 265 (2006).
- [46] P. A. Sterne, S. B. Hansen, B. G. Wilson, and W. A. Isaacs, Equation of state, occupation probabilities and conductivities in the average atom Purgatorio code, *High Energy Density Phys.* **3**, 278 (2007).
- [47] N. F. Mott, The transition to the metallic state, *Philos. Mag.* **6**, 287 (1961).
- [48] B. B. L. Witte, L. B. Fletcher, E. Galtier, E. Gamboa, H. J. Lee, U. Zastra, R. Redmer, S. H. Glenzer, and P. Sperling, Warm Dense Matter Demonstrating Non-Drude Conductivity from Observations of Nonlinear Plasmon Damping, *Phys. Rev. Lett.* **118**, 225001 (2017).
- [49] D. Kraus, T. Döppner, A. L. Kritcher, A. Yi, K. Boehm, B. Bachmann, L. Divol, L. B. Fletcher, S. H. Glenzer, O. L. Landen, N. Masters, A. M. Saunders, C. Weber, R. W. Falcone, and P. Neumayer, Platform for spectrally resolved x-ray scattering from imploding capsules at the National Ignition Facility, *J. Phys. Conf. Ser.* **717**, 012067 (2016).

## 4.5 Reaching for the stars with an ab initio perspective on collective x-ray Thomson scattering at the National Ignition Facility

### Author contributions

#### **M. Schörner**

Preparation of the manuscript, LR-TDDFT simulations, Bayesian inference, interpretation of experiment and simulations

#### **T. Döppner**

Project co-PI – beam time allocation, experimental design (lead), interpretation of experiment and simulations, preparation of the manuscript

#### **M. Bethkenhagen**

DFT-MD simulations, interpretation of experiment and simulations, preparation of the manuscript

#### **M.J. MacDonald**

Experimental design (backlighter design and analysis), data analysis (raytracing XRTS), interpretation of experiment and simulations

#### **L. Fletcher**

Data analysis (XRTS data), interpretation of experiment, and simulations

#### **C. Allen**

Data reduction and analysis

#### **B. Bachmann**

Experimental support, data analysis (imaging data)

#### **L. Divol**

Experimental design and post-shot analysis (rad-hydro simulations)

#### **M. Herrmann**

Stellar evolution simulations

#### **O. Landen**

Experimental design (co-lead)

#### **P. Neumayer**

Experimental design, data analysis (raytracing XRTS)

#### **A. Saunders**

Experimental design (backlighter design, related rad-hydro simulations)

#### **B.B.L. Witte**

Development of theoretical analysis

#### **A. Yi**

Experimental design (rad-hydro simulations)

#### **D. Kraus**

Experimental design, data reduction, and analysis, interpretation of experiment and simulations, preparation of the manuscript

#### **S.H. Glenzer**

Project co-PI – beam time allocation, interpretation of experiment and simulations, preparation of the manuscript

**R. Redmer**

Project PI – beam time allocation, interpretation of experiment and simulations, preparation of the manuscript

## Reaching for the stars – using collective x-ray Thomson scattering at the National Ignition Facility

Maximilian Schörner<sup>1</sup>, Tilo Döppner<sup>2</sup>, Mandy Bethkenhagen<sup>3,4</sup>, Michael J. MacDonald<sup>2</sup>, Luke Fletcher<sup>5</sup>, Cameron H. Allen<sup>6</sup>, Benjamin Bachmann<sup>3</sup>, Laurent Divol<sup>2</sup>, Marcel Herrmann<sup>1,7</sup>, Otto L. Landen<sup>2</sup>, Paul Neumayer<sup>8</sup>, Alston Saunders<sup>2</sup>, Bastian B.L. Witte<sup>1</sup>, Austin Yi<sup>9</sup>, Dominik Kraus<sup>1,7</sup>, Siegfried H. Glenzer<sup>3</sup>, and Ronald Redmer<sup>1</sup>

<sup>1</sup>*Institut für Physik, Universität Rostock, D-18051 Rostock, Germany*

<sup>2</sup>*Lawrence Livermore National Laboratory, Livermore, California 94550, USA*

<sup>3</sup>*École Normale Supérieure de Lyon, Université Lyon 1,*

*Laboratoire de Géologie de Lyon, CNRS UMR 5276, 69364 Lyon Cedex 07, France*

<sup>4</sup>*Institute of Science and Technology Austria, 3400 Klosterneuburg, Austria*

<sup>5</sup>*SLAC National Accelerator Laboratory, Menlo Park, California 94025, USA*

<sup>6</sup>*University of Nevada, Reno, Nevada 89557, USA*

<sup>7</sup>*Astrophysikalisches Institut und Universitäts-Sternwarte, Schillergässchen 2, D-07745 Jena, Germany*

<sup>8</sup>*GSI Helmholtz-Zentrum für Schwerionenforschung, 64291 Darmstadt, Germany*

<sup>9</sup>*Los Alamos National Laboratory, Los Alamos, New Mexico 87545, USA*

<sup>10</sup>*Helmholtz-Zentrum Dresden-Rossendorf, Bautzner Landstraße 400, 01328 Dresden, Germany*

(Dated: July 11, 2023)

Red dwarf stars constitute about 76% of all main sequence stars in the solar neighborhood and are considered to be viable hosts for habitable exoplanets. Understanding the evolution of these stars and predicting the composition and interior structure in their later evolutionary stages is essential for estimating their habitable zone, i.e., the range of orbits where water is liquid on the surface of potential planets at about atmospheric pressure. Hence, precise equation of state data and conductivities for red dwarf interior conditions, that are governed by pressures of several Gbar (1 Gbar = 1 billion atmospheres) and temperatures of hundreds of eV (i.e. well exceeding millions of Kelvin), are needed. For this purpose, we have performed the first X-ray scattering experiments in forward scattering geometry at the National Ignition Facility (NIF) which probe the collective behavior of the electrons, exposing dielectric properties via the collisional damping of the plasmon. The spectra are analyzed using a scattering model solely based on DFT simulations, resulting in pressures above 1 Gbar. The inferred electrical conductivity is approximately 50% smaller than predicted by standard analytic approaches for the extreme conditions in the deep interior of red dwarfs.

### INTRODUCTION

Red dwarf stars (spectral type M) form the low-mass end of the main sequence and possess unique properties compared to all other stars on the main sequence making them well-suited candidates for hosting habitable planets. Stellar models indicate that stars with  $M < 0.25M_{\odot}$ , where  $M_{\odot}$  is the Solar mass, are fully convective for a long time of their hydrogen burning period so that they can accumulate a large helium fraction in their interior. Full convection may also explain magnetic fields of several thousand Gauss (kG) which are the highest of all stars<sup>1</sup>. By comparison, the Sun's magnetic field appears rather quiet as its field strength is less than one Gauss in the photosphere. The strong magnetic activity of M stars is connected with frequent flares which modulate the luminosity of the star considerably. Furthermore, stars with  $M < 0.2M_{\odot}$  will never pass through the red giant phase, contrary to all other main sequence stars. M stars have smaller radii than Sun-like stars which facilitate the observation of transiting extrasolar planets, in particular in the habitable zone of the star<sup>2</sup>.

The study of matter at the extreme densities and temperatures in the central region of stars in the laboratory is challenging. For instance, our nearest neighbor red dwarf Proxima Centauri is characterized by a mass of  $0.122 M_{\odot}$

and a surface temperature of 3050 K ( $\sim 0.26$  eV). At its core, predicted densities exceed  $100 \text{ g/cm}^3$  and temperatures reach beyond  $3 \times 10^6$  K ( $\sim 259$  eV)<sup>5</sup>. Over the past two decades, experimental high-energy density facilities such as high-power lasers<sup>6</sup> and pulsed power accelerators<sup>7</sup> were commissioned which drive matter to unprecedented high densities and temperatures characteristic of conditions in the deep interior of massive giant planets, brown dwarfs, and even stars. Recent studies have shown the capability to reach these conditions<sup>8–11</sup>. This development enables a new kind of laboratory astrophysics<sup>12</sup> by directly testing theoretical predictions for the equation of state (EOS), ionization degree, electrical and thermal conductivity, and opacity for such extreme states of matter. Especially transport properties, such as electrical conductivity and opacity, have a crucial impact on interior, evolution and dynamo models of stellar objects. Still fairly simple relaxation time approximations are commonly used in these models<sup>13,14</sup>. For low-mass stars, the uncertainty in radiative opacities has a significant impact on predictions of luminosity and the central hydrogen exhaustion time<sup>15</sup>. It is vital to study transport properties at these extreme conditions by more sophisticated numerical methods and experimentally verify the results. In particular, using the National Ignition Facility (NIF) at the Lawrence Livermore National Laboratory



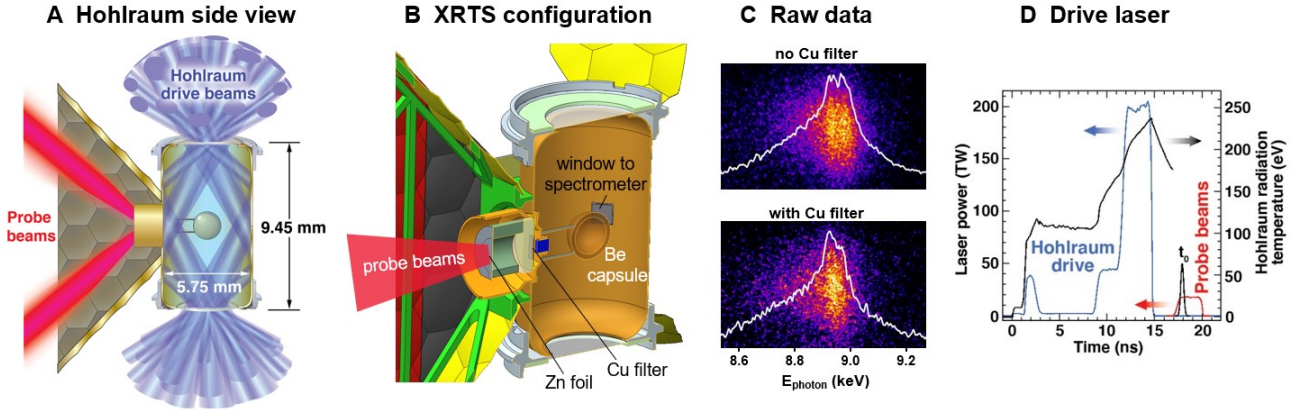


FIG. 1. Schematic of the experiment and examples of raw data. **A** Side view of the hohlraum target: 184 laser beams symmetrically implode a 1.9-mm-diameter beryllium capsule mounted with two carbon fiber stalks at the center of the hohlraum, for details see Ref.<sup>3</sup>. The X-ray source for probing is driven by 8 laser beams shown in red, combined in groups of 4 beams each. **B** Cut through of the target model illustrating the geometry of the X-ray Thomson scattering (XRTS) measurement: 8 laser beams heat a zinc foil to create 9 keV zinc He- $\alpha$  emission. These X-rays are passing through a Cu foil, which reduces the spectral width of the instrument function by a factor of about two<sup>4</sup>. **C** The effect of the Cu foil on the collected scattering signal. The fully processed spectrum is indicated in white. **D** An illustration of the drive laser timing relative to the probe beam and the evolution of Hohlräum radiation temperature.

(LLNL), as the most powerful laser facility worldwide, matter has been compressed to Gbar pressures and temperatures beyond  $10^6$  K<sup>16</sup>. This is achieved by 192 laser beamlines that deliver up to 2 MJ laser energy in pulses of up to 20 ns duration<sup>6,17</sup>. These unique capabilities combined with high-resolution X-ray diagnostic methods and the growing application of sophisticated analysis techniques like machine learning and Bayesian methods have enabled major advances on various fronts of extreme matter research<sup>9,10,17,18</sup>.

Due to the short-lived transient nature of the states created in the laboratory, diagnostics that temporally resolve the plasma evolution on pico to nanosecond time scales must be used. X-ray Thomson scattering (XRTS) generated by highly brilliant X-ray sources has proven well-suited for this endeavor, especially with recent improvements in the spectral resolution<sup>4,19,20</sup>. As opposed to scattering experiments in back-scattering geometry<sup>11</sup>, which probe the single-particle regime, collective XRTS has been used as diagnostic to derive EOS data, the ionization state, and the electrical conductivity.<sup>20–23</sup>

These experimental advances require the development of a robust framework for analyzing the scattering data, that self-consistently infers the physical processes encapsulated in the scattering spectra, in concert with an account of the influence of the experimental geometry and the X-ray source spectrum. Traditionally, different analytical approaches with various input parameters are combined to compute the ionic and electronic contributions to the XRTS signal. In such an approach, the plasma conditions of the target are inferred by a  $\chi^2$  optimization, which is performed on a subset of these input parameters, while the experimental setup is typically not

included in this optimization. In this paper, we take the evaluation of the scattering data to a new level by considering the variations of instrument and source functions when exploring the full parameter space within a Bayesian statistical analysis by using Markov Chain Monte Carlo (MCMC) sampling. Furthermore, our physical model for the compressed target is entirely based on an *ab initio* data set – no assumptions on, e.g., the ionization degree of the plasma and the form factors of the bound electrons are made. The inelastic contribution to the XRTS spectrum is computed directly from the dielectric response of the compressed target, which is closely related to its electrical conductivity.

## EXPERIMENTAL SETUP AT THE NIF

Here we present the results from the first forward scattering XRTS measurements at the NIF. The schematic of the experiments is shown in Figure 1. Details of the experimental setup and of the diagnostic configuration can be found in Refs.<sup>3,24</sup> and in the supplementary material. In brief, we used 184 beams of the NIF to drive a Be capsule implosion to compress beryllium shells to extreme mass densities as they stagnate at the center of a cylindrical gold radiation cavity (hohlraum). The laser hohlraum drive with a total of 0.8 MJ at 351 nm wavelength was converted to an intense X-ray bath with a peak radiation temperature of 235 eV that ablated the outer layer of the beryllium capsule such that the shell is accelerated inwards to a peak velocity of 200 km/s. Stagnation of the implosion was observed at about 18 ns after the start of the laser drive by X-ray radiography

TABLE I. Summary of the experimental parameters, i.e., the scattering angle, the timing  $t$  given relative to the time of peak X-ray emission  $t_0$ , and plasma conditions inferred from the scattering spectra. The density  $\rho$  and temperature  $T$  are given by the MAP and HPDI of their posterior probability, and the charge state  $Z$ , the elastic to inelastic ratio  $I_{el}/I_{inel}$  and the direct current electrical conductivity  $\sigma_{DC}$  are given by the posterior prediction of the density and temperature distribution.

#	Angle [°]	$t$ [ns]	$\rho$ [g/cm <sup>3</sup> ]	$T$ [eV]	$Z$	$I_{el}/I_{inel}$	$\sigma_{DC}$ [MS/m]
1	30	1.02	$20_{-4}^{+4}$	$123_{-10}^{+19}$	$3.32_{-0.07}^{+0.13}$	$2.07 \pm 0.18$	$7.1_{-0.7}^{+1.5}$
2	45	1.13	$19_{-2}^{+3}$	$149_{-10}^{+5}$	$3.46_{-0.07}^{+0.05}$	$1.05 \pm 0.05$	$8.2_{-0.4}^{+0.8}$
3	45	1.07	$17.4_{-1.2}^{+1.8}$	$143_{-9}^{+8}$	$3.48_{-0.06}^{+0.05}$	$1.02 \pm 0.05$	$7.7_{-0.3}^{+0.3}$

and X-ray emission from the hot spot formed at the center of the shell. We use the time of maximum X-ray hot spot emission,  $t_0$ , as a time fiducial of each implosion and reference all probe times with respect to  $t_0$ . The XRTS spectra are recorded at 0.8 - 1.2 ns after  $t_0$  when the highest compression is expected as the rebounding shock wave is sweeping up the infalling shell material<sup>3</sup>. Radiation-hydrodynamic simulations predict up to 30-fold compression of the beryllium shell at temperatures on the order of 200 eV<sup>3</sup>, which translates into gigabar pressures.

The eight remaining NIF laser beams heat a zinc foil outside of the hohlraum to generate a powerful X-ray probe at 9.0 keV from He-like zinc ions. Scattering experiments in forward geometry require a narrower spectral resolution compared to typical back-scattering experiments due to the lower excitation energies. In order to increase spectral resolution of the XRTS measurement, we utilize a novel concept to reduce the spectral width of the X-ray source. A 16  $\mu\text{m}$  copper foil is placed between the Zn foil and the imploding Be capsule to suppress the higher energy Zn He- $\alpha$  line<sup>4</sup>. As the Cu foil heats up with time, its transmission characteristics change. We use two parameters, the foil temperature and the Cu K-edge position, to model the time dependent X-ray source spectrum<sup>4</sup>. The probe X-rays, upon collimation, scatter off of the stagnating Be shell, and are collected in forward direction at an angle determined by the hohlraum target geometry by a high efficiency Bragg crystal X-ray spectrometer with two channels of cylindrically curved HOPG coatings<sup>25</sup>.

Here we present results of three implosion experiments: one collected an XRTS spectrum at a 30° scattering angle, and two collected XRTS spectra at 45°. All experiments used similar probe timings relative to  $t_0$  compared to the detector integration time of 230 ps, see Table I.

### AB INITIO SIMULATIONS AND MAPPING TO XRTS SPECTRA

Extensive *ab initio* molecular dynamics simulations based on density functional theory (DFT-MD) have been performed for the analysis of the scattering data. The entire XRTS spectrum was calculated from the corresponding electronic structure which determines the contribu-

tions of bound-bound (bb), bound-free (bf), and free-free (ff) transitions<sup>26,27</sup>. Note that the only physical input parameters are the mass density and temperature of the probed material, which directly translate to the electrical response to a perturbing photon as well as the electrical conductivity in the framework of DFT. No further tuning parameters are introduced to aid with the fitting to experimental observations and every contribution is computed in the same physical framework giving us the exact control over which approximations enter our calculations.

The spectrally and angularly resolved scattered intensity  $I$  for XRTS can be described by the electron-electron dynamic structure factor (DSF)  $S_{ee}(k, \omega)$  via

$$\frac{d^2 I}{d\omega d\Omega} \propto \int_{-\infty}^{\infty} d\omega' G(\omega - \omega') S_{ee}(k, \omega'), \quad (1)$$

where  $\omega$  is the frequency shift,  $\Omega$  is the solid angle and  $k$  denotes the wave number. The influences of the instrumental setup and the X-ray source are encoded in the function  $G(\omega)$ .

The *ab initio* XRTS spectra are computed using a modified Chihara decomposition<sup>23</sup> on a density and temperature grid ranging from  $T = 50$  eV to  $T = 200$  eV, and  $\rho = 5$  g/cm<sup>3</sup> to  $\rho = 120$  g/cm<sup>3</sup>, which is subsequently interpolated to a fine  $200 \times 200$  grid using an interpolation scheme for spectra adhering to constant sum rules<sup>28</sup>.

To model the scattering intensity in Eq. (1), we employ a model that takes two physical parameters, the temperature and mass density of the plasma, and ten parameters describing the source and instrument functions (see the supplementary material for details). Including the variance of the experimental data as a random variable, the model accounts for 13 parameters which determine the shape of the final spectrum.

Recent studies<sup>29,30</sup> have shown the instability of traditional  $\chi^2$  optimization approaches to deducing the physical parameters from an experimental observation and highlighted the importance of holistically examining the parameter space in a probabilistic framework. Therefore, we generally adopt the approach of Ref.<sup>29</sup> and choose a different likelihood function that is better suited to our study.

A Bayesian perspective on the probability that a certain set of parameters lead to the experimental observa-

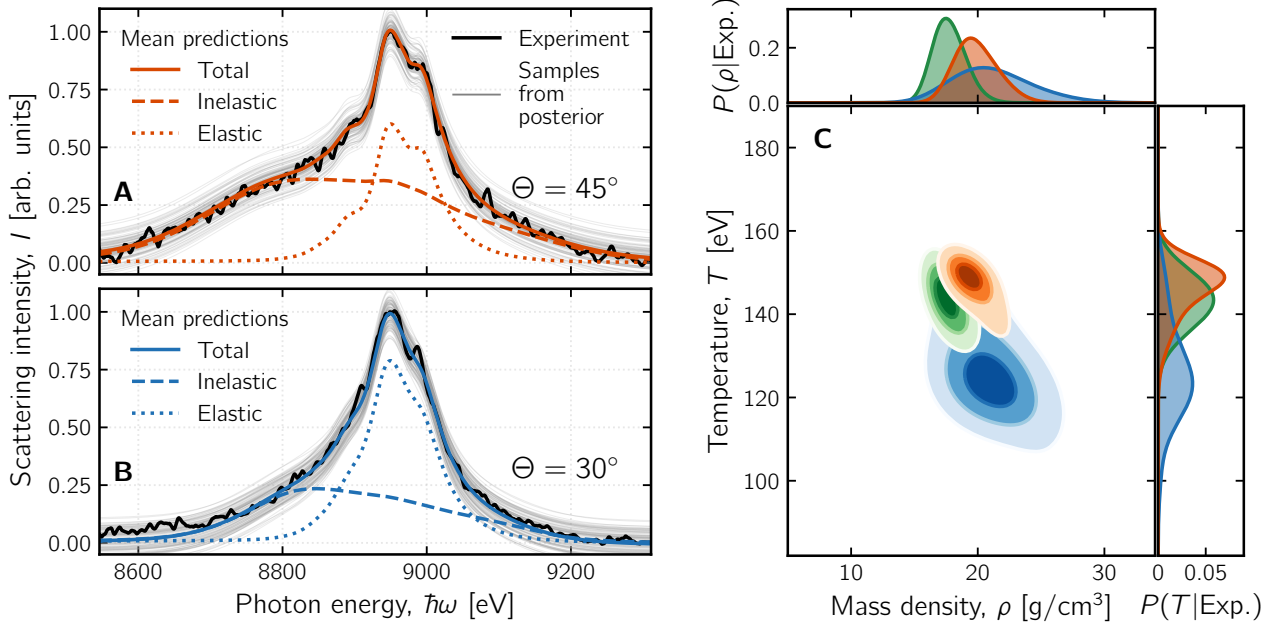


FIG. 2. Summary of the experimental results and predictions. **A** The experimental spectra collected at a  $45^\circ$  scattering angle are shown together with the mean model predictions produced by the posterior distributions of the input parameters computed through the MCMC sampling. Also shown in gray are 100 spectra randomly sampled from the posterior distribution of the parameters. **B** Same as **A** but for a  $30^\circ$  scattering angle.

**C** The probability distribution of input parameters is represented on a subspace of the full parameter space, spanned by the temperature  $T$  and the mass density  $\rho$ . The blue color code describes the measurements taken at  $30^\circ$  (cf. **B**), while the orange (cf. **A**) and green (cf. supplementary material) color codes describe the measurements of two separate experiments at  $45^\circ$ . The contour lines are given relative to the maximum probability density in this subspace at 20%, 50%, and 80%. The probability distributions of the individual input parameters are given on the marginal plots. The MAP is located at the respective peaks of the distributions in the marginal plots.

tion can be expressed as

$$P(\Theta|\text{Exp.}) = \frac{P(\text{Exp.}|\Theta)P(\Theta)}{P(\text{Exp.})}, \quad (2)$$

where  $\Theta$  is the set of parameters, that in our case includes the physical parameters of the probed plasma as well as the parameters of the source and instrument function. The likelihood of observing the experimental result  $P(\text{Exp.})$  is independent of the input parameters and therefore remains a constant. Prior knowledge about physical or experimental parameters can be encoded in the prior  $P(\Theta)$ . The likelihood  $P(\text{Exp.}|\Theta)$  quantifies how likely the experimental result would be observed if the given set of parameters in fact described the underlying physics.

Due to the high dimensionality of the parameter space, it is inefficient to sample it indiscriminately. Therefore, we use a sequential Monte Carlo algorithm<sup>31,32</sup> to perform MCMC sampling of the posterior probability distribution  $P(\Theta|\text{Exp.})$ .

To the best of our knowledge, the method outlined above represents the first evaluation of NIF scattering spectra based solely on *ab initio* data and Bayesian anal-

ysis so that plasma parameters like ionization state, density, and temperature are derived in a consistent statistical framework.

## PLASMA PARAMETER INFERENCE

We perform the MCMC sampling on the three spectra listed in Tab. I and present the measured and calculated spectra as well as the posterior distributions of the physical input parameters in Fig. 2. The analysis produces a 13-dimensional probability distribution in the input parameter space, which is reduced to the mass density and temperature dimension by integrating over all possible values in the remaining dimension. For this presentation, we perform a Gaussian kernel density estimation in the density-temperature plane on the samples collected during the MCMC sampling. Evaluating the scattering model on the parameter space according to the full probability distribution results in posterior predictions for the scattering spectra which can be compared to the experimental data. For both, the  $30^\circ$  and  $45^\circ$  scattering angles, the agreement between measured spectra and predictions

in Fig. 2 **A** and **B** is excellent. Furthermore, the agreement for an additional spectrum recorded at  $45^\circ$  in a separate experiment is similar to the results in Fig. 2 **B**, demonstrating the reproducibility of our results. The spectra are composed of the elastic and inelastic contribution, the latter of which is computed from the dielectric function (see supplementary materials) and dominates the spectrum below 8850 eV and above 9050 eV. This intimate connection to the dielectric function can be used to infer the electrical conductivity. We restrict the Bayesian inference to the energy ranges between 8500 eV and 9300 eV for the  $45^\circ$  scattering angle, and 8680 eV and 9300 eV for the  $30^\circ$  scattering angle and we scale the theoretical predictions to the same amplitude as the experimental data. Due to the inclusion of the experimental parameters in the model calculations the projection onto the density-temperature plane integrates over all possible experimental configuration, reducing biases introduced by the experimental setup.

All spectra are recorded at least 1 ns after peak X-ray emission, for which radiation hydrodynamics simulations predict fairly homogeneous conditions due to the stagnation shock breaking out into the underdense remaining Be ablator material<sup>3</sup>. The inferred mass density for all three experiments agrees well within the determined uncertainties. The temperature inference is mostly driven by the detailed balance relation, which is more apparent in broad scattering signals. Therefore, the  $45^\circ$  scattering measurements result in narrower probability distributions in the temperature dimension. Although the principal result of our analysis is the full probability distribution, point estimates and their uncertainties can be defined by the maximum a posteriori probability (MAP) and the most narrow credible interval of the distribution, called the highest posterior density interval (HPDI).

In Fig. 3 **A** we compare the conditions reached in our experiments (inset, enlarged in Fig. 3 **B** with the principal Hugoniot curve of Ding *et al.*<sup>33</sup> (dashed light blue line) and  $P$ - $T$  profiles of typical astrophysical objects. We reached conditions above 1 Gbar and temperatures between 120 and 150 eV, which places our observations on the right hand side of the principal Hugoniot curve due to the high compression achieved in the experiments. Most interestingly, the core conditions of Proxima Centauri when arriving on the zero-age main sequence line (ZAMS; which we computed using the stellar evolution toolkit MESA<sup>14,34–37</sup> for an age of  $4.6 \times 10^6$  a) coincide with the conditions probed in our NIF campaign. Furthermore, more massive and therefore hotter M stars like Lalande 21185 (computed using MESA) also lie in the range of the experimental data. The experimental setup as realized in this NIF campaign evidently is able to probe conditions relevant for M stars, ranging from those in young low-mass ones like Proxima Centauri up those in older and more massive representatives like Lalande 21185.

Figure 3 **B** zooms in on the pressure-temperature regime probed in the experiment and shows a color coded

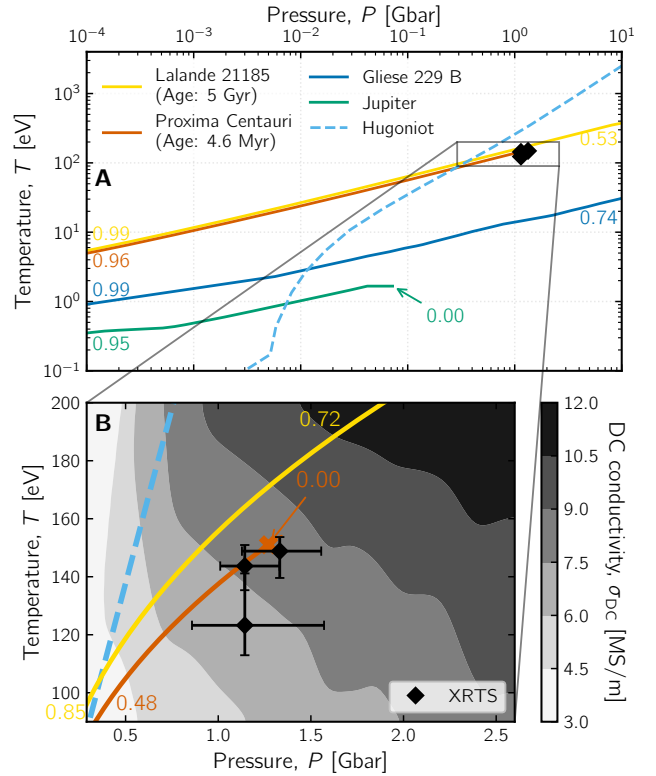


FIG. 3. **A** Typical  $P$ - $T$  profile for Jupiter (green)<sup>38</sup>, Gliese 229B (brown dwarf; dark blue)<sup>39</sup>, a young Proxima Centauri (red dwarf; dark orange), and Lalande 21185 (red dwarf; yellow) as well as the principal Hugoniot for beryllium (dashed light blue) according to Ding *et al.*<sup>33</sup>. The colored numbers denote the fractions of the object radii at the edges of the covered  $P$ - $T$  range. **B** A comparison of the pressure  $P$  and the temperature  $T$  reached during the experiment, extracted from Fig. 2. The symbols are located at the MAP and the error bars indicate the 80% highest posterior density interval around the MAP. The direct current electrical conductivity  $\sigma_{DC}$  predicted by DFT-MD is given by different shades of gray in the pressure-temperature plane. For comparison, the profile of a young Proxima Centauri at age  $4.6 \times 10^6$  a and Lalande 21185 at age  $5 \times 10^9$  a, calculated using the stellar evolution toolkit MESA,<sup>14,34–37</sup> are shown.

background that denotes the DFT-based electrical conductivities which are consistent with the observed spectra. For the experimental data, we show the MAP estimate and HPDI for the pressure and temperature. The conductivity can then be inferred from the color coded background covered by the experimental observations. The highest conductivity state of  $8.2^{+0.8}_{-0.4}$  MS/m was observed under a  $45^\circ$  scattering angle for the latest probe timing, indicating that even higher conductivity states could be reached at a later time. For more information on the individual data sets, refer to Tab. I.

Note that stellar evolution codes like MESA rely on a mix of equation of state tables in various pressure and temperature regimes.<sup>40–44</sup> Due to the lack of experimen-

tal data in the region probed during this experiment, it is vital to establish experimental capabilities to reproducibly reach these conditions. The accurate description of material properties in the interior of stars on the ZAMS influences our understanding of stellar evolution during the hydrogen burning phase along the main sequence. In particular, the simultaneous determination of EOS data and conductivities as in our study enables testing dynamo models in order to understand the high magnetic fields generated in the interior of fully convective M stars like Proxima Centauri and their violent flare activity<sup>45</sup>.

In our experiments, the electrical conductivity of beryllium plasma was inferred from collective XRTS based on *ab initio* DFT-MD data in the range 6.6–9.0 MS/m; see color code in Fig. 3 B. This corresponds to roughly half the conductivity value predicted by a recently published relaxation time approximation (RTA)<sup>46</sup> with ionization states from the widely used OPAL table<sup>47,48</sup>, which is representative of typical analytic models used in stellar evolution codes. The difference is partly due to the improved description of ionization in DFT<sup>27</sup> compared to OPAL<sup>47,48</sup>, and partly due to the missing ion correlations and the many-body description of electron-ion scattering in the RTA (see supplementary material for details).

## CONCLUSION

For the first time, inelastic plasmon scattering in forward scattering geometry has been successfully demonstrated at the NIF. The inferred plasma parameters demonstrate that our experiments reach conditions present in young M stars and massive Red Dwarfs on the main sequence, demonstrating that these conditions can be produced reliably in the laboratory. The XRTS spectra were analyzed based on *ab initio* DFT-MD calculations within a framework of Bayesian inference which also takes into account the impact of the experimental setup on the probed conditions, resulting in a robust determination of the temperature-density data with a reliable uncertainty measure. Due to the collective nature of the scattering process, the analysis of the collisionally

damped plasmon signal allows the derivation of electrical conductivities for such extreme states, which is especially relevant for the study of the magnetic dynamo effect in red dwarfs, which was suggested to impact the habitability of surrounding planets<sup>49</sup>.

## ACKNOWLEDGMENTS

We would like to thank the entire NIF operations, diagnostics, and target design and assembly teams for outstanding support. Special Thanks go to Kurt Boehm and Pascale di Nicola for coordinating the target builds, Neal Rice and Haibo Huang for making and metrologizing the beryllium capsules, Dan Kalantar and Nathan Masters for resolving any alignment and machine safety issues. The work of T.D., C.A., B.B., L.D., O.L.L., M.J.M and A.M.S. was performed under the auspices of the U.S. Department of Energy under Contract No. DE-AC52-07NA27344, and was supported by Laboratory Directed Research and Development (LDRD) Grant No. 18-ERD-033. The DFT-MD calculations were performed at the North-German Supercomputing Alliance (HLRN) facilities and at the IT and Media Center of the University of Rostock. M.S., M.B., B.B.L.W. and R.R. acknowledge support by the Deutsche Forschungsgemeinschaft (DFG) within the FOR 2440. M.B. was also partially supported by the European Horizon 2020 program within the Marie Skłodowska-Curie actions (xICE grant number 894725) and the NOMIS foundation. D.K. was supported by the Helmholtz Association under VH-NG-1141 and by Deutsche Forschungsgemeinschaft (DFG—German Research Foundation) Project No. 495324226. We also acknowledge the NIF Discovery Science program for providing access to the facility.

## SUPPLEMENTARY MATERIALS

Materials and Methods

Figs. S1 to S6

Tables S1 to S2

References [48–86]

<sup>1</sup> Shulyak, D., Reiners, A., Nagel, E., Tal-Or, L., Caballero, J. A., Zechmeister, M., Béjar, V. J. S., Cortés-Contreras, M., Martin, E. L., Kaminski, A., Ribas, I., Quirrenbach, A., Amado, P. J., Anglada-Escudé, G., Bauer, F. F., Dreizler, S., Guenther, E. W., Henning, T., Jeffers, S. V., Kürster, M., Lafarga, M., Montes, D., Morales, J. C., and Pedraz, S., *Astron. Astrophys.* **626**, A86 (2019).

<sup>2</sup> V. M. Passegger, A. Reiners, S. V. Jeffers, S. W.-v. Berg, P. Schöfer, J. A. Caballero, A. Schweitzer, P. J. Amado, V. J. S. Béjar, M. Cortés-Contreras, A. P. Hatzes, M. Kürster, D. Montes, S. Pedraz, A. Quirrenbach, I. Ribas, and W. Seifert, *Astron. Astrophys.* **615**,

a6 (2018).

<sup>3</sup> D. T. Bishel, B. Bachmann, A. Yi, D. Kraus, L. Divol, M. Bethkenhagen, R. W. Falcone, L. B. Fletcher, S. H. Glenzer, O. L. Landen, M. J. MacDonald, N. Masters, P. Neumayer, R. Redmer, A. M. Saunders, B. B. L. Witte, and T. Döppner, *Review of Scientific Instruments* **89**, 10G111 (2018), <https://doi.org/10.1063/1.5037073>.

<sup>4</sup> M. J. MacDonald, A. M. Saunders, B. Bachmann, M. Bethkenhagen, L. Divol, M. D. Doyle, L. B. Fletcher, S. H. Glenzer, D. Kraus, O. L. Landen, H. J. LeFevre, S. R. Klein, P. Neumayer, R. Redmer, M. Schörner, N. Whiting, R. W. Falcone, and T. Döppner, *Physics of Plasmas* **28**,



- 032708 (2021), <https://doi.org/10.1063/5.0030958>.
- <sup>5</sup> J. Lütgert, M. Bethkenhagen, B. Bachmann, L. Divol, D. O. Gericke, S. H. Glenzer, G. N. Hall, N. Izumi, S. F. Khan, O. L. Landen, S. A. MacLaren, L. Masse, R. Redmer, M. Schörner, M. O. Schölmerich, S. Schumacher, N. R. Shaffer, C. E. Starrett, P. A. Sterne, C. Trosseille, T. Döppner, and D. Kraus, *Physics of Plasmas* **29**, 083301 (2022), <https://doi.org/10.1063/5.0094579>.
  - <sup>6</sup> E. I. Moses, R. N. Boyd, B. A. Remington, C. J. Keane, and R. Al-Ayat, *Phys. Plasmas* **16**, 041006 (2009).
  - <sup>7</sup> D. B. Sinars *et al.*, *Physics of Plasmas* **27**, 070501 (2020), <https://doi.org/10.1063/5.0007476>.
  - <sup>8</sup> R. F. Smith, J. H. Eggert, R. Jeanloz, T. S. Duffy, D. G. Braun, J. R. Patterson, R. E. Rudd, J. Biener, A. E. Lazicki, A. V. Hamza, J. Wang, T. Braun, L. X. Benedict, P. M. Celliers, and G. W. Collins, *Nature* **511**, 330 (2014).
  - <sup>9</sup> P. M. Celliers, M. Millot, S. Brygoo, R. S. McWilliams, D. E. Fratanduono, J. R. Rygg, A. F. Goncharov, P. Loubeyre, J. H. Eggert, J. L. Peterson, N. B. Meezan, S. Le Pape, G. W. Collins, R. Jeanloz, and R. J. Hemley, *Science* **361**, 677 (2018).
  - <sup>10</sup> A. Lazicki, D. McGonegle, J. Rygg, D. Braun, D. Swift, M. Gorman, R. Smith, P. Heighway, A. Higginbotham, M. Suggit, D. Fratanduono, F. Coppari, C. Wehrenberg, R. Kraus, D. Erskine, J. Bernier, J. Mcnane, R. Rudd, G. Collins, and J. Wark, *Nature* **589**, 532 (2021).
  - <sup>11</sup> T. Döppner, M. Bethkenhagen, D. Kraus, P. Neumayer, D. A. Chapman, B. Bachmann, R. A. Baggott, M. P. Böhme, L. Divol, R. W. Falcone, L. B. Fletcher, O. L. Landen, M. J. MacDonald, A. M. Saunders, M. Schörner, P. A. Sterne, J. Vorberger, B. B. L. Witte, A. Yi, R. Redmer, S. H. Glenzer, and D. O. Gericke, *Nature* (2023), [10.1038/s41586-023-05996-8](https://doi.org/10.1038/s41586-023-05996-8).
  - <sup>12</sup> B. Remington, R. Drake, and D. Ryutov, *Rev. Mod. Phys.* **78**, 755 (2006).
  - <sup>13</sup> S. Cassisi, A. Y. Potekhin, A. Pietrinferni, M. Cate-lan, and M. Salaris, *The Astrophysical Journal* **661**, 1094 (2007).
  - <sup>14</sup> B. Paxton, L. Bildsten, A. Dotter, F. Herwig, P. Lesafre, and F. Timmes, *ApJS* **192**, 3 (2011), [arXiv:1009.1622 \[astro-ph.SR\]](https://arxiv.org/abs/1009.1622).
  - <sup>15</sup> Valle, G., Dell'Omodarme, M., Prada Moroni, P. G., and Degl'Innocenti, S., *A&A* **549**, A50 (2013).
  - <sup>16</sup> A. L. Kritcher, C. V. Young, H. F. Robey, C. R. Weber, A. B. Zylstra, O. A. Hurricane, D. A. Callahan, J. E. Ralph, J. S. Ross, K. L. Baker, D. T. Casey, D. S. Clark, T. Döppner, L. Divol, M. Hohenberger, L. B. Hopkins, S. Le Pape, N. B. Meezan, A. Pak, P. K. Patel, R. Tomasini, S. J. Ali, P. A. Amendt, L. J. Atherton, B. Bachmann, D. Bailey, L. R. Benedetti, R. Betti, S. D. Bhandarkar, J. Biener, R. M. Bionta, N. W. Birge, E. J. Bond, D. K. Bradley, T. Braun, T. M. Briggs, M. W. Bruhn, P. M. Celliers, B. Chang, T. Chapman, H. Chen, C. Choate, A. R. Christopherson, J. W. Crippen, E. L. Dewald, T. R. Dittrich, M. J. Edwards, W. A. Farmer, J. E. Field, D. Fittinghoff, J. A. Frenje, J. A. Gaffney, M. G. Johnson, S. H. Glenzer, G. P. Grim, S. Haan, K. D. Hahn, G. N. Hall, B. A. Hammel, J. Harte, E. Hartouni, J. E. Heebner, V. J. Hernandez, H. Herrmann, M. C. Herrmann, D. E. Hinkel, D. D. Ho, J. P. Holder, W. W. Hsing, H. Huang, K. D. Humbird, N. Izumi, L. C. Jarrott, J. Jeet, O. Jones, G. D. Kerbel, S. M. Kerr, S. F. Khan, J. Kilkenny, Y. Kim, H. Geppert-Kleinrath, V. Geppert-Kleinrath, C. Kong, J. M. Koning, M. K. G. Kruse, J. J. Kroll, B. Kustowski, O. L. Landen, S. Langer, D. Larson, N. C. Lemos, J. D. Lindl, T. Ma, M. J. MacDonald, B. J. MacGowan, A. J. Mackinnon, S. A. MacLaren, A. G. MacPhee, M. M. Marinak, D. A. Mariscal, E. V. Marley, L. Masse, K. Meaney, P. A. Michel, M. Millot, J. L. Milovich, J. D. Moody, A. S. Moore, J. W. Morton, T. Murphy, K. Newman, J.-M. G. Di Nicola, A. Nikroo, R. Nora, M. V. Patel, L. J. Pelz, J. L. Peterson, Y. Ping, B. B. Pollock, M. Ratledge, N. G. Rice, H. Rinderknecht, M. Rosen, M. S. Rubery, J. D. Salmonson, J. Sater, S. Schiaffino, D. J. Schlossberg, M. B. Schneider, C. R. Schroeder, H. A. Scott, S. M. Sepke, K. Sequoia, M. W. Sherlock, S. Shin, V. A. Smalyuk, B. K. Spears, P. T. Springer, M. Stadermann, S. Stoupin, D. J. Strozzi, L. J. Suter, C. A. Thomas, R. P. J. Town, C. Trosseille, E. R. Tubman, P. L. Volegov, K. Widmann, C. Wild, C. H. Wilde, B. M. Van Wonterghem, D. T. Woods, B. N. Woodworth, M. Yamaguchi, S. T. Yang, and G. B. Zimmerman, *Nature Physics* **18**, 251 (2022).
  - <sup>17</sup> A. L. Kritcher, D. C. Swift, T. Döppner, B. Bachmann, L. X. Benedict, G. W. Collins, J. L. DuBois, F. El-sner, G. Fontaine, J. A. Gaffney, S. Hamel, A. Lazicki, W. R. Johnson, N. Kostinski, D. Kraus, M. J. MacDonald, B. Maddox, M. E. Martin, P. Neumayer, A. Nikroo, J. Nilsen, B. A. Remington, D. Saumon, P. A. Sterne, W. Sweet, A. A. Correa, H. D. Whitley, R. W. Falcone, and S. H. Glenzer, *Nature* **584**, 51 (2020).
  - <sup>18</sup> P. Hatfield, J. Gaffney, G. Anderson, S. Ali, L. Antonelli, S. Pree, J. Citrin, M. Fajardo, P. Knapp, B. Kettle, B. Kustowski, M. MacDonald, D. Mariscal, M. Martin, T. Nagayama, C. Palmer, L. Peterson, S. Rose, J. Ruby, and B. Williams, *Nature* **593**, 351 (2021).
  - <sup>19</sup> J. Amann, W. Berg, V. Blank, F.-J. Decker, Y. Ding, P. Emma, Y. Feng, J. Frisch, D. Fritz, J. Hastings, Z. Huang, J. Krzywinski, R. Lindberg, H. Loos, A. Lutman, H.-D. Nuhn, D. Ratner, J. Rzepiela, D. Shu, and D. Zhu, *Nature Photonics* **6**, 693 (2012).
  - <sup>20</sup> L. Fletcher, T. Döppner, and *et al.*, *Nature Photonics* **9**, 274 (2015).
  - <sup>21</sup> S. H. Glenzer, O. L. Landen, P. Neumayer, R. W. Lee, K. Widmann, S. W. Pollaine, R. J. Wallace, G. Gregori, A. Höll, T. Bornath, R. Thiele, V. Schwarz, W.-D. Kraeft, and Redmer, *Phys. Rev. Lett.* **98**, 065002 (2007).
  - <sup>22</sup> S. H. Glenzer and R. Redmer, *Rev. Mod. Phys.* **81**, 1625 (2009).
  - <sup>23</sup> B. B. L. Witte, L. B. Fletcher, E. Galtier, E. Gamboa, H. J. Lee, U. Zastra, R. Redmer, S. H. Glenzer, and P. Sperling, *Phys. Rev. Lett.* **118**, 225001 (2017).
  - <sup>24</sup> D. Kraus, T. Döppner, A. L. Kritcher, A. Yi, K. Boehm, B. Bachmann, L. Divol, L. B. Fletcher, S. H. Glenzer, O. L. Landen, N. Masters, M. Saunders, C. Weber, R. W. Falcone, and P. Neumayer, *Journal of Physics: Conference Series* **717**, 012067 (2016).
  - <sup>25</sup> T. Döppner, D. Kraus, P. Neumayer, B. Bachmann, J. Emig, R. W. Falcone, L. B. Fletcher, M. Hardy, D. H. Kalantar, A. L. Kritcher, O. L. Landen, T. Ma, A. M. Saunders, and R. D. Wood, *Review of Scientific Instruments* **87**, 11E515 (2016), <https://aip.scitation.org/doi/pdf/10.1063/1.4959874>.
  - <sup>26</sup> B. B. L. Witte, P. Sperling, M. French, V. Recoules, S. H. Glenzer, and R. Redmer, *Physics of Plasmas* **25**, 056901 (2018).
  - <sup>27</sup> M. Bethkenhagen, B. B. L. Witte, M. Schörner, G. Röpke, T. Döppner, D. Kraus, S. H. Glenzer, P. A. Sterne, and R. Redmer, *Phys. Rev. Research* **2**, 023260 (2020).

- <sup>28</sup> H.-C. Weissker, R. Hambach, V. Olevano, and L. Reining, *Phys. Rev. B* **79**, 094102 (2009).
- <sup>29</sup> M. F. Kasim, T. P. Galligan, J. Topp-Mugglestone, G. Gregori, and S. M. Vinko, *Physics of Plasmas* **26**, 112706 (2019), <https://doi.org/10.1063/1.5125979>.
- <sup>30</sup> J. J. Ruby, J. A. Gaffney, J. R. Rygg, Y. Ping, and G. W. Collins, *Physics of Plasmas* **28**, 032703 (2021), <https://doi.org/10.1063/5.0040616>.
- <sup>31</sup> P. Del Moral, A. Doucet, and A. Jasra, *Journal of the Royal Statistical Society: Series B (Statistical Methodology)* **68**, 411 (2006), <https://rss.onlinelibrary.wiley.com/doi/pdf/10.1111/j.1467-9868.2006.00553.x>.
- <sup>32</sup> S. A. Sisson, Y. Fan, and M. M. Tanaka, *Proceedings of the National Academy of Sciences of the United States of America* **104**, 1760 (2007).
- <sup>33</sup> Y. H. Ding and S. X. Hu, *Physics of Plasmas* **24**, 062702 (2017), <https://doi.org/10.1063/1.4984780>.
- <sup>34</sup> B. Paxton, M. Cantiello, P. Arras, L. Bildsten, E. F. Brown, A. Dotter, C. Mankovich, M. H. Montgomery, D. Stello, F. X. Timmes, and R. Townsend, *ApJS* **208**, 4 (2013), arXiv:1301.0319 [astro-ph.SR].
- <sup>35</sup> B. Paxton, P. Marchant, J. Schwab, E. B. Bauer, L. Bildsten, M. Cantiello, L. Dessart, R. Farmer, H. Hu, N. Langer, R. H. D. Townsend, D. M. Townsley, and F. X. Timmes, *ApJS* **220**, 15 (2015), arXiv:1506.03146 [astro-ph.SR].
- <sup>36</sup> B. Paxton, J. Schwab, E. B. Bauer, L. Bildsten, S. Blinnikov, P. Duffell, R. Farmer, J. A. Goldberg, P. Marchant, E. Sorokina, A. Thoul, R. H. D. Townsend, and F. X. Timmes, *ApJS* **234**, 34 (2018), arXiv:1710.08424 [astro-ph.SR].
- <sup>37</sup> B. Paxton, R. Smolec, J. Schwab, A. Gaudy, L. Bildsten, M. Cantiello, A. Dotter, R. Farmer, J. A. Goldberg, A. S. Jermyn, S. M. Kanbur, P. Marchant, A. Thoul, R. H. D. Townsend, W. M. Wolf, M. Zhang, and F. X. Timmes, *ApJS* **243**, 10 (2019), arXiv:1903.01426 [astro-ph.SR].
- <sup>38</sup> M. French, A. Becker, W. Lorenzen, N. Nettelmann, M. Bethkenhagen, J. Wicht, and R. Redmer, *Astrophys. J. Suppl. Ser.* **202**, 5 (2012).
- <sup>39</sup> A. Becker, M. Bethkenhagen, C. Kellermann, J. Wicht, and R. Redmer, *The Astronomical Journal* **156**, 149 (2018).
- <sup>40</sup> F. J. Rogers and A. Nayfonov, *ApJ* **576**, 1064 (2002).
- <sup>41</sup> D. Saumon, G. Chabrier, and H. M. van Horn, *Astrophys. J. Suppl. Ser.* **99**, 713 (1995).
- <sup>42</sup> O. R. Pols, C. A. Tout, P. P. Eggleton, and Z. Han, *MNRAS* **274**, 964 (1995), astro-ph/9504025.
- <sup>43</sup> F. X. Timmes and F. D. Swesty, *ApJS* **126**, 501 (2000).
- <sup>44</sup> A. Y. Potekhin and G. Chabrier, *Contributions to Plasma Physics* **50**, 82 (2010), arXiv:1001.0690 [physics.plasm-ph].
- <sup>45</sup> R. K. Yadav, U. R. Christensen, S. J. Wolk, and K. Poppenhaeger, *The Astrophysical Journal Letters* **833**, L28 (2016).
- <sup>46</sup> M. French, G. Röpke, M. Schörner, M. Bethkenhagen, M. P. Desjarlais, and R. Redmer, *Phys. Rev. E* **105**, 065204 (2022).
- <sup>47</sup> F. J. Rogers and C. A. Iglesias, *Science* **263**, 50 (1994), <https://www.science.org/doi/pdf/10.1126/science.263.5143.50>.
- <sup>48</sup> F. J. Rogers, F. J. Swenson, and C. A. Iglesias, *The Astrophysical Journal* **456**, 902 (1996).
- <sup>49</sup> Vidotto, A. A., Jardine, M., Morin, J., Donati, J.-F., Lang, P., and Russell, A. J. B., *A&A* **557**, A67 (2013).

---

## 4.6 Virial expansion of the electrical conductivity of hydrogen plasmas

### Author contributions

**G. Röpke**

Preparation of the manuscript, virial expansion of conductivity, interpretation of simulations

**M. Schörner**

Preparation of the manuscript, creation of figures, DFT simulations and conductivity calculations, interpretation of simulations

**R. Redmer**

Supervision of the project, preparation of the manuscript

**M. Bethkenhagen**

Preparation of the manuscript, DFT-MD simulations and interpretation


## Virial expansion of the electrical conductivity of hydrogen plasmas

G. Röpke,<sup>\*</sup> M. Schörner,<sup>†</sup> and R. Redmer<sup>‡</sup>

*Institut für Physik, Universität Rostock, D-18051 Rostock, Germany*

M. Bethkenhagen<sup>§</sup>

*École Normale Supérieure de Lyon, Laboratoire de Géologie de Lyon, LGLTPE UMR 5276,  
Centre Blaise Pascal, 46 allée d'Italie, Lyon 69364, France*

 (Received 17 July 2021; accepted 22 September 2021; published 13 October 2021)

The low-density limit of the electrical conductivity  $\sigma(n, T)$  of hydrogen as the simplest ionic plasma is presented as a function of the temperature  $T$  and mass density  $n$  in the form of a virial expansion of the resistivity. Quantum statistical methods yield exact values for the lowest virial coefficients which serve as a benchmark for analytical approaches to the electrical conductivity as well as for numerical results obtained from density functional theory-based molecular dynamics simulations (DFT-MD) or path-integral Monte Carlo simulations. While these simulations are well suited to calculate  $\sigma(n, T)$  in a wide range of density and temperature, in particular, for the warm dense matter region, they become computationally expensive in the low-density limit, and virial expansions can be utilized to balance this drawback. We present new results of DFT-MD simulations in that regime and discuss the account of electron-electron collisions by comparison with the virial expansion.

DOI: [10.1103/PhysRevE.104.045204](https://doi.org/10.1103/PhysRevE.104.045204)

### I. INTRODUCTION

Besides the equation of state and the optical properties, the direct-current electrical conductivity  $\sigma$  is a fundamental characteristic of plasmas which is relevant in various fields. Examples for technical applications range from the quenching gas in high-power circuit breakers [1], which acts as an efficient dielectric medium, to fusion plasmas produced via magnetic [2] or inertial confinement [3]. The electrical conductivity is indispensable for verification of the insulator-to-metal transition in warm dense hydrogen [4]. In geophysics, the electrical conductivity determines the properties of the outer liquid core and of the ionosphere, i.e., the entire magnetic field of Earth from the dynamo region [5] up to the magnetosphere [6]. Similarly, the electrical conductivity in the convection zone of giant planets [7], brown dwarfs [8], and stars [9] determines the action of the dynamo that produces their magnetic field. Investigation of the electrical conductivity of charged particle systems is, therefore, an emerging field of quantum statistics. In this work we provide exact benchmarks for this fundamental transport property.

Theoretical approaches to calculate the electrical conductivity of plasmas have been performed first within kinetic theory [10]. In a seminal paper [11], Spitzer and Härn determined  $\sigma$  of the fully ionized plasma solving a Fokker-Planck equation. However, to calculate  $\sigma(n, T)$  in a wide region of temperature  $T$  and mass density  $n$ , a quantum

statistical many-particle theory is needed which describes screening, correlations, and degeneracy effects in a systematic approach. In a very general way, according to the fluctuation-dissipation theorem, the conductivity is expressed in terms of equilibrium correlation functions. Kubo's fundamental approach [12] relates the electrical conductivity to the current-current correlation function. For the relation between generalized linear response theory [13–15] and kinetic theory, see [16] and references therein. The evaluation of the corresponding equilibrium correlation functions can be performed using different methods:

(i) Analytical expressions are derived, e.g., by using thermodynamic Green's functions. Perturbation theory allows partial summations using diagram techniques which lead to sound results in a wide range of  $T$  and  $n$ . However, as is characteristic for perturbative approaches, exact results can be found only in some limiting cases.

(ii) This drawback is removed by numerical *ab initio* simulations of the correlation functions applicable for arbitrary interaction strength and degeneracy. Using density functional theory (DFT) for the electron system and molecular dynamics (MD) for the ion system (see [12] and [17–20]), single-electron states are calculated solving the Kohn-Sham equations for a given configuration of ions. The total energy is given by the kinetic energy of a noninteracting reference system, the classical electron-electron interaction, and an exchange-correlation energy which contains all unknown contributions in certain approximation. One of the shortcomings of this approach is that the many-particle interaction is replaced by this mean-field potential.

(iii) In principle, an exact evaluation of the equilibrium correlation functions is possible by using path-integral Monte Carlo simulations (see [21–23] and references therein). The

<sup>\*</sup>gerd.roepke@uni-rostock.de

<sup>†</sup>maximilian.schoerner@uni-rostock.de

<sup>‡</sup>ronald.redmer@uni-rostock.de

<sup>§</sup>mandy.bethkenhagen@ens-lyon.fr

shortcomings of this approach are the rather small number of particles (a few tens), the sign problem for fermions, and the computational challenges of calculating path integrals accurately.

These approaches and other closely related methods have been used to calculate  $\sigma(n, T)$  in a wide parameter range, and numerous results have been published; for a recent review see Ref. [24]. Also recently, a comparative study [25] considering different approaches has been published which revealed large differences of calculated conductivities.

In the present study, we demonstrate that the virial expansion of the inverse conductivity serves as an exact benchmark for theoretical approaches so that the accuracy and consistency of results for the conductivity [25] can be checked. In particular, we apply this framework to analytical approaches, DFT-MD results, and experimental data for hydrogen, which was chosen for simplicity. In the course of this discussion, we present new DFT-MD data to extend the previously available conductivity data [27,38] in the density-temperature region of interest. The virial expansion of  $\rho = 1/\sigma$  suggested in this work is a prerequisite to work out interpolation formulas for the conductivity. It can be used in a wide range of  $T$  and  $n$ , analogously to the Gell-Mann–Brueckner result for the virial expansion of the plasma equation of state (see [26]). Finally, the benchmark capability of the virial expansion as discussed in this work may serve as a criterion to check the accuracy of numerical approaches like DFT-MD simulations to evaluate the conductivity.

## II. VIRIAL EXPANSION OF THE INVERSE CONDUCTIVITY

Charge-neutral hydrogen plasma (ion charge  $Z = 1$ ) at thermodynamic equilibrium is characterized by the temperature  $T$  and the mass density  $n$ , or the total particle number densities of electrons  $\hat{n}_e$ , which equals that of the ions  $\hat{n}_{\text{ion}}$ . Instead, dimensionless parameters can be introduced: the plasma parameter

$$\Gamma = \frac{e^2}{4\pi\epsilon_0 k_B T} \left( \frac{4\pi}{3} \hat{n}_e \right)^{1/3}, \quad (1)$$

which characterizes the ratio of potential to kinetic energy in the nondegenerate case, and the electron degeneracy parameter

$$\Theta = \frac{2m_e k_B T}{\hbar^2} (3\pi^2 \hat{n}_e)^{-2/3}. \quad (2)$$

The dc conductivity  $\sigma(n, T)$  is usually related to a dimensionless function  $\sigma^*(n, T)$  according to

$$\begin{aligned} \sigma(n, T) &= \frac{(k_B T)^{3/2} (4\pi\epsilon_0)^2}{m_e^{1/2} e^2} \sigma^*(n, T) \\ &= \frac{32405.4}{\Omega \text{ m}} \left( \frac{k_B T}{\text{eV}} \right)^{3/2} \sigma^*(n, T). \end{aligned} \quad (3)$$

In this work, we consider both  $\sigma$  and  $\sigma^*$  as a function of the density  $n$  at a fixed temperature  $T$ . In the low-density limit, the following virial expansion for the inverse conductivity  $\rho^*(n, T) = 1/\sigma^*(n, T)$  was obtained from kinetic theory and

generalized linear response theory [13–15]:

$$\rho^*(n, T) = \rho_1(T) \ln \frac{1}{n} + \rho_2(T) + \rho_3(T) n^{1/2} \ln \frac{1}{n} + \dots \quad (4)$$

In contrast to a simple expansion in powers of  $n$ , the occurrence of terms with  $\ln n$  and  $n^{1/2} \ln n$  is due to the long-range character of the Coulomb interaction. To describe the collisions between the charged particles, an integral over the Coulomb interaction occurs which gives the so-called Coulomb logarithm, where screening of the Coulomb interaction is taken into account. Typically, such a Coulomb logarithm arises in the correlation functions within the generalized linear response theory [13–15].

By convention, virial expansions consider the dependence of physical quantities on the density  $n$ , for instance, a power series expansion. However, the density  $n$  has a dimension, and for  $\rho^*$  not to be dependent on units, the virial coefficients  $\rho_i$  also have, in general, a dimension. In particular, the term  $\rho_1 \ln(1/n)$  needs a compensating term  $\rho_1 \ln(A)$ , where  $A$  has the dimension of density, as a contribution to  $\rho_2$  so that  $\rho^*$  remains dimensionless. Usually relations like (4) are given after fixing the units in which the physical quantities are measured, but it is also convenient to introduce dimensionless variables. For motivation, we consider the Born approximation for the Coulomb logarithm.

Within static (Debye) screening of the Coulomb interaction to avoid the divergence owing to distant collisions, the Born approximation of the Coulomb logarithm leads to the result (see [13–15])

$$\begin{aligned} &\int_0^\infty \frac{x}{(x + \kappa_{\text{Debye}}^2)^2} e^{-\hbar^2 x / (8m_e k_B T)} dx \\ &= \ln \left( \frac{\Theta}{\Gamma} \right) - 0.962 203 + O \left[ \frac{\Gamma}{\Theta} \ln \left( \frac{\Theta}{\Gamma} \right) \right]. \end{aligned} \quad (5)$$

The Debye screening parameter in the low-density (nondegenerate) limit reads

$$\kappa_{\text{Debye}}^2 = 2\hat{n}_e \frac{e^2}{\epsilon_0 k_B T} \quad (6)$$

so that the integral depends only on the parameter

$$\frac{\hbar^2 \kappa_{\text{Debye}}^2}{8m_e k_B T} = \left( \frac{2}{3\pi^2} \right)^{1/3} \frac{\Gamma}{\Theta}. \quad (7)$$

We focus on the first and second terms on the right-hand side of Eq. (5), which is sufficient in order to derive the first [ $\rho_1(T)$ ] and second [ $\rho_2(T)$ ] virial coefficients of the virial expansion, (4). Further contributions are of higher order in density; for  $\Gamma/\Theta \leq 0.01$  they contribute to the integral in Eq. (5) by less than 1%.

In the virial expansion, (4), the logarithm can be transformed by introducing the dimensionless parameter

$$\frac{\Theta}{\Gamma} = \frac{2m (k_B T)^2 4\pi\epsilon_0}{\hbar^2 \hat{n}_e e^2} (36\pi^5)^{-1/3} \quad (8)$$

[see Eq. (5)], and we find a modified expression [note that  $T \propto 1/(\Gamma^2 \Theta)$ ]:

$$\rho^*(n, T) = \tilde{\rho}_1(T) \ln \left( \frac{\Theta}{\Gamma} \right) + \tilde{\rho}_2(T) + \dots \quad (9)$$



To find the relation between  $\tilde{\rho}_i$  and  $\rho_i$  we replace in Eq. (9) the variables  $\Theta, \Gamma$  with  $\hat{n}_e, T$  according to Eq. (8) so that

$$\begin{aligned} \rho^* &= \tilde{\rho}_1(T) \ln \frac{1}{\hat{n}_e} \\ &+ \tilde{\rho}_1(T) \ln \left( \frac{2m}{\hbar^2} (k_B T)^2 \frac{4\pi\epsilon_0}{e^2} (36\pi^5)^{-1/3} \right) \\ &+ \tilde{\rho}_2(T) + \dots \end{aligned} \quad (10)$$

Comparing with Eq. (4) we find  $\tilde{\rho}_1 = \rho_1$  and

$$\tilde{\rho}_2 = \rho_2 + \rho_1 \ln \left[ 2\pi (6\pi)^{2/3} a_B^3 / T_{\text{Ryd}}^2 \right], \quad (11)$$

where  $a_B$  is the Bohr radius and  $T_{\text{Ryd}} = k_B T / 13.6$  eV is the temperature measured in Rydberg units.

A highlight of plasma transport theory is that the exact value of the first virial coefficient is known for Coulomb systems from the seminal paper of Spitzer and Härm [11],

$$\rho_1 = \tilde{\rho}_1 = \rho_1^{\text{Spitzer}} = 0.846, \quad (12)$$

which does not depend on  $T$ . Note that Eq. (12) takes into account the contribution of the electron-electron ( $e$ - $e$ ) interaction. In contrast, for the Lorentz plasma model where the  $e$ - $e$  collisions are neglected so that only the electron-ion interaction is considered, the first virial coefficient amounts to

$$\rho_1^{\text{Lorentz}} = \frac{1}{16} (2\pi^3)^{1/2} = 0.492\,126. \quad (13)$$

Although  $e$ - $e$  collisions do not contribute to a change in the total momentum of the electrons because of momentum conservation, the distribution in momentum space is changed (“reshaping”) so that higher moments of the electron momentum distribution are not conserved. The indirect influence of  $e$ - $e$  collisions on the dc conductivity is clearly seen in generalized linear response theory where these higher moments are considered (see [15]).

For the second virial coefficient  $\rho_2(T)$  or  $\tilde{\rho}_2(T)$ , no exact value is known. It depends on the treatment of many-particle effects, in particular, screening of the Coulomb potential. Within a quantum statistical approach, the static (Debye) screening by electrons and ions [see Eq. (5)] should be replaced by a dynamical one. For hydrogen plasma as considered here, the Born approximation for the collision integral is justified at high temperatures  $T_{\text{Ryd}} \gg 1$ . Considering screening in the random-phase approximation leads to the quantum Lenard-Balescu (QLB) expression. Thus, at very high temperatures where the dynamically screened Born approximation becomes valid, we obtain the QLB result (see [27–29]),

$$\lim_{T \rightarrow \infty} \tilde{\rho}_2(T) = \tilde{\rho}_2^{\text{QLB}} = 0.4917. \quad (14)$$

With decreasing  $T$ , strong binary collisions (represented by ladder diagrams) become important and have to be treated beyond the Born approximation when calculating the second virial coefficient  $\tilde{\rho}_2(T)$ . According to Spitzer and Härm [11], the classical treatment of strong collisions with a statically screened potential gives for  $\rho^* = 1/\sigma^*$  the result

$$\rho_{\text{Sp}}^* = 0.846 \ln \left[ \frac{3}{2} \Gamma^{-3} \right]. \quad (15)$$

Interpolation formulas have been proposed connecting the high-temperature limit  $\tilde{\rho}_2^{\text{QLB}}$  with the low-temperature Spitzer limit. Instead, performing the sum of ladder diagrams with

the dynamically screened Coulomb potential, Gould and DeWitt [30] and Williams and DeWitt [31] proposed approximations where the lowest order of a ladder sum with respect to a statically screened potential, the Born approximation, is replaced by the Lenard-Balescu result, which accounts for dynamic screening. An improved version was proposed in Refs. [14] and [32] by introducing an effective screening parameter  $\kappa^{\text{eff}}$  such that the Born approximation coincides with the Lenard-Balescu result (see also [13–15,34]). Based on a  $T$ -matrix calculation in the quasiclassical (Wentzel-Kramers-Brillouin; WKB) approximation [35,36], the expression (temperature is given in eV:  $T_{\text{eV}} = k_B T / eV$ )

$$\tilde{\rho}_2(T_{\text{eV}}) \approx 0.4917 + 0.846 \ln \left[ \frac{1 + 8.492/T_{\text{eV}}}{1 + 25.83/T_{\text{eV}} + 167.2/T_{\text{eV}}^2} \right] \quad (16)$$

can be considered a simple interpolation which connects the QLB result with the Spitzer limit in the WKB approximation. However, the exact analytical form of the temperature dependence of the second virial coefficient  $\tilde{\rho}_2(T)$  remains an open problem.

Thus, the available exact results for the virial expansion, (9), of the resistivity of hydrogen plasma are as follows:

- (i) the value of the first virial coefficient is  $\tilde{\rho}_1 = 0.846$ ;
- (ii) the second virial coefficient has the high-temperature limit  $\lim_{T \rightarrow \infty} \tilde{\rho}_2(T) = 0.4917$ ; and
- (iii) the second virial coefficient is temperature dependent, and a promising functional form is given by Eq. (16).

### III. VIRIAL COEFFICIENTS FROM ANALYTICAL APPROACHES

To extract the first and second virial coefficients from calculated or measured dc conductivities, we plot the expression

$$\tilde{\rho}(x, T) = \frac{\rho^*}{\ln(\Theta/\Gamma)} = \frac{32\,405.4}{\sigma(n, T)(\Omega\text{m})} (T_{\text{eV}})^{3/2} \frac{1}{\ln(\Theta/\Gamma)} \quad (17)$$

as a function of  $x = 1/\ln(\Theta/\Gamma)$  and  $T$  in Fig. 1, which is denoted the *virial plot*. According to Eq. (4), the behavior of any isotherm (fixed  $T$ ) near  $n \rightarrow 0$  is linear,

$$\tilde{\rho}(x, T) = \tilde{\rho}_1(T) + \tilde{\rho}_2(T)x + \dots, \quad (18)$$

with  $\tilde{\rho}_1(T)$  as the value at  $x = 0$  and  $\tilde{\rho}_2(T)$  as the slope of the isotherm. As discussed above in the context of the Born approximation, (5), for  $x > 1/\ln(100) = 0.217$  the contributions of higher-order virial coefficients have to be taken into account. In addition, at fixed  $T$ , in the low-density region where  $\Theta \gg 1$ , the plasma is in the classical limit, and effects of degeneracy are obtained from higher-order virial coefficients.

In Fig. 1 three cases for the first virial coefficient  $\rho_1$  are shown on the axis of the ordinate (see also [13–15]):

- (i) the first virial coefficient  $\rho_1^{\text{Spitzer}}$  for the account of  $e$ - $e$  collisions according to kinetic theory (KT; Spitzer),
- (ii) for the neglect of  $e$ - $e$  collisions  $\rho_1^{\text{Lorentz}}$  as known from the Brooks-Herring approach for the Lorentz plasma model (BH; Lorentz), and

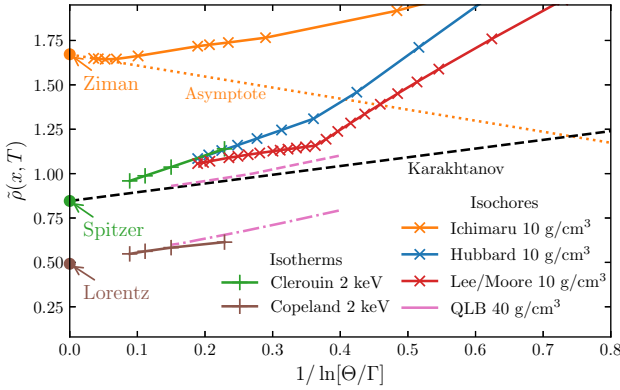


FIG. 1. Analytical results for the reduced resistivity  $\bar{\rho}(x, T)$ , (17), of hydrogen plasma as a function of  $x = 1/\ln(\Theta/\Gamma)$ . Data for  $k_B T = 2000$  eV are taken from Ref. [25] (Clérrouin, Copeland); lines are guides for the eye. Data for  $n = 10$  g/cm<sup>3</sup> are taken from Ref. [38] (Hubbard, Lee-More, Ichimaru). Lenard-Balescu results of Karakhtanov [28] as well as QLB results [27] including the  $e-e$  interaction (dashed line) and without it (only  $e-i$ ; dot-dashed line) are also shown. The values  $\rho_1^{\text{Spitzer}}$ ,  $\rho_1^{\text{Lorentz}}$ , and  $\rho_1^{\text{Ziman}}$  are defined in the text. The data for the graphs are given in the Supplemental Material [39].

(iii)

$$\rho_1^{\text{Ziman}} = \frac{2}{3}(2\pi)^{1/2} = 1.67109 \quad (19)$$

for the force-force correlation function as known from the Ziman theory (FF; Ziman). In addition, the second virial coefficient  $\bar{\rho}_2^{\text{LB}}$  of the Lenard-Balescu approximation, (14), is shown as the dashed black line, which is expected to be correct in the high-temperature limit.

Two QLB calculations of Desjarlais *et al.* [27] are shown in Fig. 1 (see also [39]). The line including  $e-e$  collisions obeys the same asymptote ( $x \rightarrow 0$ ) as that of Karakhtanov [28]. With increasing  $x = 1/\ln(\Theta/\Gamma)$ , small deviations from the linear behavior are seen. The line for calculations without  $e-e$  collisions (Lorentz plasma) points to the corresponding asymptote given by  $\rho_1^{\text{Lorentz}}$ .

Recently, the transport properties of hydrogen plasma were compiled in Ref. [25]. For a grid of lattice points in the  $n$ - $T$  plane (considering  $n = 0.1, 1, 10$ , and  $100$  g/cm<sup>3</sup> and  $T_{\text{eV}} = 0.2, 2, 20, 200$ , and  $2000$ ) the results of different approaches were given. Large deviations were obtained, which indicate not only unavoidable numerical uncertainties but also deficits in some of the theoretical approaches. Their consistency can be checked via the virial expansion as benchmark. As an example, we show data of Clérrouin *et al.* and of Copeland for the isotherm  $T_{\text{eV}} = 2000$  taken from Ref. [25] in Fig. 1.

Extrapolating to  $x = 1/\ln(\Theta/\Gamma) \rightarrow 0$ , these high-temperature isotherms already show significant differences. The data of Clérrouin *et al.* point to the correct Spitzer limit  $\rho_1^{\text{Spitzer}}$ , including  $e-e$  collisions, but have a rather steep slope. This may be caused by the approximations in treating dynamical screening and the ionic structure factor, in contrast to a strict QLB calculation. The data of Copeland clearly point to the limit  $\rho_1^{\text{Lorentz}}$  of the Lorentz model, i.e., this

approach does not include  $e-e$  collisions and fails to describe the conductivity of hydrogen plasma correctly.

Also shown in Fig. 1 are analytical results for the dc conductivity of hydrogen plasma presented by Lambert *et al.* [38] at the lowest density,  $n = 10$  g/cm<sup>3</sup>. The data denoted by Hubbard [40] are close to the data of Clérrouin *et al.* discussed above. The asymptote is the correct benchmark  $\rho_1^{\text{Spitzer}}$ , but the slope is rather large. The data of Lee and More [41] are closer to the QLB calculations. In contrast to Copeland, who also claims to use the Lee-More approach, possibly the  $e-e$  collisions are added so that the extrapolation to  $x \rightarrow 0$  is near to the correct benchmark  $\rho_1^{\text{Spitzer}}$ . Because of the approximations in evaluating the Coulomb logarithm, deviations from the QLB result are seen. The kink in the Lee-More and Hubbard data shown in Fig. 1 is due to switching the minimum impact parameter in the Coulomb logarithm from the classical distance of closest approach to the quantum thermal wave length (cf. Ref. [24]).

Ichimaru and Tanaka [42] derived an analytical expression for the conductivity which was improved in [43] by adding a tanh term to the Coulomb logarithm. The latter expression has also been used in Ref. [38]; the isochore  $n = 10$  g/cm<sup>3</sup> is shown in Fig. 1. The approach is based on a single Sonine polynomial approximation where the effect of  $e-e$  collisions is not taken into account. The empirical fit by Kitamura and Ichimaru [43] approximates the conductivity for degenerate plasmas (see also Fig. 9 in Ref. [38]). However, in the low-density limit this approach fails to describe the conductivity approaching  $\rho_1^{\text{Ziman}}$  at  $x = 0$ .

#### IV. VIRIAL REPRESENTATION OF DFT-MD SIMULATIONS

DFT-MD simulations are of great interest, since they do not suffer from the restrictions of perturbation theory as is typical for analytical results and can be confronted directly with the virial expansion. In addition, with the virial expansion the results can be extrapolated to the low-density region where DFT-MD simulations become infeasible.

In this work, we present new DFT-MD results for the electrical conductivity of hydrogen obtained from an evaluation of the Kubo-Greenwood formula [12,17,45,46]. The 125-atom simulations were performed with the Vienna *Ab initio* Simulation Package (VASP) [49–51] using the exchange-correlation functional of Perdew, Burke, and Ernzerhof (PBE) [52] and the provided Coulomb potential for hydrogen. The time steps were chosen between 0.2 and 0.1 fs and the simulations ran for at least 4000 time steps. The ion temperature was controlled with a Nosé-Hoover thermostat [53]. For all simulations, the reciprocal space was sampled at the Baldereschi mean value point [54]. Special attention has been paid to convergence with respect to the particle number. Additional details of the simulations are given in the Supplemental Material and the results are listed in Table I.

Our DFT-MD results are plotted in Fig. 2 and show a general increase with an increasing  $x = 1/\ln(\Theta/\Gamma)$ . In comparison, the virial plot contains previous DFT-MD conductivity data [27,38], which were translated into our  $\bar{\rho}$  framework. The first set of previous DFT-MD calculations has been published by Lambert *et al.* [38] and was also used by

TABLE I. Virial representation of the dc conductivity  $\sigma$  and of  $\tilde{\rho}(x, T)$  with  $x = 1/\ln(\Theta/\Gamma)$ : the values for  $\sigma$  and  $\tilde{\rho}$  result from our own DFT-MD simulations (this work; number of atoms, 125). Only positive values for  $x = 1/\ln(\Theta/\Gamma)$ , i.e.,  $\Theta/\Gamma > 1$ , are considered.

$n$ (g/cm <sup>3</sup> )	$k_B T$ (eV)	$\Gamma$	$\Theta$	$1/\ln(\Theta/\Gamma)$	$\sigma$ (MS/m)	$\tilde{\rho}(x, T)$
2	50	0.49275	1.2172	1.1059	7.170	1.767
2	75	0.3285	1.8257	0.58302	11.44	1.073
2	100	0.24637	2.4343	0.43657	15.26	0.9269
3	100	0.28203	1.8577	0.53047	16.85	1.020
3	150	0.18802	2.7866	0.37092	25.67	0.8603
4	150	0.20694	2.3003	0.41522	27.39	0.9026

Starrett [47]. Results for  $\tilde{\rho}$  for the lowest values of  $x > 0$  at three different densities are given in Fig. 2. Inspecting Fig. 2, values for 10 g/cm<sup>3</sup> at 200 eV and for 160 g/cm<sup>3</sup> at 800 eV are close together; i.e., we see a dominant dependence on  $x$ , and no additional density or temperature effect is seen. They are also close to the Lee-More approach including  $e-e$  collisions so that they are not in conflict with the correct benchmark (KT, Spitzer). Calculations are based on a formulation of the Kubo-Greenwood method for average atom models neglecting the ion structure factor [48] so that these QMD values are possibly also influenced by approximations and, therefore, deviate slightly from other calculations. However, the parameter values  $x$  are too large to estimate the virial expansion.

The second set of previous DFT-MD simulations for hydrogen plasma in the low- $x$  region was given by Desjarlais *et al.* [27] (see Fig. 2). For a density of 40 g/cm<sup>3</sup>, three temperatures,  $T_{eV} = 500, 700,$  and  $900$ , were considered.

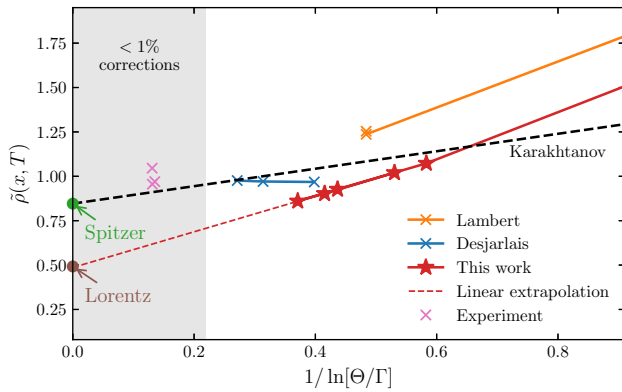


FIG. 2. Reduced resistivity  $\tilde{\rho}(x, T)$ , (17), for hydrogen plasma as a function of  $x = 1/\ln(\Theta/\Gamma)$ : QMD simulations of Lambert *et al.* [38] (the orange line points to the value for  $n = 80$  g/cm<sup>3</sup>,  $k_B T = 300$  eV), DFT-MD simulations of Desjarlais *et al.* [27] and of this work, experimental values of Günther and Radtke [44], and Lenard-Balescu results of Karakhtanov [28].  $\rho_1^{\text{Spitzer}} = 0.846$  and  $\rho_1^{\text{Lorentz}} = 0.492$  are defined in the text. The shaded area indicates the region where corrections to the linear behavior of the virial expansion amount to less than 1%. The dashed red line represents a linear extrapolation of our results based on a linear fit to our three leftmost results. Data are given in the Supplemental Material [39].

The reduced resistivity  $\tilde{\rho}_1(x, T)$  approaches the benchmark obtained from the QLB calculations. However, the linear extrapolation to  $\rho_1^{\text{Spitzer}}$  at  $x = 0$  is not seen in these data.

Interestingly, the results for  $\tilde{\rho}$  of the different DFT-MD simulations do not follow approximately a single curve as expected from the high-temperature limit of the virial expansion. The values of Lambert *et al.* are significantly higher than ours but the slope is almost the same. While we employ the generalized gradient approximated exchange-correlation energy of PBE [52], Lambert *et al.* used the local density approximation. They used orbital-free MD in order to simulate the system and obtain various snapshots for each density-pressure point. Subsequently, these snapshots were evaluated via the Kubo-Greenwood formula using the Kohn-Sham code ABINIT, which is equivalent to the VASP implementation we used. The DFT-MD simulations by Desjarlais *et al.* [27] are close to our results, but the slope of the virial plot is quite different. DFT-MD simulations are usually performed at high densities where the electrons are degenerate so that  $e-e$  collisions can be neglected. In the low-density region ( $x < 1$ ) considered here, we could improve the accuracy by studying the convergence of the DFT-MD results, in particular, with respect to the particle number and cutoff energy, using high-performance computing facilities.

A long-discussed problem in this context is the question whether or not  $e-e$  collisions are taken into account within the DFT-MD formalism. For example, in Ref. [37] it was pointed out that a mean-field approach is not able to describe two-particle correlations, in particular,  $e-e$  collisions. However,  $e-e$  interaction is taken into account by the exchange-correlation energy as shown in Ref. [27] by comparing DFT-MD data for the electrical conductivity to QLB results. The calculations of Desjarlais *et al.* [27] for  $n = 40$  g/cm<sup>3</sup> and our present ones for  $n = 2$  g/cm<sup>3</sup> were computationally demanding but are still not very close to  $x = 0$  so that extrapolation to the limit  $x = 0$  is not very precise. However, the corresponding slopes are quite different: while the present DFT-MD data favor  $\rho_1^{\text{Lorentz}}$  as asymptote at  $x = 0$ , those in Ref. [27] seem to point to the Spitzer value, Eq. (12). Thus, our results do not solve the lively debate about whether or not DFT-MD simulations include the effect of  $e-e$  collisions on the conductivity. We conclude that further DFT-MD simulations must be performed for still higher temperatures and/or lower densities in order to approach the limit  $x \rightarrow 0$  so that the value for  $\rho_1$  can be derived more accurately. Such simulations, e.g., for densities below 1 g/cm<sup>3</sup>, are computationally very challenging using the Kohn-Sham DFT-MD method so that alternative schemas like stochastic DFT [57] and the spectral quadrature method [58] have to be applied for this purpose.

We would like to mention that in the case of thermal conductivity it has been shown that the contribution of  $e-e$  collisions is not taken into account in DFT-MD simulations [27] and gives an additional term. A profound discussion on the mechanism of  $e-e$  collisions has been given recently by Shaffer and Starrett [24]. They argued that the precise nature of the incomplete account of  $e-e$  scattering may be resolved by methods going beyond the Kubo-Greenwood approximation such as time-dependent DFT and GW corrections. Considering a quantum Landau-Fokker-Planck kinetic theory, their main issue is that scattering between particles in a plasma

should be described not by the Coulomb interaction but by the potential of mean force. Obviously, if part of the interaction is already taken into account by introducing quasiparticles and mean-field effects, the corresponding contributions must be removed from the Coulomb interaction for  $e$ - $e$  scattering to avoid double-counting. Comparing with QMD results, Shaffer and Starrett [24] point out that their findings support the conclusions in Ref. [27] that the Kubo-Greenwood QMD calculations contain the indirect electron-electron reshaping effect relevant to both the electrical and the thermal conductivity, but they do not contain the direct scattering effect which further reduces the thermal conductivity.

## V. EXPERIMENTS

Ultimately, the virial expansion, (9), has to be checked experimentally but accurate data on the conductivity of hydrogen plasma in the low-density limit and/or at high temperatures are scarce. Accurate conductivity data for dense hydrogen plasma were derived by Günther and Radtke [44] and are shown in the virial plot (Fig. 2). They are close to the benchmark data of the virial expansion. Note that systematic errors are connected with the analysis of such experiments. For instance, the occurrence of bound states requires a realistic treatment of the plasma composition and of the influence of neutrals on the mobility of electrons. Alternatively, conductivity measurements in highly compressed rare gas plasmas have been performed by Ivanov *et al.* [55] and Popovic *et al.* [36,56], but the interaction of the electrons with the ions deviates from the pure Coulomb potential owing to the cloud of bound electrons. The corresponding virial plot is close to the data for hydrogen plasma (see [39]) but requires a more detailed discussion with respect to the role of bound electrons.

## VI. CONCLUSIONS

We propose an exact virial expansion, (9), for the plasma conductivity to analyze the consistency of theoretical approaches. For instance, several analytical calculations of the dc conductivity  $\sigma(T, n)$  presented in Ref. [25] miss this

strict requirement and fail to give accurate results. Results of DFT-MD simulations are presently considered to be the most reliable, and future path-integral Monte Carlo simulations can be tested by benchmarking with the virial expansion, (9), for  $x \rightarrow 0$ . Note that these *ab initio* simulations become computationally challenging in the low-density region, but the virial expansion allows the extrapolation into this region. The construction of interpolation formulas is possible (see [36]) if the limiting behavior for  $n \rightarrow 0$  and further data in the region of higher densities not accessible for analytical calculations are known.

An outstanding problem that could potentially be addressed by applying the virial expansion of the conductivity is the question whether or not the  $e$ - $e$  collisions are rigorously taken into account. Despite the work presented in [24] and [27], there is no final proof whether the Kubo-Greenwood QMD calculations with the standard approximations for the exchange-correlation energy functional give the exact value for the plasma conductivity in the low-density limit. A Green's function approach may solve this problem but this has not been performed yet. Therefore, we suggest applying our benchmark criterion to future large data sets of Kubo-Greenwood QMD calculations to investigate the contribution of  $e$ - $e$  collisions in the low-density limit.

The approach described here is applicable also to other transport properties such as thermal conductivity, thermopower, viscosity, and diffusion coefficients. Of interest is also the extension of the virial expansion to elements other than hydrogen, where different ions may be formed and the electron-ion interaction is no longer purely Coulombic.

## ACKNOWLEDGMENTS

We thank M. Desjarlais, M. French, and V. Recoules for valuable and fruitful discussions and for provision of data sets. This work was supported by the North German Supercomputing Alliance (HLRN) and the ITMZ of the University of Rostock. M.S. and R.R. thank the DFG for support within the Research Unit FOR 2440. M.B. was supported by the European Horizon 2020 program within the Marie Skłodowska-Curie actions (xICE; Grant No. 894725).

- 
- [1] C. M. Franck and M. Seeger, *Contrib. Plasma Phys.* **46**, 787 (2006).
  - [2] M. Kikuchi, *Energies* **3**, 1741 (2010).
  - [3] J. D. Lindl, *Inertial Confinement Fusion* (Springer, New York, 1998).
  - [4] S. T. Weir, A. C. Mitchell, and W. J. Nellis, *Phys. Rev. Lett.* **76**, 1860 (1996).
  - [5] P. H. Roberts and G. A. Glatzmaier, *Rev. Mod. Phys.* **72**, 1081 (2000).
  - [6] M.-B. Kallenrode, *Space Physics* (Springer, Berlin, 2004).
  - [7] M. French, A. Becker, W. Lorenzen, N. Nettelmann, M. Bethkenhagen, J. Wicht, and R. Redmer, *Astrophys. J. Suppl. S* **202**, 5 (2012).
  - [8] A. Becker, M. Bethkenhagen, C. Kellermann, J. Wicht, and R. Redmer, *Astron. J.* **156**, 149 (2018).
  - [9] A. S. Brun and M. K. Browning, *Living Rev. Sol. Phys.* **14**, 4 (2017).
  - [10] L. D. Landau and E. M. Lifshits, *Physical Kinetics, Course of Theoretical Physics* (Pergamon Press, Oxford, UK, 1981), Vol. 10.
  - [11] J. L. Spitzer and R. Härm, *Phys. Rev.* **89**, 977 (1953).
  - [12] R. Kubo, *J. Phys. Soc. Jpn.* **12**, 570 (1957); *Rep. Prog. Phys.* **29**, 255 (1966).
  - [13] G. Röpke, *Phys. Rev. A* **38**, 3001 (1988).
  - [14] G. Röpke and R. Redmer, *Phys. Rev. A* **39**, 907 (1989).
  - [15] R. Redmer, *Phys. Rep.* **282**, 35 (1997).
  - [16] H. Reinholz and G. Röpke, *Phys. Rev. E* **85**, 036401 (2012).
  - [17] D. A. Greenwood, *Proc. Phys. Soc. London* **71**, 585 (1958).
  - [18] M. P. Desjarlais, J. D. Kress, and L. A. Collins, *Phys. Rev. E* **66**, 025401(R) (2002).



- [19] S. Mazevet, M. P. Desjarlais, L. A. Collins, J. D. Kress, and N. H. Magee, *Phys. Rev. E* **71**, 016409 (2005).
- [20] B. Holst, M. French, and R. Redmer, *Phys. Rev. B* **83**, 235120 (2011).
- [21] T. Dornheim, S. Groth, and M. Bonitz, *Phys. Rep.* **744**, 1 (2018).
- [22] T. Dornheim and J. Vorberger, *Phys. Rev. E* **102**, 063301 (2020).
- [23] M. Bonitz, T. Dornheim, Zh. A. Moldabekov, S. Zhang, P. Hamann, H. Kählert, A. Filinov, K. Ramakrishna, and J. Vorberger, *Phys. Plasmas* **27**, 042710 (2020).
- [24] N. R. Shaffer and C. E. Starrett, *Phys. Rev. E* **101**, 053204 (2020).
- [25] P. E. Grabowski *et al.*, *High Energy Dens. Phys.* **37**, 100905 (2020).
- [26] W.-D. Kraeft, D. Kremp, W. Ebeling, and G. Röpke, *Quantum Statistics of Charged Particle Systems* (Akademie-Verlag, Berlin, 1986).
- [27] M. P. Desjarlais, C. R. Scullard, L. X. Benedict, H. D. Whitley, and R. Redmer, *Phys. Rev. E* **95**, 033203 (2017).
- [28] V. S. Karakhtanov, *Contrib. Plasma Phys.* **56**, 343 (2016).
- [29] Improving the static screening which gives for  $\bar{\rho}_2$  the Debye value  $-0.814047$  [see Eq. (5)], dynamical screening has been considered in [30] and [31], with the result  $-0.4129$ . Based on generalized linear response theory (Zubarev approach), the treatment of dynamical screening solving the quantum Lenard-Balescu equation [14,32,35] gives 0.406 68, also used in [36]. The value, (14), was calculated with a higher precision in [33].
- [30] H. A. Gould and H. E. DeWitt, *Phys. Rev.* **155**, 68 (1967).
- [31] R. H. Williams and H. E. DeWitt, *Phys. Fluids* **12**, 2326 (1969).
- [32] R. Redmer, G. Röpke, F. Morales, and K. Kilimann, *Phys. Fluids B* **2**, 390 (1990).
- [33] V. S. Karakhtanov, R. Redmer, H. Reinholz, and G. Röpke, *Contrib. Plasma Phys.* **53**, 639 (2013).
- [34] A. Esser and G. Röpke, *Phys. Rev. E* **58**, 2446 (1998).
- [35] H. Reinholz, R. Redmer, and D. Tamme, *Contrib. Plasma Phys.* **29**, 395 (1989).
- [36] A. Esser, R. Redmer, and G. Röpke, *Contrib. Plasma Phys.* **43**, 33 (2003).
- [37] H. Reinholz, G. Röpke, S. Rosmej, and R. Redmer, *Phys. Rev. E* **91**, 043105 (2015).
- [38] F. Lambert, V. Recoules, A. Decoster, J. Clérouin, and M. Desjarlais, *Phys. Plasmas* **18**, 056306 (2011).
- [39] See Supplemental Material at <http://link.aps.org/supplemental/10.1103/PhysRevE.104.045204> for contains tables of the data shown in Figs. 1 and 2. The convergence of the DFT-MD simulations (Fig. 2) is considered.
- [40] W. B. Hubbard, *Astrophys. J.* **146**, 858 (1966).
- [41] Y. Lee and R. More, *Phys. Fluids* **27**, 1273 (1983).
- [42] S. Ichimaru and S. Tanaka, *Phys. Rev. A* **32**, 1790 (1985).
- [43] H. Kitamura and S. Ichimaru, *Phys. Rev. E* **51**, 6004 (1995).
- [44] K. Günther and R. Radtke, *Electrical Properties of Nonideal Plasmas* (Birkhäuser, Basel, 1984).
- [45] M. French and R. Redmer, *Phys. Plasmas* **24**, 092306 (2017).
- [46] M. Gajdos, K. Hummer, G. Kresse, J. Furthmüller, and F. Bechstedt, *Phys. Rev. B* **73**, 045112 (2006).
- [47] C. E. Starrett, *High Energy Dens. Phys.* **19**, 58 (2016).
- [48] C. E. Starrett *et al.*, *Phys. Plasmas* **19**, 102709 (2012).
- [49] G. Kresse and J. Hafner, *Phys. Rev. B* **47**, 558 (1993).
- [50] G. Kresse and J. Hafner, *Phys. Rev. B* **49**, 14251 (1994).
- [51] G. Kresse and J. Furthmüller, *Phys. Rev. B* **54**, 11169 (1996).
- [52] J. P. Perdew, K. Burke, and M. Ernzerhof, *Phys. Rev. Lett.* **77**, 3865 (1996).
- [53] S. Nosé, *J. Chem. Phys.* **81**, 511 (1984).
- [54] A. Baldereschi, *Phys. Rev. B* **7**, 5212 (1973).
- [55] Yu. V. Ivanov, V. B. Mintsev, V. E. Fortov, and A. N. Dremin, *Zh. Eksp. Teor. Fiz.* **71**, 216 (1976) [*Sov. Phys. JETP* **44**, 112 (1976)].
- [56] M. M. Popovic, Y. Vitel, and A. A. Mihajlov, in *Strongly Coupled Plasmas*, edited by S. Ichimaru (Elsevier, Amsterdam, 1990), p. 561.
- [57] Y. Cytter, E. Rabani, D. Neuhauser, M. Preising, R. Redmer, and R. Baer, *Phys. Rev. B* **100**, 195101 (2019).
- [58] A. Sharma, S. Hamel, M. Bethkenhagen, J. E. Pask, and P. Suryanarayana, *J. Chem. Phys.* **153**, 034112 (2020).

## 4.7 Electronic transport coefficients from density functional theory across the plasma plane

### Author contributions

#### **M. French**

Preparation of the manuscript, DFT simulations and conductivity calculations, interpretation of simulations

#### **G. Röpke**

Preparation of the manuscript, virial expansion of conductivity

#### **M. Schörner**

Preparation of the manuscript, interpretation of simulations

#### **M. Bethkenhagen**

Preparation of the manuscript, interpretation of simulations

#### **M. Desjarlais**

Preparation of the manuscript, interpretation of simulations

#### **R. Redmer**

Supervision of the project, preparation of the manuscript, interpretation of simulations



## Electronic transport coefficients from density functional theory across the plasma plane

Martin French<sup>1</sup>, Gerd Röpke<sup>1</sup>, Maximilian Schörner<sup>1</sup>, Mandy Bethkenhagen<sup>1,2</sup>,  
Michael P. Desjarlais<sup>3</sup> and Ronald Redmer<sup>1</sup>

<sup>1</sup>Universität Rostock, Institut für Physik, Albert-Einstein-Str. 23-24, D-18059 Rostock, Germany

<sup>2</sup>École Normale Supérieure de Lyon, Université Lyon 1, Laboratoire de Géologie de Lyon, CNRS UMR 5276, 69364 Lyon Cedex 07, France

<sup>3</sup>Sandia National Laboratories, Albuquerque, New Mexico 87185, USA



(Received 1 March 2022; accepted 18 May 2022; published 10 June 2022)

We investigate the thermopower and Lorenz number of hydrogen with Kohn-Sham density functional theory (DFT) across the plasma plane toward the near-classical limit, i.e., weakly degenerate and weakly coupled states. Our results are in concordance with certain limiting values for the Lorentz plasma, a model system which only considers electron-ion scattering. Thereby, we clearly show that the widely used method of calculating transport properties via the Kubo-Greenwood (KG) formalism does not capture electron-electron scattering processes. Our discussion also addresses the inadequateness of assuming a Drude-like frequency behavior for the conductivity of nondegenerate plasmas by revisiting the relaxation time approximation within kinetic theory.

DOI: [10.1103/PhysRevE.105.065204](https://doi.org/10.1103/PhysRevE.105.065204)

### I. INTRODUCTION

Besides the equation of state and the optical properties, the transport coefficients are important quantities to characterize the state of metals and plasmas. The electrical and thermal conductivity,  $\sigma(n, T)$  and  $\lambda(n, T)$ , as well as the thermopower  $\alpha(n, T)$  and Lorenz number (named after Ludvig V. Lorenz [1])  $L(n, T)$  depend in general on the particle density  $n$  and temperature  $T$  but have well-known values for fully degenerate plasmas according to the Ziman theory [2] and in the nondegenerate limit as derived in the seminal work of Spitzer and Härm [3].

Solving fundamental geo- and astrophysical questions on structure, evolution, and magnetic field generation in stars and planets relies on accurate knowledge of  $\sigma$  and  $\lambda$  of stellar and planetary matter [4–9]. The experimental determination of transport properties for plasmas and metals at such high temperatures is very challenging, and a large part of the research in the field is carried out via theoretical and computational methods [10].

The computation of transport coefficients is possible via kinetic theory [11–15], which was introduced originally for low-density systems. Calculations for dense plasmas have to address fundamental problems, e.g., dynamical screening and strong collisions between electrons and ions, the influence of the ionic structure during the collisions (dynamic ion-ion structure factor), and partial ionization (bound states) [16–18]. The fluctuation-dissipation theorem [19] and a Hamiltonian-based linear response description [20] have been invented to relate transport coefficients to equilibrium correlation functions. A generalized linear response theory [21,22] makes this approach practically more applicable, for instance for the evaluation of the equilibrium correlation functions by perturbation theory and establishing the link to kinetic theory [23]. Alternatively, density functional theory (DFT) can be applied

to calculate transport coefficients via the Kubo-Greenwood (KG) formalism [20,24,25]. DFT-MD simulations, which combine the quantum treatment of electrons via density functional theory with the molecular-dynamical (MD) solution of the ionic motion, allow us to treat strongly coupled Coulomb systems beyond perturbation theory, e.g., dense nonideal plasmas up to condensed matter densities, the so-called warm dense matter. The effectiveness of the KG approach, which uses the Kohn-Sham orbitals and energies from DFT, has been demonstrated in particular for dense plasmas and warm dense matter [26–35].

Although the DFT-based approach to calculate transport coefficients in dense plasmas via the KG formalism is very successful, a fundamental question is still open: whether or not the influence of electron-electron (e-e) collisions is properly included. While e-e *correlations* are accounted for by the exchange-correlation energy functional in some approximation to obtain optimal electronic orbitals, it is not clear whether the exact calculation of e-e *collisions* can be performed within a single-particle description without the explicit treatment of two-particle Coulomb interactions. This problem has received increasing attention recently [36–39] and can be checked best in the low-density and high-temperature region of hydrogen plasmas, where exchange and correlation energies become irrelevant and exact results for the transport coefficients are available from the Spitzer theory [3]. Unfortunately, this is just the region where Kohn-Sham-DFT becomes computationally demanding because high temperatures and low densities require huge simulation cells and a large number of bands, so that it is very challenging to converge the calculations. For instance, Desjarlais *et al.* [37] applied a Drude-like fit to the very low-frequency behavior of the transport coefficients. From these extrapolated values, it was concluded that the electrical conductivity agreed with quantum Lenard-Balescu (QLB) [40–43] results that include

e-e scattering, whereas the thermal conductivity was too high by a factor of about two. While these results ruled out for the first time explicit e-e scattering in the DFT calculations, the agreement with the QLB results suggested that a reduction in the electrical conductivity analogous to that found in Spitzer theory due to e-e interactions was present. Shaffer and Starrett [38] supported this argument in their discussion. In contrast, a recent analysis of DFT-MD data within a virial expansion of the electrical conductivity [39] hinted toward e-e collisions not being correctly accounted for at any level.

Here we re-examine the DFT calculations from Ref. [37] and show that they were, unfortunately, not sufficiently converged and that the agreement with QLB results that included e-e scattering [37] was accidental. Although our computational capabilities to converge DFT transport properties at the conditions chosen by Desjarlais *et al.* [37] are still insufficient, we give a clear answer to the question, whether or not e-e scattering is correctly included in the KG formalism, via an alternative route which utilizes the thermopower and Lorenz number calculated at less extreme plasma conditions. Related to the DFT calculations, we also address the inadequacy of assuming a Drude-like frequency dependence in nondegenerate plasmas in a special section about the relaxation time approximation.

In short, this paper shows the first fully converged and convincing results that a DFT-based evaluation of the KG formula does not include exact contributions from e-e collisions. To make this inference, we have performed extensive DFT calculations for hydrogen plasma along a special path across the density-temperature plane. We find that the asymptotic behavior of the calculated transport coefficients converges clearly to the values of the Lorentz plasma, which is a model system (named after Hendrik A. Lorentz [11,44]) *without* e-e collisions, where only the electron-ion (e-i) interactions are considered, usually described by an effective (screened) potential.

## II. PLASMA PARAMETERS

The state of a hydrogen plasma can be generally characterized with two dimensionless parameters [45] that depend on electron density  $n_e$  and temperature  $T$ . The first is the coupling parameter, which relates the average Coulomb interaction energy to the thermal energy,

$$\Gamma = \frac{e^2}{4\pi\epsilon_0 k_B T} \left( \frac{4\pi n_e}{3} \right)^{1/3}, \quad (1)$$

where  $e$  is the elementary charge,  $\epsilon_0$  is the vacuum permittivity, and  $k_B$  is Boltzmann's constant. Second, the degeneracy parameter describes the importance of quantum effects (degeneracy, Pauli blocking, etc.) and is given by

$$\Theta = \frac{8\pi\epsilon_0 k_B T}{e^2 a_B} \left( \frac{1}{3\pi^2 n_e} \right)^{2/3}, \quad (2)$$

where  $a_B$  is the Bohr radius.

A path perpendicular to the  $\Gamma = 1$  and  $\Theta = 1$  lines, which rise on geometric average with a power of  $T \sim n_e^{1/2}$  in the

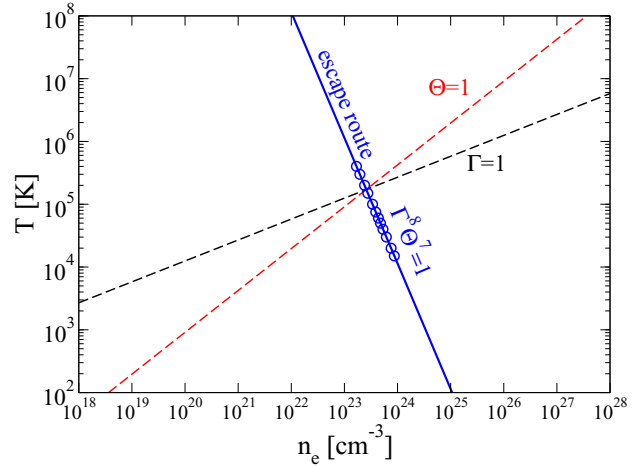


FIG. 1. Density-temperature plane of H plasma with the relevant lines:  $\Theta = 1$ ,  $\Gamma = 1$ , and  $\Gamma^8\Theta^7 = 1$ . Blue circles indicate the conditions chosen for our calculations.

plasma plane, can be defined as follows:

$$T = \left( \frac{4}{9\pi} \right)^{14/3} \left( \frac{3}{4\pi} \right)^2 \left( \frac{2}{a_B} \right)^7 \frac{e^2}{4\pi\epsilon_0 k_B n_e^2}, \quad (3)$$

or equivalently by  $\Gamma^8\Theta^7 = 1$ . We may call this path an escape route from correlation and quantum effects because it represents the shortest route from the highly degenerate ( $\Theta \ll 1$ ) and strongly coupled ( $\Gamma \gg 1$ ) region to the nondegenerate ( $\Theta \gg 1$ ) and weakly coupled ( $\Gamma \ll 1$ ) conditions, anchored at  $\Gamma = \Theta = 1$ ; see Fig. 1.

Following this route allows us to efficiently reach conditions for which certain limiting laws for the transport coefficients of plasmas are known. Our main DFT calculations were run along this path between 15 000 K and 1.46 g/cm<sup>3</sup> up to 400 000 K and 0.2826 g/cm<sup>3</sup> and closely approached characteristic limiting cases at both ends.

## III. RELAXATION TIME APPROXIMATION

Before discussing our DFT calculations, we describe a simpler and well understood approach to calculate electronic transport properties of plasmas, which will be used for various comparisons. This model considers a Lorentz plasma, where electrons scatter only at ions via a statically screened Coulomb potential and all particles are uncorrelated. It is derived by solving the Boltzmann equation within the relaxation time approximation (RTA) [11], which was done, e.g., by Lee and More [46] and can be evaluated for arbitrary degeneracy.

When assuming frequency-dependent perturbations  $\sim \exp(i\omega t)$  by an electrical field  $\mathbf{E}(\omega)$  and a temperature gradient  $\nabla T(\omega)$  at constant pressure, the following nonequilibrium distribution function for the plasma electrons is derived:

$$f(\mathbf{v}) = f_0 + \frac{\tau}{1 + i\omega\tau} \frac{\partial f_0}{\partial E} \mathbf{v} \cdot \left[ e\mathbf{E} + \left( \frac{E - h_e}{T} \right) \nabla T \right], \quad (4)$$

where  $h_e$  is the enthalpy per electron,  $\mathbf{v}$  the velocity,  $\tau = \tau(E)$  the relaxation time, and  $f_0(E)$  is the Fermi distribution

function:

$$f_0(E) = \frac{1}{z^{-1} \exp(E/k_B T) + 1}. \quad (5)$$

The Fermi function depends on the kinetic energy  $E = m_e \mathbf{v}^2/2$  and fugacity  $z = \exp(\mu_e/k_B T)$ , where  $m_e$  is the mass and  $\mu_e$  is the chemical potential of the electrons.

### A. Zero-frequency limit

After calculating the expectation values of electrical current  $\mathbf{j}$  and generalized heat current  $\mathbf{j}'_Q$  at  $\omega = 0$ ,

$$\mathbf{j} = -\frac{2em_e^3}{(2\pi\hbar)^3} \int d^3\mathbf{v} \mathbf{v} f(\mathbf{v}), \quad (6)$$

$$\mathbf{j}'_Q = \frac{2m_e^3}{(2\pi\hbar)^3} \int d^3\mathbf{v} \mathbf{v} \left( \frac{m_e \mathbf{v}^2}{2} - h_e \right) f(\mathbf{v}), \quad (7)$$

the following set of Onsager coefficients is obtained, which can be written as integrals over the energy:

$$K_n = \frac{-8(-e)^{2-n}}{3\pi^{1/2} m_e \lambda_e^3 (k_B T)^{3/2}} \int_0^\infty dE E^{n+3/2} \tau(E) \frac{\partial f_0}{\partial E}, \quad (8)$$

where  $\lambda_e = \hbar \sqrt{2\pi/m_e k_B T}$  is the thermal wavelength. When assuming only e-i scattering at a screened Coulomb potential, the relaxation time in first Born approximation reads [47–49]

$$\tau(E) = \frac{2^{7/2} \pi \varepsilon_0^2 m_e^{1/2} E^{3/2}}{n_i Z_i^2 e^4 \ln \Lambda(E)}, \quad (9)$$

where  $n_i$  and  $Z_i = 1$  are density and charge state of the ions, respectively. Due to its weak energy dependence, the Coulomb logarithm  $\ln \Lambda(E)$  may be pulled out of the integration and later evaluated at a mean value, which then leads to the following expression:

$$K_n = \frac{2^5 \varepsilon_0^2 m_e (k_B T)^3}{3\pi \hbar^3 n_i Z_i^2 e^2} \left( \frac{k_B T}{-e} \right)^n \frac{\Gamma_{n+4} F_{n+2}(z)}{\ln \Lambda(z)}, \quad (10)$$

where the Fermi integrals are defined as

$$F_j(z) = \frac{1}{\Gamma_{j+1}} \int_0^\infty dx \frac{x^j}{z^{-1} \exp(x) + 1}, \quad (11)$$

with Euler's gamma function  $\Gamma_{j+1}$ .

Here we deviate from the original Lee-More model and use the following formula for the statically screened Coulomb logarithm [48–50]:

$$\ln \Lambda = \frac{1}{2} \left[ \ln(1+b) - \frac{b}{1+b} \right], \quad (12)$$

with the following argument:

$$b(z) = \frac{8m_e \tilde{E}(z)}{\hbar^2 \kappa_e^2(z)} = \frac{6m_e (k_B T)^2 \varepsilon_0 \lambda_e^3}{\hbar^2 e^2} \frac{F_{1/2}(z)}{F_{-1/2}^2(z)}. \quad (13)$$

The equation above follows from the screening parameter of a Lorentz plasma [17]:

$$\kappa_e^2(z) = \frac{2e^2}{\varepsilon_0 \lambda_e^3 k_B T} F_{-1/2}(z), \quad (14)$$

and from calculating the mean energy of the *scattering* electrons as

$$\tilde{E}(z) = \frac{\int dE E^{1/2} E \frac{\partial f_0}{\partial E}}{\int dE E^{1/2} \frac{\partial f_0}{\partial E}} = \frac{3}{2} k_B T \frac{F_{1/2}(z)}{F_{-1/2}(z)}, \quad (15)$$

which gives  $\tilde{E} = 3k_B T/2$  in the nondegenerate limit and  $\tilde{E} = E_F$ , which is the Fermi energy, for complete degeneracy.

In summary, all transport coefficients of interest can be calculated within this RTA model by evaluating a set of six Fermi integrals and using an inversion formula for the fugacity, see, e.g., Ref. [18]. In particular, the electrical conductivity is given by

$$\sigma = K_0 = \frac{2^6 \varepsilon_0^2 m_e (k_B T)^3}{\pi \hbar^3 n_i Z_i^2 e^2} \frac{F_2(z)}{\ln \Lambda(z)}. \quad (16)$$

With the ideal enthalpy per electron,

$$h_e = \frac{5}{2} k_B T \frac{F_{3/2}(z)}{F_{1/2}(z)}, \quad (17)$$

the thermopower coefficient can be written as

$$a = -\frac{e}{k_B} \alpha_e = \frac{-eK_1}{k_B T K_0} - \frac{h_e}{k_B T} = 4 \frac{F_3(z)}{F_2(z)} - \frac{5}{2} \frac{F_{3/2}(z)}{F_{1/2}(z)}. \quad (18)$$

Finally, the Lorenz number is

$$L = \left( \frac{e}{k_B T} \right)^2 \left( \frac{K_2}{K_0} - \frac{K_1^2}{K_0^2} \right) = 20 \frac{F_4(z)}{F_2(z)} - 16 \frac{F_3^2(z)}{F_2^2(z)}. \quad (19)$$

Here the Wiedemann-Franz law,  $L = \pi^2/3$ , follows directly from the Sommerfeld expansion of Fermi integrals. Expressions for the nondegenerate limits are easily obtained, since all  $F_j(z) \approx z = n_e \lambda_e^3/2$  there, e.g., we immediately find the numbers  $a = 1.5$  and  $L = 4$ .

### B. Frequency-dependent coefficients

The frequency-dependent coefficients are derived in the same way as Eq. (8). Their real parts then read

$$K_n(\omega) = \frac{-8(-e)^{2-n}}{3\pi^{1/2} m_e \lambda_e^3 (k_B T)^{3/2}} \int_0^\infty dE \frac{E^{n+3/2} \tau(E)}{1 + \omega^2 \tau^2(E)} \frac{\partial f_0}{\partial E}. \quad (20)$$

An analytical integration shows that the coefficient  $K_0(\omega) = \sigma(\omega)$  fulfills the sum rule [37],

$$\frac{2m_e}{\pi e^2} \int_0^\infty d\omega \sigma(\omega) = \frac{2}{\lambda_e^3} F_{1/2}(z) = n_e, \quad (21)$$

for any relaxation time  $\tau(E)$  if the thermodynamics of the electron gas is ideal.

Equation (20) can be integrated numerically using the relaxation time (9). To remain fully consistent with the previous subsection, we keep the Coulomb logarithm constant here, too. Note that a Drude behavior of the coefficients  $K_n(\omega) \sim (1 + \omega^2 \tau^2)^{-1}$  is found only in the fully degenerate limit, where  $\tau = \tau(E_F)$ . For weakly degenerate electrons, the  $\sim E^{3/2}$  proportionality of the relaxation time generates significantly different frequency dependencies of the  $K_n(\omega)$ .

#### IV. DFT CALCULATIONS

We use a combination of density functional theory (DFT) [51,52] and molecular dynamics (MD) to simulate the ion dynamics in our H plasma using the VASP code [53–55], generating ionic configurations for subsequent calculations of transport coefficients. In these DFT-MD simulations, we treat exchange and correlation effects with the Perdew, Burke, Ernzerhof (PBE) approximation [56] and use a PAW pseudopotential (labeled PAW H\_h\_GW) [57,58] with a plane-wave energy cutoff of 1200 eV and the Baldereschi mean-value point [59]. We simulate either 64, 128, or 256 atoms for several 1000 time steps with a length of 0.1 fs at constant temperatures regulated with a Nosé-Hoover thermostat [60,61]. This is done for temperatures between 15 000 and 75 000 K. The pair correlation functions indicate that the ionic structures become increasingly uncorrelated as temperature rises and density decreases; see Appendix A for more details. We therefore use the same ionic configurations from the DFT-MD simulations made at 75 000 K for all calculations of transport coefficients at higher temperatures and only rescale the box sizes to have them match the required smaller densities. This simplification may introduce inaccuracies in the region of intermediate coupling. Nevertheless, it warrants the emergence of configurations of uncorrelated, distant ions toward sufficiently low density and, thus, achieve consistency with the assumptions made in the derivation of the Lorentz and Spitzer limiting values we aim to compare with.

The electronic transport coefficients are then calculated with static DFT calculations using 5–10 ionic configurations from each DFT-MD run and sufficiently large  $\mathbf{k}$ -point sets [59,62] to reach convergence. Here we exclusively use the bare Coulomb potential with a cutoff energy of 2000 eV for the electron-ion interactions. The necessary number of bands was determined for each individual density and temperature with systematic convergence tests. It increases drastically with the temperature along the  $\Gamma^8\Theta^7 = 1$  line. For example, 120 bands per atom were found to be sufficient at 300 000 K ( $\Gamma = 0.52$  and  $\Theta = 2.1$ ). The following expressions for the frequency-dependent Onsager coefficients [25] are evaluated:

$$L_n(\omega) = \frac{2\pi(-e)^{2-n}}{3V\omega} \sum_{\mathbf{k}\nu\mu} |\langle \mathbf{k}\nu | \hat{\mathbf{v}} | \mathbf{k}\mu \rangle|^2 (f_{\mathbf{k}\nu} - f_{\mathbf{k}\mu}) \times \left( \frac{E_{\mathbf{k}\mu} + E_{\mathbf{k}\nu}}{2} - h_e \right)^n \delta(E_{\mathbf{k}\mu} - E_{\mathbf{k}\nu} - \hbar\omega), \quad (22)$$

where  $\omega$  is the frequency,  $V$  the volume of the simulation box,  $E_{\mathbf{k}\mu}$  and  $f_{\mathbf{k}\mu}$  are the energy eigenvalue and Fermi occupation number of the Bloch state  $|\mathbf{k}\mu\rangle$  calculated from DFT, and  $\langle \mathbf{k}\nu | \hat{\mathbf{v}} | \mathbf{k}\mu \rangle$  are matrix elements with the velocity operator taken from the optical routines of VASP [63]. The enthalpy per electron  $h_e = \mu_e + Ts_e$  is calculated from the chemical potential  $\mu_e$  and entropy per electron  $s_e$  that are derived self-consistently in the DFT. Due to the discrete spectrum of eigenvalues caused by the periodic boundary conditions of the simulation box, it is necessary to broaden the delta function to a small, finite width, which is done here with a Gaussian function.

The static electrical conductivity is the limit of  $L_0(\omega)$  at zero frequency, also known as the Kubo-Greenwood

formula [20,24]:

$$\sigma = \lim_{\omega \rightarrow 0} L_0(\omega), \quad (23)$$

while the thermal conductivity can be calculated via

$$\lambda = \frac{1}{T} \lim_{\omega \rightarrow 0} \left( L_2(\omega) - \frac{L_1^2(\omega)}{L_0(\omega)} \right). \quad (24)$$

In addition, we can directly obtain the thermopower coefficient:

$$a = -\frac{e}{k_B} \alpha = -\frac{e}{k_B T} \lim_{\omega \rightarrow 0} \frac{L_1(\omega)}{L_0(\omega)}, \quad (25)$$

and the Lorenz number:

$$L = \left( \frac{e}{k_B T} \right)^2 \lim_{\omega \rightarrow 0} \left[ \frac{L_2(\omega)}{L_0(\omega)} - \frac{L_1^2(\omega)}{L_0^2(\omega)} \right]. \quad (26)$$

The corresponding phenomenological equations read [64]:

$$\mathbf{j} = L_0 \mathbf{E} - \frac{L_1}{T} \nabla T = \sigma \mathbf{E} - \sigma \alpha \nabla T, \quad (27)$$

$$\mathbf{j}'_Q = L_1 \mathbf{E} - \frac{L_2}{T} \nabla T = T \sigma \alpha \mathbf{E} - (\lambda - T \sigma \alpha^2) \nabla T. \quad (28)$$

Note that the coefficients  $K_n$  used in the RTA model in Sec. III differ from the coefficients  $L_n$  of the KG formalism by terms proportional to  $h_e/e$ :

$$L_0 = K_0, \quad (29)$$

$$L_1 = K_1 + \frac{h_e}{e} K_0, \quad (30)$$

$$L_2 = K_2 + \frac{2h_e}{e} K_1 + \frac{h_e^2}{e^2} K_0. \quad (31)$$

Because Eqs. (23)–(26) cannot be evaluated directly at  $\omega = 0$ , extracting their converged DC limits is challenging, especially at high temperatures due to the large number of partially occupied bands that contribute to the summations in the small- $\omega$  region. Especially, having a higher index  $n$  in the coefficients  $L_n$  results in stronger weighting of summands with higher eigenenergies  $E_{\mathbf{k}\nu}$ . This causes the quantities from Eqs. (23)–(26) to show different convergence behaviors at small  $\omega$ . For all numerical values presented here, we have ensured that sufficient convergence has been reached to guarantee unbiased extrapolations (here using linear functions) to obtain the DC numbers.

The quantities most challenging to converge at high  $T$  are the thermal conductivity (24) and the electrical conductivity (23), because they approach their ordinates with a very steep slope. These calculations require very large particle numbers to resolve the low-frequency region sufficiently well to guarantee precise extrapolations to the DC limit. Desjarlais *et al.* [37] assumed that the conductivity shows Drude-like frequency dependence at low frequency and performed extrapolations to  $\omega = 0$  accordingly. A global Drude-like frequency dependence requires that the dynamics of all electrons contributing to the conductivity is determined by a single relaxation time  $\tau$  [50]. This case holds approximately for degenerate electrons ( $\Theta \ll 1$ ), where Pauli blocking allows scattering processes only for electrons near the Fermi level. But in general, the relaxation time depends on the velocity  $v$



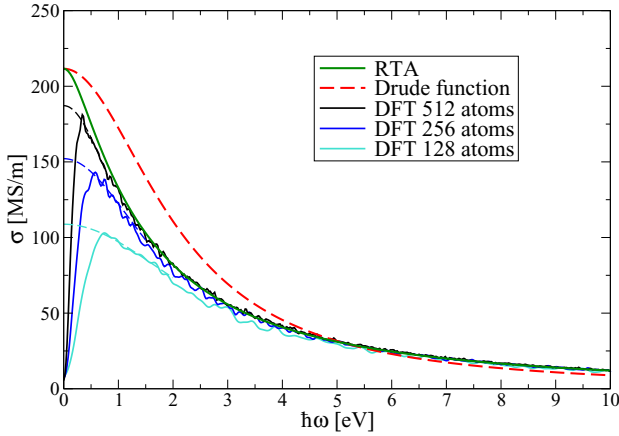


FIG. 2. Frequency-dependent electrical conductivity of hydrogen at 40 g/cm<sup>3</sup> and 500 eV from DFT in comparison with the results from RTA, Eq. (20). Thin dashed lines indicate extrapolations with Drude functions,  $\sigma = \sigma_0/(1 + \omega^2\tau^2)$ , fitted to the DFT data at frequency ranges between 0.5 and 2 eV. For comparison a Drude function scaled to match the zero-frequency value of the RTA and, simultaneously, fulfill the sum rule (21) is also shown.

of the incident electron, e.g., assuming electron-ion scattering in first Born approximation as in Eq. (9), we have  $\tau \sim v^3/\ln \Lambda(v)$ . Thus, the frequency dependence of the conductivity cannot be expected to globally match with a Drude-like form at high temperatures and this, in turn, will add uncertainty when employing low-frequency extrapolations to the DC limit. The following section illustrates this problem in more detail by re-examining an example from the work of Desjarlais *et al.* [37] who investigated hydrogen at very high density and temperature.

### V. RE-EXAMINATION OF CALCULATIONS FROM DESJARLAIS ET AL. (2017)

We have independently revisited the DFT calculations by Desjarlais *et al.* [37] at  $k_B T = 500$  eV and 40 g/cm<sup>3</sup> ( $\Gamma = 0.13$ ) by performing new DFT-MD simulations with 128, 256, and 512 hydrogen atoms. The simulations were run with a time step of 0.003 fs, 25 bands per atom, and a plane-wave cutoff energy of 5000 eV. The electrical conductivity was then calculated from several ionic configurations with 30 bands per atom and a plane-wave cutoff energy of 8000 eV. The Baldereschi  $\mathbf{k}$  point [59] was used in all calculations. Results are displayed in Fig. 2.

It is clearly seen that the DFT conductivities are missing essential contributions at low frequency the fewer particles are considered, thus, even the calculations with 512 atoms are likely still underconverged. At sufficiently high frequency, all DFT results merge with the RTA curve, which is derived independently from the DFT and whose shape is determined by the energy dependence of the relaxation time (9). This convinces us to conclude that, at these weakly coupled conditions, the RTA indicates the correct zero-frequency limit that DFT would produce if convergence could be reached.

Both the RTA and Drude models have a quadratic dependence on frequency for very low frequency, but have

differing higher-order dependence. The Drude-like extrapolation to zero frequency will introduce inaccuracy in the zero frequency limit, relative to the RTA functional form, when convergence with respect to particle number is insufficient. In Ref. [37], the zero-frequency limit was derived from simulations with 256 atoms, the limit of what was computationally feasible at the time. The zero frequency limit was obtained through an extrapolation with a Drude function fitted to data between  $\sim 0.5$  and 1 eV. These circumstances lead to an underestimation of the electrical conductivity and, consequently, to a qualitatively different interpretation of results because of an accidental concordance with Lenard-Balescu calculations. Given that the other two conditions from Ref. [37] at 700 and 900 eV are even more challenging to converge, those results for the electrical and thermal conductivity would also be expected to be unconverged with respect to particle number.

Our present inability to converge the DC electrical conductivity at  $k_B T = 500$  eV and 40 g/cm<sup>3</sup> requires us to seek alternative options to solve our scientific question. The first adjustment is reducing the density and temperature to less extreme conditions by following the escape route  $\Gamma^8\Theta^7 = 1$ . Second, instead of founding our reasoning on the electrical and thermal conductivity we will utilize the thermopower and Lorenz number instead. These quantities require less extreme particle numbers for the determination of their DC values as is explained in the next section.

### VI. THERMOPOWER AND LORENZ NUMBER ALONG THE ESCAPE ROUTE

While the considerations explained in the preceding section, in principle, also apply to the thermopower coefficient (25) and the Lorenz number (26), these quantities are a lot less prone to the convergence issues discussed. This is likely explained by Eqs. (25) and (26) being ratios of Onsager coefficients (22) by definition, which results in a partial compensation of the leading terms that determine the slopes in the  $L_n$  at small frequencies. Consequently, these functions approach their ordinates much less steeply. Their DC values can be found much more easily by standard means of comparing results obtained with different particle numbers and extrapolating the physically relevant section of the curves across the regions of artificial drops (in  $L_n$ ) or divergences (in certain ratios of different  $L_n$ ) close to  $\omega = 0$ ; see Fig. 3 for an example.

The numbers  $L$  and  $a$  are shown in Fig. 4 for conditions along the  $\Gamma^8\Theta^7 = 1$  line. Concordance of DFT results with known limits for  $\Theta \ll 1$  ( $L = \pi^2/3$  and  $a = 0$ ), which are not susceptible to e-e scattering mechanisms due to Pauli blocking [11,65], had been established in the past [25,27].

However, in the opposite limit, Fig. 4 clearly shows that the DFT calculations do not approach the Spitzer results, but instead the Lorentz plasma values (e-i scattering only), which are substantially higher; see also Table I. Thus, we conclude that e-e collisions are not accounted for in DFT when following the KG formalism, i.e., by computing electronic transport coefficients from Eqs. (22).



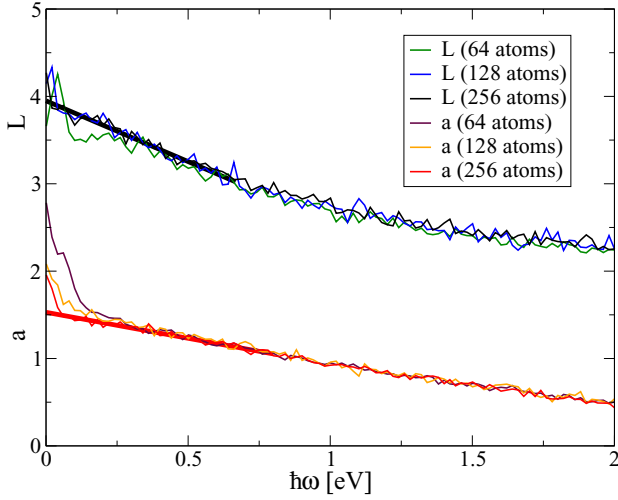


FIG. 3. Lorenz number and thermopower coefficient from our DFT calculations at 200 000 K and  $0.3997 \text{ g/cm}^3$  ( $\Gamma = 0.84$  and  $\Theta = 1.23$ ) for different particle numbers and their linear extrapolations (bold lines) to the DC limits.

## VII. FURTHER DISCUSSION

The reason why e-e scattering is absent in DFT transport properties is that the Kohn-Sham interaction operator,

$$v_{KS}(\{\mathbf{r}_i\}) = \sum_i \left[ - \sum_I \frac{e^2 Z_I}{4\pi \epsilon_0 |\mathbf{r}_i - \mathbf{R}_I|} + \frac{e^2}{4\pi \epsilon_0} \int d^3 \mathbf{r}' \frac{n_e(\mathbf{r}')}{|\mathbf{r}_i - \mathbf{r}'|} + v_{xc,i}(\mathbf{r}_i) \right], \quad (32)$$

where  $\mathbf{r}'$  is a position vector and  $\mathbf{r}_i$  and  $\mathbf{R}_I$ , respectively, are electronic and ionic position coordinates, has the same single-particle structure (separable into additive single-electron

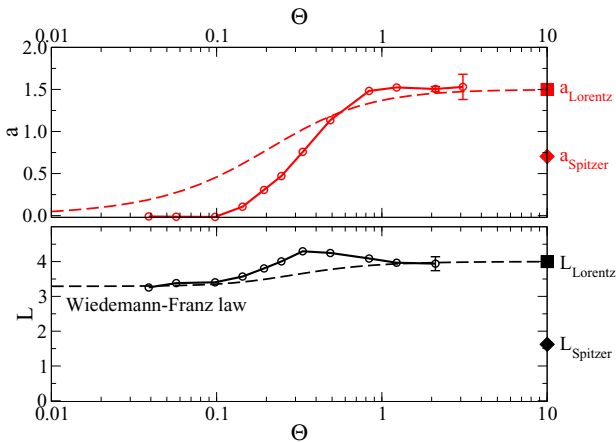


FIG. 4. Thermopower coefficient (red) and Lorenz number (black) from DFT (full) and RTA (dashed) along the  $\Gamma^8 \Theta^7 = 1$  line.

TABLE I. Values for the transport coefficients for hydrogen plasma according to the Spitzer theory [3,49] accounting for e-i and e-e scattering compared with the values from the KG formalism (DFT) at  $\Gamma = 0.52$  and  $\Theta = 2.1$ .

Quantity	Lorentz (e-i)	Spitzer (e-i and e-e)	DFT-MD
$a$	1.5	0.7033	$1.51 \pm 0.03$
$L$	4.0	1.6220	$3.94 \pm 0.2$

terms) as the interaction operator for adiabatic e-i scattering:

$$v_{ei}(\{\mathbf{r}_i\}) = - \sum_{i,I} \frac{e^2 Z_I}{4\pi \epsilon_0 |\mathbf{r}_i - \mathbf{R}_I|}, \quad (33)$$

but with the additional Hartree and exchange-correlation terms. To achieve the correct Spitzer results in a Hamiltonian-based formalism, which is possible within generalized linear response theory [21,22], e-e scattering has to be included directly via the fundamental two-particle interaction operator (not separable into additive single-electron terms):

$$v_{ee}(\{\mathbf{r}_i\}) = \sum_{i < j} \frac{e^2}{4\pi \epsilon_0 |\mathbf{r}_i - \mathbf{r}_j|}. \quad (34)$$

Such a treatment leads to mathematical structures that are significantly different from the compact set of Onsager coefficients (22) in the KG formalism [66,67]. The mean-field Hartree potential in DFT,

$$v_H(\{\mathbf{r}_i\}) = \sum_i \frac{e^2}{4\pi \epsilon_0} \int d^3 \mathbf{r}' \frac{n_e(\mathbf{r}')}{|\mathbf{r}_i - \mathbf{r}'|}, \quad (35)$$

which becomes merely a global constant in a homogeneous electron gas at very high  $T$ , is unable to reintroduce e-e collision effects in the electronic transport coefficients. The same applies to the exchange-correlation potential  $\sum_i v_{xc,i}(\mathbf{r}_i)$ , which vanishes  $\sim T^{-1/2}$  according to the Debye-Hückel limiting laws [17] in a real plasma. Within the PBE approximation [56], which is used in our practical work, it reduces to a constant energy shift according the local density approximation [68,69] for a homogeneous electron gas at very high  $T$  and, thus, does not influence the velocity matrix elements either.

Electron-electron collisions, when taken into account explicitly in the theoretical description via kinetic theory [3] or generalized linear response theory [21–23], reshape the nonequilibrium momentum distribution of electrons [3]. Whether or not e-e collisions have a particular effect on the electronic heat current that is separable from the reshaping of the distribution function as suggested in Ref. [37] remains to be shown.

For additional comparison, Fig. 5 contains results from kinetic theory within the RTA from Sec. III. This model describes a Lorentz plasma of noninteracting electrons scattering randomly at ions with small momentum transfer (weak collisions). It is not able to capture the important influences of strong collisions, electronic correlations, and ionic structure present in DFT, which explains the deviations to the DFT conductivity. Because of the more difficult convergence of DFT conductivities compared to thermopower and Lorenz

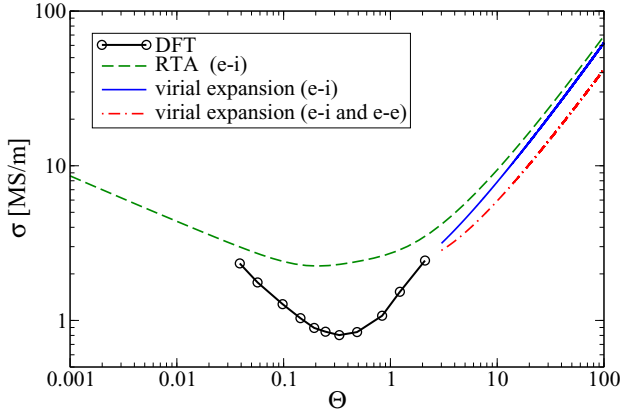


FIG. 5. Electrical conductivity from DFT, RTA, and the virial expansion with and without e-e collisions [39] as indicated in the legend along the  $\Gamma^8\Theta^7 = 1$  line.

number, we cannot yet achieve an overlap between DFT and RTA data toward the nondegenerate limit.

To illustrate the influence of e-e scattering on the electrical conductivity, we also compare with results recently derived from the virial expansion in terms of  $\Theta/\Gamma$ , which holds for  $\Gamma/\Theta \ll 1$  and  $\Theta \gg 1$ , according to Ref. [39] (formulas are given in the Appendix B). The virial expansion accounts for dynamical screening effects and strong collisions and, probably due to the latter [70], approaches the DFT results better than the RTA model. The virial expansion can be elaborated for both Lorentz and Spitzer plasmas. In the latter case, the conductivity of the hydrogen plasma is smaller by a factor of 0.58 in the large- $\Theta$  limit [3,39].

On the one hand, the lack of e-e collisions may be a reason why DFT results have not yet been brought in accordance with conductivity models for dense, partially ionized plasmas more complex than fully ionized hydrogen [49]. On the other hand, DFT has certainly achieved great success in describing the electrical and thermal conductivity of liquid and solid metals like lithium [71], molybdenum [29], aluminum [26,34], and, with a caveat due to yet incomplete description of magnetism, also iron [28,35]. In light of our present findings, this implies that e-e scattering is of minor relevance at conditions in materials at geophysically relevant temperatures of few 1000 degrees K. This must not be confused with correlations between electrons, which certainly are important there and can approximately be captured by DFT.

Note that combining DFT with dynamical mean-field theory (DMFT) [72–75] allows for the introduction of additional electronic correlation effects beyond that of DFT, which also affect the electronic transport properties. However, these correlations are introduced artificially via localized repulsive interactions of certain electronic orbitals as offered by the Hubbard model and depend on external parameters that require additional constraints. Whether the DFT + DMFT method is potentially able to describe scattering between uncorrelated electrons via a proper Coulomb interaction  $\sim 1/r$  is doubtful and has yet to be examined by an effort similar to ours, i.e., by benchmarking against the known limiting values for Spitzer and Lorentz plasmas.

While it is not obvious how e-e collisions can consistently be included into DFT approaches, a way to overcome these difficulties has been discussed in Ref. [37]. Within the generalized linear response theory [22,23,50,67], transport coefficients are expressed by higher-order correlation functions. Evaluating these with perturbation theory leads to renormalization factors that account for e-e collisions in relation to the Lorentz plasma model and depend on the degeneracy of the electron gas [36]. In the nondegenerate Spitzer limit [3], these renormalization factors are 0.5816 for  $L_0$ , 0.2727 for  $L_1$ , and 0.1970 for  $L_2$ . Directly related to them are the renormalization factors 0.4689 for  $a$  and 0.4055 for  $L$ ; see also Table I. For strongly degenerate plasmas, all of these renormalization factors converge to 1.

Time-dependent DFT [76] seems an unlikely candidate for the introduction of e-e scattering because it is, like static DFT, a description of independent quasiparticles in an effective mean-field potential. It may, however, be able to describe effects from dynamical screening that are not included in static DFT calculations.

An alternative approach beyond DFT may be future development of quantum Monte Carlo techniques [77], which, however, require much higher computational effort than DFT. This applies especially to materials with multielectron atoms in realistic stoichiometry that many practical applications of WDM require, e.g., hydrogen-helium mixtures in Jupiter and Saturn [5,7,8] or iron-silicon-oxygen mixtures in Earth [78]. So far, quantitative predictions of transport properties of such systems can be made only with DFT-based methods.

## VIII. CONCLUSION

In conclusion, we have resolved that electronic transport properties derived from DFT do not account for e-e collision effects. At present, DFT-MD simulations represent the most efficient and an indispensable approach to describe various properties of both condensed and warm dense matter. We have outlined directions for future developments to consistently include electron-electron collisions, including a promising combination of DFT with generalized linear response theory [21,22]. Our discussion indicates that such future efforts to develop transport theory [10] further can greatly benefit from systematic investigations of the Lorenz number and thermopower. Likewise, advancing experimental methods to determine thermopower and Lorenz number of warm dense matter will provide additional constraints to the theoretical methods aside from the Spitzer limiting values that the principal discussion of this article is tied to.

## ACKNOWLEDGMENTS

We thank Heidi Reinholz for helpful discussions. M.F., M.S., and R.R. acknowledge support by the Deutsche Forschungsgemeinschaft (DFG) within the FOR 2440. The *ab initio* calculations were performed at the North-German Supercomputing Alliance (HLRN) facilities and at the IT and Media Center of the University of Rostock.

## APPENDIX A: PAIR CORRELATION FUNCTION

The pair correlation function illustrated in Fig. 6 shows that protons are uncorrelated at 75 000 K and  $0.6527 \text{ g/cm}^3$  and

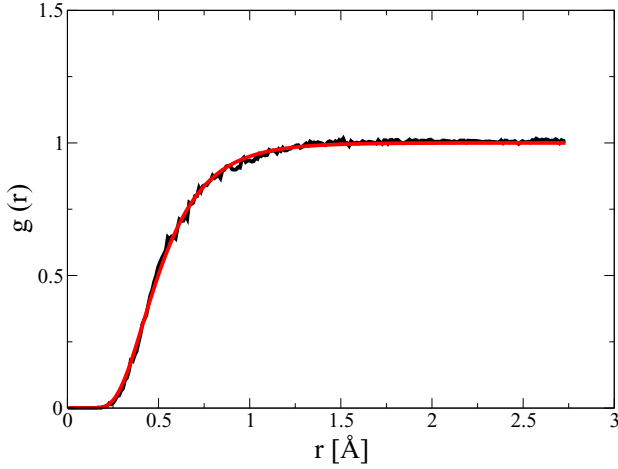


FIG. 6. Protonic pair correlation function from a DFT-MD simulation with 64 hydrogen atoms at 75 000 K and  $0.6527 \text{ g/cm}^3$  (black line). Fit to a function  $g(r) = \exp[-r_0 \exp(-\kappa r)/r]$ , where the fit parameters were determined as  $r_0 = 2.259 \text{ \AA}$  and  $\kappa = 3.77/\text{\AA}$  (red line).

are only subject to repulsive interactions at small distances  $r$ . A quantitative check of this observation is possible by fitting the pair correlation function to the expression [13]:

$$g(r) = \exp[-V(r)/k_B T], \quad (\text{A1})$$

which applies for uncorrelated particles interacting via a radial pair potential  $V(r)$ . The red line in Fig. 6 is the result of such a fit if a screened Coulomb potential for proton-proton interaction is assumed:

$$V(r) \sim \frac{\exp(-\kappa r)}{r}. \quad (\text{A2})$$

Using the same configurations of uncorrelated ions also at lower densities and higher temperatures by scaling the box

TABLE II. First and second virial coefficients for the conductivity of fully ionized hydrogen plasma with and without e-e scattering from Ref. [39].

Coefficient	Lorentz (e-i)	Spitzer (e-i and e-e)
$\rho_1$	$(2\pi^3)^{1/2}/16$	0.846
$\rho_2$	1.0	0.4917

size increases the distance between all ions further. This is sufficient to bring our system closer to the physical situation assumed in the derivation of the relevant high- $T$  limiting cases for the transport properties, i.e., resistivity through uncorrelated collision events of electrons at individual scatterers [3].

## APPENDIX B: VIRIAL EXPANSION FOR THE CONDUCTIVITY

Here we give the low-density limit of the electrical conductivity according to the virial expansion by Röpke *et al.* [39], which reads

$$\sigma[\text{S/m}] = \frac{32405.4 T_{\text{eV}}^{3/2}}{\rho_1 \ln(\Theta/\Gamma) + \rho_2 + \mathcal{O}[(\Gamma/\Theta)^{1/2} \ln(\Theta/\Gamma)]}, \quad (\text{B1})$$

with the virial coefficients as given in Table II. The virial expansion is valid for  $\Gamma/\Theta \ll 1$  and  $\Theta \gg 1$ . For the plasma parameter  $\Gamma$  we have along the escape route  $1/\Gamma = \Theta^{7/8}$ . The temperature  $T_{\text{eV}} = k_B T / \text{eV}$  in units of eV follows as

$$T_{\text{eV}} = 14.7761 \frac{1}{\Gamma^2 \Theta}. \quad (\text{B2})$$

Altogether, the virial expansion for  $\sigma$  along the escape route is given by

$$\sigma[\text{MS/m}] = \frac{1.84059 \Theta^{9/8}}{\frac{15}{8} \rho_1 \ln(\Theta) + \rho_2 + \mathcal{O}(\Theta^{-15/16} \ln \Theta)}. \quad (\text{B3})$$

[1] L. Lorenz, *Ann. Phys. Chem.* **223**, 429 (1872).  
[2] J. M. Ziman, *Philos. Mag.* **6**, 1013 (1961).  
[3] L. Spitzer and R. Härm, *Phys. Rev.* **89**, 977 (1953).  
[4] T. Guillot, D. Gautier, G. Chabrier, and B. Mosser, *Icarus* **112**, 337 (1994).  
[5] A. Y. Potekhin, D. Baiko, P. Haensel, and D. G. Yakovlev, *Astron. Astrophys.* **346**, 345 (1999).  
[6] G. Schubert and K. M. Soderlund, *Phys. Earth Planet. Inter.* **187**, 92 (2011).  
[7] M. French, A. Becker, W. Lorenzen, N. Nettelmann, M. Bethkenhagen, J. Wicht, and R. Redmer, *Astrophys. J. Suppl. Series* **202**, 5 (2012).  
[8] R. Helled, *The Interiors of Jupiter and Saturn* (Oxford University Press, New York, NY, 2019).  
[9] J. Wicht, M. French, S. Stellmach, N. Nettelmann, T. Gastine, L. Duarte, and R. Redmer, in *Magnetic Fields in the Solar System*, Vol. 448 (Springer, Astrophysics and Space Science Library, Cham, 2018), pp. 7–22

[10] P. E. Grabowski, S. B. Hansen, M. S. Murillo, L. G. Stanton, F. R. Graziani, A. B. Zylstra, S. D. Baalrud, P. Arnault, A. D. Baczewski, L. X. Benedict, C. Blancard, O. Čertík, J. Clérouin, L. A. Collins, S. Copeland, A. A. Correa, J. Dai, J. Daligault, M. P. Desjarlais, M. W. C. Dharma-wardana *et al.*, *High Energy Density Phys.* **37**, 100905 (2020).  
[11] L. D. Landau and E. M. Lifshitz, *Physical Kinetics, Course of Theoretical Physics*, Vol. 10 (Pergamon Press, Oxford, 1981).  
[12] S. R. de Groot and P. Mazur, *Non-Equilibrium Thermodynamics* (Dover Publications, New York, 1984).  
[13] J. P. Hansen and I. R. McDonald, *Theory of Simple Liquids* (Academic Press, London, 1976).  
[14] J. A. McLennan, *Introduction to Non-Equilibrium Statistical Mechanics* (Prentice Hall, Englewood Cliffs, NJ, 1989).  
[15] M. Bonitz, *Quantum Kinetic Theory*, 2nd ed. (Springer, Cham, 2016).  
[16] W. Ebeling, V. E. Fortov, Y. L. Klimontovich, N. P. Kovalenko, W. D. Kraeft, Y. P. Krasny, D. Kremp, P. P. Kulik, V. A. Riaby,

- G. Röpke, E. K. Rozanov, and M. Schlanges, *Transport Properties of Dense Plasmas* (Akademie-Verlag, Berlin, 1984).
- [17] W.-D. Kraeft, D. Kremp, W. Ebeling, and G. Röpke, *Quantum Statistics of Charged Particle Systems* (Akademie-Verlag, Berlin, 1986).
- [18] R. Zimmermann, *Many-Particle Theory of Highly Excited Semiconductors* (Teubner Verlagsgesellschaft, Leipzig, 1988).
- [19] R. Kubo, *Rep. Prog. Phys.* **29**, 255 (1966).
- [20] R. Kubo, *J. Phys. Soc. Jpn.* **12**, 570 (1957).
- [21] D. Zubarev, V. Morozov, and G. Röpke, *Statistical Mechanics of Nonequilibrium Processes*, Vol. I (Akademie-Verlag, Berlin, 1996).
- [22] D. Zubarev, V. Morozov, and G. Röpke, *Statistical Mechanics of Nonequilibrium Processes*, Vol. II (Akademie-Verlag, Berlin, 1997).
- [23] H. Reinholz and G. Röpke, *Phys. Rev. E* **85**, 036401 (2012).
- [24] D. A. Greenwood, *Proc. Phys. Soc.* **71**, 585 (1958).
- [25] B. Holst, M. French, and R. Redmer, *Phys. Rev. B* **83**, 235120 (2011).
- [26] M. P. Desjarlais, J. D. Kress, and L. A. Collins, *Phys. Rev. E* **66**, 025401(R) (2002).
- [27] V. Recoules and J.-P. Crocombette, *Phys. Rev. B* **72**, 104202 (2005).
- [28] D. Alfè, M. Pozzo, and M. P. Desjarlais, *Phys. Rev. B* **85**, 024102 (2012).
- [29] M. French and T. R. Mattsson, *Phys. Rev. B* **90**, 165113 (2014).
- [30] N. de Koker, G. Steinle-Neumann, and V. Vlček, *Proc. Natl. Acad. Sci. U.S.A.* **109**, 4070 (2012).
- [31] M. Pozzo, C. Davies, D. Gubbins, and D. Alfè, *Nature (London)* **485**, 355 (2012).
- [32] D. V. Knyazev and P. R. Levashov, *Comput. Mater. Sci.* **79**, 817 (2013).
- [33] K. R. Cochrane, R. W. Lemke, Z. Riford, and J. H. Carpenter, *J. Appl. Phys.* **119**, 105902 (2016).
- [34] B. B. L. Witte, G. Röpke, P. Neumayer, M. French, P. Sperling, V. Recoules, S. H. Glenzer, and R. Redmer, *Phys. Rev. E* **99**, 047201 (2019).
- [35] J.-A. Korell, M. French, G. Steinle-Neumann, and R. Redmer, *Phys. Rev. Lett.* **122**, 086601 (2019).
- [36] H. Reinholz, G. Röpke, S. Rosmej, and R. Redmer, *Phys. Rev. E* **91**, 043105 (2015).
- [37] M. P. Desjarlais, C. R. Scullard, L. X. Benedict, H. D. Whitley, and R. Redmer, *Phys. Rev. E* **95**, 033203 (2017).
- [38] N. R. Shaffer and C. E. Starrett, *Phys. Rev. E* **101**, 053204 (2020).
- [39] G. Röpke, M. Schörner, R. Redmer, and M. Bethkenhagen, *Phys. Rev. E* **104**, 045204 (2021).
- [40] A. Lenard, *Ann. Phys.* **10**, 390 (1960).
- [41] R. Balescu, *Phys. Fluids* **3**, 52 (1960).
- [42] R. H. Williams and H. E. DeWitt, *Phys. Fluids* **12**, 2326 (1969).
- [43] R. A. Redmer, G. Röpke, F. Morales, and K. Kilimann, *Phys. Fluids B: Plasma Phys.* **2**, 390 (1990).
- [44] H. A. Lorentz, *Arch. Néerl.* **10**, 336 (1905).
- [45] S. Ichimaru, *Statistical Plasma Physics, Volume II: Condensed Plasmas* (Addison Wesley, Menlo Park, CA, 1994).
- [46] Y. T. Lee and R. M. More, *Phys. Fluids* **27**, 1273 (1984).
- [47] G. D. Mahan, *Many-Particle Physics*, edited by J. T. Devreese, R. P. Evrard, S. Lundqvist, G. D. Mahan, and N. H. March (Plenum Press, New York, 1981).
- [48] G. Röpke, *Theor. Math. Phys.* **194**, 74 (2018).
- [49] M. French and R. Redmer, *Phys. Plasmas* **24**, 092306 (2017).
- [50] G. Röpke, *Nonequilibrium Statistical Physics* (Wiley-VCH, Weinheim, 2013).
- [51] W. Kohn and L. J. Sham, *Phys. Rev.* **140**, A1133 (1965).
- [52] N. D. Mermin, *Phys. Rev.* **137**, A1441 (1965).
- [53] G. Kresse and J. Hafner, *Phys. Rev. B* **47**, 558 (1993).
- [54] G. Kresse and J. Hafner, *Phys. Rev. B* **48**, 13115 (1993).
- [55] G. Kresse and J. Furthmüller, *Phys. Rev. B* **54**, 11169 (1996).
- [56] J. P. Perdew, K. Burke, and M. Ernzerhof, *Phys. Rev. Lett.* **77**, 3865 (1996).
- [57] P. E. Blöchl, *Phys. Rev. B* **50**, 17953 (1994).
- [58] G. Kresse and D. Joubert, *Phys. Rev. B* **59**, 1758 (1999).
- [59] A. Baldereschi, *Phys. Rev. B* **7**, 5212 (1973).
- [60] S. Nosé, *J. Chem. Phys.* **81**, 511 (1984).
- [61] W. G. Hoover, *Phys. Rev. A* **31**, 1695 (1985).
- [62] H. J. Monkhorst and J. D. Pack, *Phys. Rev. B* **13**, 5188 (1976).
- [63] M. Gajdoš, K. Hummer, G. Kresse, J. Furthmüller, and F. Bechstedt, *Phys. Rev. B* **73**, 045112 (2006).
- [64] The phenomenological equations in Ref. [25] are misprinted.
- [65] A. Sommerfeld and H. Bethe, *Elektronentheorie der Metalle* (Springer, Berlin, 1967).
- [66] H. Reinholz, R. Redmer, and D. Tammé, *Contrib. Plasma Phys.* **29**, 395 (1989).
- [67] R. Redmer, *Phys. Rep.* **282**, 35 (1997).
- [68] D. M. Ceperley and B. J. Alder, *Phys. Rev. Lett.* **45**, 566 (1980).
- [69] J. P. Perdew and A. Zunger, *Phys. Rev. B* **23**, 5048 (1981).
- [70] Dynamical screening effects are not included in static DFT calculations.
- [71] A. Kietzmann, R. Redmer, M. P. Desjarlais, and T. R. Mattsson, *Phys. Rev. Lett.* **101**, 070401 (2008).
- [72] L. V. Pourovskii, J. Mravlje, A. Georges, S. I. Simak, and I. A. Abrikosov, *New J. Phys.* **19**, 073022 (2017).
- [73] J. Xu, P. Zhang, K. Haule, J. Minar, S. Wimmer, H. Ebert, and R. E. Cohen, *Phys. Rev. Lett.* **121**, 096601 (2018).
- [74] Y. Zhang, M. Hou, G. Liu, C. Zhang, V. B. Prakapenka, E. Greenberg, Y. Fei, R. E. Cohen, and J.-F. Lin, *Phys. Rev. Lett.* **125**, 078501 (2020).
- [75] L. V. Pourovskii, J. Mravlje, M. Pozzo, and Alfè, *Nat. Commun.* **11**, 4105 (2020).
- [76] E. Runge and E. K. U. Gross, *Phys. Rev. Lett.* **52**, 997 (1984).
- [77] F. Lin, M. A. Morales, K. T. Delaney, C. Pierleoni, R. M. Martin, and D. M. Ceperley, *Phys. Rev. Lett.* **103**, 256401 (2009).
- [78] M. Pozzo, C. Davies, D. Gubbins, and D. Alfè, *Phys. Rev. B* **87**, 014110 (2013).

# Bibliography

- [1] W. Baumjohann and R. A. Treumann, *Basic Space Plasma Physics* (Imperial College Press, 1996).
- [2] S. Dunlop, T. Encrenaz, J. Bibring, M. Blanc, M. Barucci, F. Roques, and P. Zarka, *The Solar System*, Astronomy and Astrophysics Library (Springer Berlin, Heidelberg, 2004).
- [3] D. Gurnett and A. Bhattacharjee, *Introduction to Plasma Physics: With Space and Laboratory Applications* (Cambridge University Press, 2005).
- [4] D. Kremp, M. Schlanges, and W.-D. Kraeft, *Quantum Statistics of Nonideal Plasmas* (Springer Berlin, Heidelberg, 2005).
- [5] Marshall space flight center: The solar interior, <https://solarscience.msfc.nasa.gov/interior.shtml> (2018), accessed: 2023-06-30.
- [6] J. Christensen-Dalsgaard, W. Däppen, S. V. Ajukov, E. R. Anderson, H. M. Antia, S. Basu, V. A. Baturin, G. Berthomieu, B. Chaboyer, S. M. Chitre, A. N. Cox, P. Demarque, J. Donatowicz, W. A. Dziembowski, M. Gabriel, D. O. Gough, D. B. Guenther, J. A. Guzik, J. W. Harvey, F. Hill, G. Houdek, C. A. Iglesias, A. G. Kosovichev, J. W. Leibacher, P. Morel, C. R. Proffitt, J. Provost, J. Reiter, E. J. Rhodes, F. J. Rogers, I. W. Roxburgh, M. J. Thompson, and R. K. Ulrich, *Science* **272**, 1286 (1996).
- [7] A. Sakuraba and P. H. Roberts, *Nat. Geosci.* **2**, 802 (2009).
- [8] J. G. O'Rourke and D. J. Stevenson, *Nature* **529**, 387 (2016).
- [9] M. Landeau, A. Fournier, H.-C. Nataf, D. Cébron, and N. Schaeffer, *Nature Reviews Earth & Environment* **3**, 255 (2022).
- [10] J. E. Mound and C. J. Davies, *Nat. Geosci.* **16**, 380 (2023).
- [11] K. M. Soderlund and S. Stanley, *Philosophical Transactions of the Royal Society A: Mathematical, Physical and Engineering Sciences* **378**, 20190479 (2020).
- [12] W. Dietrich and J. Wicht, *Phys. Earth Planet. Inter.* **217**, 10 (2013).
- [13] H. Cao, J. M. Aurnou, J. Wicht, W. Dietrich, K. M. Soderlund, and C. T. Russell, *Geophys. Res. Lett.* **41**, 4127 (2014).
- [14] C. Jones, *Icarus* **241**, 148 (2014).
- [15] S. Stanley, *Geophys. Res. Lett.* **37** (2010).
- [16] W. Lorenzen, B. Holst, and R. Redmer, *Phys. Rev. B* **82**, 195107 (2010).
- [17] W. Lorenzen, B. Holst, and R. Redmer, *Phys. Rev. B* **84**, 235109 (2011).



- [18] M. D. Knudson, M. P. Desjarlais, A. Becker, R. W. Lemke, K. R. Cochrane, M. E. Savage, D. E. Bliss, T. R. Mattsson, and R. Redmer, *Science* **348**, 1455 (2015).
- [19] M. Ross, *Nature* **292**, 435 (1981).
- [20] D. Kraus, J. Vorberger, A. Pak, N. J. Hartley, L. B. Fletcher, S. Frydrych, E. Galtier, E. J. Gamboa, D. O. Gericke, S. H. Glenzer, E. Granados, M. J. MacDonald, A. J. MacKinnon, E. E. McBride, I. Nam, P. Neumayer, M. Roth, A. M. Saunders, A. K. Schuster, P. Sun, T. van Driel, T. Döppner, and R. W. Falcone, *Nature Astronomy* **1**, 606 (2017).
- [21] N. A. Tahir, V. Bagnoud, P. Neumayer, A. R. Piriz, and S. A. Piriz, *Sci. Rep.* **13**, 1459 (2023).
- [22] L. Scheibe, *Thermal Evolution Models for Uranus and Neptune*, Ph.D. thesis, University of Rostock (2021).
- [23] B. Cheng, S. Hamel, and M. Bethkenhagen, *Nat. Commun.* **14**, 1104 (2023).
- [24] M. Mayor and D. Queloz, *Nature* **378**, 355 (1995).
- [25] R. I. Dawson and J. A. Johnson, *Annual Review of Astronomy and Astrophysics* **56**, 175 (2018).
- [26] J. Lyman Spitzer, *Astronomy Quarterly* **7**, 131 (1990).
- [27] M. W. Werner, T. L. Roellig, F. J. Low, G. H. Rieke, M. Rieke, W. F. Hoffmann, E. Young, J. R. Houck, B. Brandl, G. G. Fazio, J. L. Hora, R. D. Gehrz, G. Helou, B. T. Soifer, J. Stauffer, J. Keene, P. Eisenhardt, D. Gallagher, T. N. Gautier, W. Irace, C. R. Lawrence, L. Simmons, J. E. V. Cleve, M. Jura, E. L. Wright, and D. P. Cruikshank, *The Astrophysical Journal Supplement Series* **154**, 1 (2004).
- [28] J. P. Gardner, J. C. Mather, M. Clampin, R. Doyon, M. A. Greenhouse, H. B. Hammel, J. B. Hutchings, P. Jakobsen, S. J. Lilly, K. S. Long, J. I. Lunine, M. J. Mccaughrean, M. Mountain, J. Nella, G. H. Rieke, M. J. Rieke, H.-W. Rix, E. P. Smith, G. Sonneborn, M. Stiavelli, H. S. Stockman, R. A. Windhorst, and G. S. Wright, *Space Sci. Rev.* **123**, 485 (2006).
- [29] H. Rauer, C. Catala, C. Aerts, T. Appourchaux, W. Benz, A. Brandeker, J. Christensen-Dalsgaard, M. Deleuil, L. Gizon, M.-J. Goupil, M. Güdel, E. Janot-Pacheco, M. Mas-Hesse, I. Pagano, G. Piotto, D. Pollacco, Santos, A. Smith, J.-C. Suárez, R. Szabó, *et al.*, *Exp. Astron.* **38**, 249 (2014).
- [30] R. K. Yadav, U. R. Christensen, S. J. Wolk, and K. Poppenhaeger, *The Astrophysical Journal Letters* **833**, L28 (2016).
- [31] Vidotto, A. A., Jardine, M., Morin, J., Donati, J.-F., Lang, P., and Russell, A. J. B., *A&A* **557**, A67 (2013).

- [32] D. Silver, A. Huang, C. J. Maddison, A. Guez, L. Sifre, G. van den Driessche, J. Schrittwieser, I. Antonoglou, V. Panneershelvam, M. Lanctot, S. Dieleman, D. Grewe, J. Nham, N. Kalchbrenner, I. Sutskever, T. Lillicrap, M. Leach, K. Kavukcuoglu, T. Graepel, and D. Hassabis, *Nature* **529**, 484 (2016).
- [33] D. Silver, T. Hubert, J. Schrittwieser, I. Antonoglou, M. Lai, A. Guez, M. Lanctot, L. Sifre, D. Kumaran, T. Graepel, T. Lillicrap, K. Simonyan, and D. Hassabis, *Science* **362**, 1140 (2018).
- [34] J. Jumper, R. Evans, A. Pritzel, T. Green, M. Figurnov, O. Ronneberger, K. Tunyasuvunakool, R. Bates, A. Žídek, A. Potapenko, A. Bridgland, C. Meyer, S. A. A. Kohl, A. J. Ballard, A. Cowie, B. Romera-Paredes, S. Nikolov, R. Jain, J. Adler, T. Back, S. Petersen, D. Reiman, E. Clancy, M. Zielinski, M. Steinegger, M. Pacholska, T. Berghammer, S. Bodenstein, D. Silver, O. Vinyals, A. W. Senior, K. Kavukcuoglu, P. Kohli, and D. Hassabis, *Nature* **596**, 583 (2021).
- [35] A. Vaswani, N. Shazeer, N. Parmar, J. Uszkoreit, L. Jones, A. N. Gomez, L. u. Kaiser, and I. Polosukhin, in *Advances in Neural Information Processing Systems*, Vol. 30, edited by I. Guyon, U. V. Luxburg, S. Bengio, H. Wallach, R. Fergus, S. Vishwanathan, and R. Garnett (Curran Associates, Inc., 2017).
- [36] OpenAI, Gpt-4 technical report (2023), [arXiv:2303.08774 \[cs.CL\]](https://arxiv.org/abs/2303.08774) .
- [37] S. Wang, K. Fan, N. Luo, Y. Cao, F. Wu, C. Zhang, K. A. Heller, and L. You, *Nat. Commun.* **10**, 4354 (2019).
- [38] H. Y. D. Sigaki, E. K. Lenzi, R. S. Zola, M. Perc, and H. V. Ribeiro, *Sci. Rep.* **10**, 7664 (2020).
- [39] P. Baumeister, S. Padovan, N. Tosi, G. Montavon, N. Nettelmann, J. MacKenzie, and M. Godolt, *The Astrophysical Journal* **889**, 42 (2020).
- [40] H. Verdier, M. Duval, F. Laurent, A. Cassé, C. L. Vestergaard, and J.-B. Masson, *J. Phys. A: Math. Theor.* **54**, 234001 (2021).
- [41] S. Sharma, *Annual Review of Astronomy and Astrophysics* **55**, 213 (2017).
- [42] J. Clérouin, N. Desbiens, V. Dubois, and P. Arnault, *Phys. Rev. E* **94**, 061202 (2016).
- [43] M. F. Kasim, T. P. Galligan, J. Topp-Mugglestone, G. Gregori, and S. M. Vinko, *Phys. Plasmas* **26**, 112706 (2019).
- [44] S. Ressel, J. J. Ruby, G. W. Collins, and J. R. Rygg, *Phys. Plasmas* **29**, 072713 (2022).
- [45] H. Poole, D. Cao, R. Epstein, I. Golovkin, T. Walton, S. X. Hu, M. Kasim, S. M. Vinko, J. R. Rygg, V. N. Goncharov, G. Gregori, and S. P. Regan, *Phys. Plasmas* **29**, 072703 (2022).
- [46] B. Cheng and D. Frenkel, *Phys. Rev. Lett.* **125**, 130602 (2020).

- [47] Q. Zeng, X. Yu, Y. Yao, T. Gao, B. Chen, S. Zhang, D. Kang, H. Wang, and J. Dai, *Phys. Rev. Research* **3**, 033116 (2021).
- [48] D. Langhammer, D. Di Genova, and G. Steinle-Neumann, *Geochem. Geophys. Geosyst.* **23**, e2022GC010673 (2022).
- [49] J. A. Soininen, A. L. Ankudinov, and J. J. Rehr, *Phys. Rev. B* **72**, 045136 (2005).
- [50] E. E. Salpeter and H. A. Bethe, *Phys. Rev.* **84**, 1232 (1951).
- [51] B. A. Mattern and G. T. Seidler, *Phys. Plasmas* **20**, 022706 (2013).
- [52] K. Ramakrishna and J. Vorberger, *J. Phys.: Condens. Matter* **32**, 095401 (2019).
- [53] F. Graziani, M. Desjarlais, R. Redmer, and S. Trickey, *Frontiers and Challenges in Warm Dense Matter*, Lecture Notes in Computational Science and Engineering (Springer International Publishing, 2014).
- [54] R. Redmer, *Phys. Rep.* **282**, 35 (1997).
- [55] T. Dornheim, Z. A. Moldabekov, K. Ramakrishna, P. Tolias, A. D. Baczewski, D. Kraus, T. R. Preston, D. A. Chapman, M. P. Böhme, T. Döppner, F. Graziani, M. Bonitz, A. Cangi, and J. Vorberger, *Phys. Plasmas* **30**, 032705 (2023).
- [56] P. Helander, C. D. Beidler, T. M. Bird, M. Drevlak, Y. Feng, R. Hatzky, F. Jenko, R. Kleiber, J. H. E. Proll, Y. Turkin, and P. Xanthopoulos, *Plasma Phys. Controlled Fusion* **54**, 124009 (2012).
- [57] S. X. Hu, B. Militzer, V. N. Goncharov, and S. Skupsky, *Phys. Rev. B* **84**, 224109 (2011).
- [58] N. Hussein, D. Eisa, and E. Sayed, *Natural Science* **7**, 42 (2015).
- [59] M. French, A. Becker, W. Lorenzen, N. Nettelmann, M. Bethkenhagen, J. Wicht, and R. Redmer, *The Astrophysical Journal Supplement Series* **202**, 5 (2012).
- [60] A. Becker, M. Bethkenhagen, C. Kellermann, J. Wicht, and R. Redmer, *The Astronomical Journal* **156**, 149 (2018).
- [61] J. Lütgert, M. Bethkenhagen, B. Bachmann, L. Divol, D. O. Gericke, S. H. Glenzer, G. N. Hall, N. Izumi, S. F. Khan, O. L. Landen, S. A. MacLaren, L. Masse, R. Redmer, M. Schörner, M. O. Schölmerich, S. Schumacher, N. R. Shaffer, C. E. Starrett, P. A. Sterne, C. Trosseille, T. Döppner, and D. Kraus, *Phys. Plasmas* **29**, 083301 (2022).
- [62] V. E. Fortov, *Phys. Usp.* **52**, 615 (2009).
- [63] R. Drake, *High-Energy-Density Physics: Foundation of Inertial Fusion and Experimental Astrophysics*, 2nd ed., Graduate Texts in Physics (Springer Cham, 2018) p. 658.
- [64] D. Kraus, A. Ravasio, M. Gauthier, D. O. Gericke, J. Vorberger, S. Frydrych, J. Helfrich, L. B. Fletcher, G. Schaumann, B. Nagler, B. Barbrel, B. Bachmann, E. J. Gamboa, S. Göde, E. Granados, G. Gregori, H. J. Lee, P. Neumayer, W. Schumaker, T. Döppner,

- R. W. Falcone, S. H. Glenzer, and M. Roth, *Nat. Commun.* **7**, 10970 (2016).
- [65] S. Frydrych, J. Vorberger, N. J. Hartley, A. K. Schuster, K. Ramakrishna, A. M. Saunders, T. van Driel, R. W. Falcone, L. B. Fletcher, E. Galtier, E. J. Gamboa, S. H. Glenzer, E. Granados, M. J. MacDonald, A. J. MacKinnon, E. E. McBride, I. Nam, P. Neumayer, A. Pak, K. Voigt, M. Roth, P. Sun, D. O. Gericke, T. Döppner, and D. Kraus, *Nat. Commun.* **11**, 2620 (2020).
- [66] O. A. Hurricane, D. A. Callahan, D. T. Casey, P. M. Celliers, C. Cerjan, E. L. Dewald, T. R. Dittrich, T. Döppner, D. E. Hinkel, L. F. B. Hopkins, J. L. Kline, S. Le Pape, T. Ma, A. G. MacPhee, J. L. Milovich, A. Pak, H.-S. Park, P. K. Patel, B. A. Remington, J. D. Salmonson, P. T. Springer, and R. Tommasini, *Nature* **506**, 343 (2014).
- [67] S. E. Wurzel and S. C. Hsu, *Phys. Plasmas* **29**, 062103 (2022).
- [68] T. R. Boehly, D. L. Brown, R. S. Craxton, R. L. Keck, J. P. Knauer, J. H. Kelly, T. J. Kessler, S. A. Kumpan, S. J. Loucks, S. A. Letzring, F. J. Marshall, R. L. McCrory, S. F. B. Morse, W. Seka, J. M. Soures, and C. P. Verdon, *Opt. Commun.* **133**, 495 (1997).
- [69] N. Fleurot, C. Cavaller, and J. Bourgade, *Fusion Eng. Des.* **74**, 147 (2005), proceedings of the 23rd Symposium of Fusion Technology.
- [70] Department of Energy: DOE National Laboratory Makes History by Achieving Fusion Ignition, <https://www.energy.gov/articles/doe-national-laboratory-makes-history-achieving-fusion-ignition> (2023), accessed: 2023-06-30.
- [71] S. H. Glenzer and R. Redmer, *Rev. Mod. Phys.* **81**, 1625 (2009).
- [72] T. Ott, H. Thomsen, J. W. Abraham, T. Dornheim, and M. Bonitz, *Eur. Phys. J. D* **72**, 84 (2018).
- [73] M. Bonitz, T. Dornheim, Z. A. Moldabekov, S. Zhang, P. Hamann, H. Kählert, A. Filinov, K. Ramakrishna, and J. Vorberger, *Phys. Plasmas* **27**, 042710 (2020).
- [74] V. V. Karasiev, T. Sjostrom, and S. Trickey, *Comput. Phys. Commun.* **185**, 3240 (2014).
- [75] H. Sun, D. Kang, Y. Hou, and J. Dai, *Matter and Radiation at Extremes* **2**, 287 (2017).
- [76] K. Yabana and G. F. Bertsch, *Phys. Rev. B* **54**, 4484 (1996).
- [77] A. Castro, H. Appel, M. Oliveira, C. A. Rozzi, X. Andrade, F. Lorenzen, M. A. L. Marques, E. K. U. Gross, and A. Rubio, *physica status solidi (b)* **243**, 2465 (2006).
- [78] A. D. Baczewski, L. Shulenburger, M. P. Desjarlais, S. B. Hansen, and R. J. Magyar, *Phys. Rev. Lett.* **116**, 115004 (2016).
- [79] K. Ramakrishna, M. Lokamani, A. Baczewski, J. Vorberger, and A. Cangi, *Phys. Rev. B* **107**, 115131 (2023).

- [80] D. M. Ceperley and B. J. Alder, *Phys. Rev. Lett.* **45**, 566 (1980).
- [81] T. Dornheim, S. Groth, A. Filinov, and M. Bonitz, *New J. Phys.* **17**, 073017 (2015).
- [82] T. Dornheim, S. Groth, T. Sjostrom, F. D. Malone, W. M. C. Foulkes, and M. Bonitz, *Phys. Rev. Lett.* **117**, 156403 (2016).
- [83] S. Groth, T. Dornheim, T. Sjostrom, F. D. Malone, W. M. C. Foulkes, and M. Bonitz, *Phys. Rev. Lett.* **119**, 135001 (2017).
- [84] V. Cerantola, A. D. Rosa, Z. Konôpková, R. Torchio, E. Brambrink, A. Rack, U. Zastra, and S. Pascarelli, *J. Phys.: Condens. Matter* **33**, 274003 (2021).
- [85] P. Emma, R. Akre, J. Arthur, R. Bionta, C. Bostedt, J. Bozek, A. Brachmann, P. Bucksbaum, R. Coffee, F.-J. Decker, Y. Ding, D. Dowell, S. Edstrom, A. Fisher, J. Frisch, S. Gilevich, J. Hastings, G. Hays, P. Hering, Z. Huang, R. Iverson, H. Loos, M. Messerschmidt, A. Miahnahri, S. Moeller, H.-D. Nuhn, G. Pile, D. Ratner, J. Rzepiela, D. Schultz, T. Smith, P. Stefan, H. Tompkins, J. Turner, J. Welch, W. White, J. Wu, G. Yocky, and J. Galayda, *Nat. Photonics* **4**, 641 (2010).
- [86] S. H. Glenzer, L. B. Fletcher, E. Galtier, B. Nagler, R. Alonso-Mori, B. Barbrel, S. B. Brown, D. A. Chapman, Z. Chen, C. B. Curry, F. Fiuza, E. Gamboa, M. Gauthier, D. O. Gericke, A. Gleason, S. Goede, E. Granados, P. Heimann, J. Kim, D. Kraus, M. J. MacDonald, A. J. Mackinnon, R. Mishra, A. Ravasio, C. Roedel, P. Sperling, W. Schumaker, Y. Y. Tsui, J. Vorberger, U. Zastra, A. Fry, W. E. White, J. B. Hasting, and H. J. Lee, *J. Phys. B: At., Mol. Opt. Phys.* **49**, 092001 (2016).
- [87] J. Galayda, in *Proc. 9th International Particle Accelerator Conference (IPAC'18), Vancouver, BC, Canada, April 29-May 4, 2018*, International Particle Accelerator Conference No. 9 (JACoW Publishing, Geneva, Switzerland, 2018) pp. 18–23.
- [88] T. Tschentscher, C. Bressler, J. Grünert, A. Madsen, A. P. Mancuso, M. Meyer, A. Scherz, H. Sinn, and U. Zastra, *Applied Sciences* **7**, 592 (2017).
- [89] U. Zastra, K. Appel, C. Baecht, O. Baehr, L. Batchelor, A. Berghäuser, M. Banjafar, E. Brambrink, V. Cerantola, T. E. Cowan, H. Damker, S. Dietrich, S. Di Dio Cafiso, J. Dreyer, H.-O. Engel, T. Feldmann, S. Findeisen, M. Foese, D. Fulla-Marsa, S. Göde, M. Hassan, J. Hauser, T. Herrmannsdörfer, H. Höppner, J. Kaa, P. Kaefer, K. Knöfel, Z. Konôpková, A. Laso García, H.-P. Liermann, J. Mainberger, M. Makita, E.-C. Martens, E. E. McBride, D. Möller, M. Nakatsutsumi, A. Pelka, C. Plueckthun, C. Prescher, T. R. Preston, M. Röper, A. Schmidt, W. Seidel, J.-P. Schwinkendorf, M. O. Schoelmerich, U. Schramm, A. Schropp, C. Strohm, K. Sukharnikov, P. Talkovski, I. Thorpe, M. Toncian, T. Toncian, L. Wollenweber, S. Yamamoto, and T. Tschentscher, *Journal of Synchrotron Radiation* **28**, 1393 (2021).
- [90] O. Hurricane and M. Herrmann, *Annu. Rev. Nucl. Part. Sci.* **67**, 213 (2017).



- [91] B. Remington, in *APS Division of Plasma Physics Meeting Abstracts*, APS Meeting Abstracts, Vol. 2021 (2021) p. UO03.001.
- [92] T. R. Boehly, R. S. Craxton, T. H. Hinterman, J. H. Kelly, T. J. Kessler, S. A. Kumpan, S. A. Letzring, R. L. McCrory, S. F. B. Morse, W. Seka, S. Skupsky, J. M. Soures, and C. P. Verdon, *Rev. Sci. Instrum.* **66**, 508 (1995).
- [93] S. H. Glenzer, G. Gregori, R. W. Lee, F. J. Rogers, S. W. Pollaine, and O. L. Landen, *Phys. Rev. Lett.* **90**, 175002 (2003).
- [94] S. H. Glenzer, O. L. Landen, P. Neumayer, R. W. Lee, K. Widmann, S. W. Pollaine, R. J. Wallace, G. Gregori, A. Höll, T. Bornath, R. Thiele, V. Schwarz, W.-D. Kraeft, and R. Redmer, *Phys. Rev. Lett.* **98**, 065002 (2007).
- [95] H. J. Lee, P. Neumayer, J. Castor, T. Döppner, R. W. Falcone, C. Fortmann, B. A. Hammel, A. L. Kritcher, O. L. Landen, R. W. Lee, D. D. Meyerhofer, D. H. Munro, R. Redmer, S. P. Regan, S. Weber, and S. H. Glenzer, *Phys. Rev. Lett.* **102**, 115001 (2009).
- [96] A. L. Kritcher, T. Döppner, C. Fortmann, T. Ma, O. L. Landen, R. Wallace, and S. H. Glenzer, *Phys. Rev. Lett.* **107**, 015002 (2011).
- [97] T. Ma, T. Döppner, R. W. Falcone, L. Fletcher, C. Fortmann, D. O. Gericke, O. L. Landen, H. J. Lee, A. Pak, J. Vorberger, K. Wünsch, and S. H. Glenzer, *Phys. Rev. Lett.* **110**, 065001 (2013).
- [98] T. Ma, L. Fletcher, A. Pak, D. A. Chapman, R. W. Falcone, C. Fortmann, E. Galtier, D. O. Gericke, G. Gregori, J. Hastings, O. L. Landen, S. Le Pape, H. J. Lee, B. Nagler, P. Neumayer, D. Turnbull, J. Vorberger, T. G. White, K. Wünsch, U. Zastra, S. H. Glenzer, and T. Döppner, *Phys. Plasmas* **21**, 056302 (2014).
- [99] L. B. Fletcher, A. L. Kritcher, A. Pak, T. Ma, T. Döppner, C. Fortmann, L. Divol, O. S. Jones, O. L. Landen, H. A. Scott, J. Vorberger, D. A. Chapman, D. O. Gericke, B. A. Mattern, G. T. Seidler, G. Gregori, R. W. Falcone, and S. H. Glenzer, *Phys. Rev. Lett.* **112**, 145004 (2014).
- [100] P. Ni, M. Kulish, V. Mintsev, D. Nikolaev, V. Ternovoi, D. Hoffmann, S. Udrea, A. Hug, N. Tahir, D. Varentsov, and et al., *Laser Part. Beams* **26**, 583–589 (2008).
- [101] T. Stöhlker, V. Bagnoud, K. Blaum, A. Blazevic, A. Bräuning-Demian, M. Durante, F. Herfurth, M. Lestinsky, Y. Litvinov, S. Neff, R. Pleskac, R. Schuch, S. Schippers, D. Severin, A. Tauschwitz, C. Trautmann, D. Varentsov, and E. Widmann, *Nucl. Instrum. Methods Phys. Res., Sect. B* **365**, 680 (2015).
- [102] K. Schoenberg, V. Bagnoud, A. Blazevic, V. E. Fortov, D. O. Gericke, A. Golubev, D. H. H. Hoffmann, D. Kraus, I. V. Lomonosov, V. Mintsev, S. Neff, P. Neumayer, A. R. Piriz, R. Redmer, O. Rosmej, M. Roth, T. Schenkel, B. Sharkov, N. A. Tahir, D. Varentsov, and Y. Zhao, *Phys. Plasmas* **27**, 043103 (2020).

- [103] GSI Helmholtzzentrum für Schwerionenforschung, Darmstadt and FAIR GmbH, Darmstadt, *GSI-FAIR Scientific Report 2022*, GSI Report, Vol. 2023-1 (GSI Helmholtzzentrum für Schwerionenforschung GmbH, Darmstadt, 2023) p. 181.
- [104] N. Huang, H. Deng, B. Liu, D. Wang, and Z. Zhao, *The Innovation* **2**, 100097 (2021).
- [105] B. A. Remington, R. P. Drake, and D. D. Ryutov, *Rev. Mod. Phys.* **78**, 755 (2006).
- [106] D. B. Sinars, M. A. Sweeney, C. S. Alexander, D. J. Ampleford, T. Ao, J. P. Apruzese, C. Aragon, D. J. Armstrong, K. N. Austin, T. J. Awe, A. D. Baczewski, J. E. Bailey, K. L. Baker, C. R. Ball, H. T. Barclay, S. Beatty, K. Beckwith, K. S. Bell, J. Benage, J. F., N. L. Bennett, *et al.*, *Phys. Plasmas* **27**, 070501 (2020).
- [107] Z. Li, Y. Leng, and R. Li, *Laser & Photonics Reviews* **17**, 2100705 (2023).
- [108] P. Asimow, in *Treatise on Geophysics (Second Edition)*, edited by G. Schubert (Elsevier, Oxford, 2015) second edition ed., pp. 393–416.
- [109] T. S. Duffy and R. F. Smith, *Front. Earth Sci.* **7** (2019).
- [110] P. Hugoniot, *J. École Polytech* **57**, 3 (1887).
- [111] P. Hugoniot, *J. École Polytech* **58**, 1 (1889).
- [112] W. J. M. Rankine, *Lond. Edinb. Dublin Philos. Mag. J. Sci.* **1**, 225 (1851).
- [113] W. J. M. Rankine, *Philos. Trans. Royal Soc.* **160**, 277 (1870).
- [114] M. Millot, S. Hamel, J. R. Rygg, P. M. Celliers, G. W. Collins, F. Coppari, D. E. Fratanduono, R. Jeanloz, D. C. Swift, and J. H. Eggert, *Nat. Phys.* **14**, 297 (2018).
- [115] A. Ravasio, M. Bethkenhagen, J.-A. Hernandez, A. Benuzzi-Mounaix, F. Datchi, M. French, M. Guarguaglini, F. Lefevre, S. Ninet, R. Redmer, and T. Vinci, *Phys. Rev. Lett.* **126**, 025003 (2021).
- [116] W. J. Nellis, N. C. Holmes, A. C. Mitchell, R. J. Trainor, G. K. Governo, M. Ross, and D. A. Young, *Phys. Rev. Lett.* **53**, 1248 (1984).
- [117] W. J. Nellis, S. T. Weir, and A. C. Mitchell, *Phys. Rev. B* **59**, 3434 (1999).
- [118] M. Denny, *Eur. J. Phys.* **34**, 1327 (2013).
- [119] T. J. Ahrens, in *Geophysics, Methods in Experimental Physics*, Vol. 24, edited by C. G. Sammis and T. L. Henyey (Academic Press, 1987) pp. 185–235.
- [120] C. Ragan III, M. Silbert, and B. Diven, *J. Appl. Phys.* **48**, 2860 – 2870 (1977).
- [121] L. V. Al'tshuler, V. S. Zhuchenko, and A. D. Levin, Detonation of condensed explosives, in *High-Pressure Shock Compression of Solids VII: Shock Waves and Extreme States of Matter*, edited by V. E. Fortov, L. V. Al'tshuler, R. F. Trunin, and A. I. Funtikov (Springer New York, New York, NY, 2004) pp. 39–75.

- [122] C. A. Hall, J. R. Asay, M. D. Knudson, W. A. Stygar, R. B. Spielman, T. D. Pointon, D. B. Reisman, A. Toor, and R. C. Cauble, *Rev. Sci. Instrum.* **72**, 3587 (2001).
- [123] R. F. Smith, J. H. Eggert, R. Jeanloz, T. S. Duffy, D. G. Braun, J. R. Patterson, R. E. Rudd, J. Biener, A. E. Lazicki, A. V. Hamza, J. Wang, T. Braun, L. X. Benedict, P. M. Celliers, and G. W. Collins, *Nature* **511**, 330 (2014).
- [124] L. E. Hansen, D. E. Fratanduono, S. Zhang, D. G. Hicks, T. Suer, Z. K. Sprowal, M. F. Huff, X. Gong, B. J. Henderson, D. N. Polsin, M. Zaghoo, S. X. Hu, G. W. Collins, and J. R. Rygg, *Phys. Rev. B* **104**, 014106 (2021).
- [125] R. G. Kraus, S. T. Stewart, D. C. Swift, C. A. Bolme, R. F. Smith, S. Hamel, B. D. Hammel, D. K. Spaulding, D. G. Hicks, J. H. Eggert, and G. W. Collins, *Journal of Geophysical Research: Planets* **117** (2012).
- [126] R. G. Kraus, S. Root, R. W. Lemke, S. T. Stewart, S. B. Jacobsen, and T. R. Mattsson, *Nat. Geosci.* **8**, 269 (2015).
- [127] M. J. MacDonald, C. A. Di Stefano, T. Döppner, L. B. Fletcher, K. A. Flippo, D. Kalantar, E. C. Merritt, S. J. Ali, P. M. Celliers, R. Heredia, S. Vonhof, G. W. Collins, J. A. Gaffney, D. O. Gericke, S. H. Glenzer, D. Kraus, A. M. Saunders, D. W. Schmidt, C. T. Wilson, R. Zacharias, and R. W. Falcone, *Phys. Plasmas* **30**, 062701 (2023).
- [128] J. C. Jamieson, A. W. Lawson, and N. D. Nachtrieb, *Rev. Sci. Instrum.* **30**, 1016 (1959).
- [129] C. E. Weir, E. R. Lippincott, A. Van Valkenburg, and E. N. Bunting, *J Res Natl Bur Stand A Phys Chem* **63A**, 55 (1959).
- [130] S. Anzellini, A. Dewaele, M. Mezouar, P. Loubeyre, and G. Morard, *Science* **340**, 464 (2013).
- [131] W. J. Evans, C.-S. Yoo, G. W. Lee, H. Cynn, M. J. Lipp, and K. Visbeck, *Rev. Sci. Instrum.* **78**, 073904 (2007).
- [132] L. Dubrovinsky, N. Dubrovinskaia, V. B. Prakapenka, and A. M. Abakumov, *Nat. Commun.* **3**, 1163 (2012).
- [133] L. Dubrovinsky, N. Dubrovinskaia, E. Bykova, M. Bykov, V. Prakapenka, C. Prescher, K. Glazyrin, H.-P. Liermann, M. Hanfland, M. Ekholm, Q. Feng, L. V. Pourovskii, M. I. Katsnelson, J. M. Wills, and I. A. Abrikosov, *Nature* **525**, 226 (2015).
- [134] N. Dubrovinskaia, L. Dubrovinsky, N. A. Solopova, A. Abakumov, S. Turner, M. Hanfland, E. Bykova, M. Bykov, C. Prescher, V. B. Prakapenka, S. Petitgirard, I. Chuvashova, B. Gasharova, Y.-L. Mathis, P. Ershov, I. Snigireva, and A. Snigirev, *Sci. Adv.* **2**, e1600341 (2016).
- [135] A. Dewaele, P. Loubeyre, F. Occelli, O. Marie, and M. Mezouar, *Nat. Commun.* **9**, 2913 (2018).
- [136] L. Ming and W. A. Bassett, *Rev. Sci. Instrum.* **45**, 1115 (1974).

- [137] S. Anzellini and S. Boccatto, *Crystals* **10** (2020).
- [138] S. Tateno, K. Hirose, Y. Ohishi, and Y. Tatsumi, *Science* **330**, 359 (2010).
- [139] Y. Kono, C. Park, C. Kenney-Benson, G. Shen, and Y. Wang, *Phys. Earth Planet. Inter.* **228**, 269 (2014), high-Pressure Research in Earth Science: Crust, Mantle, and Core.
- [140] S. Anzellini, D. Errandonea, C. Cazorla, S. MacLeod, V. Monteseuro, S. Boccatto, E. Bandiello, D. D. Anichtchenko, C. Popescu, and C. M. Beavers, *Sci. Rep.* **9**, 14459 (2019).
- [141] R. Jeanloz, P. M. Celliers, G. W. Collins, J. H. Eggert, K. K. M. Lee, R. S. McWilliams, S. Brygoo, and P. Loubeyre, *Proceedings of the National Academy of Sciences* **104**, 9172 (2007).
- [142] A. Dewaele, P. Loubeyre, R. André, and J. Härtwig, *J. Appl. Phys.* **99**, 104906 (2006).
- [143] P. K. Patel, A. J. Mackinnon, M. H. Key, T. E. Cowan, M. E. Foord, M. Allen, D. F. Price, H. Ruhl, P. T. Springer, and R. Stephens, *Phys. Rev. Lett.* **91**, 125004 (2003).
- [144] P. Sperling, E. J. Gamboa, H. J. Lee, H. K. Chung, E. Galtier, Y. Omarbakiyeva, H. Reinholz, G. Röpke, U. Zastrau, J. Hastings, L. B. Fletcher, and S. H. Glenzer, *Phys. Rev. Lett.* **115**, 115001 (2015).
- [145] Y. Waseda and M. Ohtani, *Philos. Mag.* **32**, 273 (1975).
- [146] L. M. Barker, *Exp. Mech.* **12**, 209 (1972).
- [147] M. Li, S. Zhang, H. Zhang, G. Zhang, F. Wang, J. Zhao, C. Sun, and R. Jeanloz, *Phys. Rev. Lett.* **120**, 215703 (2018).
- [148] P. M. Celliers and M. Millot, *Review of Scientific Instruments* **94**, 011101 (2023).
- [149] A. Ng, D. Parfeniuk, and L. Dasilva, *Opt. Commun.* **53**, 389 (1985).
- [150] J. E. Miller, T. R. Boehly, A. Melchior, D. D. Meyerhofer, P. M. Celliers, J. H. Eggert, D. G. Hicks, C. M. Sorce, J. A. Oertel, and P. M. Emmel, *Rev. Sci. Instrum.* **78**, 034903 (2007).
- [151] R. Roycroft, B. Bowers, H. Smith, E. McCary, F. Aymond, G. M. Dyer, H. J. Quevedo, P. A. Bradley, E. L. Vold, L. Yin, and B. M. Hegelich, *AIP Adv.* **10**, 045220 (2020).
- [152] D. H. Froula, S. H. Glenzer, N. C. Luhmann, and J. Sheffield, *Plasma Scattering of Electromagnetic Radiation*, 2nd ed. (Academic Press, Boston, 2011) p. 497.
- [153] B. Crowley and G. Gregori, *High Energy Density Phys.* **13**, 55 (2014).
- [154] J. Chihara, *J. Phys. F: Met. Phys.* **17**, 295 (1987).
- [155] J. Chihara, *J. Phys.: Condens. Matter* **12**, 231 (2000).
- [156] K. Sturm, *Zeitschrift für Naturforschung A* **48**, 233 (1993).

- [157] P. Debye and E. Hückel, *Phys. Z.* **24**, 305 (1923).
- [158] P. Sperling, R. Thiele, B. Holst, C. Fortmann, S. Glenzer, S. Toleikis, T. Tschentscher, and R. Redmer, *High Energy Density Phys.* **7**, 145 (2011).
- [159] D. Bohm and D. Pines, *Phys. Rev.* **82**, 625 (1951).
- [160] D. Pines and D. Bohm, *Phys. Rev.* **85**, 338 (1952).
- [161] D. Bohm and D. Pines, *Phys. Rev.* **92**, 609 (1953).
- [162] J. Lindhard, *Kgl. Danske Videnskab. Selskab Mat.-fys. Medd.* **28**, 1 (1954).
- [163] P. Eisenberger and P. M. Platzman, *Phys. Rev. A* **2**, 415 (1970).
- [164] M. Schumacher, F. Smend, and I. Borchert, *J. Phys. B: At. Mol. Phys.* **8**, 1428 (1975).
- [165] P. Holm and R. Ribberfors, *Phys. Rev. A* **40**, 6251 (1989).
- [166] B. B. L. Witte, L. B. Fletcher, E. Galtier, E. Gamboa, H. J. Lee, U. Zastra, R. Redmer, S. H. Glenzer, and P. Sperling, *Phys. Rev. Lett.* **118**, 225001 (2017).
- [167] M. Schörner, M. Bethkenhagen, T. Döppner, D. Kraus, L. B. Fletcher, S. H. Glenzer, and R. Redmer, *Phys. Rev. E* **107**, 065207 (2023).
- [168] H. Bethe, *Ann. Phys.* **397**, 325 (1930).
- [169] M. Inokuti, *Rev. Mod. Phys.* **43**, 297 (1971).
- [170] R. Thiele, P. Sperling, M. Chen, T. Bornath, R. R. Fäustlin, C. Fortmann, S. H. Glenzer, W.-D. Kraeft, A. Pukhov, S. Toleikis, T. Tschentscher, and R. Redmer, *Phys. Rev. E* **82**, 056404 (2010).
- [171] M. J. MacDonald, A. M. Saunders, B. Bachmann, M. Bethkenhagen, L. Divol, M. D. Doyle, L. B. Fletcher, S. H. Glenzer, D. Kraus, O. L. Landen, H. J. LeFevre, S. R. Klein, P. Neumayer, R. Redmer, M. Schörner, N. Whiting, R. W. Falcone, and T. Döppner, *Phys. Plasmas* **28**, 032708 (2021).
- [172] G. Gregori, S. H. Glenzer, W. Rozmus, R. W. Lee, and O. L. Landen, *Phys. Rev. E* **67**, 026412 (2003).
- [173] M. von Laue, *Die interferenz der Röntgenstrahlen* (Akademische verlagsgesellschaft m.b.h., Leipzig, 1923) p. 111.
- [174] C. Kittel, *Introduction to Solid State Physics* (Wiley, 2004) p. 704.
- [175] P. Debye, *Ann. Phys.* **348**, 49 (1913).
- [176] I. Waller, *Zeitschrift für Physik* **17**, 398 (1923).
- [177] W. J. Murphy, A. Higginbotham, J. S. Wark, and N. Park, *Phys. Rev. B* **78**, 014109 (2008).



- [178] M. Z. Mo, V. Becker, B. K. Ofori-Okai, X. Shen, Z. Chen, B. Witte, R. Redmer, R. K. Li, M. Dunning, S. P. Weathersby, X. J. Wang, and S. H. Glenzer, *Rev. Sci. Instrum.* **89**, 10C108 (2018).
- [179] E. Schrödinger, *Phys. Rev.* **28**, 1049 (1926).
- [180] R. G. Parr, *Annu. Rev. Phys. Chem.* **34**, 631 (1983).
- [181] A. E. Mattsson, P. A. Schultz, M. P. Desjarlais, T. R. Mattsson, and K. Leung, *Modell. Simul. Mater. Sci. Eng.* **13**, R1 (2004).
- [182] A. D. Becke, *The Journal of Chemical Physics* **140**, 10.1063/1.4869598 (2014), 18A301.
- [183] E. S. Kryachko and E. V. Ludeña, *Phys. Rep.* **544**, 123 (2014), density functional theory: Foundations reviewed.
- [184] R. O. Jones, *Rev. Mod. Phys.* **87**, 897 (2015).
- [185] W. Koch and M. Holthausen, *A Chemist's Guide to Density Functional Theory*, 2nd ed. (Wiley-VCH, Weinheim, 2001).
- [186] D. Frenkel and B. Smit, *Understanding Molecular Simulation*, 2nd ed. (Academic Press, San Diego, 2002).
- [187] R. M. Martin, *Electronic Structure: Basic Theory and Practical Methods* (Cambridge University Press, 2004).
- [188] J. Kohanoff, *Electronic Structure Calculations for Solids and Molecules: Theory and Computational Methods* (Cambridge University Press, 2006).
- [189] D. Marx and J. Hutter, *Ab Initio Molecular Dynamics: The Virtual Laboratory Approach* (John Wiley & Sons, Incorporated, 2010).
- [190] E. Engel and R. M. Dreizler, *Density Functional Theory* (Springer Berlin, Heidelberg, 2011).
- [191] D. Rapaport, *The Art of Molecular Dynamics Simulation* (Cambridge University Press, 2004).
- [192] M. Tuckerman, *Statistical Mechanics: Theory and Molecular Simulation* (Oxford University Press, Oxford, 2010).
- [193] N. C. Handy and A. M. Lee, *Chem. Phys. Lett.* **252**, 425 (1996).
- [194] M. Born and R. Oppenheimer, *Ann. Phys.* **389**, 457 (1927).
- [195] J. C. Tully and R. K. Preston, *The Journal of Chemical Physics* **55**, 562 (1971).
- [196] J. C. Tully, *The Journal of Chemical Physics* **93**, 1061 (1990).
- [197] N. L. Doltsinis and D. Marx, *Phys. Rev. Lett.* **88**, 166402 (2002).

- [198] C. Li, R. Requist, and E. K. U. Gross, *The Journal of Chemical Physics* **148**, 084110 (2018).
- [199] I. D. Fedorov, N. D. Orekhov, and V. V. Stegailov, *Phys. Rev. B* **101**, 100101 (2020).
- [200] P. Ehrenfest, *Zeitschrift für Physik* **45**, 455 (1927).
- [201] H. Hellmann, *Einführung in die Quantenchemie* (Franz Deuticke, Leipzig, 1937).
- [202] R. P. Feynman, *Phys. Rev.* **56**, 340 (1939).
- [203] W. Kohn, *Rev. Mod. Phys.* **71**, 1253 (1999).
- [204] P. Hohenberg and W. Kohn, *Phys. Rev.* **136**, B864 (1964).
- [205] W. Ritz, *Journal für die reine und angewandte Mathematik* **135**, 1 (1909).
- [206] N. D. Mermin, *Phys. Rev.* **137**, A1441 (1965).
- [207] W. Kohn and L. J. Sham, *Phys. Rev.* **140**, A1133 (1965).
- [208] L. J. Sham and W. Kohn, *Phys. Rev.* **145**, 561 (1966).
- [209] E. Fermi, *Zeitschrift für Physik* **36**, 902 (1926).
- [210] P. A. M. Dirac and R. H. Fowler, *Proceedings of the Royal Society of London. Series A, Containing Papers of a Mathematical and Physical Character* **112**, 661 (1926).
- [211] J. P. Perdew, A. Ruzsinszky, J. Tao, V. N. Staroverov, G. E. Scuseria, and G. I. Csonka, *The Journal of Chemical Physics* **123**, 062201 (2005).
- [212] L. H. Thomas, *Math. Proc. Cambridge Philos. Soc.* **23**, 542–548 (1927).
- [213] E. Fermi, *Zeitschrift für Physik* **48**, 73 (1928).
- [214] P. A. M. Dirac, *Math. Proc. Cambridge Philos. Soc.* **26**, 376–385 (1930).
- [215] J. P. Perdew and A. Zunger, *Phys. Rev. B* **23**, 5048 (1981).
- [216] J. P. Perdew and Y. Wang, *Phys. Rev. B* **45**, 13244 (1992).
- [217] J. P. Perdew and W. Yue, *Phys. Rev. B* **33**, 8800 (1986).
- [218] C. Lee, W. Yang, and R. G. Parr, *Phys. Rev. B* **37**, 785 (1988).
- [219] J. P. Perdew, J. A. Chevary, S. H. Vosko, K. A. Jackson, M. R. Pederson, D. J. Singh, and C. Fiolhais, *Phys. Rev. B* **46**, 6671 (1992).
- [220] J. P. Perdew, K. Burke, and M. Ernzerhof, *Phys. Rev. Lett.* **77**, 3865 (1996).
- [221] R. Armiento and A. E. Mattsson, *Phys. Rev. B* **72**, 085108 (2005).
- [222] J. P. Perdew, A. Ruzsinszky, G. I. Csonka, O. A. Vydrov, G. E. Scuseria, L. A. Constantin, X. Zhou, and K. Burke, *Phys. Rev. Lett.* **100**, 136406 (2008).

- [223] É. D. Murray, K. Lee, and D. C. Langreth, *J. Chem. Theory Comput.* **5**, 2754 (2009).
- [224] J. Tao, J. P. Perdew, V. N. Staroverov, and G. E. Scuseria, *Phys. Rev. Lett.* **91**, 146401 (2003).
- [225] J. P. Perdew, A. Ruzsinszky, G. I. Csonka, L. A. Constantin, and J. Sun, *Phys. Rev. Lett.* **103**, 026403 (2009).
- [226] J. Sun, A. Ruzsinszky, and J. P. Perdew, *Phys. Rev. Lett.* **115**, 036402 (2015).
- [227] J. Heyd, G. E. Scuseria, and M. Ernzerhof, *The Journal of Chemical Physics* **118**, 8207 (2003).
- [228] J. Heyd, G. E. Scuseria, and M. Ernzerhof, *The Journal of Chemical Physics* **124**, 219906 (2006).
- [229] A. D. Becke, *Phys. Rev. A* **38**, 3098 (1988).
- [230] A. D. Becke, *The Journal of Chemical Physics* **104**, 1040 (1996).
- [231] J. P. Perdew, M. Ernzerhof, and K. Burke, *The Journal of Chemical Physics* **105**, 9982 (1996).
- [232] C. Adamo and V. Barone, *The Journal of Chemical Physics* **110**, 6158 (1999).
- [233] J. Muscat, A. Wander, and N. Harrison, *Chem. Phys. Lett.* **342**, 397 (2001).
- [234] E. Runge and E. K. U. Gross, *Phys. Rev. Lett.* **52**, 997 (1984).
- [235] P. Giannozzi, S. Baroni, N. Bonini, M. Calandra, R. Car, C. Cavazzoni, D. Ceresoli, G. L. Chiarotti, M. Cococcioni, I. Dabo, A. D. Corso, S. de Gironcoli, S. Fabris, G. Fratesi, R. Gebauer, U. Gerstmann, C. Gougoussis, A. Kokalj, M. Lazzeri, L. Martin-Samos, N. Marzari, F. Mauri, R. Mazzarello, S. Paolini, A. Pasquarello, L. Paulatto, C. Sbraccia, S. Scandolo, G. Sclauzero, A. P. Seitsonen, A. Smogunov, P. Umari, and R. M. Wentzcovitch, *J. Phys.: Condens. Matter* **21**, 395502 (2009).
- [236] P. Giannozzi, O. Andreussi, T. Brumme, O. Bunau, M. B. Nardelli, M. Calandra, R. Car, C. Cavazzoni, D. Ceresoli, M. Cococcioni, N. Colonna, I. Carnimeo, A. D. Corso, S. de Gironcoli, P. Delugas, R. A. DiStasio, A. Ferretti, A. Floris, G. Fratesi, G. Fugallo, R. Gebauer, U. Gerstmann, F. Giustino, T. Gorni, J. Jia, M. Kawamura, H.-Y. Ko, A. Kokalj, E. Küçükbenli, M. Lazzeri, M. Marsili, N. Marzari, F. Mauri, N. L. Nguyen, H.-V. Nguyen, A. O. de-la Roza, L. Paulatto, S. Poncé, D. Rocca, R. Sabatini, B. Santra, M. Schlipf, A. P. Seitsonen, A. Smogunov, I. Timrov, T. Thonhauser, P. Umari, N. Vast, X. Wu, and S. Baroni, *J. Phys.: Condens. Matter* **29**, 465901 (2017).
- [237] X. Gonze, B. Amadon, G. Antonius, F. Arnardi, L. Baguet, J.-M. Beuken, J. Bieder, F. Bottin, J. Bouchet, E. Bousquet, N. Brouwer, F. Bruneval, G. Brunin, T. Cavignac, J.-B. Charraud, W. Chen, M. Côté, S. Cottenier, J. Denier, G. Geneste, P. Ghosez, M. Giantomassi, Y. Gillet, O. Gingras, D. R. Hamann, G. Hautier, X. He, N. Helbig, N. Holzwarth, Y. Jia, F. Jollet, W. Lafargue-Dit-Hauret, K. Lejaeghere, M. A. L. Mar-

- ques, A. Martin, C. Martins, H. P. C. Miranda, F. Naccarato, K. Persson, G. Petretto, V. Planes, Y. Pouillon, S. Prokhorenko, F. Ricci, G.-M. Rignanese, A. H. Romero, M. M. Schmitt, M. Torrent, M. J. van Setten, B. V. Troeye, M. J. Verstraete, G. Zérah, and J. W. Zwanziger, *Comput. Phys. Commun.* **248**, 107042 (2020).
- [238] A. H. Romero, D. C. Allan, B. Amadon, G. Antonius, T. Applencourt, L. Baguet, J. Bieder, F. Bottin, J. Bouchet, E. Bousquet, F. Bruneval, G. Brunin, D. Caliste, M. Côté, J. Denier, C. Dreyer, P. Ghosez, M. Giantomassi, Y. Gillet, O. Gingras, D. R. Hamann, G. Hautier, F. Jollet, G. Jomard, A. Martin, H. P. C. Miranda, F. Naccarato, G. Petretto, N. A. Pike, V. Planes, S. Prokhorenko, T. Rangel, F. Ricci, G.-M. Rignanese, M. Royo, M. Stengel, M. Torrent, M. J. van Setten, B. V. Troeye, M. J. Verstraete, J. Wiktor, J. W. Zwanziger, and X. Gonze, *J. Chem. Phys.* **152**, 124102 (2020).
- [239] G. Kresse and J. Hafner, *Phys. Rev. B* **47**, 558 (1993).
- [240] G. Kresse and J. Hafner, *Phys. Rev. B* **49**, 14251 (1994).
- [241] G. Kresse and J. Furthmüller, *Phys. Rev. B* **54**, 11169 (1996).
- [242] J. Hafner, *J. Comput. Chem.* **29**, 2044 (2008).
- [243] J. J. Mortensen, L. B. Hansen, and K. W. Jacobsen, *Phys. Rev. B* **71**, 035109 (2005).
- [244] J. Enkovaara, C. Rostgaard, J. J. Mortensen, J. Chen, M. Dulak, L. Ferrighi, J. Gavnholt, C. Glinsvad, V. Haikola, H. A. Hansen, H. H. Kristoffersen, M. Kuisma, A. H. Larsen, L. Lehtovaara, M. Ljungberg, O. Lopez-Acevedo, P. G. Moses, J. Ojanen, T. Olsen, V. Petzold, N. A. Romero, J. Stausholm-Møller, M. Strange, G. A. Tritsaridis, M. Vanin, M. Walter, B. Hammer, H. Häkkinen, G. K. H. Madsen, R. M. Nieminen, J. K. Nørskov, M. Puska, T. T. Rantala, J. Schiøtz, K. S. Thygesen, and K. W. Jacobsen, *J. Phys.: Condens. Matter* **22**, 253202 (2010).
- [245] A. H. Larsen, J. J. Mortensen, J. Blomqvist, I. E. Castelli, R. Christensen, M. Dulak, J. Friis, M. N. Groves, B. Hammer, C. Hargus, E. D. Hermes, P. C. Jennings, P. B. Jensen, J. Kermode, J. R. Kitchin, E. L. Kolsbjerg, J. Kubal, K. Kaasbjerg, S. Lysgaard, J. B. Maronsson, T. Maxson, T. Olsen, L. Pastewka, A. Peterson, C. Rostgaard, J. Schiøtz, O. Schütt, M. Strange, K. S. Thygesen, T. Vegge, L. Vilhelmsen, M. Walter, Z. Zeng, and K. W. Jacobsen, *J. Phys.: Condens. Matter* **29**, 273002 (2017).
- [246] J. Yan, J. J. Mortensen, K. W. Jacobsen, and K. S. Thygesen, *Phys. Rev. B* **83**, 245122 (2011).
- [247] F. Bloch, *Zeitschrift für Physik* **52**, 555 (1929).
- [248] A. Baldereschi, *Phys. Rev. B* **7**, 5212 (1973).
- [249] H. J. Monkhorst and J. D. Pack, *Phys. Rev. B* **13**, 5188 (1976).
- [250] P. E. Blöchl, *Phys. Rev. B* **50**, 17953 (1994).
- [251] S. Nosé, *The Journal of Chemical Physics* **81**, 511 (1984).

- [252] W. G. Hoover, *Phys. Rev. A* **31**, 1695 (1985).
- [253] D. J. Evans and B. L. Holian, *The Journal of Chemical Physics* **83**, 4069 (1985).
- [254] G. J. Martyna, M. L. Klein, and M. Tuckerman, *The Journal of Chemical Physics* **97**, 2635 (1992).
- [255] L. Verlet, *Phys. Rev.* **159**, 98 (1967).
- [256] W. C. Swope, H. C. Andersen, P. H. Berens, and K. R. Wilson, *The Journal of Chemical Physics* **76**, 637 (1982).
- [257] N. Wiener, *Acta Mathematica* **55**, 117 (1930).
- [258] A. Khintchine, *Mathematische Annalen* **109**, 604 (1934).
- [259] L. D. Landau and E. M. Lifshitz, *Fluid mechanics*, 2nd ed., Course of theoretical physics (Pergamon Press, Oxford, England, 1987).
- [260] D. Acheson, *Elementary Fluid Dynamics*, Comparative Pathobiology - Studies in the Postmodern Theory of Education (Clarendon Press, 1990).
- [261] J. P. Hansen and I. R. McDonald, *Theory of simple liquids*, 3rd ed. (Elsevier Academic Press, London, 2006).
- [262] D. Chaturvedi, M. Rovere, G. Senatore, and M. Tosi, *Physica B+C* **111**, 11 (1981).
- [263] T. B. Blank, S. D. Brown, A. W. Calhoun, and D. J. Doren, *The Journal of Chemical Physics* **103**, 4129 (1995).
- [264] A. Calhoun and D. Doren, *The Journal of Physical Chemistry* **97**, 2251 (1993).
- [265] A. P. Bartók, M. C. Payne, R. Kondor, and G. Csányi, *Phys. Rev. Lett.* **104**, 136403 (2010).
- [266] A. P. Bartók and G. Csányi, *Int. J. Quantum Chem.* **115**, 1051 (2015).
- [267] A. Thompson, L. Swiler, C. Trott, S. Foiles, and G. Tucker, *J. Comput. Phys.* **285**, 316 (2015).
- [268] Z. Deng, C. Chen, X.-G. Li, and S. P. Ong, *npj Comput. Mater.* **5**, 75 (2019).
- [269] H. Wang, L. Zhang, J. Han, and W. E, *Comput. Phys. Commun.* **228**, 178 (2018).
- [270] L. Zhang, J. Han, H. Wang, R. Car, and W. E, *Phys. Rev. Lett.* **120**, 143001 (2018).
- [271] R. C. Jiequn Han, Linfeng Zhang and W. E, *Comm. Comput. Phys.* **23**, 629 (2018).
- [272] J. Behler and M. Parrinello, *Phys. Rev. Lett.* **98**, 146401 (2007).
- [273] J. Behler, *The Journal of Chemical Physics* **134**, 074106 (2011).
- [274] M. Gastegger, L. Schwiedrzik, M. Bittermann, F. Berzsenyi, and P. Marquetand, *The Journal of Chemical Physics* **148**, 241709 (2018).



- [275] M. P. Bircher, A. Singraber, and C. Dellago, *Machine Learning: Science and Technology* **2**, 035026 (2021).
- [276] J. Behler, *Chem. Rev.* **121**, 10037 (2021).
- [277] G. Imbalzano, A. Anelli, D. Giofré, S. Klees, J. Behler, and M. Ceriotti, *The Journal of Chemical Physics* **148**, 241730 (2018).
- [278] D. E. Rumelhart, G. E. Hinton, and R. J. Williams, *Nature* **323**, 533 (1986).
- [279] E. Chong and S. Žak, *An Introduction to Optimization*, Wiley Series in Discrete Mathematics and Optimization (Wiley, 2013).
- [280] D. P. Kingma and J. Ba, Adam: A method for stochastic optimization (2017), [arXiv:1412.6980 \[cs.LG\]](https://arxiv.org/abs/1412.6980) .
- [281] R. E. Kalman, *Journal of Basic Engineering* **82**, 35 (1960).
- [282] T. B. Blank and S. D. Brown, *J. Chemom.* **8**, 391 (1994).
- [283] T. Morawietz, A. Singraber, C. Dellago, and J. Behler, *PNAS* **113**, 8368 (2016).
- [284] A. Singraber, T. Morawietz, J. Behler, and C. Dellago, *J. Chem. Theory Comput.* **15**, 3075 (2019).
- [285] A. Singraber, *n2p2 - a neural network potential package* (2021), computer software.
- [286] A. P. Thompson, H. M. Aktulga, R. Berger, D. S. Bolintineanu, W. M. Brown, P. S. Crozier, P. J. in 't Veld, A. Kohlmeyer, S. G. Moore, T. D. Nguyen, R. Shan, M. J. Stevens, J. Tranchida, C. Trott, and S. J. Plimpton, *Comput. Phys. Commun.* **271**, 108171 (2022).
- [287] G. Bebis and M. Georgiopoulos, *IEEE Potentials.* **13**, 27 (1994).
- [288] S. Raschka and V. Mirjalili, *Python Machine Learning*, 2nd ed. (Packt Publishing, Birmingham, 2017).
- [289] K. P. Murphy, *Machine Learning* (MIT Press, Cambridge, 2012).
- [290] W. E. Alley and B. J. Alder, *Phys. Rev. A* **27**, 3158 (1983).
- [291] I. M. de Schepper and E. G. D. Cohen, *Phys. Rev. A* **22**, 287 (1980).
- [292] C. Bruin, J. Michels, J. Van Rijs, L. De Graaf, and I. De Schepper, *Phys. Lett. A* **110**, 40 (1985).
- [293] B. Kamgar-Parsi, E. G. D. Cohen, and I. M. de Schepper, *Phys. Rev. A* **35**, 4781 (1987).
- [294] I. M. de Schepper, E. G. D. Cohen, C. Bruin, J. C. van Rijs, W. Montfrooij, and L. A. de Graaf, *Phys. Rev. A* **38**, 271 (1988).
- [295] R. Zwanzig, *Lectures in theoretical physics*, edited by W. Britten, B. Downs, and J. Downs, Vol. 3 (Interscience, New York, 1961) pp. 106–141.

- [296] R. Zwanzig, *Phys. Rev.* **124**, 983 (1961).
- [297] R. Zwanzig, *Annu. Rev. Phys. Chem.* **16**, 67 (1965).
- [298] H. Mori, *Progress of Theoretical Physics* **33**, 423 (1965).
- [299] H. Mori, *Progress of Theoretical Physics* **34**, 399 (1965).
- [300] I. Mryglod, *Condens. Matter Phys.* **1**, 753 (1998).
- [301] T. Bryk, *Eur. Phys. J. Spec. Top.* **196**, 65 (2011).
- [302] I. Mryglod, I. Omelyan, and M. Tokarchuk, *Mol. Phys* **84**, 235 (1995).
- [303] T. Bryk, I. Mryglod, and G. Kahl, *Phys. Rev. E* **56**, 2903 (1997).
- [304] G. G. Simeoni, T. Bryk, F. A. Gorelli, M. Krisch, G. Ruocco, M. Santoro, and T. Scopigno, *Nat. Phys.* **6**, 503 (2010).
- [305] T. Bryk and A. B. Belonoshko, *Phys. Rev. B* **86**, 024202 (2012).
- [306] T. Bryk and G. Ruocco, *Mol. Phys.* **111**, 3457 (2013).
- [307] J.-F. Wax and T. Bryk, *J. Phys. Condens. Matter* **25**, 325104 (2013).
- [308] C. R. Harris, K. J. Millman, S. J. van der Walt, R. Gommers, P. Virtanen, D. Cournapeau, E. Wieser, J. Taylor, S. Berg, N. J. Smith, R. Kern, M. Picus, S. Hoyer, M. H. van Kerkwijk, M. Brett, A. Haldane, J. F. del Río, M. Wiebe, P. Peterson, P. Gérard-Marchant, K. Sheppard, T. Reddy, W. Weckesser, H. Abbasi, C. Gohlke, and T. E. Oliphant, *Nature* **585**, 357 (2020).
- [309] P. Virtanen, R. Gommers, T. E. Oliphant, M. Haberland, T. Reddy, D. Cournapeau, E. Burovski, P. Peterson, W. Weckesser, J. Bright, S. J. van der Walt, M. Brett, J. Wilson, K. J. Millman, N. Mayorov, A. R. J. Nelson, E. Jones, R. Kern, E. Larson, C. J. Carey, *et al.*, *Nat. Methods* **17**, 261 (2020).
- [310] P. Talias, T. Dornheim, Z. A. Moldabekov, and J. Vorberger, *Europhys. Lett.* **142**, 44001 (2023).
- [311] S. L. Adler, *Phys. Rev.* **126**, 413 (1962).
- [312] N. Wiser, *Phys. Rev.* **129**, 62 (1963).
- [313] H. Ehrenreich and M. H. Cohen, *Phys. Rev.* **115**, 786 (1959).
- [314] P. Nozières and D. Pines, *Phys. Rev.* **109**, 741 (1958).
- [315] P. Nozières and D. Pines, *Phys. Rev.* **113**, 1254 (1959).
- [316] P. C. Martin and J. Schwinger, *Phys. Rev.* **115**, 1342 (1959).
- [317] S. Waidmann, M. Knupfer, B. Arnold, J. Fink, A. Fleszar, and W. Hanke, *Phys. Rev. B* **61**, 10149 (2000).

- [318] R. Kubo, *J. Phys. Soc. Jpn.* **12**, 570 (1957).
- [319] R. Kubo, *Rep. Prog. Phys.* **29**, 255 (1966).
- [320] E. K. U. Gross and W. Kohn, *Phys. Rev. Lett.* **55**, 2850 (1985).
- [321] C. A. Ullrich, U. J. Gossmann, and E. K. U. Gross, *Phys. Rev. Lett.* **74**, 872 (1995).
- [322] H. Wendel and R. M. Martin, *Phys. Rev. B* **19**, 5251 (1979).
- [323] R. Car, E. Tosatti, S. Baroni, and S. Leelaprute, *Phys. Rev. B* **24**, 985 (1981).
- [324] M. Petersilka, U. J. Gossmann, and E. K. U. Gross, *Phys. Rev. Lett.* **76**, 1212 (1996).
- [325] T. Olsen and K. S. Thygesen, *Phys. Rev. B* **86**, 081103 (2012).
- [326] M. Panholzer, M. Gatti, and L. Reining, *Phys. Rev. Lett.* **120**, 166402 (2018).
- [327] A. D. Kaplan, N. K. Nepal, A. Ruzsinszky, P. Ballone, and J. P. Perdew, *Phys. Rev. B* **105**, 035123 (2022).
- [328] Z. Moldabekov, M. Böhme, J. Vorberger, D. Blaschke, and T. Dornheim, *J. Chem. Theory Comput.* **19**, 1286 (2023).
- [329] Z. A. Moldabekov, M. Pavanello, M. P. Böhme, J. Vorberger, and T. Dornheim, *Phys. Rev. Res.* **5**, 023089 (2023).
- [330] Z. A. Moldabekov, M. Lokamani, J. Vorberger, A. Cangi, and T. Dornheim, *The Journal of Physical Chemistry Letters* **14**, 1326 (2023).
- [331] S. Baroni and R. Resta, *Phys. Rev. B* **33**, 7017 (1986).
- [332] M. S. Hybertsen and S. G. Louie, *Phys. Rev. B* **35**, 5585 (1987).
- [333] M. A. L. Marques and E. K. U. Gross, Time-dependent density functional theory, in *A Primer in Density Functional Theory*, edited by C. Fiolhais, F. Nogueira, and M. A. L. Marques (Springer Berlin Heidelberg, Berlin, Heidelberg, 2003) pp. 144–184.
- [334] Y.-M. Byun, J. Sun, and C. A. Ullrich, *Electronic Structure* **2**, 023002 (2020).
- [335] V. Recoules and J.-P. Crocombette, *Phys. Rev. B* **72**, 104202 (2005).
- [336] M. Pozzo, C. Davies, D. Gubbins, and D. Alfè, *Nature* **485**, 355 (2012).
- [337] D. Alfè, M. Pozzo, and M. P. Desjarlais, *Phys. Rev. B* **85**, 024102 (2012).
- [338] M. French and T. R. Mattsson, *Phys. Rev. B* **90**, 165113 (2014).
- [339] J.-A. Korell, M. French, G. Steinle-Neumann, and R. Redmer, *Phys. Rev. Lett.* **122**, 086601 (2019).
- [340] M. French, *Ab-initio-Berechnung von Transporteigenschaften von warmer dichter Materie*, Habilitation, University of Rostock (2021).

- [341] B. Holst, M. French, and R. Redmer, *Phys. Rev. B* **83**, 235120 (2011).
- [342] D. A. Greenwood, *Proceedings of the Physical Society* **71**, 585 (1958).
- [343] M. French and R. Redmer, *Phys. Plasmas* **24**, 092306 (2017).
- [344] M. Gajdoš, K. Hummer, G. Kresse, J. Furthmüller, and F. Bechstedt, *Phys. Rev. B* **73**, 045112 (2006).
- [345] D. Knyazev and P. Levashov, *Computational Materials Science* **79**, 817 (2013).
- [346] T. Schoof, S. Groth, J. Vorberger, and M. Bonitz, *Phys. Rev. Lett.* **115**, 130402 (2015).
- [347] T. Dornheim, T. Schoof, S. Groth, A. Filinov, and M. Bonitz, *The Journal of Chemical Physics* **143**, 204101 (2015).
- [348] S. Moroni, D. M. Ceperley, and G. Senatore, *Phys. Rev. Lett.* **75**, 689 (1995).
- [349] G. Ortiz, M. Harris, and P. Ballone, *Phys. Rev. Lett.* **82**, 5317 (1999).
- [350] T. Dornheim, S. Groth, F. D. Malone, T. Schoof, T. Sjostrom, W. M. C. Foulkes, and M. Bonitz, *Phys. Plasmas* **24**, 056303 (2017).
- [351] T. Dornheim, S. Groth, and M. Bonitz, *Phys. Rep.* **744**, 1 (2018).
- [352] G. Ortiz and P. Ballone, *Phys. Rev. B* **50**, 1391 (1994).
- [353] T. Dornheim, S. Groth, J. Vorberger, and M. Bonitz, *Phys. Rev. Lett.* **121**, 255001 (2018).
- [354] S. Groth, T. Dornheim, and J. Vorberger, *Phys. Rev. B* **99**, 235122 (2019).
- [355] M. Böhme, Z. A. Moldabekov, J. Vorberger, and T. Dornheim, *Phys. Rev. Lett.* **129**, 066402 (2022).
- [356] L. Spitzer and R. Härm, *Phys. Rev.* **89**, 977 (1953).
- [357] J. M. Ziman, *The Philosophical Magazine: A Journal of Theoretical Experimental and Applied Physics* **6**, 1013 (1961).
- [358] S. Ichimaru and S. Tanaka, *Physical Review A* **32**, 1790 – 1798 (1985).
- [359] S. Ichimaru, H. Iyetomi, and S. Tanaka, *Physics Reports* **149**, 91 (1987).
- [360] Y. T. Lee and R. M. More, *The Physics of Fluids* **27**, 1273 (1984).
- [361] A. Esser, R. Redmer, and G. Röpke, *Contrib. Plasma Phys.* **43**, 33 (2003).
- [362] T. Bayes and R. Price, *Philos. Trans. Roy. Soc. London* **53**, 370 (1763).
- [363] S. Tomic, M. Beko, L. M. Camarinha-Matos, and L. B. Oliveira, *Applied Sciences* **10**, 272 (2020).

- [364] N. Metropolis, A. W. Rosenbluth, M. N. Rosenbluth, A. H. Teller, and E. Teller, *The Journal of Chemical Physics* **21**, 1087 (1953).
- [365] W. K. Hastings, *Biometrika* **57**, 97 (1970).
- [366] A. Doucet, S. Godsill, and C. Andrieu, *Statistics and Computing* **10**, 197 (2000).
- [367] P. Del Moral, A. Doucet, and A. Jasra, *Journal of the Royal Statistical Society: Series B (Statistical Methodology)* **68**, 411 (2006).
- [368] S. A. Sisson, Y. Fan, and M. M. Tanaka, *Proc. Natl. Acad. Sci. U.S.A.* **104**, 1760 (2007).
- [369] J. Salvatier, T. V. Wiecki, and C. Fonnesbeck, *PeerJ Computer Science* **2**, e55 (2016).
- [370] C. P. Robert, G. Casella, and G. Casella, *Monte Carlo statistical methods*, Vol. 2 (Springer, 1999).
- [371] A. Gelman, *Bayesian data analysis*, 2nd ed., Texts in statistical science (Chapman & Hall/CRC, Boca Raton, Fla., 2004).
- [372] D. F. R. Brown, M. N. Gibbs, and D. C. Clary, *The Journal of Chemical Physics* **105**, 7597 (1996).
- [373] S. Manzhos, X. Wang, R. Dawes, and T. Carrington, *J. Phys. Chem. A* **110**, 5295 (2006).
- [374] S. Lorenz, A. Groß, and M. Scheffler, *Chem. Phys. Lett.* **395**, 210 (2004).
- [375] S. Lorenz, M. Scheffler, and A. Gross, *Phys. Rev. B* **73**, 115431 (2006).
- [376] J. P. Mithen, J. Daligault, and G. Gregori, *Phys. Rev. E* **83**, 015401 (2011).
- [377] J. P. Mithen, *Phys. Rev. E* **89**, 013101 (2014).
- [378] M. Schörner, H. R. Rüter, M. French, and R. Redmer, *Phys. Rev. B* **105**, 174310 (2022).
- [379] M. Schörner, B. B. L. Witte, A. D. Baczewski, A. Cangi, and R. Redmer, *Phys. Rev. B* **106**, 054304 (2022).
- [380] Y. Waseda, *The Structure of Non-Crystalline Materials* (McGraw-Hill, New York, 1980).
- [381] T. Scopigno, U. Balucani, G. Ruocco, and F. Sette, *Phys. Rev. E* **63**, 011210 (2000).
- [382] J. Schnakenberg, *Thermodynamik und Statistische Physik*, 1st ed. (Wiley, Hoboken, NJ, 1998).
- [383] M. French, *New J. Phys.* **21**, 023007 (2019).
- [384] R. M. Nicklow, G. Gilat, H. G. Smith, L. J. Raubenheimer, and M. K. Wilkinson, *Phys. Rev.* **164**, 922 (1967).
- [385] B. Henke, E. Gullikson, and J. Davis, *At. Data Nucl. Data Tables* **54**, 181 (1993).
- [386] O. J. Eder, B. Kunsch, M. Suda, E. Erdpresser, and H. Stiller, *J. Phys. F: Met. Phys.* **10**, 183 (1980).

- [387] S. Hagen, *Untersuchung der kollektiven Bewegungen im polykristallinen und fluessigen Kupfer durch inelastische Neutronenstreuung*, Ph.D. thesis, University of Kalsruhe, Germany (1973).
- [388] P. G. De Gennes, *Physica* **25**, 825 (1959).
- [389] A. Mitchell and W. Nellis, *J. Appl. Phys.* **52**, 3363 (1981).
- [390] A. C. Mitchell, W. J. Nellis, J. A. Moriarty, R. A. Heinle, N. C. Holmes, R. E. Tipton, and G. W. Repp, *J. Appl. Phys.* **69**, 2981 (1991).
- [391] L. Al'Tshuler, S. Kormer, A. Bakanova, and R. Trunin, *Sov. Phys. JETP* **11**, 573 (1960).
- [392] L. Al'Tshuler, A. Bakanova, and R. Trunin, *Sov. Phys. JETP* **15**, 65 (1962).
- [393] R. McQueen, S. Marsh, J. Taylor, J. Fritz, and W. Carter, *High-Velocity Impact Phenomena*, edited by R. Kinslow (Academic, New York, 1970).
- [394] C. A. McCoy, M. D. Knudson, and S. Root, *Phys. Rev. B* **96**, 174109 (2017).
- [395] B. L. Glushak, A. P. Zharkov, M. V. Zhernokletov, V. Y. Ternovoi, A. S. Filimonov, and V. E. Fortov, *Sov. Phys. JETP* **69**, 739 (1989).
- [396] S. B. Kormer, A. I. Funtikov, V. D. Urlin, and A. N. Kolesnikova, *Sov. Phys. JETP* **15**, 477 (1962).
- [397] K. S. Trainor, *J. Appl. Phys.* **54**, 2372 (1983).
- [398] T. Döppner, O. Landen, H. Lee, P. Neumayer, S. Regan, and S. Glenzer, *High Energy Density Phys.* **5**, 182 (2009).
- [399] N. D. Mermin, *Phys. Rev. B* **1**, 2362 (1970).
- [400] G. Röpke, A. Selchow, A. Wierling, and H. Reinholz, *Phys. Lett. A* **260**, 365 (1999).
- [401] A. Selchow and K. Morawetz, *Phys. Rev. E* **59**, 1015 (1999).
- [402] H. Reinholz, R. Redmer, G. Röpke, and A. Wierling, *Phys. Rev. E* **62**, 5648 (2000).
- [403] K.-U. Plagemann, P. Sperling, R. Thiele, M. P. Desjarlais, C. Fortmann, T. Döppner, H. J. Lee, S. H. Glenzer, and R. Redmer, *New J. Phys.* **14**, 055020 (2012).
- [404] M. Bethkenhagen, B. B. L. Witte, M. Schörner, G. Röpke, T. Döppner, D. Kraus, S. H. Glenzer, P. A. Sterne, and R. Redmer, *Phys. Rev. Res.* **2**, 023260 (2020).
- [405] C. Lin, G. Röpke, H. Reinholz, and W.-D. Kraeft, *Contrib. Plasma Phys.* **57**, 518 (2017).
- [406] G. Röpke, D. Blaschke, T. Döppner, C. Lin, W.-D. Kraeft, R. Redmer, and H. Reinholz, *Phys. Rev. E* **99**, 033201 (2019).
- [407] T. J. Callow, E. Kraisler, and A. Cangi, *Phys. Rev. Res.* **5**, 013049 (2023).



- [408] K. Ramakrishna, A. Cangi, T. Dornheim, A. Baczewski, and J. Vorberger, *Phys. Rev. B* **103**, 125118 (2021).
- [409] W. Thomas, *Naturwissenschaften* **13**, 627 (1925).
- [410] F. Reiche and W. Thomas, *Z. Phys.* **34**, 510 (1925).
- [411] W. Kuhn, *Z. Phys.* **33**, 408 (1925).
- [412] G. D. Mahan, *Many-Particle Physics* (Plenum Publishers, New York, 2000).
- [413] S. M. Vinko, O. Ciricosta, and J. S. Wark, *Nat. Commun.* **5**, 3533 (2014).
- [414] S. X. Hu, *Phys. Rev. Lett.* **119**, 065001 (2017).
- [415] K. P. Driver, F. Soubiran, and B. Militzer, *Phys. Rev. E* **97**, 063207 (2018).
- [416] H. A. Gould and H. E. DeWitt, *Phys. Rev.* **155**, 68 (1967).
- [417] A. Wierling, T. Millat, G. Röpke, R. Redmer, and H. Reinholz, *Phys. Plasmas* **8**, 3810 (2001).
- [418] R. Thiele, R. Redmer, H. Reinholz, and G. Röpke, *J. Phys. A: Math. Gen.* **39**, 4365 (2006).
- [419] G. Röpke, M. Schörner, R. Redmer, and M. Bethkenhagen, *Phys. Rev. E* **104**, 045204 (2021).
- [420] M. French, G. Röpke, M. Schörner, M. Bethkenhagen, M. P. Desjarlais, and R. Redmer, *Phys. Rev. E* **105**, 065204 (2022).
- [421] A. L. Kritcher, C. V. Young, H. F. Robey, C. R. Weber, A. B. Zylstra, O. A. Hurricane, D. A. Callahan, J. E. Ralph, J. S. Ross, K. L. Baker, D. T. Casey, D. S. Clark, T. Döppner, L. Divol, M. Hohenberger, L. B. Hopkins, S. Le Pape, N. B. Meezan, A. Pak, P. K. Patel, *et al.*, *Nat. Phys.* **18**, 251 (2022).
- [422] D. T. Bishel, B. Bachmann, A. Yi, D. Kraus, L. Divol, M. Bethkenhagen, R. W. Falcone, L. B. Fletcher, S. H. Glenzer, O. L. Landen, M. J. MacDonald, N. Masters, P. Neumayer, R. Redmer, A. M. Saunders, B. B. L. Witte, and T. Döppner, *Rev. Sci. Instrum.* **89**, 10G111 (2018).
- [423] H.-C. Weissker, R. Hambach, V. Olevano, and L. Reining, *Phys. Rev. B* **79**, 094102 (2009).
- [424] T. Dornheim, Z. A. Moldabekov, J. Vorberger, and B. Militzer, *Sci. Rep.* **12**, 708 (2022).
- [425] F. J. Rogers, F. J. Swenson, and C. A. Iglesias, *The Astrophysical Journal* **456**, 902 (1996).
- [426] S. Cassisi, A. Y. Potekhin, A. Pietrinferni, M. Catelan, and M. Salaris, *The Astrophysical Journal* **661**, 1094 (2007).

- [427] B. Paxton, L. Bildsten, A. Dotter, F. Herwig, P. Lesaffre, and F. Timmes, *ApJS* **192**, 3 (2011).
- [428] R. de L. Kronig, *J. Opt. Soc. Am.* **12**, 547 (1926).
- [429] H. A. Kramers, *Atti Cong. Intern. Fisici* **2**, 545 (1927).
- [430] G. Röpke, *Phys. Rev. A* **38**, 3001 (1988).
- [431] G. Röpke and R. Redmer, *Phys. Rev. A* **39**, 907 (1989).
- [432] H. Brooks and C. Herring, *Phys. Rev.* **83**, 879 (1951).
- [433] F. J. Blatt, *J. Phys. C: Solid State Phys.* **4**, 199 (1957).
- [434] G. Röpke, *Contrib. Plasma Phys.* **n/a**, e202300002 (2023).
- [435] K. Günther and R. Radtke, *Band 7 Electric Properties of Weakly Nonideal Plasmas* (De Gruyter, Berlin, Boston, 1984).
- [436] Y. V. Ivanov, V. Mintsev, V. Fortov, and A. Dremin, *Sov. Phys. JETP* **44**, 112 (1976).
- [437] M. M. Popovic, Y. Vitel, and A. Mihajlov, in *Strongly Coupled Plasma Physics*, edited by S. Ichimaru (Elsevier, Yamada, 1990) Chap. 9, p. 561.
- [438] M. P. Desjarlais, C. R. Scullard, L. X. Benedict, H. D. Whitley, and R. Redmer, *Phys. Rev. E* **95**, 033203 (2017).
- [439] F. Lambert, V. Recoules, A. Decoster, J. Clérouin, and M. Desjarlais, *Phys. Plasmas* **18**, 10.1063/1.3574902 (2011), 056306.
- [440] V. S. Karakhtanov, *Contrib. Plasma Phys.* **56**, 343 (2016).
- [441] P. Grabowski, S. Hansen, M. Murillo, L. Stanton, F. Graziani, A. Zylstra, S. Baalrud, P. Arnault, A. Baczewski, L. Benedict, C. Blancard, O. Čertík, J. Clérouin, L. Collins, S. Copeland, A. Correa, J. Dai, J. Daligault, M. Desjarlais, M. Dharma-wardana, G. Faussurier, J. Haack, T. Haxhimali, A. Hayes-Sterbenz, Y. Hou, S. Hu, D. Jensen, G. Jungman, G. Kagan, D. Kang, J. Kress, Q. Ma, M. Marciante, E. Meyer, R. Rudd, D. Saumon, L. Shulenburg, R. Singleton, T. Sjostrom, L. Stanek, C. Starrett, C. Ticknor, S. Valaitis, J. Venzke, and A. White, *High Energy Density Phys.* **37**, 100905 (2020).
- [442] L. Brillouin, *Comptes Rendus de l'Académie des Sciences* **183**, 24 (1926).
- [443] H. A. Kramers, *Zeitschrift für Physik* **39**, 828 (1926).
- [444] G. Wentzel, *Zeitschrift für Physik* **38**, 518 (1926).
- [445] H. Reinholz, R. Redmer, and D. Tamme, *Contrib. Plasma Phys.* **29**, 395 (1989).
- [446] E. Lifshitz and L. Pitaevskii, *Physical Kinetics: Volume 10*, Course of theoretical physics (Elsevier Science, 1995).
- [447] G. Röpke, *Nonequilibrium Statistical Physics*, 1st ed. (Wiley-VCH, Berlin, 2013).

- [448] G. Röpke, *Theor. Math. Phys.* **194**, 74 (2018).
- [449] T. Döppner, M. Bethkenhagen, D. Kraus, P. Neumayer, D. A. Chapman, B. Bachmann, R. A. Baggott, M. P. Böhme, L. Divol, R. W. Falcone, L. B. Fletcher, O. L. Landen, M. J. MacDonald, A. M. Saunders, M. Schörner, P. A. Sterne, J. Vorberger, B. B. L. Witte, A. Yi, R. Redmer, S. H. Glenzer, and D. O. Gericke, *Nature* **618**, 270 (2023).
- [450] A. Descamps, B. K. Ofori-Okai, J. K. Baldwin, Z. Chen, L. B. Fletcher, S. H. Glenzer, N. J. Hartley, J. B. Hasting, D. Khaghani, M. Mo, B. Nagler, V. Recoules, R. Redmer, M. Schörner, P. Sun, Y. Q. Wang, T. G. White, and E. E. McBride, *Journal of Synchrotron Radiation* **29**, 931 (2022).
- [451] Z. Chen, X. Na, C. B. Curry, S. Liang, M. French, A. Descamps, D. P. DePonte, J. D. Korablek, J. B. Kim, S. Lebovitz, M. Nakatsutsumi, B. K. Ofori-Okai, R. Redmer, C. Roedel, M. Schörner, S. Skruszewicz, P. Sperling, S. Toleikis, M. Z. Mo, and S. H. Glenzer, *Matter and Radiation at Extremes* **6**, 054401 (2021).
- [452] M. Frost, E. E. McBride, M. Schörner, R. Redmer, and S. H. Glenzer, *Phys. Rev. B* **101**, 224108 (2020).
- [453] J. Lütgert, J. Vorberger, N. J. Hartley, K. Voigt, M. Rödel, A. K. Schuster, A. Benuzzi-Mounaix, S. Brown, T. E. Cowan, E. Cunningham, T. Döppner, R. W. Falcone, L. B. Fletcher, E. Galtier, S. H. Glenzer, A. Laso Garcia, D. O. Gericke, P. A. Heimann, H. J. Lee, E. E. McBride, A. Pelka, I. Prencipe, A. M. Saunders, M. Schölmerich, M. Schörner, P. Sun, T. Vinci, A. Ravasio, and D. Kraus, *Sci. Rep.* **11**, 12883 (2021).
- [454] N. J. Hartley, S. Brown, T. E. Cowan, E. Cunningham, T. Döppner, R. W. Falcone, L. B. Fletcher, S. Frydrych, E. Galtier, E. J. Gamboa, A. Laso Garcia, D. O. Gericke, S. H. Glenzer, E. Granados, P. A. Heimann, H. J. Lee, M. J. MacDonald, A. J. MacKinnon, E. E. McBride, I. Nam, P. Neumayer, A. Pak, A. Pelka, I. Prencipe, A. Ravasio, M. Rödel, K. Rohatsch, A. M. Saunders, M. Schölmerich, M. Schörner, A. K. Schuster, P. Sun, T. van Driel, J. Vorberger, and D. Kraus, *Sci. Rep.* **9**, 4196 (2019).
- [455] D. Kraus, N. J. Hartley, S. Frydrych, A. K. Schuster, K. Rohatsch, M. Rödel, T. E. Cowan, S. Brown, E. Cunningham, T. van Driel, L. B. Fletcher, E. Galtier, E. J. Gamboa, A. Laso Garcia, D. O. Gericke, E. Granados, P. A. Heimann, H. J. Lee, M. J. MacDonald, A. J. MacKinnon, E. E. McBride, I. Nam, P. Neumayer, A. Pak, A. Pelka, I. Prencipe, A. Ravasio, R. Redmer, A. M. Saunders, M. Schölmerich, M. Schörner, P. Sun, S. J. Turner, A. Zettl, R. W. Falcone, S. H. Glenzer, T. Döppner, and J. Vorberger, *Phys. Plasmas* **25**, 056313 (2018).
- [456] A. Yoshiasa, T. Nagai, O. Ohtaka, O. Kamishima, and O. Shimomura, *Journal of Synchrotron Radiation* **6**, 43 (1999).
- [457] K. Voigt, M. Zhang, K. Ramakrishna, A. Amouretti, K. Appel, E. Brambrink, V. Cerantola, D. Chekrygina, T. Döppner, R. W. Falcone, K. Falk, L. B. Fletcher, D. O. Gericke, S. Göde, M. Harmand, N. J. Hartley, S. P. Hau-Riege, L. G. Huang, O. S. Humphries,

- M. Lokamani, M. Makita, A. Pelka, C. Prescher, A. K. Schuster, M. Šmíd, T. Toncian, J. Vorberger, U. Zastra, T. R. Preston, and D. Kraus, *Phys. Plasmas* **28**, 082701 (2021).
- [458] W. H. Bragg, *Proc. Physical Soc.* **33**, 304 (1921).
- [459] P. P. Ewald and H. Hönl, *Ann. Phys.* **25**, 281 (1936).
- [460] E. E. McBride, T. G. White, A. Descamps, L. B. Fletcher, K. Appel, F. P. Condamine, C. B. Curry, F. Dallari, S. Funk, E. Galtier, M. Gauthier, S. Goede, J. B. Kim, H. J. Lee, B. K. Ofori-Okai, M. Oliver, A. Rigby, C. Schoenwaelder, P. Sun, T. Tschentscher, B. B. L. Witte, U. Zastra, G. Gregori, B. Nagler, J. Hastings, S. H. Glenzer, and G. Monaco, *Rev. Sci. Instrum.* **89**, 10F104 (2018).
- [461] L. Wollenweber, T. R. Preston, A. Descamps, V. Cerantola, A. Comley, J. H. Eggert, L. B. Fletcher, G. Geloni, D. O. Gericke, S. H. Glenzer, S. Göde, J. Hastings, O. S. Humphries, A. Jenei, O. Karnbach, Z. Konopkova, R. Loetzsch, B. Marx-Glowna, E. E. McBride, D. McGonegle, G. Monaco, B. K. Ofori-Okai, C. A. J. Palmer, C. Plückthun, R. Redmer, C. Strohm, I. Thorpe, T. Tschentscher, I. Uschmann, J. S. Wark, T. G. White, K. Appel, G. Gregori, and U. Zastra, *Rev. Sci. Instrum.* **92**, 013101 (2021).
- [462] A. Descamps, B. K. Ofori-Okai, K. Appel, V. Cerantola, A. Comley, J. H. Eggert, L. B. Fletcher, D. O. Gericke, S. Göde, O. Humphries, O. Karnbach, A. Lazicki, R. Loetzsch, D. McGonegle, C. A. J. Palmer, C. Plueckthun, T. R. Preston, R. Redmer, D. G. Senesky, C. Strohm, I. Uschmann, T. G. White, L. Wollenweber, G. Monaco, J. S. Wark, J. B. Hastings, U. Zastra, G. Gregori, S. H. Glenzer, and E. E. McBride, *Sci. Rep.* **10**, 14564 (2020).
- [463] L. Obst, S. Göde, M. Rehwald, F.-E. Brack, J. Branco, S. Bock, M. Bussmann, T. E. Cowan, C. B. Curry, F. Fiuza, M. Gauthier, R. Gebhardt, U. Helbig, A. Huebl, U. Hübnner, A. Irman, L. Kazak, J. B. Kim, T. Kluge, S. Kraft, M. Loeser, J. Metzkes, R. Mishra, C. Rödel, H.-P. Schlenvoigt, M. Siebold, J. Tiggesbäumker, S. Wolter, T. Ziegler, U. Schramm, S. H. Glenzer, and K. Zeil, *Sci. Rep.* **7**, 10248 (2017).
- [464] G. Galinis, J. Strucka, J. C. T. Barnard, A. Braun, R. A. Smith, and J. P. Marangos, *Rev. Sci. Instrum.* **88**, 083117 (2017).
- [465] J. D. Koralek, J. B. Kim, P. Brůža, C. B. Curry, Z. Chen, H. A. Bechtel, A. A. Cordones, P. Sperling, S. Toleikis, J. F. Kern, S. P. Moeller, S. H. Glenzer, and D. P. DePonte, *Nat. Commun.* **9**, 1353 (2018).
- [466] J. Amann, W. Berg, V. Blank, F.-J. Decker, Y. Ding, P. Emma, Y. Feng, J. Frisch, D. Fritz, J. Hastings, Z. Huang, J. Krzywinski, R. Lindberg, H. Loos, A. Lutman, H.-D. Nuhn, D. Ratner, J. Rzepiela, D. Shu, Y. Shvyd'ko, S. Spampinati, S. Stoupin, S. Terentyev, E. Trakhtenberg, D. Walz, J. Welch, J. Wu, A. Zholents, and D. Zhu, *Nat. Photonics* **6**, 693 (2012).
- [467] J. Clérouin, A. Blanchet, C. Blancard, G. Faussurier, F. m. c. Soubiran, and M. Bethkenhagen, *Phys. Rev. E* **106**, 045204 (2022).

- 
- [468] T. J. Callow, S. B. Hansen, E. Kraisler, and A. Cangi, *Phys. Rev. Res.* **4**, 023055 (2022).
- [469] S. Botti, F. Sottile, N. Vast, V. Olevano, L. Reining, H.-C. Weissker, A. Rubio, G. Onida, R. Del Sole, and R. W. Godby, *Phys. Rev. B* **69**, 155112 (2004).
- [470] Kellermann, C., Becker, A., and Redmer, R., *A&A* **615**, A39 (2018).
- [471] A. L. Kutepov, *Phys. Rev. B* **95**, 195120 (2017).
- [472] C.-N. Yeh, S. Iskakov, D. Zgid, and E. Gull, *Phys. Rev. B* **106**, 235104 (2022).
- [473] L. Hedin, *Phys. Rev.* **139**, A796 (1965).
- [474] W. G. Aulbur, L. Jönsson, and J. W. Wilkins, *J. Phys. C: Solid State Phys.* **54**, 1 (2000).

# Curriculum vitae

Born on 05.07.1995 in Witten

## Education

- Since 07/2019 Ph.D. student in the Statistical Physics Group, University of Rostock  
Supervisor: Prof. Dr. R. Redmer
- 08/2019 Participant in *Hands-On DFT and Beyond summer school*, Barcelona, Spain
- 10/2017 - 04/2019 Master of Science in physics, University of Rostock, Germany  
Master thesis: *Ab initio Calculation of the Dynamic Structure Factor in Warm Dense Copper*  
Supervisors: Prof. Dr. R. Redmer and Dr. B.B.L. Witte
- 10/2016 - 04/2017 Master of Science in physics, Technical University Dortmund, Germany
- 10/2013 - 10/2016 Bachelor of Science in physics, Technical University Dortmund, Germany  
Bachelor thesis: *Asymptotische Sicherheit in Eich-Yukawa-Theorien*  
Supervisors: Prof. Dr. G. Hiller and Dr. K. Kowalska
- 2005 - 2013 Schiller Schule Bochum, General qualification for university entrance (German: Abitur)

## Research experience

- Since 07/2019 Scientific Assistant, Institute of Physics, University of Rostock, Germany
- Since 10/2017 Visiting Researcher, SLAC National Accelerator Laboratory, USA
- Since 03/2023 Reviewer for the journal Matter and Radiation at Extremes (MRE)
- Since 02/2023 Reviewer for the journal Contributions to Plasma Physics (CPP)
- Since 03/2022 Reviewer for the journal High Energy Density Physics (HEDP)
- 04/2017 - 10/2017 Research internship, SLAC National Accelerator Laboratory, USA  
Supervisor: Prof. Dr. S.H. Glenzer



---

**Teaching at University of Rostock**

- WS 2022/23 Seminars for *Physics of Dense Plasmas* (received teaching award from the faculty of natural sciences and mathematics)
- WS 2021/22 Seminars for *Physik für Humanmediziner*
- SS 2021 Seminars for *Experimentalphysik II für Lehramt*
- WS 2020/21 Seminars for *Experimentalphysik I für Lehramt*
- SS 2020 Lab course *Grundpraktikum I*
- WS 2019/20 Lab course *Einführungspraktikum Experimentalphysik I*
- SS 2021, WS 2021/22 Co-supervisor of Bachelor theses
- SS 2020 - SS 2023 Advanced lab course *Density Functional Theory Molecular Dynamics Simulations for Carbon*

## List of publications

### Articles included in this thesis

1. M. Schörner, H. Rüter, M. French, and R. Redmer  
*Extending ab initio simulations for the ion-ion structure factor of warm dense aluminum to the hydrodynamic limit using neural network potentials*  
Physical Review B **105**, 174310 (2022)  
12 Seiten
2. M. Schörner, B.B.L. Witte, A.D. Baczewski, A. Cangi, and R. Redmer  
*Ab initio study of shock-compressed copper*  
Physical Review B **106**, 054304 (2022)  
12 Seiten
3. M. Schörner, M. Bethkenhagen, T. Döppner, D. Kraus, L.B. Fletcher, S.H. Glenzer, and R. Redmer  
*X-ray Thomson scattering spectra from DFT-MD simulations based on a modified Chihara formula*  
Physical Review E **107**, 065207 (2023)  
14 Seiten
4. M. Bethkenhagen, B.B.L. Witte, M. Schörner, G. Röpke, T. Döppner, D. Kraus, S.H. Glenzer, and R. Redmer  
*Carbon ionization at gigabar pressures: An ab initio perspective on astrophysical high-density plasmas*  
Physical Review Research **2**, 023260 (2020)  
7 Seiten
5. M. Schörner, T. Döppner, M. Bethkenhagen, M.J. MacDonald, L. Fletcher, C. Allen, B. Bachmann, L. Divol, M. Herrmann, O.L. Landen, P. Neumayer, A. Saunders, B.B.L. Witte, A. Yi, D. Kraus, S.H. Glenzer, and R. Redmer  
*Reaching for the stars with an ab initio perspective on collective x-ray Thomson scattering at the National Ignition Facility*  
submitted at Science (2023)  
8 Seiten
6. G. Röpke, M. Schörner, R. Redmer, and M. Bethkenhagen  
*Virial expansion of the electrical conductivity of hydrogen plasmas*  
Physical Review E **104**, 045204 (2021)  
7 Seiten
7. M. French, G. Röpke, M. Schörner, M. Bethkenhagen, M. Desjarlais, and R. Redmer  
*Electronic transport coefficients from density functional theory across the plasma plane*  
Physical Review E **105**, 065204 (2022)  
9 Seiten

## Articles beyond this thesis

8. T. Döppner, M. Bethkenhagen, D. Kraus, P. Neumayer, D.A. Chapman, B. Bachmann, R.A. Baggott, M. Böhme, L. Divol, R.W. Falcone, L.B. Fletcher, O.L. Landen, M.J. MacDonald, A.M. Saunders, M. Schörner, P.A. Sterne, J. Vorberger, B.B.L. Witte, A. Yi, R. Redmer, S.H. Glenzer, and D.O. Gericke  
*Observing the onset of pressure-driven K-shell delocalization*  
Nature **618**, 270 (2023)  
5 Seiten
9. J. Lütgert, M. Bethkenhagen, B. Bachmann, L. Divol, D.O. Gericke, S.H. Glenzer, G.N. Hall, N. Izumi, S.F. Khan, O.L. Landen, S.A. MacLaren, L. Masse, R. Redmer, M. Schörner, M. Schölmerich, S. Schumacher, N.R. Shaffer, C.E. Starrett, P.A. Sterne, C. Trosseille, T. Döppner, and D. Kraus  
*Platform for probing radiation transport properties of hydrogen at conditions found in the deep interiors of red dwarfs*  
Physics of Plasmas **29**, 083301 (2022)  
9 Seiten
10. A. Descamps, B.K. Ofori-Okai, J.K. Baldwin, Z. Chen, L.B. Fletcher, S.H. Glenzer, N.J. Hartley, J.B. Hasting, D. Khaghani, M. Mo, B. Nagler, V. Recoules, R. Redmer, M. Schörner, P. Sun, Y.Q. Wang, T.G. White, and E.E. McBride  
*Towards performing high-resolution inelastic X-ray scattering measurements at hard X-ray free-electron lasers coupled with energetic laser drivers*  
Journal of Synchrotron Radiation **29**, 931 (2022)  
8 Seiten
11. Z. Chen, X. Na, C.B. Curry, S. Liang, M. French, A. Descamps, D.P. DePonte, J.D. Koralek, J.B. Kim, S. Lebovitz, M. Nakatsutsumi, B.K. Ofori-Okai, R. Redmer, C. Roedel, M. Schörner, S. Skruszewicz, P. Sperling, S. Toleikis, M.Z. Mo, and S.H. Glenzer  
*Observation of a highly conductive warm dense state of water with ultrafast pump-probe free-electron-laser measurements*  
Matter and Radiation at Extremes **6**, 054401 (2021)  
12 Seiten
12. J. Lütgert, J. Vorberger, N.J. Hartley, K. Voigt, M. Rödel, A. Schuster, A. Benuzzi-Mounaix, S. Brown, T.E. Cowan, E. Cunningham, T. Döppner, R.W. Falcone, L.B. Fletcher, E.C. Galtier, S.H. Glenzer, A. Laso Garcia, D.O. Gericke, P.A. Heimann, H.J. Lee, E.E. McBride, A. Pelka, I. Prencipe, A.M. Saunders, M. Schölmerich, M. Schörner, P. Sun, T. Vinci, A. Ravasio, and D. Kraus  
*Measuring the structure and equation of state of polyethylene terephthalate at megabar pressures*  
Scientific Reports **11**, 12883 (2021)  
9 Seiten
13. M.J. MacDonald, A.M. Saunders, B. Bachmann, M. Bethkenhagen, L. Divol, M.D. Doyle, L.B. Fletcher, S.H. Glenzer, D. Kraus, O.L. Landen, H.J. LeFevre, S.R. Klein, P. Neu-

- mayer, R. Redmer, M. Schörner, N. Whiting, R.W. Falcone, and T. Döppner  
*Demonstration of laser-driven, narrow spectral bandwidth x-ray source for collective x-ray scattering experiments*  
Physics of Plasmas **28**, 032708 (2021)  
8 Seiten
14. M. Frost, E.E. McBride, M. Schörner, R. Redmer, and S.H. Glenzer  
*Sodium-potassium system at high pressure*  
Physical Review B **101**, 224108 (2020)  
7 Seiten
15. N.J. Hartley, S. Brown, T.E. Cowan, E. Cunningham, T. Döppner, R.W. Falcone, L.B. Fletcher, S. Frydrych, E.C. Galtier, E.J. Gamboa, A. Laso Garcia, D.O. Gericke, S.H. Glenzer, E. Granados, P.A. Heimann, H.J. Lee, M.J. MacDonald, A.J. MacKinnon, E.E. McBride, I. Nam, P. Neumayer, A. Pak, A. Pelka, I. Prencipe, A. Ravasio, M. Rödel, K. Rohatsch, A.M. Saunders, M. Schölmerich, M. Schörner, A. Schuster, P. Sun, T. Van Driel, J. Vorberger, and D. Kraus  
*Evidence for Crystalline Structure in Dynamically-Compressed Polyethylene up to 200 GPa*  
Scientific Reports **9**, 4196 (2019)  
7 Seiten
16. D. Kraus, N.J. Hartley, S. Frydrych, A. Schuster, K. Rohatsch, M. Rödel, T.E. Cowan, S. Brown, E. Cunningham, T. Van Driel, L.B. Fletcher, E.C. Galtier, E.J. Gamboa, A. Laso Garcia, D.O. Gericke, E. Granados, P.A. Heimann, H.J. Lee, M.J. MacDonald, A.J. MacKinnon, E.E. McBride, I. Nam, P. Neumayer, A. Pak, A. Pelka, I. Prencipe, A. Ravasio, R. Redmer, A.M. Saunders, M. Schölmerich, M. Schörner, P. Sun, S.J. Turner, A. Zettl, R.W. Falcone, S.H. Glenzer, T. Döppner, and J. Vorberger  
*High-pressure chemistry of hydrocarbons relevant to planetary interiors and inertial confinement fusion*  
Physics of Plasmas **25**, 056313 (2018)  
9 Seiten
17. A. Descamps, B.K. Ofori-Okai, O. Bistoni, Z. Chen, E. Cunningham, L.B. Fletcher, N.J. Hartley, J.B. Hasting, D. Khaghani, M. Mo, B. Nagler, V. Recoules, R. Redmer, M. Schörner, D.G. Senesky, P. Sun, H-E. Tsai, T.G. White, S.H. Glenzer, and E.E. McBride  
*Evidence for phonon hardening in laser excited gold using X-ray diffraction at a hard X-ray free electron laser*  
Submitted at Science Advances (2023)  
6 Seiten
18. J. Lütgert, P. Hesselbach, M. Schörner, V. Bagnoud, R. Belikov, B. Heuser, O. Humphries, B. Lindqvist, C. Qu, D. Riley, G. Schaumann, S. Schumacher, A. Tauschwitz, D. Varentsov, K. Weyrich, X. Yu, B. Zielbauer, Zs. Major, P. Neumayer, and D. Kraus  
*Temperature and Graphitization Measurement of Ion-Heated Diamond using X-ray Diag-*

*nostics*

In preparation (2023)

19. A. Descamps, M. Schörner, R. Redmer, S.H. Glenzer, and E.E McBride

*Measurement of ion acoustic modes in warm dense argon*

In preparation (2023)

20. M. Bethkenhagen<sup>†</sup>, M. Schörner<sup>†</sup>, and R. Redmer

†: Equal contribution

*Ab initio simulations of beryllium at extreme pressures*

In preparation (2023)

## List of talks

- *Ab initio simulations for the ion-ion structure factor of warm dense matter in the hydrodynamic limit*  
28th AIRAPT and 60th EHPRG Conference,  
Edinburgh, Scotland (2023)
- *Dynamic behavior of matter at high energy densities*  
Defense of Helmholtz Institute for High Energy Density at university of Rostock,  
Rostock, Germany (2023)
- *X-ray Thomson scattering spectra from DFT-MD simulations based on a modified Chihara formula*  
43rd Workshop on High-Energy-Density Physics with laser and Ion beams,  
Hirschegg, Austria (2023)
- *Ab initio study of shock-compressed copper*  
10th Joint Workshop on High Pressure, Planetary and Plasma Physics (HP4),  
Brussels, Belgium (2022)
- *Ab initio simulations for the ion-ion structure factor of warm dense aluminum*  
Strongly Coupled Coulomb Systems (SCCS) 2022,  
Görlitz, Germany (2022)
- *Ab initio simulations for the ion-ion structure factor of warm dense aluminum and copper*  
DFG Research Unit update meeting,  
Berlin, Germany (2022)
- *Ab initio simulations for the ion-ion structure factor of warm dense aluminum*  
DFT Methods for matter under extreme conditions 2022,  
Görlitz, Germany (2022)
- *Ab initio simulations for the ion-ion structure factor of warm dense aluminum*  
42nd Workshop on High-Energy-Density Physics with laser and Ion beams,  
Online meeting (2022)
- *Collective x-ray Thomson scattering for conditions inside brown dwarfs using the National Ignition Facility*  
Graduate school of the institute of physics at university of Rostock,  
Rostock, Germany (2021)
- *Collective x-ray Thomson scattering for conditions inside brown dwarfs using the National Ignition Facility*  
Matter in extreme conditions: from material science to planetary physics (MECMAT-PLA),  
Online meeting (2021)



- 
- *Transport Properties and Dynamic Structure of Iron Near Earth's Core Conditions*  
9th Joint Workshop on High Pressure, Planetary and Plasma Physics (HP4),  
Münster, Germany (2021)

---

## List of poster presentations

- Matter in Extreme Conditions: from MATerial science to Plasmas for Laboratory Astrophysics,  
Montgenevre, France (2022)
- 17th International Conference on the Physics of Non-Ideal Plasmas,  
Dresden, Germany (2021)
- Matter under Extreme Conditions, 732. WE-Heraeus-Seminar,  
Online conference (2020)
- High Power Laser Workshop at SLAC National Accelerator Laboratory,  
Menlo Park, USA (2019)
- Hands-On DFT and Beyond,  
Barcelona, Spain (2019)



# Danksagung

Zunächst möchte ich meinem Betreuer Ronald Redmer für die Bereitstellung des Themas und die fortlaufende Ermutigung, neue interessante Aspekte des Themas zu verfolgen danken. Ich konnte mich zu jeder Zeit auf kompetente und hilfreiche Ratschläge bezüglich wissenschaftlicher, aber auch persönlicher Themen verlassen. Weiterhin danke ich Siegfried Glenzer, der es mir über den Forschungsaufenthalt in den USA ermöglicht hat, das Forschungsfeld von WDM kennenzulernen. Seitdem hat er mich trotz der komplizierten Coronazeit immer aus den USA unterstützt. Von Bastian Witte habe ich viele der Grundlagen der WDM Theorie während meiner Masterzeit gelernt und von Martin French konnte ich immer kompetenten Rat erwarten, wenn sich mir Fragen gestellt haben. Meiner Büronachbarin in den ersten Monaten meiner Doktorzeit, Mandy Bethkenhagen, spreche ich auch großen Dank aus für die vielen Sachen, die ich in dieser Zeit gelernt habe. Obwohl sie seitdem in anderen Ländern gelebt hat, hat Mandy meine gesamte Doktorzeit mit begleitet und insbesondere für diese Arbeit zahllose hilfreiche Kommentare gegeben. Außerdem möchte ich der gesamten AG Statistische Physik, aber auch der AG Hochenergiedichtephysik von Dominik Kraus für ein wunderbares Arbeitsklima danken. Speziell muss ich mich bei Anna Julia, Martin P. und Clemens bedanken, die mich während meiner gesamten Doktorzeit begleitet haben und auf die ich mich immer für ein gutes Gespräch und ein bisschen Ablenkung verlassen konnte. I also want thank Argha for being my punching bag every now and then. It is greatly appreciated!

Außerhalb der Arbeit möchte ich mich bei meinen alten Schulfreunden und allen, die unserem Freundeskreis seitdem hinzugestoßen sind, bedanken. Vor allem bei Jan möchte ich mich bedanken. Auch wenn du am anderen Ende von Deutschland wohnst, tut es doch immer gut deine Stimme zu hören. Ebenso danke ich meinen Teamkollegen vom Basketball, allen voran Laurenz. Die sportliche Tätigkeit und die gute Unterhaltung beim Training war immer ein wichtiger Ausgleich zu der Arbeit. Der größte Dank gilt meiner Familie. Meine Eltern haben mich während meiner gesamten Ausbildung immer unterstützt und ich wusste, dass sie bei jeder meiner Entscheidungen voll hinter mir stehen würden. Auf meine "kleine" Schwester kann ich mich immer verlassen und ich kann ihr nicht genug für die vielen Telefonate und Diskussion bezüglich dieser Arbeit danken. Letztlich möchte ich meiner Freundin Marie danken. Ohne dich wäre diese Arbeit nicht möglich gewesen und du kannst dir nicht vorstellen, wie wichtig es war, dich auch zu stressigen Zeiten immer an meiner Seite zu wissen!

# Selbstständigkeitserklärung

Ich versichere hiermit an Eides statt, dass ich die vorliegende Arbeit selbstständig angefertigt und ohne fremde Hilfe verfasst habe. Dazu habe ich keine außer den von mir angegebenen Hilfsmitteln und Quellen verwendet und die den benutzten Werken inhaltlich und wörtlich entnommenen Stellen habe ich als solche kenntlich gemacht.

Rostock, den 21. August 2023

Maximilian Schörner